New Insights into Cosmological Tensions

Department of Physics
PhD in Astronomy, Astrophysics and Space Science (XXXVIII cycle)

Arianna Favale
ID number 2077198

Advisors
Prof. Marina Migliaccio
Dr. Adrià Gómez-Valent

Academic Year 2024/2025

This doctoral thesis has been carried out under a cotutela agreement between Sapienza University of Rome and the University of Barcelona.

New Insights into Cosmological Tensions

PhD thesis.

Sapienza University of Rome, University of Rome Tor Vergata, Istituto Nazionale di Astrofisica, University of Barcelona

© 2025 Arianna Favale. All rights reserved

Version: November 27, 2025

Author's email: arianna.favale@uniroma1.it

Dedicated to my family.

Abstract

From the tiny anisotropies of the cosmic microwave background (CMB) to the distribution of galaxies in the large-scale structure (LSS), observations across multiple wavelengths and redshift ranges have converged on a simple yet powerful theoretical framework: the ΛCDM model. However, as measurement precision has improved, significant tensions have emerged between parameters inferred from early- and late-Universe probes, including CMB, Type Ia supernovae (SNIa) and baryon acoustic oscillations (BAO). The most prominent is the *Hubble tension*, a $\gtrsim 5\sigma$ discrepancy between the value of the Hubble parameter, H_0, inferred from the CMB under ΛCDM and that measured independently via the local distance ladder. Alongside other inconsistencies, such as those in the growth of structure, this challenges the completeness of the standard cosmological model and raises the pressing question of whether these tensions arise from unaccounted systematics or new physics.

This thesis addresses these issues from a *model-independent* perspective, a timely and essential approach to refining the statistical interpretation of current cosmological tensions. By combining complementary cosmological probes, we reassess the calibration of the cosmic distance ladder, test fundamental relations underpinning the ΛCDM model and its extensions, and evaluate the robustness and mutual consistency of several key cosmological observables.

Leveraging data from BAO, SNIa, and cosmic chronometers, we estimate the spatial curvature of the Universe and refine the distance ladder calibration independently of the main drivers of the current tensions. This methodology is further extended to calibrate high-z probes – Gamma-Ray Bursts and Quasars – yielding a Hubble diagram up to $z \sim 7$ which provides an independent avenue for probing the expansion history beyond the reach of current SNIa and BAO data. In parallel, this thesis examines possible late-time solutions to the Hubble tension by investigating the shape of the Hubble function, the calibration of SNIa, and the impact of different BAO datasets. A new diagnostic is indeed introduced to test the consistency of different distance measurements, which allows us to reveal an unexpectedly strong mismatch between anisotropic and angular BAO data, underscoring the need for independent verification and methodology for future surveys. We further contribute to studies of LSS by advocating alternative LSS parameterizations that reduce biases in evaluating the growth of structure arising from the dependence on H_0. This approach provides a more physically consistent framework for assessing the impact of new physics on structure formation and the Hubble tension.

This thesis provides novel, data-driven insights into key challenges in modern cosmology, critically assessing the ΛCDM framework and paving the way for future high-precision surveys to uncover the physical origin of current cosmological tensions.

Resum

Des de les minúscules anisotropies del fons còsmic de microones (CMB) fins a la distribució de les galàxies que conformen l'estructura a gran escala de l'univers, les observacions en múltiples longituds d'ona i rangs de desplaçament cap al vermell han convergit en un marc teòric senzill, però d'alt nivell predictiu: el model ΛCDM. Malgrat això, amb la millora de la precisió de les mesures observacionals han aparegut tensions significatives entre els paràmetres inferits a partir de l'anàlisi del CMB i els obtinguts fent ús d'altres mitjans, com ara les supernoves de tipus Ia (SNIa) i les oscillacions acústiques de barions (BAO). La més destacada és la tensió de Hubble, una discrepància de més de 5σ entre el valor del paràmetre de Hubble, H_0, inferit del CMB assumint el model ΛCDM i el mesurat de manera independent mitjançant l'escala de distàncies local. Juntament amb altres inconsistències, com les relacionades amb la formació d'estructura, això posa en dubte la completesa del model cosmològic estàndard i planteja la qüestió urgent de si aquestes tensions deriven d'errors sistemàtics en un o més conjunts de dades o bé de nova física. Aquesta tesi aborda aquestes qüestions des d'una perspectiva que és en gran mesura independent de qualsevol model, un enfocament oportú i essencial per refinar la interpretació estadística de les tensions cosmològiques actuals. Combinant conjunts de dades complementaris, analitzem la calibració de l'escala de distàncies còsmica, testegem assumpcions fonamentals del model ΛCDM i les seves extensions, i avaluem la robustesa i consistència de diversos observables cosmològics que juguen un paper clau en la formulació i la discussió de les tensions. Utilitzant dades de BAO, SNIa i cronòmetres còsmics, mesurem la curvatura de l'Univers i refinem la calibració de l'escala còsmica de distàncies de manera independent a les dades que impulsen les tensions actuals (el CMB i la calibració de SNIa de SH0ES). Aquesta metodologia s'estén, a més, per calibrar objectes més llunyans que també poden funcionar com a espelmes estàndard – esclats de raigs gamma (GRB) i quàsars –, obtenint un diagrama de Hubble fins a $z \sim 7$ que ofereix una via alternativa per explorar la història de l'expansió de l'univers més enllà de l'abast de les dades actuals de SNIa i BAO. Aquesta tesi també examina possibles solucions en l'univers tardà a la tensió H_0, investigant la forma de la funció de Hubble, la calibració de les SNIa i l'impacte de diferents conjunts de dades de BAO a baix z. S'hi introdueix un nou diagnòstic per comprovar la consistència de diverses mesures de distàncies cosmològiques que permet revelar una discrepància inesperadament forta entre les dades de BAO anisotròpiques i angulars, posant de manifest la necessitat de verificar la seva consistència en futurs estudis. A més, contribuïm als estudis de formació d'estructura a gran escala defensant parametritzacions alternatives de l'amplitud de l'espectre de potències amb l'objectiu de reduir els biaixos en la seva

quantificació. Aquest enfocament proporciona un marc físicament més coherent per avaluar l'impacte de nova física sobre la formació d'estructura i la tensió de Hubble. En conjunt, aquesta tesi ofereix noves aportacions als principals reptes de la cosmologia moderna, avaluant críticament el model ΛCDM i obrint noves vies per tal que futurs estudis puguin desvetllar l'origen físic de les tensions cosmològiques actuals.

List of publications

The research carried out during this PhD and on which this thesis is about has resulted in the following publications:

1. **Favale A.**, Dainotti M. G., Gómez-Valent A. & Migliaccio M., "Refining the Cosmic Distance Scale: on the calibration of Quasars". *In prep.*

2. **Favale A.**, Gómez-Valent A. & Migliaccio M., "Revisiting model-independent constraints on spatial curvature and cosmic ladders calibration: updated and forecast analyses". arXiv: `2511.19332 [astro-ph.CO]`.

3. Ruchika, Mukherjee P. & **Favale A.**, "Revisiting Gaussian Process reconstruction for cosmological inference: the Generalised GP (Gen GP) framework". arXiv: `2510.03742 [astro-ph.CO]`.

4. *CosmoVerse* (including **Favale A.**), "The CosmoVerse White Paper: Addressing observational tensions in cosmology with systematics and fundamental physics". *Phys.Dark Univ.* (2025) 101965.
DOI: `https://doi.org/10.1016/j.dark.2025.101965`. arXiv: `2504.01669 [astro-ph.CO]`.

5. Forconi M., **Favale A.** & Gómez-Valent A., "Illustrating the consequences of a misuse of σ_8 in cosmology". *Phys.Rev.D* 112 (2025) 2, 023517.
DOI: `https://doi.org/10.1103/rpf5-ldks`. arXiv: `2501.11571 [astro-ph.CO]`.

6. **Favale A.**, Gómez-Valent A. & Migliaccio M., "Quantification of 2D vs 3D BAO tension using SNIa as a redshift interpolator and test of the Etherington relation". *Phys. Lett. B* 858 (2024) 139027.
DOI: `10.1016/j.physletb.2024.139027`. arXiv: `2405.12142 [astro-ph.CO]`.

7. **Favale A.**, Dainotti M. G., Gómez-Valent A. & Migliaccio M., "Towards a new model-independent calibration of Gamma-Ray Bursts". *JHEAp* 44 (2024) 323-339. DOI: `10.1016/j.jheap.2024.10.010`. arXiv: `2402.13115 [astro-ph.CO]`.

8. Gómez-Valent A., **Favale A.**, Migliaccio M. & Sen, Anjan A., "Late-time phenomenology required to solve H_0 tension in view of the cosmic ladders

and the anisotropic and angular BAO data sets". *Phys. Rev. D* 109 (2024) 2, 023525.
DOI: `10.1103/PhysRevD.109.023525`. arXiv: `2309.07795 [astro-ph.CO]`.

9. **Favale A.**, Gómez-Valent A. & Migliaccio M., "Cosmic chronometers to calibrate the ladders and measure the curvature of the Universe. A model-independent study". *Mon. Not. Roy. Astron. Soc.* 523 (2023) 3, 3406-3422.
DOI: `10.1093/mnras/stad1621`. arXiv: `2301.09591 [astro-ph.CO]`.

Part of this scientific production has contributed to the following conference proceedings:

1. **Favale A.**, Gómez-Valent A. & Migliaccio M., "Low-redshift model-independent approach to calibrate the ladders and measure the curvature of the universe". Proceedings of the *17th Marcel Grossmann Meeting*, Pescara, Italy, July 2024.

2. **Favale A.**, Gómez-Valent A. & Migliaccio M., "A model-independent treatment of cosmic ladder calibration and Ω_k measurement through low-z observations". Proceedings of the *58th Rencontres de Moriond*, La Thuile, Italy, April 2024.

Contents

Abstract **v**

Resum **vii**

List of publications **ix**

Introduction **1**

I Cosmology – Theory and Observations **5**

1 The Standard Model of Cosmology **7**
1.1 Foundations of standard Cosmology 8
1.2 Hot Big Bang Model 11
1.3 Distances in Cosmology 29

2 The cosmic distance ladder **33**
2.1 Standard candles and the local distance ladder 34
2.1.1 Standardizable candles 38
2.2 Standard rulers and the inverse distance ladder 43

3 Tensions and current status of ΛCDM **47**
3.1 The Hubble tension 48
3.2 The growth tension 52
3.3 Other anomalies 56
3.4 Alternatives to the ΛCDM model 58

4 Observables **65**
4.1 Cosmic Chronometers 66
4.2 Supernovae of Type Ia 69
4.3 Baryon Acoustic Oscillations 71
4.4 Cosmic Microwave Background 75
4.5 Gamma-Ray Bursts 76
4.6 Quasars 78

II Statistical methods **81**

5 Bayesian Inference **83**
5.1 Gaussian Processes 86
5.2 Markov Chain Monte Carlo 90

III Model-independent calibration of the cosmic distance ladder **95**

6 Calibrating the ladders and measuring Ω_k **97**
6.1 Reconstructing background quantities: the role of GPs 99
6.2 Consistency tests for low-z data and tests of some theoretical assumptions behind ΛCDM 102
6.2.1 Testing the constancy of M 102
6.2.2 Testing the homogeneity property of the Universe 104
6.2.3 Internal consistency of 3D BAO data 104
6.3 Simultaneous calibration of the ladders and measurement of Ω_k . . . 107
6.3.1 Constraints from current data 109
6.3.2 Constraints from current data: an updated analysis 114
6.3.3 Forecasts 119
6.4 Final discussion 125

IV Extending the distance ladder beyond $z \sim 2.5$ **129**

7 GRBs calibration **131**
7.1 Calibrating the 3D and 2D Dainotti relations 132
7.2 Redshift evolution corrections 141
7.3 Extended ladder with GRBs 144
7.4 Final discussion 146

8 QSOs calibration **149**
8.1 Calibrating the Risaliti-Lusso relation 149

V On the consistency of BAO data and their impact on low-z solutions to the Hubble tension **155**

9 A late-time solution to the H_0 tension in view of BAO data **157**
9.1 The modification to $H(z)$ at low-redshifts 159
9.2 The weak energy condition 162
9.3 Results: the impact of the BAO data 164
9.4 Results of the WEC violation 170
9.5 Final discussion 172

10 Tension between 2D and 3D BAO data sets **175**
10.1 A model-independent estimator for the tension between anisotropic and angular BAO 177

10.2 Test of the Etherington relation 182
10.3 Final discussion 184

VI LSS tensions: consequences of using σ_8 in cosmology 187

11 The bias introduced by σ_8 189
11.1 The problem in light of current data 190
11.1.1 Some first examples 190
11.1.2 σ_8 vs σ_{12} in model fitting analyses 194
11.2 Final discussion 202

Conclusions and Prospects 205

Bibliography 211

Appendix A 261

Appendix B 265

Appendix C 267

List of figures 276

List of tables 277

Introduction

The past century has witnessed a remarkable advancement in our understanding of the Universe, leading to the establishment of the standard cosmological model, commonly referred to as ΛCDM. This "concordance model" provides a coherent picture of cosmic evolution, successfully describing the expansion history of the Universe, the growth of large-scale structures, and the tiny anisotropies observed in the cosmic microwave background (CMB). Its empirical foundation rests on several key observations: precise measurements of the CMB, the imprint of baryon acoustic oscillations (BAO) in the large-scale distribution of galaxies, and the measured apparent magnitudes of Type Ia supernovae (SNIa). Despite these successes, ΛCDM relies on strong theoretical assumptions, including the validity of General Relativity at all length and time scales, the existence of dark matter, and a constant source of late-time cosmic acceleration – the cosmological constant Λ, whose origin remains elusive. Quantum field theory predicts a vacuum energy density vastly larger than what is inferred from cosmology – a discrepancy of many orders of magnitude, known as the cosmological constant problem. Furthermore, despite evolving differently over cosmic history, the energy densities of matter and dark energy are of the same order precisely today, a coincidence problem that, along with other issues, leads ΛCDM to face profound conceptual challenges.

Deviations from the standard cosmological paradigm are actually still allowed by the data. In fact, over the last decade, a growing body of evidence from observations has revealed discrepancies that challenge the completeness of the model and our understanding of the cosmos, ushering in an intriguing and exciting era for cosmology.

In particular, several non-negligible tensions have emerged between ΛCDM and some background and large-scale structure (LSS) observations.

Foremost among these is the so-called "Hubble tension": a striking disagreement between local and early-Universe measurements of the Hubble-Lemaître parameter, H_0, currently exceeding 5σ. From Edwin Hubble's groundbreaking discovery of the Universe's expansion nearly a century ago to the precision measurements enabled by the Planck satellite, cosmologists have sought ever more accurate determinations of H_0, which sets the absolute scale of cosmic distances, time, and energy content. Yet, despite decades of progress, there is still no consensus value for it.

The local distance ladder, built on observations of Cepheids and SNIa, provides a direct, local measurement of H_0 by linking absolute distances of nearby objects to increasingly distant cosmic tracers. In contrast, the CMB and BAO yield H_0 indirectly, through the physics of the early Universe. This duality has transformed H_0 from a single number into a powerful probe of cosmology: any tension between these approaches may indicate unknown systematic effects or, more intriguingly, new

physics beyond the standard cosmological model. Potential explanations include an ultra-late time transition in the SNIa absolute magnitude, M, an extension of the SNIa standardization method, or a change of the comoving sound horizon at the baryon drag epoch, r_d, which can be thought of as the BAO calibrator. The latter involves early- and late-time modifications of the gravitational sector, early dark energy, primordial magnetic fields or time-varying physical constants at the last scattering surface. Alternative probes, such as cosmic chronometers (CCH), strong lensing time delays, or gravitational-wave standard sirens, have yet to resolve this tension.

Alongside the Hubble tension, discrepancies in the growth of cosmic structure have also emerged. Weak lensing surveys and galaxy clustering observations of the late-Universe matter distribution appear smoother than predicted by the CMB/ΛCDM cosmology, thereby pointing to a lower amplitude of matter fluctuations, often expressed in terms of the σ_8 or S_8 parameters. Depending on the probe, these deviations reach 2–3σ significance. Simultaneously resolving the Hubble and growth tensions remains extremely challenging, as no single cosmological model convincingly addresses both. Remarkably, recent analyses combining CMB, SNIa, and BAO data have reported strong hints of a non-constant evolution of dark energy, potentially ruling out the cosmological constant Λ and further challenging the standard cosmological scenario. Other minor anomalies – e.g., small-scale inconsistencies in the CMB or lack of power at low multipoles of the CMB temperature power spectrum – further complicate the entire puzzle. Whether these arise from new physics or residual systematics remains a critical open question in modern cosmology.

To tackle these challenges, model-independent approaches offer a unique window in this context. Rather than assuming a specific cosmological model, these methods extract information directly from observational data, allowing the Universe to "speak for itself."

The motivation behind this thesis stems from these considerations. By focusing on a model-independent perspective, we aim to explore the behavior of the Universe across cosmic time, investigate the calibration of the cosmic distance ladder, and understand the interplay between local and high-redshift measurements. We examine a variety of relevant observational data sets, including CCH, SNIa, and BAO measurements. Each of these probes contributes complementary information: CCH provide direct measurements of $H(z)$, SNIa act as standard candles over a wide range of redshifts, and BAO encode the sound horizon scale imprinted on the distribution of matter, providing us a standard ruler of our cosmos. Since both M and r_d are deeply involved in the current discrepancy on H_0, it is of utmost importance to measure them independently of the CMB or the first rungs of the local distance ladder. Their robust calibration not only enables a critical assessment of proposed solutions to the Hubble tension, but also provides a powerful consistency check against results derived from standard methods.

Beyond traditional distance indicators, this thesis also investigates the potential of Gamma-Ray Bursts (GRBs) and Quasars (QSOs) as "standardizable candles". These sources rank among the most luminous persistent objects in the Universe, observable up to redshifts $z \sim 7$, well beyond the reach of SNIa. By exploiting specific empirical relations in their emission properties, it is possible to construct a Hubble diagram for both, thereby extending cosmological analyses into largely

unexplored high-redshift regimes. Although the intrinsic scatter in these relations is greater than that of SNIa, careful calibration and selection of high-quality samples significantly reduce the dispersion, rendering them valuable for cosmology. This approach offers a unique opportunity to test the consistency of cosmological models at high redshift and provides an independent probe of the expansion history. In this way, GRBs and QSOs complement traditional distance indicators, reaching epochs where potential deviations from ΛCDM may be more pronounced.

Among the challenges we face is ensuring the consistency of the data sets we rely upon. BAO provide a clear example: from the same tracers catalog, one can extract either angular or anisotropic measurements, depending on the methodology. Despite their common origin, these two routes paint contrasting pictures when probing late-time solutions to the Hubble tension. Therefore, understanding what is causing this mismatch is crucial to ensure robust conclusions.

Lastly, we explore the insights offered by LSS measurements, in particular through σ_8, which captures the amplitude of matter fluctuations on a scale tied to H_0. This intrinsic connection makes it challenging to interpret LSS data directly, or to disentangle the effects when testing models that aim to resolve the Hubble or growth tensions.

With these considerations in mind, we structure this thesis as follows.

Chapter 1 begins our journey, guiding the reader through the evolution of the cosmos from its earliest moments to the formation of the large-scale structures we observe today. Along the way, we examine the theoretical conundrums posed by the standard cosmological model, introduce the metric that describes space-time, and review the evolution of the cosmic species that constitute our Universe. Within this framework, after defining essential concepts of cosmic distances, Chapter 2 leads the reader up the *cosmic distance ladder*, which allows us to reach distant objects using standard candles and standard rulers. We also discuss other astrophysical phenomena that can be treated as standardizable candles, setting the stage for understanding Chapter 3, where we comprehensively review current observational evidence of significant discrepancies within the standard model. This includes Hubble tension, growth tension, and other minor anomalies that affect the robustness of ΛCDM, along with an overview of alternative models proposed to resolve these issues. By this point, the reader gains a clear understanding of the main directions and motivations underlying the research carried out in this thesis.

In Chapter 4, we present the key observables used throughout this thesis — CCH, SNIa, BAO, CMB, GRBs, and QSOs. While these probes were introduced in previous chapters, here we delve deeper into the specific data sets, highlighting their main characteristics and providing insights into the methodologies used to extract the relevant measurements. Chapter 5 then introduces the main statistical tools exploited in our analyses. A Bayesian framework underpins our approach, complemented by a strong emphasis on minimizing assumptions about the underlying cosmological model. In particular, we discuss *Gaussian Processes*, a Machine Learning methodology that helps us to pursue this objective, allowing for a model-independent reconstruction of cosmological functions directly from the data.

Having established the necessary background and methodology, we are ready to embark on the main investigations of this thesis.

A central theme is the calibration of the cosmic distance ladder in a model-

independent manner. By combining CCH, SNIa, and BAO distances, in Chapter 6, we develop a methodology to simultaneously constrain the calibrators of the ladders, M and r_d, together with the spatial curvature of the Universe, Ω_k, a pivotal parameter in cosmology which encodes information about the early Universe. This approach not only allows us to test some of the fundamental assumptions underlying ΛCDM but also enables an independent determination of the Hubble parameter, free from the main drivers of the current tensions. In this way, our methodology provides a framework for assessing whether these tensions arise from systematic uncertainties in the data, intrinsic limitations of the model, or hints of new physics. Building on this potential, we also present forecast analyses that explore the constraining power of upcoming surveys, highlighting how improvements in redshift coverage or data quality could most significantly enhance our results.

However, we know that current distance indicators only reach $z \sim 2.5$, motivating the exploration of probes that extend the cosmic ladder to higher redshifts. In Chapters 7 and 8, we extend our methodology to calibrate GRBs and QSOs, respectively, exploiting specific relations in their emission properties and evaluating their current strengths and limitations as high-redshift cosmological probes.

In Chapter 9, we turn our attention to the inverse distance ladder, examining the role of its main characters, the BAO data, in the quest for a possible late-time resolution of the Hubble tension. Interestingly, we will see that anisotropic (3D) BAO favor distinct shapes for $H(z)$ and $M(z)$, as well as a different evolution of the effective dark energy fluid, compared to angular (2D) BAO. The latter, being less affected by model assumptions, exhibit better agreement with the local determination of H_0, underscoring the challenges in assessing the reliability of these complementary measurements. Indeed, in Chapter 10, we will clearly illustrate that 2D and 3D BAO are found to be in tension at the 2.5σ-4.6σ level, depending on the SNIa data sets employed. This result is obtained by a model- and calibrator-independent method, paving the way for future applications once BAO measurements are extracted with a unified methodology.

In Chapter 11, we shift our attention to LSS studies. Here, we reflect on how the commonly used parameter σ_8 can sometimes mislead our interpretation of clustering data, since its definition depends on the value of the Hubble parameter. We show that adopting alternative LSS parameterizations, such as σ_{12} – defined at a scale independent of H_0 – provides a more robust characterization of structure formation and leads to more reliable conclusions in fitting analyses of models proposed to alleviate current tensions.

Finally, we summarize the main findings of this thesis and outline possible directions for future research.

After the main matter of the thesis, the Bibliography, Appendices and lists of figures and tables can be found.

All the work presented in this thesis has been conducted under the *cotutela* regime between Sapienza University of Rome and University of Barcelona.

Part I

Cosmology – Theory and Observations

Chapter 1

The Standard Model of Cosmology

Cosmology encompasses the study of the Universe — its origin, composition, and evolution. The modern era of cosmology began in 1915, when Albert Einstein formulated the theory of General Relativity (GR) [1], a profound and elegant description of gravitation. In 1929, Edwin Hubble discovered the empirical relationship between the recessional velocity of galaxies and their distances, allowing for the first measurement of the Hubble parameter [2]. This result confirmed the theoretical predictions of Georges Lemaître [3] (1927) and the dynamic solutions to Einstein equations obtained by Alexander Friedmann [4, 5] (1922–1924), which ascribe this phenomenon to the expansion of the Universe. These results established the picture of an expanding Universe originating from a hot and dense singularity, the Big Bang. Two major predictions soon reinforced this paradigm.

The first was the theory of primordial nucleosynthesis, described by Alpher, Bethe & Gamow (1948), which explains the observed light-element abundances in the first minutes of the Universe and leaves some verifiable predictions. Notably, the deuterium-to-helium ratio (D/He) and the helium-to-baryon density ratio $\rho(^4\mathrm{He})/\rho_b$, were crucial to validate the theory because no other astrophysical processes could explain their measured values [6].

The second was the Cosmic Microwave Background (CMB), the relic radiation from the epoch of last scattering, first predicted in 1965 by Dicke et al. [7] and accidentally discovered the same year by Penzias & Wilson [8]. The CMB became a cornerstone of modern cosmology. Its precise measurement began with the COBE satellite in the 1990s, which confirmed its near-perfect blackbody spectrum [9], strongly supporting the Hot Big Bang model. Subsequent missions — WMAP (Wilkinson Microwave Anisotropy Probe) [10], *Planck* [11], ACT (Atacama Cosmology Telescope) [12] — have refined our understanding of its temperature anisotropies, revealing the primordial fluctuations that seeded the large-scale structure (LSS) of the Universe.

At the end of the 20th century, two independent research groups, led by Riess et al. [13] and Perlmutter et al. [14], showed through Type Ia supernova observations that cosmic expansion is accelerating, implying — under the assumption of GR — a dominant energy component with negative pressure, termed *dark energy*. Although

dark energy appears to account for most of the current energy budget, its fundamental nature remains elusive.

In this Chapter, we provide the reader with an overview of the predictions and probes introduced in this preface. Alongside a concise introduction to the essential concepts of cosmology, we present a rich picture of the standard cosmological model, also known as ΛCDM. The model considers an expanding Universe with geometry described by Riemannian principles and dynamics governed by GR. The present energy budget consists of baryonic matter and radiation ($\sim 5\%$), cold dark matter ($\sim 27\%$), and a cosmological constant ($\sim 68\%$) driving acceleration. The large-scale structure arises from the growth of primordial density perturbations amplified after an early phase of inflation, a rapid expansion occurring $\sim 10^{-35}$s after the Big Bang and proposed in the late 1970s by Alan Guth and A. Starobinsky and A. D. Linde [15, 16, 17]. However, while ΛCDM successfully explains a wide range of data, persistent observational tensions and our incomplete understanding of its main components suggest the need for further refinement. This discussion will be addressed in Chapter 3 and paves the way for the research carried out in this thesis.

1.1 Foundations of standard Cosmology

Focusing on the description of the Cosmos at the largest scales, any viable cosmological model can safely disregard both weak and strong nuclear forces, since their interaction ranges are extremely short, of order 10^{-15} m and 10^{-18} m, respectively [18]. Even though baryonic matter tends to be ionized on scales larger than a few kiloparsecs, the Universe as a whole is electrically neutral on average, which justifies neglecting electromagnetic interactions as well. Consequently, the only fundamental interaction relevant for a cosmological description is gravity, which, according to our current knowledge, is accurately formulated by Einstein's theory of General Relativity [19, 20, 21].

Within the framework of GR, once a reference frame is chosen, any event is uniquely specified by four coordinates: three corresponding to its spatial position and one to its temporal occurrence. While in everyday experience *space* and *time* are perceived as separate, GR demonstrates that they are intrinsically linked, forming a single unified entity: *space-time*. The separation between two events in space-time is governed by the metric tensor $g_{\mu\nu}$, a symmetric rank-2 tensor with ten independent components.

Although on small and intermediate scales the matter distribution appears highly inhomogeneous (stars, galaxies, clusters), cosmological models usually assume the validity of the *Cosmological Principle* (hereafter CP) [22, 23], which postulates that the Universe is homogeneous and isotropic when observed on sufficiently large scales (> 100 Mpc):

- **Homogeneity**: the Universe has no privileged spatial location — it looks statistically the same regardless of where the observer is.

- **Isotropy**: the Universe has no preferred direction — from any point, its properties appear identical in all orientations.

The most significant observational evidences of this principle derive from the high degree of isotropy in the CMB. This can be inferred from the fact that we observe a roughly uniform CMB mean temperature T with super-tiny fluctuations of the order of $\sim 10^{-5}$ (see Sec. 1.2). Homogeneity is supported by galaxy survey measurements which show that, when averaged over scales larger than ~ 100 Mpc, the matter distribution appears effectively uniform.

To impose these symmetry requirements on the metric $g_{\mu\nu}$, one first selects a suitable coordinate system. A common choice is the *synchronous gauge*, which corresponds to a family of comoving observers sharing the same time coordinate. In this frame, the mixed time-space components vanish ($g_{0k} = 0$), ensuring clock synchronization, while the purely temporal component satisfies $g_{00} = 1$, guaranteeing a universal flow of time. The cosmic time t then becomes the natural time coordinate. At each instant t, the comoving observers define a spatial hypersurface fully described by the spatial components g_{ik}.

Applying the CP in this gauge yields the Friedmann-Lemaître-Robertson-Walker (FLRW) metric, which takes the (trigonometrical) form [24]

$$ds^2 = c^2 dt^2 - \mathcal{R}^2(t)[d\chi^2 + \Sigma^2(\chi) d\Omega^2]\,, \tag{1.1}$$

where c is the speed of light, $\mathcal{R}(t)$ is the so-called scale factor, χ is a comoving "radial" coordinate (which is fixed for each cosmic observer) and $d\Omega$ includes the infinitesimal solid angle ($d\Omega^2 \equiv d\theta^2 + sin^2(\theta) d^2(\phi)$). In general, $\Sigma(\chi)$ depends on the curvature of the spatial hypersurface (see Fig. 1.1) as

$$\Sigma(\chi) \equiv \begin{cases} \sin(\chi) & \text{if} \quad k = +1 \\ \chi & \text{if} \quad k = 0 \\ \sinh(\chi) & \text{if} \quad k = -1\,. \end{cases} \tag{1.2}$$

The matter content of the Universe can be approximated to a perfect fluid, that is, a fluid with zero viscosity and no heat conduction, which is described by the energy-momentum tensor

$$T_{\mu\nu} = -p g_{\mu\nu} + (p + \rho c^2) u^\mu u^\nu\,, \tag{1.3}$$

with ρ, p, u^μ the proper density, proper pressure and four-velocity of the fluid under consideration. According to the GR, the metric of space-time and the energy content of the Universe are deeply linked through the Einstein equation:

$$G_{\mu\nu} = R_{\mu\nu} - \frac{1}{2} g_{\mu\nu} R = \frac{8\pi G}{c^4} T_{\mu\nu} + \Lambda g_{\mu\nu}\,, \tag{1.4}$$

where $R_{\mu\nu}$ is the Ricci tensor, $R \equiv R^\mu_\mu = g^{\mu\nu} R_{\mu\nu}$ is the Ricci scalar, G is the Newtonian gravitational constant and Λ is the cosmological constant, originally introduced by Einstein to accommodate a static Universe [19].

It is possible to define a normalized scale factor $a(t) = \mathcal{R}(t)/\mathcal{R}_0$, where $\mathcal{R}_0 = \mathcal{R}(t_0)$ is the scale factor today, being t_0 the age of the Universe. It follows that $a = 1$ identifies the present time.

In an expanding Universe, the distance between two well-separated galaxies (i.e. galaxies far enough apart that their mutual gravitational interactions can be

neglected) $l(t)$ is proportional to the scale factor as $l(t) \propto a(t)$ and it changes with velocity

$$v = dl/dt = Hl\,, \tag{1.5}$$

where H is the Hubble expansion rate,

$$H(t) \equiv \frac{\dot{a}}{a}\,. \tag{1.6}$$

The *dot* denotes the time derivative.

At t_0, $H(t_0) \equiv H_0$ and Eq. (1.5) is called the Hubble law. H_0 is the *Hubble-Lemaître parameter*, which quantifies the amount of the expansion as measured today. A full treatment of the importance of this parameter will be done in Chapter 3.

The expansion of the Universe can also be described in terms of the stretching of the observed light wavelength from a distant source, such as a galaxy. If the wavelength detected today is denoted by λ_O and the wavelength at emission by λ_e, then one can redefine the scale factor $a(t)$ using the concept of redshift z:

$$z = \frac{\lambda_O - \lambda_e}{\lambda_e} = \frac{\lambda_O}{\lambda_e} - 1\,. \tag{1.7}$$

To infer the relation between the redshift and the scale factor, we make use of the constancy of the comoving distance between two given galaxies in a FLRW Universe. Two photons emitted consecutively from one galaxy will travel through null geodesics, until reaching the second galaxy, and hence,

$$\chi = c\int_{t_e}^{t_O} \frac{dt}{a(t)} = c\int_{t_e+T_e}^{t_O+T_O} \frac{dt}{a(t)}\,, \tag{1.8}$$

where t_e and t_O are the emission and observation times, and T_e and T_O are the periods of light at the emission and observation points. After a bit of algebra, considering that $a(t)$ remain approximately constant during T_e and T_O, one obtains,

$$\frac{T_e}{a(t_e)} = \frac{T_O}{a(t_O)} \longrightarrow \frac{\lambda_e}{\lambda_O} = \frac{a(t_e)}{a(t_O)}\,. \tag{1.9}$$

If we set $a(t_O) = 1$, using (1.7) we finally obtain,

$$a(t) = \frac{1}{1+z}\,, \tag{1.10}$$

which makes z a convenient parameter for identifying different epochs in the cosmic history.

We can now derive the time dependence of the scale factor in a FLRW metric. Starting from Eq. (1.4) and the energy-momentum tensor $T_{\mu\nu}$ in Eq. (1.3), one obtains the relation connecting the Hubble expansion rate, the spatial curvature, and the matter/energy content of the Universe:

$$H^2 = \left(\frac{\dot{a}}{a}\right)^2 = \frac{8\pi G}{3}\rho - \frac{kc^2}{a^2} + \frac{1}{3}\Lambda c^2 \tag{1.11}$$

$$\frac{\ddot{a}}{a} = -\frac{4\pi G}{3}\left(\rho + \frac{3p}{c^2}\right) + \frac{1}{3}\Lambda c^2\,, \tag{1.12}$$

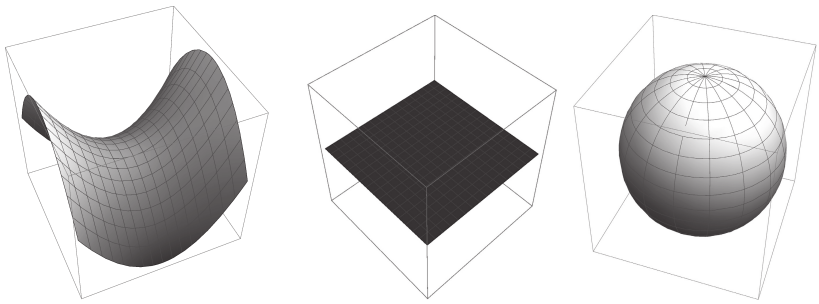

Figure 1.1. Illustrations of homogeneous and isotropic two-dimensional surfaces. The closed (left), flat (middle), and open (right) surfaces correspond to closed ($k = +1$), flat ($k = 0$), and open ($k = -1$) three-dimensional hypersurfaces, respectively [24]. The curvature term modifies the metric by altering the functional form of $\Sigma(\chi)$ in Eq.(1.2).

with ρ and p representing the energy density and the pressure terms of all the cosmic components considered.

Equations (1.11) and (1.12) are known as the *Friedmann equations*. The first one states that, under the assumption of perfect cosmological fluids, the expansion (or contraction) rate is dictated by the energy density, the curvature, and the cosmological constant. The second equation highlights that both the energy density and the pressure of the cosmic fluids determine whether the expansion of the Universe accelerates or decelerates.

Imposing energy conservation ($T_{\mu\nu;\nu} = 0$), one obtains the time evolution of the density of each cosmic component $i = m, r$ (with m denoting pressureless matter and r radiation):

$$\dot{\rho}_i + 3H(\rho_i + p_i) = 0\,, \tag{1.13}$$

with both $p = p(t)$ and $\rho = \rho(t)$ depending on cosmic time. The equation of state of a cosmological fluid relates pressure and density as $p = p(\rho)$, so that, in general

$$p = w\rho c^2\,, \tag{1.14}$$

where w is the equation of state parameter, whose value depends on the type of fluid considered. Under the assumption of a perfect fluid, w remains constant in time, and the density evolution can be obtained from the adiabatic condition in Eq. 1.13, leading to

$$\rho_i \propto a^{-3(1+w_i)}\,. \tag{1.15}$$

Thus, for a non-relativistic component ($w = 0$) the density scales as a^{-3}, while for a relativistic component ($w = 1/3$) it scales as a^{-4}. The cosmological constant in Eq. (1.11) behaves like a vacuum fluid with $w = -1$, so its associated energy density (and pressure) remains constant, $\rho \approx a^0$.

1.2 Hot Big Bang Model

Modern cosmological data are in excellent agreement with the so-called *Hot Big Bang scenario*, according to which the Universe has been expanding since its origin, starting from a state of extremely high density and temperature and gradually

cooling down as the expansion progressed. Among the various realizations of this framework, the ΛCDM ("Lambda Cold Dark Matter") model stands out as the most consistent with present observations (although with some shortcomings, see Chapter 3). In this model, the energy content of the Universe is described in terms of several distinct cosmic fluids:

- **Baryonic matter**, comprising stars, interstellar gas and dust, planets, stellar remnants, and essentially all luminous structures. Being non-relativistic and pressureless, it is characterized by an equation-of-state parameter $w_b = 0$.
- **Cold dark matter (CDM)**, consisting of non-relativistic particles ($w_{\rm CDM} = 0$) which interact only gravitationally and play a fundamental role in forming the potential wells required for baryonic matter collapse. Although not directly observable, CDM reveals its presence through its dynamical effects across many astrophysical and cosmological probes.
- **Relativistic species**, with $w_r = 1/3$, including photons and neutrinos. Their energy contribution is negligible today, but they dominated the energy budget during the earliest epochs. It has to be noticed that neutrino oscillation experiments indicate that at least some neutrino species are massive ($\sum m_\nu \sim 0.06 - 0.12$ eV) [25] and can therefore be non-relativistic today. However, their energy contribution remains subdominant compared to baryons and cold dark matter.
- **Cosmological constant**, an enigmatic component responsible for the present accelerated expansion of the Universe, effectively described by the term Λ in Eq. 1.4, with equation of state $w_\Lambda = -1$ [13, 14, 26, 27].

To quantify these contributions, one introduces the *critical energy density*,

$$\rho_{\rm crit}(t) = \frac{3H^2(t)}{8\pi G}\,, \tag{1.16}$$

which denotes the total energy density in the Universe and provides a natural reference scale. Indeed, the present-day abundance of each component i can then be defined by the dimensionless density parameter

$$\Omega_i = \frac{\rho_i(t_0)}{\rho_{\rm crit}(t_0)}\,. \tag{1.17}$$

Analogously, the curvature density parameter is

$$\Omega_k = -\frac{kc^2}{H_0^2}\,, \tag{1.18}$$

which defines the geometry of the Universe. A negative Ω_k corresponds to a closed Universe ($k = +1$), while a positive Ω_k leads to an open Universe ($k = -1$). See Fig. 1.1.

Using the above definitions, Eq. (1.11) can be recast in the compact form

$$H^2 = H_0^2\left(\frac{\Omega_r}{a^4} + \frac{\Omega_{nr}}{a^3} + \frac{\Omega_k}{a^2} + \Omega_\Lambda\right), \tag{1.19}$$

where $\Omega_{nr} = \Omega_b + \Omega_{\rm CDM}$ includes all non-relativistic matter, except massive neutrinos. As anticipated, their contribution to the total energy budget is subdominant, yet their effect is visible in the LSS, since they suppress the matter power spectrum at small scales.

Recent cosmological observations seem to point to a spatially flat Universe, i.e. $\Omega_k \sim 0$ [11][1]. Accordingly, looking at Eq. (1.19), three distinct post-inflationary periods can be identified depending on which cosmic component dominates the energy budget of the Universe at that time:

- Radiation domination:

$$H \sim H_0 \frac{\sqrt{\Omega_r}}{a^2}, \qquad a(t) \propto t^{1/2}. \tag{1.20}$$

- Matter domination:

$$H \sim H_0 \frac{\sqrt{\Omega_{nr}}}{a^{3/2}}, \qquad a(t) \propto t^{2/3}. \tag{1.21}$$

- Λ domination:

$$H \sim H_0 \sqrt{\Omega_\Lambda}, \qquad a(t) \propto e^{H_0 \sqrt{\Omega_\Lambda} t}. \tag{1.22}$$

The transition from radiation to matter domination occurs at the *matter–radiation equality epoch* (or simply *equivalence epoch*), when the two components contribute equally to the energy density, $a_{\rm eq} = \Omega_r/\Omega_{nr}$. Analogously, the transition from a matter-dominated to a Λ-dominated Universe occurs at $a_{{\rm eq},\Lambda} = (\Omega_{nr}/\Omega_\Lambda)^{1/3}$. Both follow from Eq. (1.15). In the ΛCDM model, $z_{{\rm eq},\Lambda} = 1/a_{{\rm eq},\Lambda} - 1 \approx 0.33$.

By imposing $a(t_0) = 1$ and $H(t_0) = H_0$ by definition, Eq. 1.19 implies the following *closure condition*

$$\Omega_r + \Omega_{nr} + \Omega_k + \Omega_\Lambda = 1\,. \tag{1.23}$$

This relation enables the connection of a purely geometrical property to the matter density parameter and the cosmological constant.

The second Friedmann equation can likewise be rewritten as

$$\frac{\ddot{a}}{a} = H^2 \left(\Omega_\Lambda - \frac{1}{2}\Omega_{nr} - \Omega_r \right)\,, \tag{1.24}$$

which clearly shows that dark energy is the only component capable of driving accelerated expansion, while both radiation and matter tend to slow it down. It is thus useful to compare the moment at which this transition to $\ddot{a} > 0$ occurs ($z_{\rm acc}$) and the epoch at which $\rho_{nr} = \rho_\Lambda$. As we have seen above, the latter occurs at $z_{{\rm eq},\Lambda} \approx 0.33$. The transition from deceleration to acceleration can instead be found by setting $\ddot{a} = 0$ in Eq. (1.24), so that $z_{\rm acc} = 1/a_{\rm acc} - 1 = (2\Omega_\Lambda/\Omega_{nr})^{1/3} - 1 \approx 0.67$. Therefore, $z_{\rm acc} > z_{{\rm eq},\Lambda}$, meaning that the Universe started its positive acceleration before the domination of the cosmological constant.

[1]Within the ΛCDM framework, CMB data from *Planck* prefer a closed Universe at $< 2\sigma$ C.L. for the *Planck* 2018 TT,TE,EE + lensing likelihood, $\Omega_k = -0.0106 \pm 0.0065$ [11, 28, 29]. However, the compatibility with a flat Universe is recovered as soon as data on BAO, SNIa or the full-shape galaxy power spectrum are added on top of CMB [11, 30, 31, 32, 33], or when using only CMB data from ACT [34]. Moreover, the final (PR4) *Planck* data release yields $\Omega_k = -0.012 \pm 0.010$ [35, 36], again consistent with the flat scenario. See [37] for a review.

A brief excursus on ***dark energy***

In the late 1990s, the High-z Supernova Search team led by Adam Riess & Brian P. Schmidt and the Supernovae Cosmology Project led by Saul Perlmutter agreed that more distant SNIa were dimmer than expected in a matter-dominated Universe with a vanishing cosmological constant [13, 14]. Although other probes were pointing to the need for a positive cosmological constant before this discovery[2], this was the first probe to directly support a Universe characterised by a late phase of accelerated expansion. Figure 1.2 shows the observed magnitude-redshift SNIa points that led to the detection of a non-null positive Λ with a confidence level of more than 3σ.

This discovery motivated the development of many dark energy theoretical scenarios in the literature [40]. The simplest theory identifies dark energy with the cosmological constant Λ (firstly introduced by Einstein in 1917 [19][3]). From Eq. (1.11), the non-vanishing cosmological constant can be interpreted as an equivalent energy-density

$$\rho_\Lambda = \frac{\Lambda c^2}{8\pi G} \,. \tag{1.25}$$

If we assume that Λ behaves as a perfect fluid, we can identify the last term of the second Friedmann equation (1.12) as

$$\frac{1}{3}\Lambda c^2 = -\frac{4\pi G}{3}\left[\rho_\Lambda + 3\frac{p_\Lambda}{c^2}\right] \,. \tag{1.26}$$

The last two equations provide the equation of state, which follows from Eq. (1.14) as

$$p_\Lambda = w_\Lambda \rho_\Lambda c^2 \,, \tag{1.27}$$

with $w_\Lambda = -1$. From Eqs. (1.14) and (1.25), the energy-momentum tensor for the cosmological constant can be written as

$$T^{(\Lambda)}_{\mu\nu} = \frac{\Lambda c^4}{8\pi G} g_{\mu\nu} \,, \tag{1.28}$$

which describes a perfect fluid with the equation of state given by Eq. (1.27). From the second Friedmann equation (1.12), it is easy to understand that a positive Λ acts as a source of positive acceleration. The cosmological constant can be reinterpreted as the vacuum energy density, which receives the contribution of the zero-point energies from all the fields (e.g., fermions, or scalar fields, as the Higgs). However,

[2]Before 1998, several independent probes had already hinted at the presence of a non-vanishing cosmological constant. For instance, matter-dominated models with $\Lambda = 0$ predicted a Universe younger than the oldest globular clusters, whereas a positive Λ would alleviate this tension [38]. Measurements of galaxy clustering and LSS in the 1980s and 1990s indicated a matter density of only $\Omega_m \sim 0.2 - 0.3$, much smaller than the critical density required for flatness and thus in conflict with inflationary expectations [39]. Early CMB anisotropy data also supported a spatially flat geometry, further reinforcing the discrepancy between low Ω_m and $\Omega_{\rm tot} = 1$. Taken together, these observations provided converging hints that a cosmological constant might be needed.

[3]After the discovery of Edwin Hubble of an expanding Universe in 1929, Einstein recognized that the cosmological constant was no longer needed, since he had originally introduced the term solely to enforce a static Universe. By 1931, he published a paper adopting an expanding model without Λ [41].

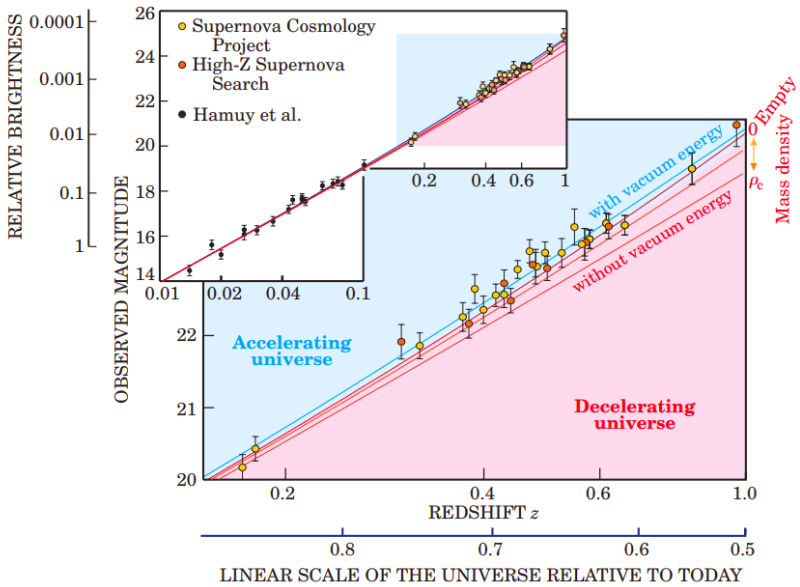

Figure 1.2. Observed magnitude versus redshift for well-measured high-redshift ($0.2 < z < 0.8$) and (in the inset) nearby ($z < 0.1$) SNIa previously measured by the Calán/Tololo Project [45]. The best fit (blue line) assumes a mass density of about $\rho_c/3$ plus a vacuum energy density twice that large, thereby implying an accelerating cosmic expansion. Figure from [46].

the value of Λ needed to explain cosmological observations is by many orders of magnitude smaller than the vacuum energy density predicted from particle physics (the so-called *cosmological constant problem* [42, 43, 44]). This seems to be a very delicate fine-tuning issue. One may abandon the identification of dark energy with $w = -1$ and invoke models of *dynamical* dark energy, such as those in which a scalar field with a slowly varying potential drives the accelerated expansion. However, none of them is currently able to solve the problem. We leave this discussion for Sec. 3.4, where we will introduce alternatives to the standard cosmological model.

Referring back to (1.19), knowing the cosmological parameters $\{H_0, \Omega_r, \Omega_{nr}, \Omega_k, \Omega_\Lambda\}$ is sufficient to reconstruct the expansion history of the Universe from the end of inflation onward. Having established the background framework, it is useful to review the sequence of major physical processes that shaped the cosmic timeline.

- **Grand unified and Inflationary epochs:** At the earliest moment of the Universe, corresponding to the highest energy scales, the fundamental interactions are believed to have been unified. As the temperature dropped, spontaneous symmetry breaking separated gravity first, and subsequently the electroweak interaction from the strong force. This phase likely included a brief but dramatic accelerated expansion called *cosmic inflation*.

- **Baryogenesis:** A slight imbalance between matter and antimatter was generated, leaving behind the small but crucial excess of baryons that make up the visible Universe.

- **Big Bang nucleosynthesis** (BBN) ($180\ \mathrm{s} \lesssim t \lesssim 10^3\ \mathrm{s}$): about three minutes after the Big Bang, the plasma temperature drops to roughly 10^9 K, enabling atomic fusion in the phase called *Primordial nucleosynthesis*. During this process, a portion of neutrons gets bound into helium (He) nuclei, while the rest decay into protons. Other elements, such as deuterium and lithium, are also produced in smaller amounts. After ~ 20 minutes, the nucleosynthesis phase ends, leaving the baryonic matter of the plasma composed primarily of ionized hydrogen (H) and helium, with minor traces of additional elements. Neutrinos, which decoupled slightly earlier, are still present as a cosmic background and contribute to the total radiation density, influencing the expansion rate of the Universe and the neutron-to-proton ratio. At this stage, photons still dominate the energy density and remain tightly coupled to baryons due to the high Thomson scattering cross-section, so both components continue to cool together as the Universe expands.

- **Recombination and photon decoupling** ($t \sim 400\ \mathrm{kyr}, z \sim 1090$): when the plasma temperature falls to $T \sim 0.3$ eV, neutral hydrogen atoms begin to form through the reaction $e^- + p \to H + \gamma$. Since the reverse process becomes energetically suppressed at such low temperatures, the abundance of free electrons suddenly drops. As a result, Thomson scattering between electrons and photons becomes inefficient, leading to the decoupling of matter and radiation. From this epoch onward, photons propagate freely through space, giving rise to the CMB that we detect today.

- **Dark ages** ($380\ \mathrm{kyr} \lesssim t \lesssim 200\ \mathrm{Myr}, 20 \lesssim z \lesssim 1090$): the interval between recombination and the formation of the first luminous sources is known as the Dark Ages. During this phase, the Universe is filled with neutral hydrogen, whose 21 cm hyperfine transition imprints a characteristic spectral feature, observable in absorption or emission against the background radiation.

- **Reionization** ($200\ \mathrm{Myr} \lesssim t \lesssim 1000\ \mathrm{Myr}, 6 \lesssim z \lesssim 20$): as the first stars and quasars ignite, their radiation ionizes the previously neutral medium. Although the density of free electrons increases again, it never reaches the level needed to render the Universe opaque. In this epoch, cosmic structures begin forming hierarchically: smaller objects collapse first and subsequently merge under the pull of gravity, producing progressively larger structures.

- **Dark energy dominated era** ($t \sim 9800\ \mathrm{Myr}, z \sim 0.4$): after the epoch of matter–radiation equality, non-relativistic matter governs cosmic dynamics. However, as the Universe expands, the matter density decreases while the energy density of dark energy remains constant. At redshift $z \sim 0.4$, the two densities become comparable, after which dark energy dominates, driving the accelerated expansion of the Universe (see Eq. (1.24)).

- **Today** ($t \sim 13800\ \mathrm{Myr}, z = 0$)

This sequence of events is summarized in Fig. 1.3, which highlights the key phases of the evolution of the Universe according to the Hot Big Bang model.

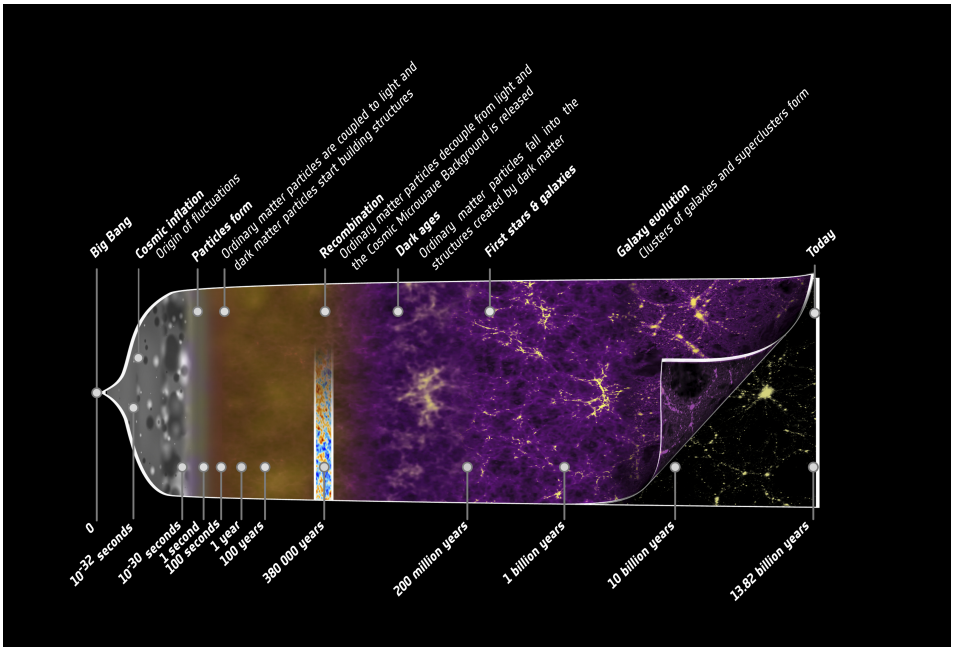

Figure 1.3. Timeline of the Universe, from inflation to the present accelerated expansion. Credit: European Space Agency (ESA).

As already mentioned at the beginning of this Chapter, the Hot Big Bang scenario, and specifically the ΛCDM framework, has received multiple observational confirmations: the discovery of the CMB, the measurements of primordial abundances of light elements that agree with the predictions of the BBN, and the discovery of the accelerated cosmic expansion thanks to SNIa. Moreover, extensive evidence from galactic dynamics, galaxy cluster studies, CMB anisotropies, and the growth of structures indicates that the amount of non-relativistic matter vastly exceeds the baryonic contribution, thus supporting the existence of dark matter, a non-radiating, weakly interacting component that interacts primarily through gravity [47, 48, 49].

Despite its remarkable success, the ΛCDM model still faces a number of open issues. Beyond observational tensions that we leave for discussion in Chapter 3, several conceptual problems remain unresolved:

- The nature of **dark matter** and **dark energy** is still unknown, despite their dominance in the cosmic energy budget.

- The **cosmological constant problem**: Quantum field theory predicts a vacuum energy density that exceeds the observed value of the cosmological constant by about 120 orders of magnitude [42, 50].

- The **curvature problem**: it can be proved that the curvature parameter $\Omega_k(t)$ decreases going back in cosmic time. Consequently, its present-day small value [11] implies that it must have been much lower in the early Universe, requiring an extraordinarily fine-tuning at that epoch — an initial condition lacking any compelling physical explanation.

- The **horizon problem**: the angular scale of the comoving particle horizon at the last scattering surface, i.e., the maximum comoving distance light could have traveled from the Big Bang up to recombination, can be estimated as $\theta_H \approx 1.5° \cdot \Omega_{nr}^{0.72}$ [24]. This prediction, however, conflicts with the nearly perfect isotropy of the observed CMB across all angular scales. It would require that causally disconnected regions of the sky had nevertheless been in thermal equilibrium before recombination, posing a fundamental conceptual difficulty.

Both the horizon and curvature problems can be naturally addressed by postulating the theory of **cosmic inflation**. This theory was formulated at the end of the 1970s, with pioneering contributions by Alexei Starobinsky, Alan Guth, and Andrei Linde [51, 17, 52]. It proposes that, during the very early stages of cosmic history ($10^{-36} \lesssim t \lesssim 10^{-32}$ s), the Universe underwent a phase of accelerated expansion.

Such rapid expansion cannot be generated by ordinary matter sources (see Eq. (1.12)), implying the necessity of introducing a new physical component, one that dominated cosmic evolution only during the primordial epoch.

Inflation has become a cornerstone of modern cosmology for several reasons: it not only provides elegant solutions to longstanding shortcomings of the standard Hot Big Bang scenario but also offers a consistent framework to account for the primordial density perturbations that seeded the formation of the LSS [53, 16, 54].

In order for the Universe to undergo a phase of accelerated expansion at early epochs ($\ddot{a} > 0$), the dominant matter component during this stage must obey the condition (see Eq. (1.12)):

$$\rho + 3\frac{p}{c^2} < 0\,. \tag{1.29}$$

Adopting the equation of state parametrization in Eq. (1.14), this inequality can be fulfilled whenever $w < -\frac{1}{3}$. Since inflation occurs at very high energy scales, a proper description requires quantum field theory rather than a purely fluid-dynamical approach. The most straightforward mechanism to trigger such accelerated expansion is to postulate the existence of a single scalar field $\phi_0(t)$, generally referred to as the *inflaton*, whose expectation value depends solely on cosmic time, in agreement with the CP [55]. A single-field inflationary model is fully specified once the potential $V(\phi_0)$ is chosen. Such potentials are generally motivated by underlying high-energy theories. Extensions include, e.g., non-standard kinetic terms or non-minimal couplings to gravity. While phenomenologically successful, the underlying mechanism and its embedding in fundamental physics remain uncertain.

Cosmic seeds: generation and evolution of perturbations

As previously mentioned, inflation also provides a mechanism for the origin of cosmic structures. The observed inhomogeneities in matter — stars, galaxies, and clusters — arise from tiny primordial quantum fluctuations that were stretched to cosmological scales during inflation [53, 16, 54].

The Hubble radius,

$$R_H = \frac{c}{H}\,, \tag{1.30}$$

represents the distance traveled by particles throughout one expansion time and corresponds roughly to the time needed by the scale factor to double. During quasi-de Sitter expansion ($H \approx$ const.), R_H remains nearly constant while physical scales grow exponentially, causing perturbation modes to exit the horizon and re-enter later during the radiation- or matter-dominated eras. On super-horizon scales, fluctuations freeze and source metric perturbations. Scalar (or curvature) modes seed structure formation, while tensor modes correspond to primordial gravitational waves.

We can describe perturbations by splitting the inflaton field into a classical background and quantum fluctuations:

$$\phi(\vec{x}, t) = \phi_0(t) + \delta\phi(\vec{x}, t)\,, \tag{1.31}$$

with $\delta\phi \ll \phi_0$. A first approximation is to consider the evolution of $\delta\phi$ in a fixed FRW background by neglecting metric perturbations, which leads to the linearized Klein-Gordon equation:

$$\delta\ddot{\phi} + 3H\delta\dot{\phi} - \frac{\nabla^2\delta\phi}{a^2} + V''(\phi_0)\delta\phi = 0\,, \tag{1.32}$$

where $V(\phi)$ denotes the inflaton potential. Including metric perturbations consistently requires the gauge-invariant Mukhanov-Sasaki variable [56, 57]

$$v = a\left(\delta\phi + \frac{\dot{\phi}_0}{H}\Psi\right)\,, \tag{1.33}$$

whose Fourier modes satisfy the Mukhanov-Sasaki equation:

$$v_k'' + \left(k^2 - \frac{z''}{z}\right)v_k = 0, \quad z \equiv \frac{a\dot{\phi}_0}{H}\,, \tag{1.34}$$

where primes denote derivatives with respect to conformal time and the variable v_k represents the canonically normalized scalar perturbations.

The coupled system of inflaton and metric perturbations can be studied by expanding the metric around the FRW background:

$$g_{\mu\nu} = g_{\mu\nu}^{(0)} + \delta g_{\mu\nu}(t, \vec{x})\,, \tag{1.35}$$

where the symmetric perturbation $\delta g_{\mu\nu}$ can be decomposed into scalar, vector, and tensor modes as follows

$$\begin{aligned} \delta g_{00} &= -a^2(1 + 2\Phi), \\ \delta g_{0i} &= a^2(V_i - B_{,i}), \\ \delta g_{ij} &= a^2\Big[(1 - 2\Psi)\delta_{ij} + D_{ij}E - \frac{1}{2}(C_{i,j} + C_{j,i}) + h_{ij}\Big]\,, \end{aligned} \tag{1.36}$$

with $D_{ij} = \partial_i\partial_j - \frac{1}{3}\delta_{ij}\nabla^2$ and the quantities Φ, B, Ψ and E identify the scalar modes, V and C the vector modes, h_{ij} the tensor ones. Vector modes are typically negligible in inflationary models, while scalar and tensor modes are dependent in linear theory and can be studied separately [58].

The inhomogeneous distribution of the density of cosmic components across the Universe should be reflected in an anisotropic pattern of the CMB intensity across the sky, which, indeed, was observed for the first time by the COBE satellite. The amplitude of these anisotropies is measured to be 10^{-5} lower than the average background value [59]. Therefore, the evolution of cosmic perturbations can be studied at linear order at least up to the recombination epoch. This means that we can perform a first order expansion of the relevant fluid-dynamical quantities of each cosmic component:

$$\begin{aligned} \rho(t,\vec{x}) &= \bar{\rho}(t) + \delta\rho(t,\vec{x}) = \bar{\rho}(t)(1+\delta(t,\vec{x})), \\ p(t,\vec{x}) &= \bar{p}(t) + \delta p(t,\vec{x})\,, \end{aligned} \tag{1.37}$$

where $\bar{\rho}(t)$ and $\bar{p}(t)$ are the average background density and pressure, while $\delta(t,\vec{x})$ and $\delta p(t,\vec{x})$ are, respectively, the relative density and the absolute pressure fluctuations at comoving position $\vec{x}$ and cosmic time t. At linear order, the Newtonian gravitational potential is modified accordingly as

$$\Phi(t,\vec{x}) = \bar{\Phi}(t) + \delta\Phi(t,\vec{x})\,. \tag{1.38}$$

If local potential wells are present in the Universe, the comoving coordinates of a fluid element will evolve with time, so that its proper velocity can be expressed as

$$\vec{v}(t,\vec{x}) = \vec{v}_H + \vec{v}_p = \frac{\dot{a}}{a}\vec{r} + a\frac{d\vec{x}}{dt}\,, \tag{1.39}$$

where $a\frac{d\vec{x}}{dt} \equiv \vec{v_p}$ denotes the *peculiar velocity* of the fluid elements, which quantifies how their motion deviates from the Hubble flow. In this framework, any fluid element must obey the linearized perturbed matter and momentum conservations and the Poisson equation for a fluid element, which in comoving coordinates ($\vec{x} = \vec{r}/a$) read:

$$\begin{aligned} \frac{\partial\delta}{\partial t} + \frac{1}{a}\vec{\nabla}_x\cdot\vec{v}_p &= 0, \\ \frac{\partial\vec{v}_p}{\partial t} + \frac{\dot{a}}{a}\vec{v}_p + \frac{c_s^2}{a\bar{\rho}}\vec{\nabla}_x\delta\rho + \frac{1}{a}\vec{\nabla}_x\delta\Phi &= 0, \\ \frac{1}{a^2}\nabla_x^2\delta\Phi &= 4\pi G\bar{\rho}\delta\,, \end{aligned} \tag{1.40}$$

with $c_s^2 = \delta p/\delta\rho$ the adiabatic sound speed and $\vec{\nabla}_x$ the divergence in comoving units. The three equations introduced above can be combined into the so-called *gravitational instability* (or *Jeans*) equation, which governs the time evolution of density inhomogeneities for each cosmic component:

$$\ddot{\delta} + 2\left(\frac{\dot{a}}{a}\right)\dot{\delta} = 4\pi G\bar{\rho}\,\delta + \frac{c_s^2}{a^2}\vec{\nabla}_x^2\delta\,. \tag{1.41}$$

Considering the Fourier transform of $\delta(t,\vec{x})$, it is convenient to express the density contrast in Fourier space as

$$\delta_k(t) = \frac{1}{(2\pi)^3}\int d^3x\,\delta(t,\vec{x})\,\exp(i\vec{k}\cdot\vec{x}), \tag{1.42}$$

which reduces Eq.(1.41) to

$$\ddot{\delta}_k + 2\left(\frac{\dot{a}}{a}\right)\dot{\delta}_k = \left[4\pi G\bar{\rho} - \frac{k^2 c_s^2}{a^2}\right]\delta_k = 4\pi G\bar{\rho}\,\delta_k\left[1 - \frac{{k^{(p)}}^2}{{k_J^{(p)}}^2}\right], \tag{1.43}$$

where we have introduced the proper wavenumber $k^{(p)} = k/a$ and the proper Jeans wavenumber

$$k_J^{(p)} = \frac{2\pi}{\lambda_J^{(p)}} = \sqrt{\frac{4\pi G\bar{\rho}}{c_s^2}}\,. \tag{1.44}$$

Equation (1.43) shows that density perturbation modes with different wavelengths evolve independently, being their behavior determined by the competition between two terms: gravitational attraction and pressure. The latter contribution originates from scattering interactions among different components and therefore plays a key role in the evolution of baryonic and photon density fluctuations. In contrast, for non-interacting components such as CDM, only the gravitational term on the right-hand side of Eq.(1.41) is relevant.

Large-scale modes ($\lambda \gg \lambda_J$) are gravity-dominated:

$$\ddot{\delta}_k + 2\frac{\dot{a}}{a}\dot{\delta}_k = 4\pi G\bar{\rho}\delta_k\,. \tag{1.45}$$

Small-scale modes ($\lambda \ll \lambda_J$) are pressure-dominated, yielding damped oscillations:

$$\ddot{\delta}_k + 2\frac{\dot{a}}{a}\dot{\delta}_k + \frac{k^2 c_s^2}{a^2}\delta_k = 0\,. \tag{1.46}$$

Statistics of perturbations

The standard theory of structure formation predicts that, as a first approximation, density inhomogeneities can be statistically described by a Gaussian random field [60]. This implies that the probability of observing a specific initial fluctuation at a given spatial point follows a Gaussian distribution. Although the initial conditions are only statistically defined, their subsequent evolution is deterministic, which allows us to predict how the statistical properties of the density perturbation field evolve over time.

For a perfectly Gaussian field, its statistical properties are entirely captured by the two-point correlation function $\xi(r,t)$, which quantifies the average correlation of density fluctuations at points separated by a comoving distance r at cosmic time t:

$$\xi(r,t) = \langle \delta(\vec{x},t)\,\delta(\vec{x}+\vec{r},t)\rangle\ , \tag{1.47}$$

where $\langle\cdot\rangle$ denotes the ensemble average. For a Gaussian field, all higher-order moments either vanish or can be expressed in terms of the two-point correlation function.

The correlation function defined in Eq. (1.47) is independent of both the direction of the separation vector $\vec{r}$ and the location $\vec{x}$, implying that the statistical properties of density fluctuations are homogeneous and isotropic. This provides a statistical interpretation of the CP. In practice, $\xi(r,t)$ can be estimated from the

observed distribution of galaxies or other tracers, under the assumption of ergodicity. Ergodicity allows replacement of the ensemble average with a spatial average over a sufficiently large volume, meaning that the observed Universe is representative of the underlying ensemble statistics.

The Fourier transform of the correlation function gives rise to the power spectrum $P(k,t)$, as

$$P(k,t) = \frac{1}{(2\pi)^3} \int d^3r\, \xi(r,t)\, \exp(-i\vec{k}\cdot\vec{r})\,, \tag{1.48}$$

and, using Eq. (1.42), it can equivalently be written as

$$P(k,t) = \left\langle |\delta_k(t)|^2 \right\rangle\,. \tag{1.49}$$

Since $\langle \delta_k(t) \rangle = 0$, the power spectrum quantifies the variance of the Fourier components of the matter density perturbations.

As discussed above, the most widely accepted scenario for the generation of matter inhomogeneities is inflation. Quantum fluctuations of the inflaton are amplified by the exponential expansion and become classical density perturbations on cosmological scales. The initial power spectrum of scalar perturbations predicted by inflation is commonly described by a power law, $P(k,t_{in}) = A_s k^{n_s-1}$. Here, A_s and n_s quantify, respectively, the amplitude and the spectral index of the initial power spectrum.

The evolution of these initial conditions into the matter power spectrum at any cosmic time t is described by a scale-dependent transfer function $T(k,t)$:

$$P(k,t) = A_s k^{n_s-1} T^2(k,t)\,, \tag{1.50}$$

which encapsulates all physical processes that regulate the evolution of density perturbations in both the linear and non-linear regimes.

In a ΛCDM framework, the matter power spectrum $P(k)$ grows as redshift decreases, illustrating the growth of matter overdensities over cosmic time. At small scales (high k), non-linear processes become important and affect the evolution of the matter perturbations. A characteristic wavenumber, $k_{\rm eq}$, marks the scale at which the spectrum changes its profile. This scale corresponds to the horizon size at matter-radiation equivalence. Modes with $k > k_{\rm eq}$ enter the horizon before equality and undergo a period of "stagnation" due to *acoustic oscillations*. These modes resume growth only during the matter-dominated era, causing the power spectrum to transition from a blue to a red tilt. The position of this feature is directly linked to the time of equivalence, $a_{\rm eq} = \Omega_r/\Omega_{nr}$. For larger values of Ω_{nr}, fewer modes enter the horizon during the radiation-dominated epoch ($a \lesssim a_{\rm eq}$), shifting the peak to higher k values. Later, we take a closer look at how acoustic oscillations leave measurable imprints on particular cosmological probes. To better understand this connection, we now move on to discuss the relic radiation from our early Universe.

The Cosmic Microwave Background

In 1964, A. A. Penzias and R. W. Wilson, using a microwave antenna originally designed to study the reflection of radio waves from Echo balloon satellites, detected a radio interference corresponding to a temperature of 3.5 K at 4 GHz. The signal was *"isotropic, unpolarized, and free from seasonal variations"* [8]. Subsequent

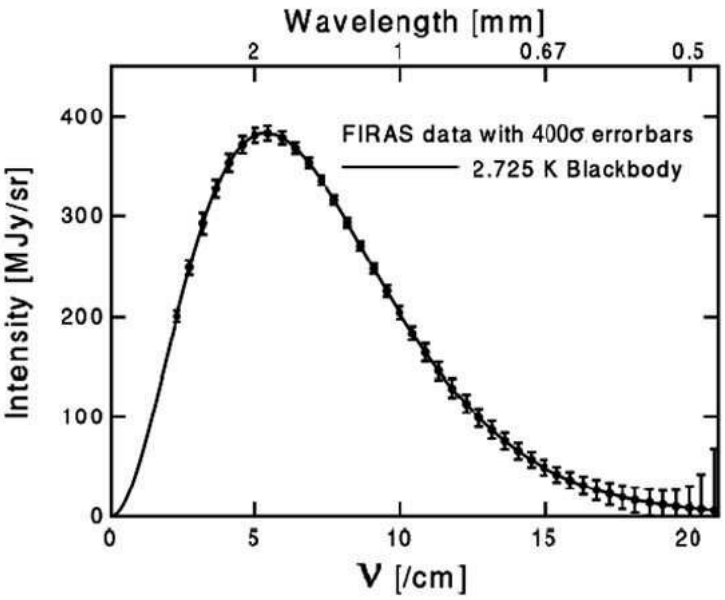

Figure 1.4. Comparison of the CMB intensity observed by FIRAS on COBE with a blackbody spectrum at $T = 2.725$ K [62].

studies confirmed that this signal matched the cosmic radiation predicted by the Hot Big Bang model [61], nowadays known as the Cosmic Microwave Background.

In 1989, the FIRAS instrument on COBE measured the CMB spectrum with remarkable precision, finding near-perfect agreement with a blackbody distribution [62] (see Fig. 1.4):

$$I_\nu(\hat{\gamma}) = \frac{2h\nu^3}{c^2}\frac{1}{\exp(h\nu/kT)-1} = 2\frac{(kT)^3}{(hc)^2}\left[\frac{x^3}{e^x-1}\right], \tag{1.51}$$

where $x = h\nu/(kT)$, h is here the Planck constant, $\hat{\gamma}$ is a direction in the sky, and T is the blackbody temperature. The observed average temperature is $T_0 = 2.725 \pm 0.001$ K [62], and its isotropy at the level of 10^{-5} across the sky provides a strong confirmation of the CP. Moreover, observing a blackbody spectrum today indicates that photons were once tightly coupled to matter in thermal equilibrium, as predicted by the Hot Big Bang model. This is one of the strongest pieces of evidence ruling out stationary Universe models.

As the Universe cooled and expanded, radiation and baryons decoupled and neutral atoms formed, marking the epoch of recombination. At this point, photons began to travel freely, essentially without further interaction. The optical depth of radiation interacting with free electrons depends on the Thomson scattering cross section σ_T and the free electron number density $n_e(z)$:

$$d\tau(z) = n_e(z)\sigma_T ds\,, \tag{1.52}$$

where ds is an infinitesimal line element along the photon path. The probability that a photon last scattered at redshift z is described by the visibility function:

$$g(z) = e^{-\tau(z)}\frac{d\tau}{dz}\,. \tag{1.53}$$

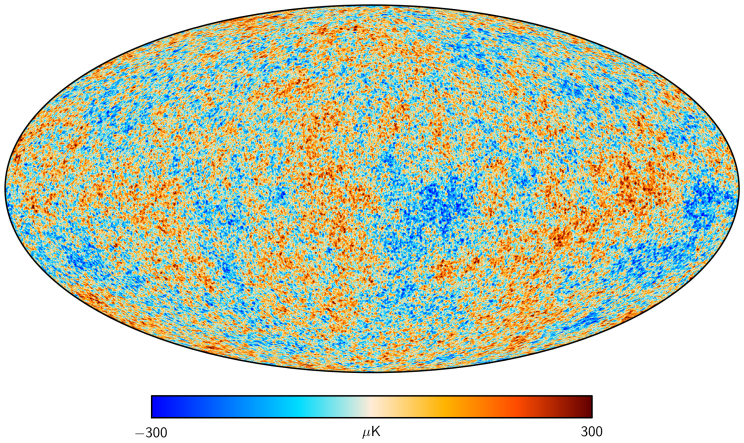

Figure 1.5. Mollweide projection of CMB intensity anisotropies observed by *Planck*. Temperature fluctuations are represented by cold and hot spots, measured in microkelvin (μK). Figure from Planck Legacy Archive.

The function $g(z)$ can be computed for any cosmological model, though its peak is relatively insensitive to model variations [63]. In ΛCDM, the visibility function peaks at $z \sim 1089$ and has a Gaussian dispersion $\sigma_z \approx 80$, corresponding to a redshift width $\Delta z \sim 210$. This indicates that recombination is not instantaneous, and observing the CMB corresponds to sampling a finite region of the Universe in redshift space. CMB measurements therefore provide not only a precise test of the Hot Big Bang model but also a direct glimpse into the physical conditions of the early Universe, linking photon decoupling to the formation of the first neutral atoms and the subsequent evolution of large-scale structure.

Tiny inhomogeneities in the CMB intensity — and hence in the photon energy density — were first detected by the COBE satellite [59]. Following this discovery, numerous experiments have mapped CMB anisotropies in both intensity and polarization with increasing precision, including BOOMERanG [64], WMAP [65], *Planck* [66], BICEP [67], Keck-Array [68], ACT [12] and SPT (South Pole Telescope) [69].

Figure 1.5 shows the most accurate map of the CMB intensity anisotropies to date, as observed by *Planck*. These anisotropies are the fingerprints of cosmic perturbations tracing back to the inflationary epoch, providing a unique window into the conditions of the early, perturbed Universe. The standard deviation of CMB temperature anisotropies is of order $\delta T/T \sim 10^{-5}$, justifying — as we have seen above — the use of linear perturbation theory to describe their evolution.

The observed CMB temperature anisotropies can be regarded as a stochastic scalar field on the 2D celestial sphere. Consequently, they can be expanded in spherical harmonics $\mathrm{Y}_{\ell m}$ as

$$\frac{\delta T}{T}(\theta, \varphi) = \sum_{\ell,m} a_{\ell m}\, \mathrm{Y}_{\ell m}(\theta, \varphi), \tag{1.54}$$

where the angular variables (θ, φ) identify the direction of observation on the sky, the order m describes the angular orientation of the fluctuations, and the degree ℓ refers to their angular size.

According to standard inflationary scenarios, these fluctuations are expected to be highly Gaussian and isotropic, a prediction confirmed by recent *Planck* measurements [11]. In this case, the statistics of the temperature anisotropy field in harmonic space are fully characterized by the variance of the $a_{\ell m}$ coefficients:

$$C_\ell = \langle |a_{\ell m}|^2 \rangle, \tag{1.55}$$

where $\langle \cdot \rangle$ denotes an ensemble average over infinitely many realizations of the stochastic field. Due to isotropy, C_ℓ is independent of m. We can now define an angular correlation function as

$$C(\alpha) = \left\langle \frac{\delta T}{T}(\hat{\gamma}_1) \frac{\delta T}{T}(\hat{\gamma}_2) \right\rangle , \tag{1.56}$$

where $\hat{\gamma}_1$ and $\hat{\gamma}_2$ are two lines of sight separated by an angle α, with $\hat{\gamma}_1 \cdot \hat{\gamma}_2 = \cos\alpha$.

Using the harmonic expansion (1.54) and the statistical independence of the $a_{\ell m}$ coefficients,

$$\langle a_{\ell m} a^*_{\ell' m'} \rangle = C_\ell \, \delta_{\ell \ell'} \, \delta_{m m'} , \tag{1.57}$$

(where δ is the Kronecker delta), and the relation between spherical harmonics and the Legendre polynomials $P_\ell(x)$,

$$P_\ell(\cos\alpha) = \frac{4\pi}{2\ell+1} \sum_{m=-\ell}^{\ell} \mathrm{Y}_{\ell m}(\hat{\gamma}_1) \mathrm{Y}^*_{\ell m}(\hat{\gamma}_2) , \tag{1.58}$$

the angular correlation function can be rewritten in terms of C_ℓ as follows:

$$C(\alpha) = \frac{1}{4\pi} \sum_\ell (2\ell+1) C_\ell P_\ell(\cos\alpha) . \tag{1.59}$$

Just as the power spectrum $P(k)$ is the Fourier transform of the correlation function $\xi(r)$ (see Eq. 1.48), the C_ℓ define the angular power spectrum of CMB anisotropies.

The theoretical quantity in Eq. (1.56) includes an ensemble average that is operated on all possible realizations of the system. However, in practice, we have access to only a single realization of the sky. To obtain an estimator of this quantity, one can take advantage of the statistical isotropy, that is, at each l, averaging all the available orientations m. The best empirical estimate of the angular power spectrum, therefore, will be:

$$C_\ell^{\mathrm{obs}} = \frac{1}{2\ell+1} \sum_{m=-\ell}^{\ell} |a_{\ell m}^{\mathrm{obs}}|^2 . \tag{1.60}$$

Since C_ℓ^{obs} is a sum of squares of Gaussian variables, it follows a chi-squared distribution with $(2\ell+1)$ degrees of freedom. Its variance is therefore:

$$\mathrm{Var}[C_\ell^{\mathrm{obs}}] = \frac{2}{2\ell+1} C_\ell^2 , \tag{1.61}$$

with $\langle C_\ell^{\mathrm{obs}} \rangle = C_\ell$. This intrinsic statistical uncertainty is called *cosmic variance*:

$$\sigma(C_\ell^{\mathrm{obs}}) = \sqrt{\frac{2}{2\ell+1}} \langle C_\ell^{\mathrm{obs}} \rangle , \tag{1.62}$$

and is unrelated to instrumental limitations. Cosmic variance decreases at higher multipoles because the number of $a_{\ell m}$ modes grows, allowing the sample average to better approximate the ensemble average.

Cosmology from CMB

Each multipole ℓ can be approximately associated with an angular scale θ (in degrees) through the relation

$$\ell \simeq \frac{180^\circ}{\theta} \,. \tag{1.63}$$

This angular scale is of fundamental importance, as it provides a direct handle for extracting cosmological information from CMB observations. Indeed, θ (in radians) is related to a comoving linear length on the last-scattering surface, $L^{(c)}$. Making use of the comoving angular diameter distance (see Sec. 1.3) at recombination defined as

$$D_A^{(c)}(z_{\rm rec}) = \frac{1}{\sqrt{|\Omega_k|}}\, f_K\left(\sqrt{|\Omega_k|}\int_0^{z_{\rm rec}} \frac{cdz}{H(z)}\right), \tag{1.64}$$

where

$$f_K(x) = \begin{cases} \sin(x) & \Omega_k < 0, \\ x & \Omega_k = 0, \\ \sinh(x) & \Omega_k > 0\,, \end{cases} \tag{1.65}$$

one can obtain

$$L^{(c)} = D_A^{(c)}(z_{\rm rec}) \cdot \theta \,. \tag{1.66}$$

With these relations, the shape of the angular power spectrum can be physically interpreted in terms of the evolution of perturbation modes before recombination using the so-called *monochromatic approximation*. In this approach, the power of the perturbations at each multipole ℓ is assumed to be sourced by modes on the last-scattering surface with comoving wavelength equal to the associated linear scale $L^{(c)}(\ell)$, estimated from Eqs. (1.63)-(1.66). This way, three main regions can be identified in the angular power spectrum of CMB temperature anisotropies (see Fig. 1.6).

For $\ell \lesssim 100$, angular scales are larger than the horizon at last scattering. Modes on these scales have not undergone acoustic oscillations, so the power spectrum directly reflects the primordial conditions, constraining parameters such as A_s and n_s. At these scales, anisotropies are produced by the ordinary Sachs-Wolfe effect, and the power spectrum is almost flat [70].

At $100 \lesssim \ell \lesssim 1000$, an oscillatory pattern corresponding to modes that entered the horizon before photon decoupling is present. The anisotropies here are sourced by gravity-driven acoustic oscillations of the photon-baryon fluid. At decoupling, modes are frozen at different oscillation phases, producing peaks in the power spectrum: odd peaks correspond to maximum compression, even peaks to rarefaction.

At $\ell \gtrsim 1000$, the power spectrum decreases exponentially due to *Silk damping* and the finite thickness of the last-scattering surface. Silk damping arises from photon diffusion: during tight coupling, photons have a finite mean free path and tend to smooth out fluctuations on scales smaller than the diffusion length [71]. The non-instantaneous nature of recombination adds a finite thickness to the last-scattering surface, causing multiple modes with different phases to overlap and partially cancel, further reducing power at these small scales.

The multipoles at which acoustic peaks appear in the CMB angular power spectrum can be approximately determined by [24]:

$$\ell_n \simeq n\pi \frac{D_A^{(c)}(z_{\rm rec})}{r_s^{(c)}(t_{\rm rec})}\,, \tag{1.67}$$

where n is the peak number, $D_A^{(c)}(z_{\rm rec})$ is given in Eq. (1.64)), and $r_s^{(c)}(t_{\rm rec})$ is the comoving sound horizon at recombination:

$$r_s^{(c)}(t_{\rm rec}) = \int_0^{t_{\rm rec}} \frac{c_s\,dt}{a(t)} = \int_0^{a_{\rm rec}} \frac{c_s\,da}{H_0\sqrt{\Omega_r + \Omega_{nr}a + \Omega_k a^2 + \Omega_\Lambda a^4}}\,. \tag{1.68}$$

Here, c_s is the sound speed in the photon-baryon fluid. Both $r_s^{(c)}$ and $D_A^{(c)}$ depend on the cosmological parameters, so the observed positions of the acoustic peaks provide stringent constraints on the physical properties of the Universe.

The angular power spectrum of the CMB temperature anisotropies can be related to the initial primordial perturbations through the transfer function formalism:

$$C_\ell = \frac{2}{\pi}\int_0^\infty dk\,k^2\,P_{\mathcal{R}}(k)\,|\mathcal{T}_\ell(k)|^2, \tag{1.69}$$

where $P_{\mathcal{R}}(k)$ is the primordial scalar power spectrum and $\mathcal{T}_\ell(k)$ is the transfer function linking primordial perturbations to CMB anisotropies. This transfer function encodes the evolution of perturbations through all relevant cosmic epochs.

It is thus easy to understand that the CMB power spectra provide a powerful tool to infer the values of several cosmological parameters. Since the observed anisotropies mainly reflect conditions on the last-scattering surface, these parameters can influence the CMB either through the acoustic physics of the pre-recombination plasma or through the angular diameter distance to last scattering (see Eq. (1.64)).

The parameters affecting perturbations up to decoupling are primarily the baryon and CDM densities, as well as those of photons and neutrinos. However, the energy densities of the latter are quite well-known: the photon energy density is fixed by CMB temperature, while the neutrino contribution also depends on the effective number of neutrino species. These parameters influence two characteristic length scales: the sound horizon at recombination r_s (Eq. (1.68)) and the photon diffusion (damping) scale, as well as the relative heights of the acoustic peaks. For fixed baryon and CDM densities, these two scales serve as "standard rulers" on the last-scattering surface (see Sec. 2.2). The angular size of these rulers depends on D_A, so the geometry of space, the presence of dark energy, and light neutrinos primarily affect the CMB power spectra via their impact on the angular diameter distance. They also influence late-time structure formation, but this only affects the linear CMB anisotropies through the late-time Integrated Sachs-Wolfe effects (ISW) effect on large scales where cosmic variance is large.

In summary, primary CMB anisotropies are mainly sensitive to:

- Matter densities, $\boldsymbol{\Omega_{\rm b}}$ and $\boldsymbol{\Omega}_{\rm CDM}$, through the pre-recombination evolution of the baryon-photon fluid.

  An increase in Ω_b, at fixed total non-relativistic matter density $\Omega_{nr} = \Omega_b + \Omega_{\rm CDM}$, raises the inertia of the baryon-photon fluid, lowering the sound speed

before recombination. This shifts the midpoint of acoustic oscillations to larger over-densities and enhances the height of the compressional peaks ($n = 1, 3, \ldots$ in Eq. 1.67 for adiabatic initial conditions). The reduced sound horizon shifts all peaks to smaller scales (higher ℓ).

An increase in $\Omega_{\rm CDM}$, at fixed Ω_b and $D_A(z_{\rm rec})$, shifts matter-radiation equality to earlier times, reducing both the sound horizon and the diffusion scale. The resonant driving effect that enhances acoustic oscillations for modes entering the horizon during radiation domination is limited to small-scale compressions, enhancing the third and higher peaks relative to the first two. The smaller sound horizon also shifts peaks to higher ℓ.

- Curvature and dark energy parameters, $\mathbf{\Omega_k}$ and $\mathbf{\Omega_\Lambda}$, through D_A.

  Both parameters primarily affect the CMB anisotropies through the angular diameter distance and therefore mainly shift the positions of the acoustic peaks. At fixed baryon and cold dark matter densities, an increase in Ω_Λ reduces D_A, shifting peaks to lower multipoles, while an increase in Ω_k enhances D_A, moving peaks to higher multipoles. Disentangling the effects of dark energy and curvature requires external datasets to break the geometric degeneracy.

- Re-scattering of CMB photons with free electrons after recombination, accounted for by τ, the optical depth to reionization:

$$\tau = \sigma_T \int_0^{z_{\rm re}} n_e(z) dz \,, \tag{1.70}$$

  where $z_{\rm re}$ marks the beginning of reionization. This parameter essentially denotes how opaque the Universe is at that specific epoch.

  During reionization, at $\ell > 10$, radiation perturbations vary across the free electrons last-scattering surfaces. Scattering out of the line of sight suppresses anisotropies by $e^{-\tau}$, yielding a multiplicative factor $e^{-2\tau}$ in the power spectrum on these scales. On large scales ($\ell < 10$), reionization does not affect temperature anisotropies, but it generates new polarization power proportional to τ^2.

Moreover, the initial conditions for the primordial scalar density perturbations are described by the amplitude, $\mathbf{A_s}$, and the spectral index, $\mathbf{n_s}$, which indicates how the fluctuations change with the scale.

The parameters mentioned above (Ω_b, $\Omega_{\rm CDM}$, τ, A_s, n_s) constitute the simplest incarnation of the ΛCDM model, with the addition of the angular scale of the sound horizon at decoupling, θ_*. This parameter slightly differs from the one at recombination defined in Eq. (1.68). Indeed, decoupling happened at $z_* \sim 1089$, when photons last scattered off the few free electrons left available after recombination (at $z \sim 1100$). Thus,

$$\theta_* = \frac{r_s(z_*)}{D_{A,c}(z_*)} \,. \tag{1.71}$$

CMB anisotropies observed by the *Planck* satellite (see Fig. 1.6) have provided the tightest constraints on these cosmological parameters, strongly supporting the ΛCDM

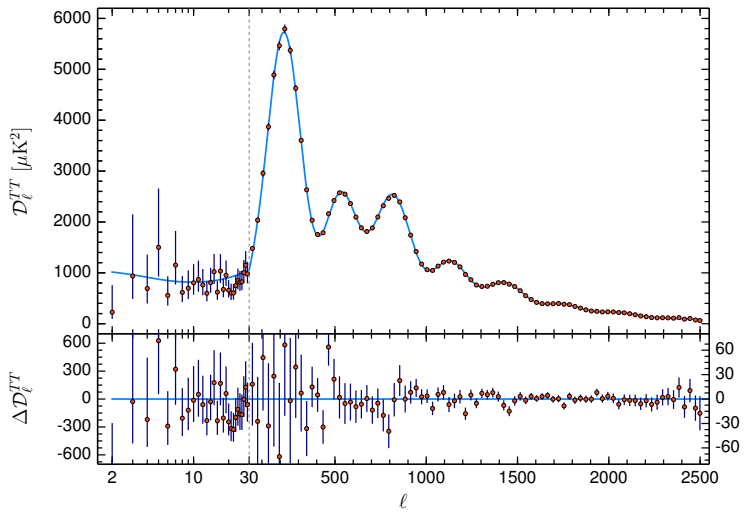

Figure 1.6. The TT angular power spectrum from *Planck* 2018 data [11]. The light blue curves represent the best-fit ΛCDM theoretical prediction. Residuals between data and the model are shown in the lower panels. Error bars include Gaussian 1σ uncertainties including cosmic variance. At $\ell = 30$ the horizontal axis switches from logarithmic to linear scale.

model [11][4] To mention some of them: $\Omega_k = -0.0106 \pm 0.0065$, $\Omega_\Lambda = 0.6847 \pm 0.0073$, $\Omega_m = 0.3153 \pm 0.0073$, $100\theta_* = 1.04110 \pm 0.00031$ and $\tau = 0.0543 \pm 0.0073$ (from TT,TE,EE+lowE+lensing analysis) [11]. See also Sec. 4.4.

While CMB observations provide a precise picture of the early Universe, their interpretation often requires a consistent connection to the late-time expansion history. In the following section, we turn to the concept of cosmological distances, which play a central role in linking early- and late-Universe probes and in interpreting observables such as BAO and SNIa, main characters of Chapter 2.

1.3 Distances in Cosmology

As already seen in the previous sections of this Chapter, the Universe expansion is naturally described in comoving coordinates, a reference frame that moves with the Hubble flow. In this system, let us consider two observers located at A and B and a light propagation (null geodetics, $ds^2 = 0$) between them. If a photon emitted at time t by the observer in A is received at time t_{obs} by the second observer in B, the

[4]The ESA *Planck* mission currently provides the primary benchmark against which constraints from other probes on the key parameters of the ΛCDM model are compared. Launched on 14 May 2009, the satellite produced high-resolution all-sky maps with 74 detectors across nine frequency bands from 30 to 857 GHz [72]. It scanned the full sky twice per year, achieving unprecedented sensitivity, angular resolution, and frequency coverage. Its primary goal was to measure temperature anisotropies with an accuracy up to the cosmic variance limit. The final data release by Planck in 2018 [11] established it as the definitive experiment of its kind. The satellite also provided insights into galaxy clusters via the Sunyaev-Zeldovich effect [73] and the interstellar medium of the Milky Way.

comoving distance between them is defined as

$$D_c = \int_t^{t_{\rm obs}} \frac{cdt'}{a(t')}\,, \tag{1.72}$$

which is simply a reformulation of Eq. (1.8).

The *proper* distance at the observation time is simply the comoving distance scaled by the scale factor:

$$D_p(t_{\rm obs}) = a(t_{\rm obs})D_c\,. \tag{1.73}$$

If the photon is observed at the present time, $t_{obs} = t_0$, proper and comoving distances coincide due to the normalization of the scaling factor, $a_0 = 1$. For nearby events (close in redshift) moving with the Hubble flow, the comoving distance represents the separation we would measure today. In cosmography, D_c suits an important role since all other distances can be quite simply derived from it [74], resulting extremely important to measure aspects of the LSS imprinted in the Hubble flow.

A central observational quantity is the *luminosity distance*, D_L, which relates the intrinsic luminosity of a source, L, to the observed flux, F. Without any geometrical assumption on the Universe, the luminosity L emitted by a source at a point P and the flux F (or the luminosity per unit area) observed at $\tilde{P}$, are related in the following way

$$D_L^2 = \frac{L}{4\pi F}\,. \tag{1.74}$$

This defines the luminosity distance from the emitting source. Taking into account the expansion of the Universe, the area of a spherical surface centered at P and passing through $\tilde{P}$ becomes $4\pi a_0^2\Sigma(\chi)^2$, where $\Sigma(\chi)$ is the geometrical function introduced in Eq. (1.2). Due to cosmic expansion, photons emitted by the source are redshifted by a factor a/a_0. Additionally, time dilation implies that photons emitted over an interval δt at the source are received over a longer interval $\delta t_0 = (a_0/a)\,\delta t$ at $\tilde{P}$ (see Eq. (1.10)). Consequently, the flux observed at $\tilde{P}$ is

$$F = \frac{L}{4\pi a_0^2\Sigma(\chi)^2}\left(\frac{a}{a_0}\right)^2\,, \tag{1.75}$$

and therefore

$$D_L = \frac{a_0^2}{a}\Sigma(\chi) = (1+z)a_0\Sigma(\chi)\,. \tag{1.76}$$

For radial light propagation ($ds^2 = 0$, $d\theta = d\phi = 0$), the comoving distance in Eq. (1.72) can be expressed in terms of the redshift. Equivalently, this means that we can rewrite Eq. (1.8) as

$$\chi = \frac{1}{a_0}\int_0^z \frac{dz'}{H(z')}\,, \tag{1.77}$$

being $H(t) = \dot{a}/a$. This provides a complete framework for expressing luminosity and other cosmological distances in terms of observable redshift.

Recalling the definition of Ω_k introduced in Eq. (1.18), we can rewrite the luminosity distance in the following compact form:

$$D_L(z) = \frac{c}{H_0}(1+z)\kappa(z)\,, \tag{1.78}$$

where, as already seen similarly in Eq. (1.65),

$$\kappa(z) \equiv \begin{cases} \frac{1}{\sqrt{\Omega_k}} \sinh(\sqrt{\Omega_k}\zeta(z)) & if \quad \Omega_k > 0 \\ \zeta(z) & if \quad \Omega_k = 0 \\ \frac{1}{\sqrt{-\Omega_k}} \sin(\sqrt{-\Omega_k}\zeta(z)) & if \quad \Omega_k < 0 \end{cases} \tag{1.79}$$

and being

$$\zeta(z) = \int_0^z \frac{H_0}{H(z')} dz' \,. \tag{1.80}$$

Given Ω_k and $H(z)$, the previous relations allow the computation of the luminosity distance for any redshift z. Conversely, if the apparent and absolute luminosity of a sufficient number of objects is known, $D_L(z)$ can be measured and it can be used to infer Ω_k and $H(z)$. This forms the basis of the distance ladder method, which will be discussed in Chapter 2.

The luminosity distance in Eq. (1.78) is related to the angular diameter distance, $D_A(z)$ (see Sec. 1.2), through the Etherington (or *cosmic distance duality*, CDDR) relation as [75]

$$D_A(z) = \frac{D_L(z)}{(1+z)^2} \,. \tag{1.81}$$

This expression holds in any metric theory of gravity with a conserved number of photons that propagate along null geodesics[5]. Angular diameter distances can be used to map the expansion history and the geometry of the Universe, as they relate the physical size of an object to its observed angular size on the sky. It is useful to express Eq. (1.81) in terms of the comoving angular diameter distance, which we introduced in Eq. (1.64) as $D_A^{(c)}(z_{rec})$, being in that case referred to the recombination epoch. For convenience, hereafter, we will denote the comoving angular diameter distance at a given redshift z by $D_M(z) \equiv D_A^{(c)}(z)$, which is related to the angular diameter distance via

$$D_M(z) = (1+z) D_A(z) \,, \tag{1.82}$$

which is the standard notation adopted in literature.

Once astrophysical objects of known size are identified, measurements of their angular sizes can be translated into angular diameter distances, which in turn can be employed to constrain cosmological parameters. Such objects serve as standard rulers, which will be addressed in Sec. 2.2.

Now that the essential theoretical framework and the concepts of cosmological distances have been established, we can naturally move to the next chapter, where we introduce the *cosmic distance ladder*, the stepwise framework that allows us to determine distances across the Universe.

[5]Recently, departures for CDDR have been the subject of several studies [76, 77, 78, 79, 80]. In this thesis, we will also assess the validity of the relation by applying a model- and calibrator-independent method, see Sec. 10.2.

Chapter 2

The cosmic distance ladder

Determining distances in astronomy is a fundamental yet challenging task, as no single method can encompass the vast range of scales in the Universe. To overcome this, astronomers and cosmologists rely on a hierarchy of techniques known as the *cosmic distance ladder*. Each rung of this ladder provides measurements over a limited distance range and must be calibrated using methods that are valid at shorter distances.

At the lowest rungs lie the *direct* or geometric methods, which do not rely on assumptions about the intrinsic properties of an object. Examples include stellar parallax, which allows distances to nearby stars to be inferred from the apparent shift of their positions as the Earth orbits the Sun. These measurements establish a firm foundation for calibrating more indirect methods.

Moving to larger scales, *standard candles* — objects with predictable intrinsic luminosities — allow astronomers to infer distances by comparing observed brightness with known luminosity. Standard and well-established examples include Cepheid variable stars and SNIa, which form the backbone of the local and intermediate rungs of the ladder. By carefully calibrating these sources, it becomes possible to extend distance measurements far beyond the Milky Way, reaching nearby galaxies and even cosmological scales (see Sec. 2.1).

Analogously, one can employ objects of known size in the Universe — *standard rulers* — as the comoving sound horizon at the baryon drag epoch, imprinted in both the CMB temperature anisotropies and in the large-scale distribution of galaxies. This approach, therefore, starts from high-redshift observations and anchors them to the early Universe (see Sec. 2.2).

The cosmic distance ladder thus provides a systematic framework for mapping our cosmos. It enables the determination of fundamental quantities such as H_0, strongly intervening in the Hubble tension and, more broadly, informs our understanding of the expansion history and large-scale structure of the Universe. Despite its undeniable utility, there remain ongoing debates regarding potential biases or systematic effects that may affect the reliability of some rungs of the ladder. We will discuss this in Chapter 3, while we devote the following Chapter to outlining the methods at each rung of the ladder, starting with the local – directly calibrated – measurements and progressing to the more indirect techniques that extend our reach to the distant Universe.

2.1 Standard candles and the local distance ladder

The most straightforward way to measure distances to nearby Solar System objects is by reflecting electromagnetic radiation off them. Since the speed of light is constant, measuring the time interval between emission and detection directly yields the surface-to-surface distance. This can be achieved with radar ranging experiments within the Solar System, such as the Lunar Laser Ranging [81]. However, because electromagnetic signals weaken according to the inverse-square law with distance, this technique becomes impractical beyond the Solar System.

Geometric *parallaxes* — the apparent shift in the angular position of nearby stars relative to a background of more distant ones as Earth orbits the Sun — provide a well-established geometric anchor. This method allows the definition of the *parsec* as the distance at which a star would exhibit a parallax angle of exactly 1 arcsecond, corresponding to approximately 3.26 light years. The calculation relies on an accurate measurement of the orbital radius of the Earth, itself determined via electromagnetic reflection techniques. With current instrumentation, like the ESA satellite Gaia [82], parallax measurements can reach stars at distances up to a few tens of thousands of light-years.

However, every technique operates only within a limited range. Extending the reach of the cosmic distance ladder beyond the limits of direct methods requires exploiting the intrinsic properties of objects, such as their luminosity. By combining our understanding of stellar physics, the nature of light, and spectroscopic observations, astronomers identify classes of objects with predictable intrinsic brightness. The goal is to determine this intrinsic luminosity with sufficient accuracy to turn an observed flux into a precise distance via the inverse-square law as in Eq. (1.75).

These objects are called *standard candles* and are invaluable for indirectly measuring distances that would otherwise be inaccessible. In our local neighbourhood, pulsating stars known as Cepheid variables are excellent standard candles. It is worth, at this point, providing a historical insight.

*A brief excursus on the **Hubble law***

A pivotal step toward the establishment of the extragalactic distance scale was made by Henrietta Swan Leavitt in the early 20th century. While studying variable stars in the Small Magellanic Cloud at the Harvard College Observatory, Leavitt discovered in 1908 and firmly established by 1912, the period–luminosity relation of Cepheid variables [83]: brighter Cepheids exhibit longer pulsation periods. That is, the shape of their light curves reveals a rapid rise to peak brightness followed by a slower decline. Since all stars in the Magellanic Clouds could be assumed to be at roughly the same distance, the observed correlation revealed an intrinsic property of Cepheids. Once the zero point of the relation was calibrated using geometric methods, Cepheids became powerful standard candles, enabling the first reliable measurements of extragalactic distances. Her pioneering contribution is recognized as one of the most significant milestones in observational cosmology, as her work set the stage for the discovery of the linear relation between galaxy distances, d, and recession velocities, v, by Edwin Hubble [2] (see Fig. 2.1). This relation, expressed as

$$v = H_0 d \tag{2.1}$$

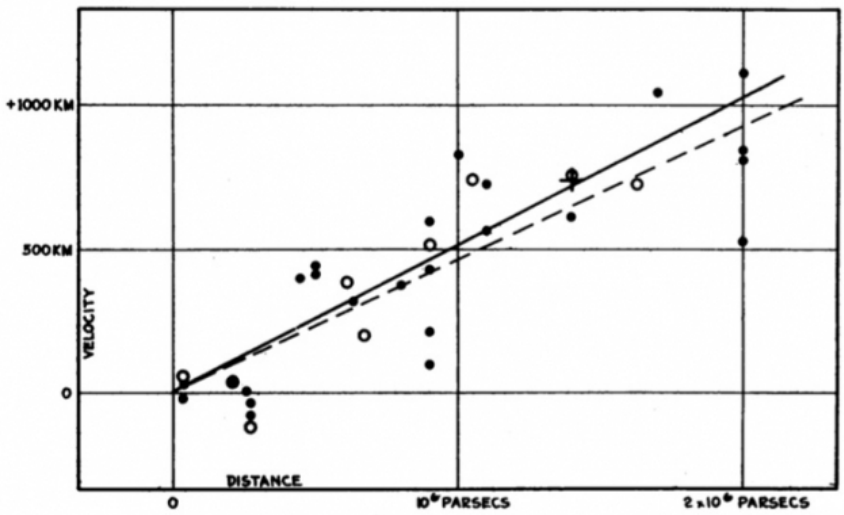

FIGURE 1
Velocity-Distance Relation among Extra-Galactic Nebulae.

Figure 2.1. The Hubble law for the velocity-distance relation for galaxies measured by Edwin Hubble in 1929 and published in [2].

is known as the *Hubble law* and provided the first direct observational evidence for the expansion of the Universe[1]. Almost simultaneously, Georges Lemaître independently formulated the same relation on theoretical grounds [3] using Einstein's theory of relativity [1]. These milestones not only established the first rungs of the cosmic distance ladder but also laid the foundation of modern cosmology.

The Hubble law is valid at small distances, when $v \ll c$. In this regime, redshift is related to velocity via the relation $z = v/c$. Thus, in the limit $z \approx 0$, one can also write a redshift-distance relation, $cz = H_0 d$. The Hubble parameter H_0 characterizes the slope of this relation. However, nearby systems are dominated by local gravitational interactions and therefore they are not good tracers of the expansion of the Universe. To reach the regime of distant galaxies, i.e. the Hubble flow in $0.02 \lesssim z \lesssim 0.15$, one can use a distance ladder built on a succession of distance indicators. A simple sketch of this approach is shown in Fig. 2.2.

The most precise implementation of the distance ladder currently relies on a three-step procedure, which is summarized below.

1. First, geometric distances are employed to calibrate the period–luminosity relation of Cepheid variables in nearby galaxies. Parallaxes from the Gaia mission have provided sub-percent level precision for thousands of nearby stars [85], dramatically improving the calibration of *classical* Cepheid variables, i.e. young, massive, population I stars with luminosities observable to distances of 20–30 Mpc. Complementary geometric anchors include detached eclipsing

[1]The first observational hint suggesting that the universe was expanding was actually provided by the American astronomer Vesto Slipher. In 1912–1917, he measured the radial velocities of spiral nebulae using spectroscopy at Lowell Observatory, finding that most of these nebulae were redshifted [84]. These velocity data were later used by Edwin Hubble in 1929, together with distance estimates, to formulate the empirical Hubble Law.

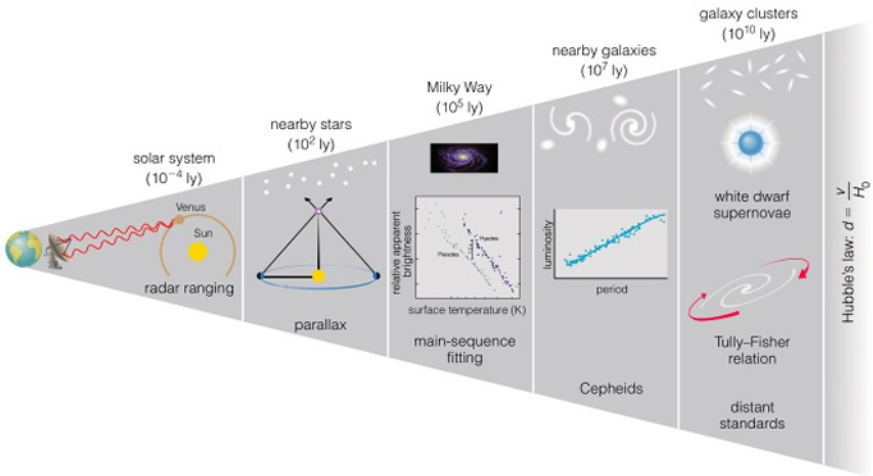

Figure 2.2. Sketch of the succession of objects and techniques used to build the standard local distance ladder, from our Solar System up to the Hubble flow.

binaries (particularly in the Large Magellanic Cloud, LMC) [86] and water masers in nearby galaxies, such as NGC 4258 [87]. These anchors establish absolute distance scales with robust error budgets.

While Cepheids provide the most homogeneous and reliable set of distances to many nearby galaxies, resolving individual stars at great distances becomes increasingly difficult. Alternative standard candles to be employed as primary indicators include, for instance, the Tip of the Red Giant Branch (TRGB) [88, 89][2], Mira variables [90] or J-regions of the asymptotic giant branch (JAGB) [91, 92]. They have also been employed to cross-check Cepheid-based results and assess potential systematics.

2. With their zero-point calibrated by Gaia parallaxes, Cepheids can be observed in host galaxies that also contain SNIa. The Hubble Space Telescope (HST) has been crucial in extending Cepheid observations to these galaxies with high precision. Because SNIa explosions occur near the same critical mass, their intrinsic luminosities — or absolute magnitude, M — are relatively uniform (see Sec. 4.2), making them excellent candidates for standard candles. However, since the typical rate of SNIa explosions is about one per galaxy per century, far too low to provide multiple events within the handful of galaxies suitable for geometric calibration, it is impractical to bypass the second rung by directly calibrating SNIa with geometric distance anchors (e.g., the Milky Way, the LMC). Thus, calibration of M requires linking SNIa in nearby galaxies with primary indicator distances. The period-luminosity relation is thus adopted to calibrate SNIa on the second rung, up to $d < 40$ Mpc.

   To briefly report the relevant relations, the distance modulus μ of a source is

[2]TRGB in particular has gained prominence as a complementary calibration tool, given its lower sensitivity to dust extinction and stellar crowding.

$$\mu_0 = m_0 - M_0 = 25 + 5\log_{10}\left(\frac{D_L(z)}{1\text{Mpc}}\right), \tag{2.2}$$

with D_L its luminosity distance as given in Eq. (1.78). m is the apparent magnitude, related to the observed flux of the source via

$$m = -2.5\log F + const.\,, \tag{2.3}$$

where the constant depends on the zero point of the magnitude system. M is the absolute magnitude, i.e. the apparent magnitude a source would have if it were at a distance of 10 parsecs, which is related to the luminosity L through

$$M = M_\odot - 2.5\log\left(\frac{L}{L_\odot}\right). \tag{2.4}$$

The subscript 0 in Eq. (2.2) denotes a magnitude free of (or corrected for) intervening absorption by interstellar dust. As detailed in [93, 94], a set of hosts of both SNIa and Cepheids connects the two distance indicators. Thus, for an SNIa in the i-th Cepheid host,

$$m^B_{0,i} = \mu_{0,i} - M^B_0\,. \tag{2.5}$$

Here, $m^0_{B,i}$ denotes the standardized maximum-light apparent magnitude of the i-th SNIa (i.e., corrected for variations around the fiducial color, luminosity, and possible host-galaxy dependencies; see [95]), M^0_B is the fiducial SNIa absolute magnitude, and μ^0_i corresponds to the distance modulus as defined in Eq. (2.2).

Just as Cepheids can be replaced in the first rung, SNIa can also be replaced by methods such as surface brightness fluctuations [96], Type II supernovae [97], or the Tully–Fisher relation [98] (see Sec. 2.1.1).

3. On the third rung, the calibrated absolute magnitude of SNIa enables distance determinations in the Hubble flow (∼100-600 Mpc, or $z < 0.15$), where peculiar velocities are small compared to the Hubble expansion. This allows a direct determination of H_0. More concretely, given a set of SNIa, one can measure the intercept of the distance (or magnitude)-redshift relation, a_B. This intercept is obtained by $a_B = \log_{10} cz - 0.2m^0_B$ in the limit $z \approx 0$. However, for an arbitrary expansion history and $z > 0$, a cosmographic expansion up to the third order leads to [94]

$$a_B = \log_{10} cz\left\{1 + \frac{1}{2}[1-q_0]z - \frac{1}{6}[1-q_0-3q_0^2+j_0]z^2 + O(z^3)\right\} - 0.2m_B\,, \tag{2.6}$$

where q_0 is the *deceleration* parameter and j_0 is the *jerk* parameter, respectively defined as

$$\begin{aligned} q_0 &\equiv -\left(\frac{\ddot{a}}{aH_0^2}\right)_{t=t_0}, \\ j_0 &\equiv \left(\frac{\dddot{a}}{aH_0^3}\right)_{t=t_0}. \end{aligned} \tag{2.7}$$

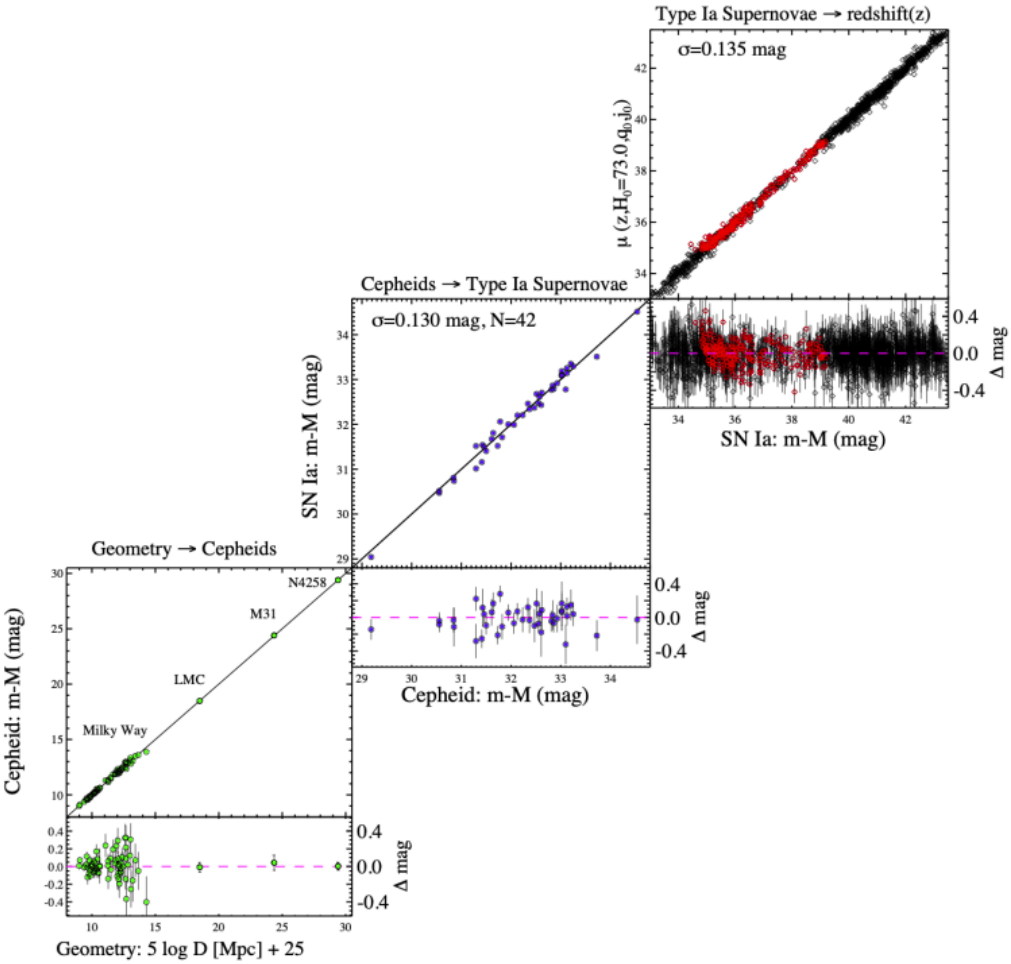

Figure 2.3. The schematic visualization of the three-rungs of the local distance ladder from [94]. From left to right: geometric and Cepheid-based, Cepheid- and SNIa-based, and SNIa and redshift-based. This last rung provides the measurement of H_0 by SNIa in the Hubble flow (in red), at $0.0233 < z < 0.15$.

The Hubble parameter can be finally obtained from the following expression

$$\log_{10} H_0 = 0.2M_B + a_B + 5\,. \tag{2.8}$$

The most comprehensive three-rung ladder determination of H_0 using Cepheids that we just summarized is shown in Fig. 2.3. This figure is taken from [94], where the SH0ES collaboration provided the 1% determination of the Hubble parameter calibrating 42 SNIa with Cepheid using the local distance ladder.

2.1.1 Standardizable candles

While SNIa dominate the role of standard candles in modern cosmology, several other astrophysical sources offer promising, though often less precise, distance measures. These candidates differ in their underlying physical mechanisms, calibration

strategies, and redshift applicability. Indeed, there exists a large redshift gap between measurements of SNIa, which currently cover up to $z \sim 2.3$ [95], and CMB observations, which encode information from the last-scattering surface ($z \sim 1100$) and beyond. Data in that gap could enhance our comprehension of the underlying physical mechanism responsible for the expansion of the Universe. They may be crucial for understanding the origin of cosmological tensions (see Chapter 3), including the anomalous existence of very massive galaxies at $z \gtrsim 10$ [99]. Moreover, recently, a mismatch has been found between ΛCDM predictions and the Hubble diagram built out from high-z quasars (QSOs) [100, 101, 102, 103], which have been employed as standardizable candles [104, 105, 106, 107, 108, 109, 110, 111]. Therefore, it has now become necessary to extend the research to new cosmological probes at intermediate redshifts, which can come to our aid, widening the unexplored range of redshifts and serving as distance indicators.

Exploring higher z requires observing more luminous objects than SNIa. This can be the case not only of QSOs, which reach up to $z \sim 7.5$ [112], but also of Gamma-Ray Bursts (GRBs), the most intense explosions in the Universe after the Big Bang. These objects have been detected up to $z \sim 9.4$ so far [113], but their observation might reach $z \sim 20$ [114]. QSOs and GRBs represent two of the most promising observables beyond SNIa. In the following, we summarize their principal features and relevance for cosmological studies. We will detail some key aspects of both in Secs. 4.5 and 4.6, respectively.

Gamma-Ray Bursts

GRBs are extremely luminous but not uniform in their brightness. So, to standardize them and use them as cosmological tools, it is necessary to find tight empirical correlations between the parameters of their light curves (or spectra) and their luminosity (or energy). There exist a great amount of these relationships that have been studied in the literature. For instance, the $E_p - E_{iso}$ Amati correlation connects the spectral peak energy in the GRB cosmological rest frame and the isotropic equivalent radiated energy released during the prompt phase [115, 116].

Another significant correlation in the prompt emission is the Yonetoku relation [117] between E_p and the intrinsic peak luminosity, L_p. Also relations between L_p and the spectrum lag, $L_p - \tau_{lag}$ [118], or the bulk Lorentz factor with E_{iso} [119] or with L_{iso} [120] are valid alternatives in the literature. However, the issue with many of these correlations is that they have not been demonstrated to be reliable after the truncation and selection effect tests, and when these corrections are applied, the dispersion of the relation itself increases [121, 122, 123]. The source of this scatter is due to both instrumental biases and the underlying mechanism that governs the GRB emission, such as the energy and frequency at which it occurs. Indeed, the physical meaning of many of these relations is still under debate after many years since more than one interpretation is often viable, showing that the emission processes that rule GRBs still need further investigations. All these aspects might significantly limit the applicability of such relations for cosmological purposes. We refer the reader to [124] for a discussion on selection and instrumental biases and to [125] or [126] for a comprehensive review of the several correlations existing in the literature and their possible physical explanation.

In this thesis, we will focus on a particular relation which involves features of the GRB plateau emission phase, that is, the luminosity at the end of the plateau emission, L_X, and its rest frame duration, T_X^* [127, 128, 129, 130, 131, 132, 133]. This relation succeeds in standardizing GRBs by utilizing the shape of their lightcurves. Indeed, around 500 GRBs observed by Swift exhibit a distinct, plateau phase in X-rays [134]. This two-dimensional relation has been used as a cosmological tool for 15 years [135, 136, 137] and has been extended to a three-dimensional correlation — the so-called *3D Dainotti relation* [127, 138, 139] — by incorporating the peak luminosity L_p. Indeed, considering three or more parameters could lead to tighter correlations. We will detail the main aspects of these relations in Sec. 4.5.

A key advantage over prompt-emission correlations is that the plateau phase can be more directly linked to well-established theoretical models, such as magnetar spin-down [140, 141, 142, 143, 144] or forward/reverse shock processes [145, 146]. They also present a reduced scatter in the afterglow features compared to more varied prompt emission properties [147]. Lastly, prompt-emission correlations have the advantage of mitigating selection biases that might otherwise undermine the reliability of the relation [130, 131].

So far, GRBs data and their correlations have been used for many applications in cosmology, such as the investigation of the components of our Universe, the nature of dark energy, and the Hubble constant tension (see, e.g., [148, 149, 150, 151]). However, if a cosmological model is assumed when calibrating GRBs (or other standardizable objects), the so-called *circularity problem* [152, 153, 154] can be encountered if the resulting correlations are then used to constrain parameters of models different from the one employed in the calibration. Up to now, two solutions have been proposed to overcome this problem. One is to fit simultaneously the correlation parameters and the parameters of a cosmological model of interest using GRB data [155, 156, 116, 157, 151, 158, 159]. In this way, cosmological constraints are uniquely determined by GRBs. On the other hand, based on the idea of the distance ladder, one can calibrate GRBs with low-redshift probes, such as calibrated SNIa [160, 157], given that objects at the same redshift should have the same luminosity distance regardless of the underlying cosmology, if the latter respects the CP. Most of the calibrated-GRB cosmological analyses are based on this idea. They make use of cosmographical methods [161, 162] or Gaussian Processes as in [163]. The calibration occurs at $z \lesssim 2.5$ (i.e. below the maximum redshift in the SNIa samples) and then the calibrated GRB relations can be employed to build an extended Hubble diagram up to the high-z region covered by the GRBs. In doing so, analogously to the calibration of SNIa, it is usually assumed that the GRB correlation does not evolve with redshift, although this evolution could actually have a non-negligible impact [164]. For a discussion of the differences between SNIa-based and independent GRB calibrations, and the impact of evolutionary effects, see [130, 165, 159]. Another possible caveat of this method is that some unaccounted-for systematic biases of SNIa may propagate into the calibration results (see ongoing discussions in [166, 167, 168, 169, 170]). Avoiding these biases might be important in light of the Hubble tension.

Looking for alternative calibrators becomes thus fundamental. In the future, the use of standard sirens up to $z \sim 4$ appears to be a promising route [171]. As of now, data on galaxy clusters in the redshift range $0.14 \leq z \leq 0.89$ [172] or Observational

Hubble Data (OHD) at $z \approx 2$ [148] have been employed in the calibration. This is usually done in combination with reconstruction techniques such as Gaussian Processes [173, 164] or the Bézier parametric curve obtained through the linear combination of Bernstein basis polynomials [174, 161, 175, 176]. These studies seek to extend the Hubble diagram by calibrating GRBs and then integrating them with complementary data sets (such as SNIa and BAO) to test and constrain cosmological models.

In Chapter 7, we leverage these potential standardizable candles to study the extended Hubble diagram by applying a low-redshift calibration of GRBs. We do so with a specific subset of OHD and a mostly agnostic technique.

Quasars

Quasars are the most luminous persistent objects in the Universe, with integrated luminosities in the range $10^{44} - 10^{48}\,\mathrm{erg\,s^{-1}}$ spanning the ultraviolet (UV) to X-ray bands. Their UV emission, arising from the accretion disc surrounding a supermassive black hole, contributes up to $\sim 90\%$ of the quasar bolometric output, while the remaining fraction is emitted in X-rays, which are believed to originate from a hot plasma of relativistic electrons that Compton up-scatters photons from the disc [177].

The use of QSOs at cosmological scales allows us to probe redshifts up to $z \sim 7$ [112, 106]. Unlike GRBs, QSOs follow a relation that is relatively well established within the community. Indeed, observations reveal a non-linear correlation between the rest-frame UV luminosity at 2500 Å (L_{UV}) and the X-ray luminosity at 2 keV (L_{X}), usually parameterized as

$$L_{\mathrm{X}} \propto L_{\mathrm{UV}}^{\gamma}, \quad \gamma \simeq 0.6, \tag{2.9}$$

as first noted in e.g., [178]. The precise mechanism responsible for the transfer of gravitational energy from the accretion disc to the corona, preventing its rapid cooling through inverse Compton scattering, however, remains poorly understood. The generalization of Eq. (2.9) is called *Risaliti-Lusso* relation [179], and it will be discussed in detail in Sec. 4.6.

So far, QSOs have done a remarkable job as promising tools for cosmological applications. The use of QSOs as cosmological probes relies on the aforementioned non-linear relation to provide independent distance estimates, effectively transforming quasars into standardizable candles. This extends the SNIa Hubble diagram to a largely unexplored redshift range.

Studies combining QSO catalogs with GRB observations have achieved notably small uncertainties on cosmological parameters [111, 110]. Recent analyses confirm the validity of the Risaliti-Lusso relation [109, 180, 108], while its combination for QSOs with SNIa enables corrections on the redshift evolution as a function of cosmology [109], on the same line as what is done for GRBs. Despite systematics in QSO measurements that should be carefully considered in future probes [181], the relation remains promising: its average observed dispersion is ~ 0.20–0.25 dex, decreasing significantly when only sources with the highest-quality X-ray data are used [182]. This suggests an intrinsic scatter below 0.1 dex, pointing toward a tight

and universal physical process regulating the energy transfer between the accretion disk and the X-ray emitting corona in QSOs.

Within this framework, QSOs have been applied to constrain extended theories of gravity. For instance, $f(T)$ cosmologies have been tested through cosmography in both flat and non-flat geometries [183], while high-quality UV and X-ray QSO fluxes up to $z \sim 5.1$ have been combined with GRBs in [101]. From a cosmographic perspective, tensions between ΛCDM and best-fit cosmographic models have been highlighted using QSOs in combination with other probes: QSOs, SNIa, and GRBs [101]; QSOs and SNIa [102]; and QSOs combined with GRBs, BAO, and SNIa [184]. It is still unclear whether these tensions signal departures from ΛCDM or are driven by the presence of systematics in the data or in the methodology. Therefore, it is important to continue combining these alternative probes while improving the characterization of their physical properties, ensuring they can be reliably used as cosmological tools.

Another strategy to improve precision consists of selecting a QSO sub-sample that best follows the Risaliti-Lusso relation, minimizing intrinsic scatter. Various selection techniques [185, 186, 187] have demonstrated that such QSO sub-samples can act as standalone cosmological probes, achieving precisions comparable to those from SNIa. We will describe these samples in Sec. 4.6 and, on the same line of GRBs, we calibrate these objects to build the QSO-based Hubble diagram, whose analysis is presented in Chapter 8.

Although not subjects of this thesis, it is worth mentioning other astrophysical objects that can potentially serve as standard candles, albeit generally with greater limitations and reduced precision.

- *Type II supernovae* (SNII), resulting from the core collapse of massive stars, can be standardized through empirical correlations between plateau luminosity and expansion velocity [188], yielding distances with typical scatters of ~ 0.4 mag. Unlike SNIa, the standardization of SNII requires spectroscopic information, specifically line velocity measurements. Recently, [97] applied this technique to determine H_0 using SNII as the final rung of the distance ladder, obtaining a precision of 5%.

- The *Tully–Fisher relation* links the intrinsic luminosity of spiral galaxies to their rotation velocity, providing a steady supply of distance estimates up to ~ 100 Mpc, particularly effective in the infrared where dust effects are reduced. A recent study by [98] provided a catalog of ∼10,000 spiral galaxies using this method, which has been employed to measure the Hubble parameter with a precision of 3.3%.

- *Surface Brightness Fluctuations* (SBF) exploit the statistical variation in the number of bright stars per resolution element in early-type galaxies, allowing accurate distances when calibrated against local indicators [189]. The SBF method is particularly effective for elliptical galaxies, reaching up to ∼150 Mpc (and potentially ∼300 Mpc with JWST). The main challenge lies in separating the intrinsic Population II signal from contaminants such as globular clusters, star-forming regions, and background galaxies. Using the SBF calibration

in a Cepheid–SBF–SNIa route introduces an additional rung in the distance ladder, which increases both systematic and statistical uncertainties. However, it provides the important advantage of enlarging the calibration sample of local SNIa, thanks to the greater overlap between galaxies hosting SNIa and those with SBF measurements, as it has been exploited recently in [190].

- *HII galaxies* are dwarf galaxies characterized by intense star formation, often exhibiting strong emission lines. Their luminosities are primarily determined by young stellar populations, making them valuable for distance measurements. A notable distance indicator is the L–σ relation, which correlates the luminosity of HII galaxies with the width of their emission lines. This relation has been calibrated using local galaxies with well-known distances and has shown promise for extending distance measurements to higher redshifts. For instance, a study incorporating data from JWST expanded the sample of HII galaxies to $z \sim 7.5$ [191], obtaining cosmological results which align with those obtained using SNIa from Pantheon+ [192]. This is the case, for instance, of the higher measured value of $H_0 \sim 73$ km/s/Mpc, although determined with a precision of 5%. Indeed, challenges remain in using HII galaxies as standard candles. The L–σ relation accuracy is influenced by the star formation history of the galaxy, as multiple starbursts of varying ages can affect the emission line widths.

Although the local distance ladder provides a robust framework for calibrating nearby distances, it still depends sensitively on the properties of the anchors and on the assumption that SNIa (or similar) can be reliably treated as standardizable objects. Moreover, this approach is subject to several sources of systematic errors. The current discrepancy in the determination of H_0 (see Sec. 3.1) has stimulated several studies aimed at reassessing the robustness of this method. For instance, some works have highlighted potential systematics in the intermediate rung of the local distance ladder, which may bias the current expansion rate to higher values, see, e.g., [193, 194, 195, 196, 197]. Consolidations on the use of anchors are also ongoing [198, 89]. As already mentioned, other standard candles, like, e.g., the TRGB ([88, 89]), are viable alternatives for estimating H_0 without relying on early-time processes and possibly bypassing some of the Cepheid-related systematics. Notably, some of these alternative studies lead to smaller values of H_0 [89, 92], more compatible with the early-time estimate by *Planck*, unlike other local measurements.

Conversely, one can approach the problem using objects of known size in our universe that serve as *standard rulers*, and which are the subject of the next Section.

2.2 Standard rulers and the inverse distance ladder

In Chapter 1, we discussed the behavior of the primordial photon–baryon fluid in the early Universe and its influence on the large-scale structures observed today. It is worth recalling that acoustic oscillations in this tightly coupled fluid, before the decoupling of CMB photons at $z_* \simeq 1089$, left characteristic imprints in the temperature anisotropies of the CMB. However, since galaxies trace the matter content of the universe, the BAO feature is transferred into galaxy clustering as well, where it manifests itself as a peak in the two-point galaxy correlation function. This

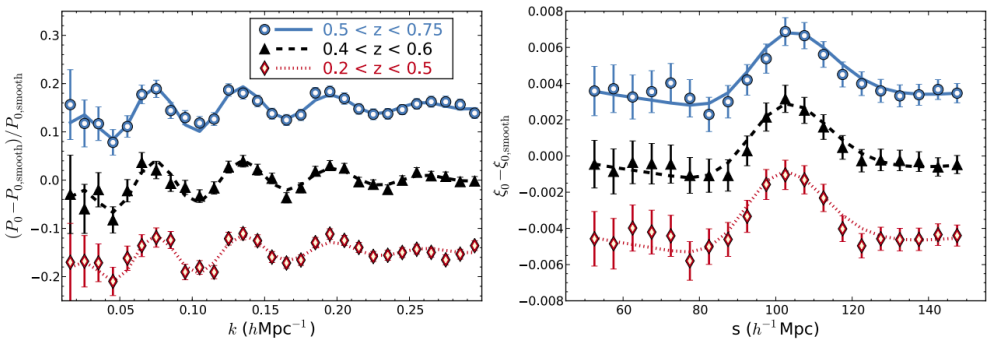

Figure 2.4. Example of BAO signal in the measured power spectrum (left panel) and correlation function (right panel) and predictions of the best-fit BAO models (curves), taken from the work by the BOSS Collaboration [203]. To isolate the BAO information in the monopole ($\ell = 0$) of clustering measurements, predictions of a smooth model with the best-fit cosmological parameters have been subtracted (or divided out in the power spectrum).

peak is located at the maximum distance traveled by the sound wave, i.e. the *sound horizon at the baryon drag epoch*, r_d, and translates into an oscillatory signature, or "wiggles", in the matter galaxy power spectrum, its Fourier transform. Moreover, the BAO signature is detectable in other tracers of matter, such as fluctuations in the Lyman-α forest, which map the radial distribution of neutral hydrogen clouds along the line of sight to distant quasars. Several galaxy surveys have measured these features in the last twenty years with increasing degree of precision and spanning different redshift ranges [199, 200, 201]. We report an example in Fig. 2.4, from the Baryon Oscillation Spectroscopic Survey (BOSS) Collaboration [202].

In Sec. 1.2, we provided an expression for the comoving sound horizon at recombination (cf. Eq. (1.68)). More generally, the comoving sound horizon at a redshift z is defined as

$$r_s(z) = \int_z^\infty \frac{c_s(z')}{H(z')}\, dz' \,. \tag{2.10}$$

Furthermore, we can also give an expression for the sound speed of waves in the photon-baryon fluid, which, prior to recombination, is given by

$$c_s(z) \;=\; \frac{c}{\sqrt{3(1+R(z))}}\,, \tag{2.11}$$

with

$$R(z) \;\equiv\; \frac{3\rho_b(z)}{4\rho_\gamma(z)}\,, \tag{2.12}$$

where ρ_b and ρ_γ are the baryon and photon energy densities.

The *drag epoch* corresponds to the time when baryons are released from the Compton drag of photons and occurs at redshift $z_d \approx 1059$, slightly later than photon decoupling, since baryons are much less abundant than photons and, hence, feel the presence of the latter for a longer period of time. The comoving sound horizon at this epoch is:

$$r_d \;\equiv\; r_s(z_d) = \int_{z_d}^\infty \frac{c_s(z)}{H(z)}\, dz \,. \tag{2.13}$$

The sound speed is approximately $c_s \simeq c/\sqrt{3}$ well before recombination, after which it gradually decreases and eventually drops sharply at decoupling. Eq. (2.13) turns therefore to

$$r_d = \int_{z_d}^{\infty} \frac{c}{\sqrt{3(1+R(z))}\, H(z)}\, dz\,. \tag{2.14}$$

Assuming standard early-time physics, r_d can be further approximated by

$$r_d = 147.05 \left(\frac{\omega_m}{0.1432}\right)^{-0.23} \left(\frac{N_{\rm eff}}{3.04}\right)^{-0.10} \left(\frac{\omega_b}{0.02236}\right)^{-0.13} \text{Mpc}\,. \tag{2.15}$$

where $\omega_m \equiv \Omega_m h^2$ and $\omega_b \equiv \Omega_b h^2$ are the physical matter and baryon density parameters today, while $N_{\rm eff}$ is the effective number of relativistic species. In the *Planck* ΛCDM cosmology, assuming standard pre-recombination physics, $r_d = (147.09 \pm 0.26)$ Mpc [11].

Galaxy surveys use r_d as a standard ruler with respect to which they measure cosmological distances at various redshifts. This can be employed to constrain cosmological models in a quite robust way [204, 205, 206, 207, 208].

Indeed, a prior on r_d derived from CMB or a prior on the physical baryon matter density ω_m from BBN can be used to calibrate anisotropic BAO data (see Sec. 4.3), allowing for a measurement of H_0 under the assumption of standard pre-recombination physics (see, e.g., [209]). Hence, this approach is strongly model-dependent.

These calibrated BAO absolute distances can be used to anchor the relative distances from SNIa independently of the local distance ladder and enable the inference of H_0 (and also the absolute magnitude, M) by extending the distance-redshift relation down to $z = 0$. This methodology, known as the *inverse distance ladder*, was first applied by Cuesta et al. [210] and Aubourg et al. [211].

The basic idea starts from the fact that the intrinsic luminosity of SNIa is not precisely known, therefore supernova distances alone cannot provide absolute distances. However, they trace the expansion history of the Universe with high precision, and by anchoring their distance scale to absolute measurements, one can obtain absolute distance determinations that are largely insensitive to specific cosmological models. Although this method reduces dependence on late-time cosmology, the inferred H_0 remains sensitive to assumptions about the sound horizon scale r_d. Further studies employing this technique ([212, 209, 213, 214, 215, 216, 217]) found indeed consistency with CMB-based estimates of H_0 under ΛCDM. Any deviation from standard early-universe physics (e.g., extra relativistic species, early dark energy) alters r_d and hence the inferred H_0 (see discussion in Section 3.4).

Alternatively, one can anchor the SNIa distance scale using strongly lensed quasars, although obtaining H_0 estimates with $\sim 10\%$ uncertainty [218], essentially limited by uncertainties in the modeling of the lenses. See also [219].

In Sec. 4.3, we will provide a more detailed description of the BAO data sets and illustrate that the BAO signal can be extracted using two fundamentally different methodologies. However, when these different measurements are employed in cosmological analyses, they yield notably different results, as will be illustrated in Chapters 9 and 10. Given that BAO play a central role in constructing the

inverse distance ladder, such discrepancies could significantly affect attempts to address the Hubble tension. Therefore, the cosmic distance ladder not only helps in determining H_0 independently of direct early-time probes, but also provides a means to extract intrinsic information about the data involved. If these data are found to hide internal inconsistencies or unaccounted-for systematics, it becomes therefore crucial to explore alternative methods for measuring H_0 that are free from potential biases associated with the local or inverse distance ladder.

Chapter 3

Tensions and current status of ΛCDM

As discussed in the previous Chapters, despite the remarkable success of GR and the concordance cosmological model, ΛCDM, in explaining a wide range of cosmological observations, the standard framework is not without its shortcomings. On the theoretical side, the model relies on the presence of a cosmological constant Λ, whose physical origin remains elusive. The interpretation of Λ is plagued by a severe fine-tuning issue to obtain the right amount of dark energy observed today. Moreover, ΛCDM postulates the existence of cold dark matter, which dominates the matter content of the Universe, yet has not been directly detected despite decades of experimental searches. Closely related is the coincidence problem, which questions why the energy densities of matter and dark energy are of the same order of magnitude precisely in the current epoch, despite their very different evolutionary histories.

In addition to these theoretical puzzles, recent years have witnessed the emergence of observational tensions that further challenge the robustness of the standard model. The most prominent among them is the *Hubble tension*, a significant discrepancy between measurements of the H_0 inferred from early-Universe probes (such as the CMB) and those obtained from local, late-time observations (such as SNIa within the distance ladder method). Having an accurate measurement of this quantity is crucial for an unbiased estimation of the total energy content of the Universe via the Friedmann equation, its age, and also for a correct determination of cosmic distances. We will address this in Sec. 3.1.

Another important issue, discussed in Sec. 3.2, is the *growth tension*, referring to inconsistencies between the amplitude of matter fluctuations measured via the CMB and those inferred from large-scale structure observations at low redshifts.

Beyond these primary tensions, other cosmological anomalies have emerged in the last few years. To give a feeling on how much the standard cosmology picture is still questionable, we will briefly discuss some of them in Sec. 3.3.

All these discrepancies mainly arise from differences in the inferred values of key cosmological parameters with varying levels of statistical significance. While some of these tensions could be attributed to systematic uncertainties in specific observations or probes, the persistence and consistency of the mismatches increasingly point

toward the possibility of new physics beyond the standard cosmological model. The main proposals will be discussed in Sec. 3.4. For dedicated reviews, we refer the reader, to, e.g., [220, 134].

In this Chapter, we examine these open questions, placing particular emphasis on discussing their origin, current status, and possible interpretations. These considerations will provide the broader context for the methodological developments and analyses that will follow in this thesis.

3.1 The Hubble tension

The absolute distance and time scales in cosmology are set by the Hubble–Lemaître parameter, H_0, which also sets the energy scale of the Universe expansion through the Friedmann equation (Eq. (1.19)). Its accurate determination is therefore of utmost importance and has been a long-pursued goal since the very birth of modern (relativistic) cosmology and the idea of an expanding Universe, almost one century ago with Edwin Hubble [221]. Yet, we still do not have a consensus value for this parameter. Determining H_0 and understanding its origin has become one of the most actively pursued objectives in the cosmological community [222, 223, 224].

The SH0ES collaboration has measured H_0 making use of the distance ladder method, discussed in Sec. 2.1. They employ 42 SNIa contained in host galaxies with Cepheids at $z < 0.01$, i.e. at distances $d \lesssim 40$ Mpc, to calibrate the absolute magnitude of SNIa, $M^{R22} = (-19.253 \pm 0.027)$ mag. By extending the ladder to the Hubble flow, up to $z \sim 0.15$, i.e. $d \sim 600$ Mpc, they obtain $H_0^{R22} = (73.04 \pm 1.04)$ km/s/Mpc [94] (see Fig. 2.3). Most recently, using Cepheid variables as primary indicators from HST and JWST, they improved the precision by obtaining $H_0 = 73.17 \pm 0.86$ km/s/Mpc [198].

We recall here that H_0 measurements based on the distance ladder are basically model-independent, since they only rely on the CP and the assumption of standardizable objects, i.e., with a standardized luminosity which remains constant from our vicinity to the far end of the Hubble flow. The current discrepancy in the determination of H_0 has stimulated many studies aimed at reassessing the robustness of the local distance ladder method. As already discussed in Sec. 2.1.1, these can include potential systematics in the intermediate rung of the local distance ladder or the use of different anchors than Cepheids. Moreover, there have been some critical discussions about the SH0ES measurements [225, 226]. Indeed, while SNIa offer the strongest leverage in the local distance ladder, alternative standard candles, while varying in calibration techniques and stellar populations, can be independent methods to cross-check the results obtained with SNIa. Examples include TRGB, JAGB or Mira variables (see Sec. 2.1). Notably, while the majority of them consistently report SNIa-like values of H_0, recent studies point out that some of these alternative studies lead to smaller values of H_0, in lesser or no tension with ΛCDM, see, e.g., [227, 228, 88, 166, 89, 197, 229, 92, 230].

CMB observations, on the other hand, allow us to measure in a model-independent way and very precisely the position of the first acoustic peak of the CMB temperature angular power spectrum or, equivalently, the angle θ_* (Eq. (1.71)). Pre-recombination physics, which depends of course on the model, fixes the sound

horizon at recombination and this, in turn, fixes the comoving angular diameter distance to the last-scattering surface to fulfill the tight constraint on θ_*[1]. In the context of the ΛCDM, the fit to the full TT,TE,EE+lensing CMB likelihood from *Planck* leads to $H_0^{P18} = (67.36 \pm 0.54)$ km/s/Mpc [11]. The latter is in $\sim 5\sigma$ tension with SH0ES. This constitutes the well-known H_0 tension, the biggest mismatch between the standard model of cosmology and current observations. For dedicated reviews, we refer the reader to, e.g., [231, 220].

The robustness of *Planck* inference has been corroborated by ground-based experiments such as the ACT [232], which achieve precise measurements of the damping tail and the lensing-induced smoothing of the CMB spectrum, thereby strengthening the preference for a lower value of H_0.

The angle θ_* is the CMB analogue of the transverse BAO scale, $r_d/D_M(z)$, which has been measured by several galaxy surveys (see Sec. 4.3). As r_*, r_d is also set by the physics in the pre-recombination era. An independent and complementary avenue to H_0 is provided by this scale. Major surveys, including BOSS, eBOSS, and DESI (Dark Energy Spectroscopic Instrument), have reported determinations of H_0 in agreement with CMB-based estimates. In particular, the latest DESI results (DR2) [201], relying on over ~ 6 million galaxies across a wide range of redshifts and calibrated with the *Planck*/ΛCDM measurement of the sound horizon, $r_d^{P18} = (147.09 \pm 0.26)$ Mpc [11], yield $H_0 = 68.17 \pm 0.28$ km/s/Mpc. When a BBN prior on ω_b is used, they consistently find $H_0 = 68.45 \pm 0.47$ km/s/Mpc.

On the other hand, a prior on r_d by assuming standard physics before decoupling can be employed in the inverse distance ladder to extract a model-dependent estimate of H_0 (see Sec. 2.2). A similar level of tension with SH0ES is indeed found when r_d^{P18} is employed to calibrate the anisotropic BAO data in fitting analyses of the standard model (see e.g. [209]) or by using these calibrated data with SNIa apparent magnitudes in parametric and cosmographical analyses [233, 234, 212, 216, 213, 214, 217].

Considering on top of CMB, data from BAO and uncalibrated low- and high-redshift SNIa, one gets $r_d = (147.17 \pm 0.20)$ Mpc and $M = (-19.403 \pm 0.010)$ mag in the standard cosmological model [235]. This value of M is again in $\sim 5\sigma$ tension with the one reported by SH0ES. This is expected, since their large determination of H_0 is induced by the large value of M (M^{R22}) obtained from the calibration in the host galaxies[2].

There is still not a general consensus on which value of the Hubble parameter is the correct one or the nearest to being correct. This statistically significant tension between the two methods could potentially reveal some unknown systematics, underestimation of the uncertainties on H_0 measurements, or flaws in the theoretical assumptions, which could be the signature of some new physical phenomenon in action.

The H_0 tension has also motivated the development of independent paths to measure the Hubble parameter. For instance, the detection of the gravitational wave and the electromagnetic counterpart produced by the merger of the binary

[1]The *Planck* collaboration has measured the CMB acoustic angular scale to 0.03% precision, $100\theta_* = 1.04110 \pm 0.00031$ [11].

[2]In analyses with uncalibrated BAO and SNIa, H_0 and M are intrinsically degenerated, see Eqs. (2.2), (2.8).

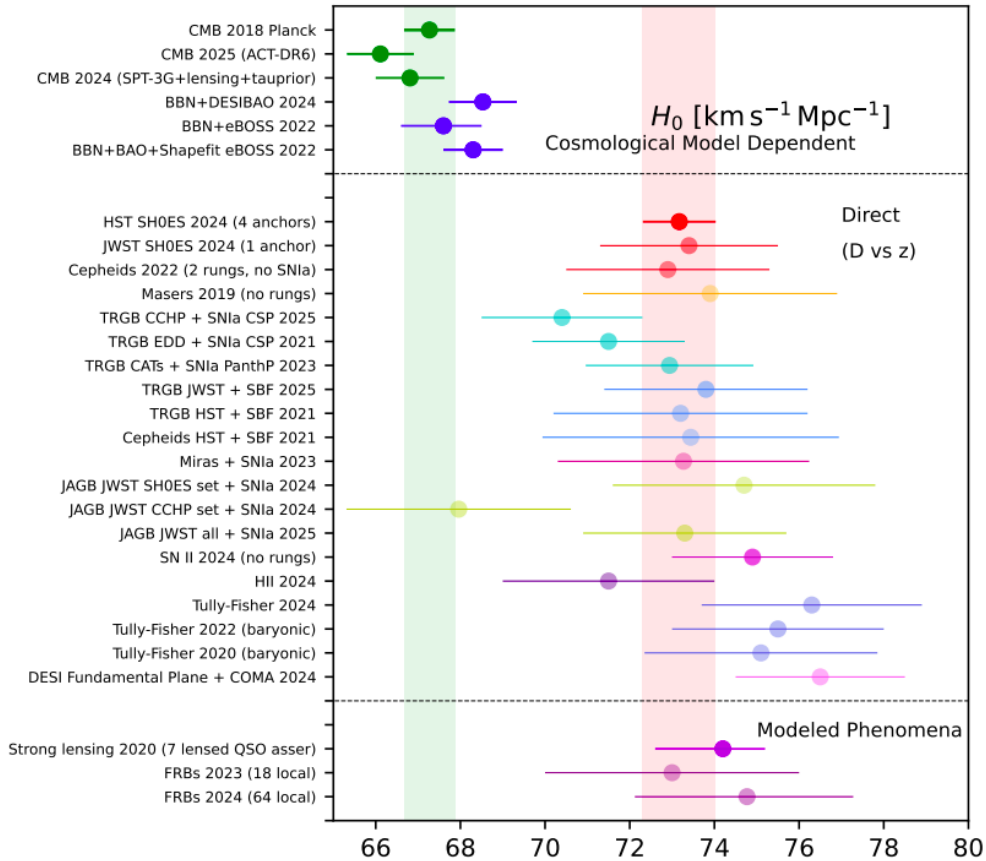

Figure 3.1. List of some of the latest H_0 estimates obtained with different cosmological probes and methodologies. Only those with error bars smaller than 3.5 km/s/Mpc are shown. Figure from [134].

neutron-star system GW170817 has allowed to use this event as a standard siren and to measure $H_0 = (70.0^{+12.0}_{-8.0})$ km/s/Mpc [236], which lies between the *Planck* and the SH0ES values. Although these relatively loose constraints are still insufficient to distinguish between the two competing values, it is worth to remark that they have been obtained without using any form of cosmic distance ladder, and therefore are free of systematic errors that could affect the determinations of cosmological distances in the first rungs (see Sec. 2.1).

To give the reader a perception of how broad the topic has became and how much attention and effort has gained in the last few years, in Fig. 3.1, we report a summary of the latest and most prominent estimates of H_0 from a pletora of methodologies and probes.

A tension in the calibrators of the cosmic distance ladder

In light of the preceding discussion, the Hubble tension can be naturally reinterpreted as a *tension in the calibrators of the direct and inverse distance ladders*, M and r_d. This perspective forms a foundational pillar of this thesis, shaping the direction and focus of our research.

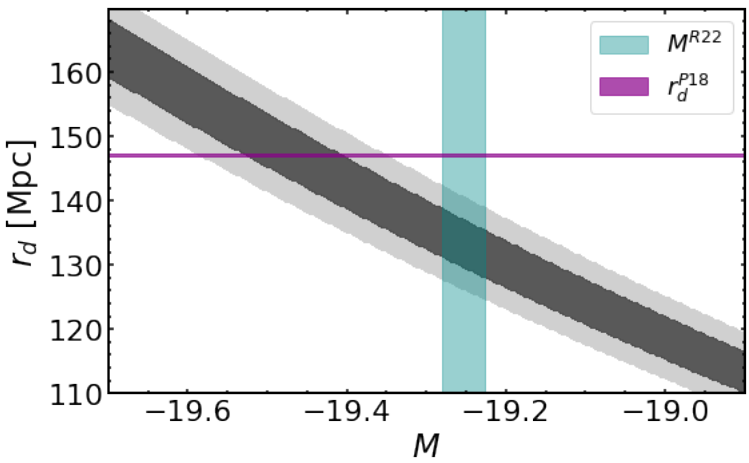

Figure 3.2. Degeneracy band at 68% and 95% C.L. in the M-r_d plane (in gray) inferred from uncalibrated BAO and SNIa data. We have obtained these constraints using the method previously employed in [241], which is based on the Index of Inconsistency by Lin and Ishak [243]. We also include the vertical band with the SH0ES measurement of M (M^{R22}) [94] and the horizontal band with the ΛCDM value of r_d obtained by *Planck* (r_d^{P18}) [11], both at 1σ C.L. The intersection of these two bands lie far away from the region preferred by the uncalibrated 3D BAO and SNIa data (see discussion in the main text).

The discrepancy between the two cosmic ladders in the context of the standard model could be due to some issue with their calibrators [237, 238, 239, 240, 241], either by unaccounted-for systematic errors or by new physics.

It is useful to analyze the constraints in the $M - r_d$ plane that are obtained by studying the compatibility of uncalibrated SNIa and 3D BAO data. This is obtained in our work [242], which is part of this thesis[3].

Fig. 3.2 shows that the calibrators of the direct and inverse distance ladders lie in a quite narrow degeneracy band (see the gray contours). In the same Figure, we also plot the SH0ES constraint M^{R22} and the *Planck*/ΛCDM constraint r_d^{P18}. The mismatch between the overlapping region of these two bands and the SNIa+BAO degeneracy band is nothing but the clear manifestation of the Hubble tension[4].

[3]To obtain these constraints, we make use of the method previously employed in [241], which is based on the Index of Inconsistency (IOI) by Lin & Ishak [243]. This method is usually employed to quantify the level of inconsistency between two data sets in the context of a concrete model when the posterior distributions of the parameters of the model are Gaussian in good approximation, but it can also be employed to calibrate Gaussian data sets in a model-independent way. The IOI between two data sets i, j is $\mathrm{IOI[i,j]} = \frac{1}{2}\mu^{\mathrm{T}}(\mathrm{C}^{(\mathrm{i})} + \mathrm{C}^{(\mathrm{j})})^{-1}\mu$, where μ and C denote, respectively, the difference between the corresponding data vectors and the covariance matrices. The calibrators of two data sets are constrained by minimizing the IOI between them. Here, for each pair (M, r_d), we extract measurements of $D_A(z)$ at several redshifts, by making use by using Eqs. (1.81) and (2.2), and we explore the space of the calibrators by employing the weights $w = \exp(-\mathrm{IOI[BAO, SNIa]})$. The SNIa apparent magnitudes at the BAO redshifts ($m(z_{\mathrm{BAO}})$) and the corresponding covariance matrix are obtained via linear interpolation of SNIa that fall right below and above the angular BAO data points. This is justified by the small redshift spacing of consecutive SNIa in this range. This procedure enables the computation of the weights and the resulting 68% and 95% confidence contours for M and r_d (gray bands in Fig. 3.2).

[4]See also [226] for a similar conclusion.

Indeed, if we believe in standard pre-recombination physics, i.e. if $r_d \sim 147$ Mpc, the absolute magnitude of SNIa, considered to be constant in time, must be $M \sim -19.4$ mag. This value is in clear tension with the one measured by SH0ES in the second rung of the direct distance ladder, M^{R22}, with a discrepancy of about 0.2 mag.

As these two calibrators play an important role in the Hubble tension, it is therefore fundamental to measure them independently from the CMB and the first rungs of the direct distance ladder, as a means of cross-checking the results obtained with the standard methods described above. This way, estimates of M and r_d can be employed to identify the presence of possible systematic errors in the ladders, and also to evaluate and discriminate among alternatives to the ΛCDM model. This will be part of the work carried out in this thesis, and we will examine it in Chapter 6.

A wide range of approaches and theories have been implemented attempting to explain the Hubble crisis. This leads to the introduction of new degrees of freedom. We will discuss some of these alternative scenarios in Sec. 3.4, as now we leave the stage for another crucial issue affecting the standard predictions, which, as we will see, is related to the one presented in this section.

3.2 The growth tension

As we have seen in Sec. 1.2, primordial fluctuations in our Universe manifest as inhomogeneities imprinted on the CMB, providing a snapshot at the last scattering surface. However, these fluctuations also shape the large-scale structure of the Universe, which is measured by galaxy and weak lensing (WL) surveys [203, 244, 245, 246] and also through the impact of WL and the ISW effect on the CMB. Indeed, the amplitude of the CMB power spectrum, particularly through CMB lensing, places strong constraints on the matter density, thereby constraining also the clustering amplitude. At linear cosmological scales, this clustering amplitude — or the amplitude of matter fluctuations — is commonly quantified by the parameter σ_8. This quantity represents the root-mean-square (rms) mass fluctuations on a scale of $R_8 = 8h^{-1}$ Mpc, where $h = H_0/(100\text{km/s/Mpc})$ is the reduced (dimensionless) Hubble parameter. Analogously, the parameter S_8,

$$S_8 \equiv \sigma_8 \sqrt{\Omega_m/0.3}\,, \tag{3.1}$$

combines the clustering amplitude σ_8 with the present-day matter density Ω_m. As such, it provides a key probe of the growth of cosmic structures, and hence of the standard cosmological model.

As H_0, also this parameter undergoes a persistent discrepancy between early- and late-time measurements. We refer to the *growth tension* as a $2-3\sigma$ mismatch between the Planck best-fit values of σ_8 and S_8 obtained under the assumption of the ΛCDM model and some LSS measurements extracted from the analysis of redshift-space distortions (RSD)[5] and WL [247].

[5]Redshift-space distortions occur because the observed redshift of a galaxy is affected not only by the Hubble flow but also by its peculiar velocity. In particular, galaxies falling into gravitational potential wells acquire additional line-of-sight velocity components, distorting the inferred spatial distribution in redshift space.

Specifically, early-time constraints from the *Planck* 2018 CMB temperature and polarization measurements yield $S_8 = 0.834 \pm 0.016$ within the ΛCDM framework [11]. CMB-derived estimates of S_8 are model-dependent and sensitive to parameters that affect the growth and amplitude of matter fluctuations, such as the optical depth to reionization τ (see Eq. (1.70)), which has the largest uncertainty among the ΛCDM parameters, and the sum of the neutrino mass $\sum m_\nu$, which is poorly constrained by CMB data alone and is therefore typically fixed in baseline analyses. These uncertainties can affect the constraints on S_8 [134]. However, the discrepancy persists in independent datasets, such as ACT+WMAP, which reports $S_8 = 0.857 \pm 0.020$ [248].

The late-Universe distribution of galaxies and matter appears instead smoother than predicted by the evolution of fluctuations observed in the CMB. The first indication of a lower value of S_8 was reported in RSD measurements by [249] and further confirmed by several subsequent analyses (see, e.g. [250, 251, 252, 253, 254]). The Dark Energy Survey (DES) also consistently indicate lower clustering. In particular, DES Y3 results combining galaxy clustering and WL data report $S_8 = 0.776 \pm 0.017$ [245]. However, the very recent KiDS-Legacy (Kilo-Degree Survey-Legacy) result, $S_8 = 0.815^{+0.016}_{-0.021}$, seems to reconcile with the ΛCDM prediction, showing consistency with Planck at the level of 1σ [255] (see also [246]).

Beyond these WL measurements, discrepancies at the 2–3σ level persist across independent datasets, suggesting a potential systematic or physical deviation between early and late-time probes of structure formation. Also cross-correlation studies between WL and other probes, such as CMB lensing from Planck, ACT, and SPT, and galaxy clustering from BAO surveys, show general consistency across early and late-time datasets, complicating the interpretation.

The origin of the growth tension remains under debate. It could be partially driven by systematic uncertainties in WL analyses, such as shear calibration errors, photometric redshift uncertainties or suppression of the small-scale power spectrum due to AGN activity [134]. Alternatively, the discrepancy may indicate new physics beyond ΛCDM. Potential explanations include dynamical dark energy, modifications to gravity such as $f(R)$ or scalar-tensor theories, or the influence of massive neutrinos, which suppress late-time structure formation below the free-streaming scale (see Sec. 3.4). However, while solving or partially alleviating the growth tension, these proposals in most cases exacerbate the discrepancy in the Hubble parameter. This intricate interplay further complicates theoretical and phenomenological studies.[6]

However, this is not the only issue. Let us just come back to the definition of σ_8.

The bias introduced by σ_8 and the use of σ_{12}

The amplitude of density perturbations (see Eq. (1.37)) on a scale R is quantified using the rms of mass fluctuations,

[6]For some studies about the growth tension and possible solutions, see, e.g., [249, 251, 256, 257, 252, 254, 258, 259, 260, 261]. Just to mention one: quintessence models could help alleviate the excess of LSS by allowing for a larger fraction of dark energy in the past. However, such models typically predict lower values of H_0, because early dark energy slows down expansion before recombination, thereby worsening the Hubble tension [262].

$$\sigma_R^2(z) \equiv < [\delta_R(\vec{r}, z)]^2 > , \tag{3.2}$$

where the average is performed over the volume of the entire universe at a given z and

$$\delta_R(\vec{r}, z) = \int d^3r' \, \delta(\vec{r} + \vec{r}', z) W_R(r') \tag{3.3}$$

is the matter density contrast $\delta = \delta\rho/\bar{\rho}$ smoothed with a normalized spherical top-hat window function of radius R, $W_R(r)$. Eq. (3.2) can be also written as follows [263],

$$\sigma_R^2(z) = \frac{1}{2\pi^2} \int dk \, k^2 P(k, z) W^2(kR) \, , \tag{3.4}$$

with $P(k, z)$ the matter power spectrum and

$$W(kR) = \frac{3}{k^2 R^2} \left(\frac{\sin(kR)}{kR} - \cos(kR) \right) \tag{3.5}$$

the Fourier transform of $W_R(r)$.

The scale R is taken to be $R_8 = 8h^{-1}$ Mpc, which has an explicit dependence on h. It is important to highlight that this scale has a historical origin. Indeed, it was chosen because galaxy surveys in the 1980s showed clustering strength on scales of a few h^{-1}Mpc. This scale is large enough to probe the quasi-linear regime (not dominated by nonlinear small-scale physics), yet small enough to be measured with galaxy clustering. At these relatively short cosmological distances, the Hubble law can be employed to translate redshift measurements directly into distances in units of h^{-1}Mpc without assuming a fiducial cosmology. In modern surveys exploring a much larger redshift range, a fiducial cosmology is typically used to build three-dimensional maps. In this context, the function (3.4) is simply known as $\sigma_8(z)$.

The problem. Due to the dependence of the scale R_8 on h, the use of σ_8 can introduce important biases in our interpretation of LSS measurements and the results for σ_8 obtained from fitting analyses of cosmological models. This concern was raised for the first time by A.G. Sánchez in [264]. Considering different priors on H_0 in the processing of galaxy clustering data within the framework of a specific model essentially yields values of σ_8 that describe the amplitude of fluctuations at varying scales. This complicates the direct comparison of the various measurements[7]. On the other hand, fitting analyses of two models with dissimilar posterior distributions of H_0 produce derived values of σ_8 that cannot be directly compared due to the exactly same reason. Therefore, interpreting the values of σ_8 in these cases as corresponding to the same physical scale is inappropriate and can crucially bias our conclusions.

A possible solution. In [264], Sánchez suggested to solve this issue by replacing σ_8 with the new parameter σ_{12}, defined as the rms of mass fluctuations at the linear scale of $R_{12} = 12$ Mpc, which does not depend on h and coincides with R_8 only if $h = h_*$, with $h_* = 8/12 \simeq 0.667$. The comparison of σ_{12} values obtained from different galaxy clustering experiments or from fitting analyses of models with

[7]We note here that WL measurements are not affected by the bias of σ_8. Indeed, their constraints on S_8 are nearly insensitive to the prior on h because they are fundamentally angular measurements [265], and it has already been demonstrated that S_8 is an optimal parameter for this cosmological probe [266, 267].

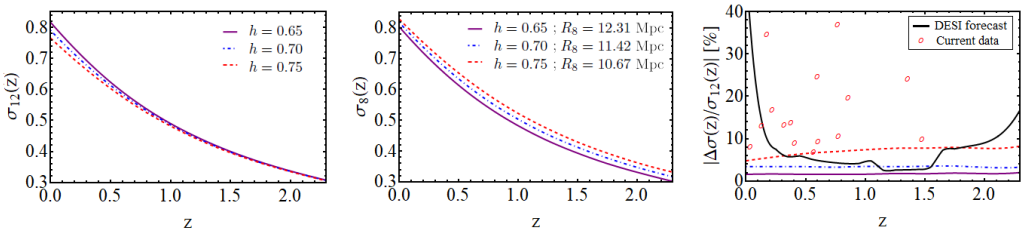

Figure 3.3. *Left plot:* Curves of $\sigma_{12}(z)$ obtained in ΛCDM using the best-fit values of the parameters ω_b, ω_{cdm}, n_s and A_s from the Planck 2018 TT,TE,EE+lowE+lensing analysis [11] and considering three different values of H_0. *Middle plot:* The same, but for $\sigma_8(z)$. *Right plot:* Relative difference $\Delta\sigma(z)/\sigma_{12} \equiv \sigma_8(z)/\sigma_{12}(z) - 1$ for the three scenarios under consideration, which coincides with the relative difference between $f(z)\sigma_8(z)$ and $f(z)\sigma_{12}(z)$. We compare them with the relative uncertainties of current RSD data (red circles) (from, e.g., [268]) and mock RSD data from DESI [269], in black. Some current data points already exhibit a sensitivity comparable to the differences between σ_{12} and σ_8 and this issue will clearly become even more critical with the advent of new data.

different posteriors of h can be carried out without problems, since in this case there is no mixing of scales and, therefore, the differences in σ_{12} can only arise from changes in the experimental results or the models. Some authors have already made use of the parameter σ_{12} in several observational and theoretical works [270, 271, 272, 235, 273, 266, 274, 267, 275, 276, 277], although it still remains largely underappreciated within the cosmological community.

This is not a trivial issue since most of the current tensions (see Secs. 3.1, 3.3) impact the description of LSS in one way or another and are therefore interconnected. For instance, it is straightforward to understand the connection between the growth and the H_0 tensions: the physical scale k used in defining σ_8 depends on h (cf. Eqs. (3.4), (3.1)). Because the matter power spectrum declines as k^{-3}, discrepancies in h can mimic differences in σ_8 by effectively probing different physical scales [264, 278]. For this reason, any new physics introduced to resolve the H_0 tension can directly affect σ_8. Hence, the discussion on the validity of σ_8 in this context can have a substantial impact on these matters.

At this stage, to complement the discussion, we find it instructive to present a simple example illustrating the impact of the bias introduced by σ_8, which is shown in Fig. 3.3. In the two leftmost plots, we compare the shapes of $\sigma_{12}(z)$ and σ_8(z) obtained by using different values of H_0 (or, equivalently, different values of Λ) in ΛCDM, while fixing the primordial power spectrum through the parameters A_s and n_s, as well as ω_b and ω_{CDM}, which in turn fix their entire cosmic evolution. At high redshifts, $\sigma_{12}(z)$ tend to the same function regardless of the value of H_0, since the cosmological constant, which is the only differing piece among the various models, only plays a role at $z \lesssim \mathcal{O}(1)$. The energy densities of the other species evolve exactly in the same way, and the initial conditions for the perturbations are also identical. Hence, the amplitude of fluctuations in these epochs of the cosmic expansion are indistinguishable. However, the $\sigma_8(z)$ behavior tells us something different (see the central plot). There is a non-null vertical shift between the various curves even at large redshifts, which is fully counterintuitive and unphysical. It is caused by the

difference in the scale R_8 induced by the change of h. In addition, the larger h (or, equivalently, Λ), the larger the amplitude of matter fluctuations. This result once again challenges our most basic intuition, since at small redshifts we expect to have a larger suppression of structures for larger values of H_0. Interpreting the results through this plot is challenging, if not impossible. The left plot, in contrast, demonstrates that $\sigma_{12}(z)$ is actually behaving exactly as we would expect, i.e., the curves start to depart from each other at $z \lesssim 1$, when Λ starts to be sizable compared to non-relativistic matter, and larger values of h suppress σ_{12} in the accelerated phase of the Universe. The interpretation of the results shown for $\sigma_{12}(z)$ is unequivocal, as we are now comparing the amplitude of fluctuations at the same physical scale. It is also very illustrative to compute the relative difference between the curves of $\sigma_8(z)$ and $\sigma_{12}(z)$ obtained for a given value of H_0, using the setup explained above. This is equivalent to computing the relative difference between the RSD observables $f(z)\sigma_8(z)$ and $f(z)\sigma_{12}(z)$, since the value of the growth rate $f(z) = d\ln\delta/d\ln a$ cancels in the ratio. We show the results in the rightmost plot. The interesting point here is that the relative difference $\Delta\sigma(z)/\sigma_{12}(z)$ obtained for $h = 0.75$, which is a value pretty close to the SH0ES measurement, is already comparable to the sensitivity of some current RSD data at 1σ C.L., and the situation will become even more pressing in the future, with the advent of data from Euclid [279, 280] and the next data releases from DESI. In fact, using the forecasted final-year DESI data [269], we find that they will be very sensitive to the differences between σ_8 and σ_{12} even for much smaller values of h, lying below the SH0ES measurement, $h \lesssim 0.7$, and in a very broad redshift range which might be as high as $z \sim 2$. Current CMB data, on the other hand, already constrain σ_8 at the $\lesssim 1-2\%$ level [11, 34]. Thus, the comparison of σ_8 values from models fitted to CMB data and with substantial differences in the posteriors of H_0 can already lead to statistically significant biases, as we will explicitly show in Chapter 11.

The work by Sánchez [264] has motivated us to extensively re-analyse the σ_8 bias in cosmological fitting analysis of models that could potentially solve or alleviate the Hubble tension without increasing the growth one. This work is part of this thesis and has resulted in the paper [278]. We will present this analysis in Chapter 11.

3.3 Other anomalies

Beyond the primary H_0 and growth tensions, several additional anomalies have been reported in recent years, posing further challenges to the ΛCDM framework. These discrepancies arise across multiple cosmological probes and scales and, while not covering the research of this thesis, we deem it worth mentioning some of the most relevant.

- *CMB anisotropic anomalies*: Features such as hemispherical asymmetry, lack of large-angle correlations and the so-called *cold spot* persist at modest levels of statistical significance (2-3σ) across WMAP and *Planck* temperature data (see, e.g., [10, 281, 28, 29, 23, 282, 283, 284]). Although generally attributed to cosmic variance, their recurrence motivates studies of more sensitive observations of CMB anisotropies in temperature and polarization, which could

help in assessing if such anomalies are simply statistical flukes or hints for new physics.

- *Cosmic dipole anomalies*: Discrepancies have been reported between the dipole inferred from the CMB and that measured from large-scale radio galaxy and QSO surveys (see, e.g., [285, 23]). The dipole anomaly is detected primarily in its amplitude rather than in its direction. While the CMB dipole is largely interpreted as a kinematic effect from our motion relative to the CMB rest frame, the amplitude measured in galaxy surveys, which sometimes deviates from expectations, could potentially reflect unknown LSS effects. Moreover, statistically significant directional variations in H_0 have been observed, both in the CMB and in local probes. These findings may represent alternative manifestations of the CMB anisotropy anomalies or of large-scale bulk flow anomalies. The "bulk flow" in the local Universe refers to the collective motion of matter structures whose peculiar velocities, rather than being randomly distributed, exhibit a coherent dipole-like flow pattern. The detection of bulk flows with amplitudes larger than those predicted within the ΛCDM framework could signal a departure from statistical isotropy, manifesting observationally as dipolar signatures in multiple cosmological probes [286, 287].

- $A_{\rm lens}$ *anomaly*: The phenomenological parameter $A_{\rm lens}$, which quantifies the smoothing of CMB acoustic peaks due to lensing, is measured by *Planck* at values ∼2-3σ higher than predicted by ΛCDM. This may indicate unmodeled effects in CMB lensing or the need for physics beyond the standard paradigm. However, it is worth mentioning that improvements in the latest *Planck* PR4 CMB maps allowed to update the likelihoods for temperature and polarization spectra [288, 35], reducing small-scale noise and tightening constraints on cosmological parameters by up to 10%. Both likelihoods now indicate a shift toward $A_{\rm lens} = 1$, yielding to a much smaller or non-existent level of tension. See also [36].

- *BBN anomalies*: Mild tension between the primordial helium-4 abundance predicted by standard BBN and that inferred from astronomical observations, as well as the long-standing lithium problem, where BBN predicts the primordial lithium-7 abundance by a factor of ∼3 compared to metal-poor stars [289, 290]. While such discrepancies may be due to systematics, they are also considered potential hints of non-standard physics in the early Universe.

- *Neutrino sector*: Massive neutrinos slow down structure formation [291] and, consequently, the neutrino mass can be measured by comparing the amplitude of fluctuations in the local Universe (from the CMB lensing data and galaxy surveys) with that at the last scattering surface (i.e. A_s). Specifically, it is possible to estimate the sum of neutrino masses $\sum m_\nu$ [292, 293, 294]. Cosmological datasets such as *Planck*, ACT, and DESI BAO, provide tight upper limits on this quantity (e.g. $\sum m_\nu < 0.064$ eV at 2σ [201]), which strongly disfavors the inverted hierarchy (two heavy, one light) and supports the normal ordering (one heavy, two light) with high statistical significance [295]. See also [296] for a comprehensive understanding of the cosmological

neutrino-mass bound physical origin. Additionally, the statistics of CMB polarization anisotropies is sensitive to the effective number of relativistic species $N_{\rm eff}$ and to the thermal history of the Universe with non-standard particle contents. A precise measurement of the former could signal the presence of any radiation-like components at the time of CMB decoupling, such as thermal axions [297] or sterile neutrinos [298], while the latter could reveal the decay of non-relativistic massive particles [299].

- *Dynamical dark energy*: Constraints on w_0 and w_a derived from late-time probes (SNIa, BAO) have suggested deviations from the cosmological constant prediction $w_0 = -1$ (see Sec. 3.4). This may reflect evolving dark energy or unrecognized systematics. As first reported by the DESI-DR1 results [300] and subsequently confirmed with DR2 [201], the joint analysis of DESI BAO measurements with CMB data from *Planck* and different SNIa samples provides moderate to strong evidence in favor of a time-varying dark energy component. A particularly noteworthy feature of this preference is the indication of a phantom crossing scenario, where the dark energy equation of state transitions across the $w = -1$ threshold [301, 302]. The DESI indications for evolving dark energy have already been investigated in the context of general scalar-tensor Horndeski theories and in models with non-minimal coupling in modified gravity [303, 304], but also in the context of interactions in the dark sector or $f(R)$ gravity models [305, 306].

- *Extremely massive galaxies at high-z*: Unexpected large population of this type of galaxies at $z \gtrsim 10$ have been measured by JWST [307, 308, 309, 310], which challenges existing models of galaxy formation and evolution due to their surprising size and luminosity at such early times. This could suggest revisiting our understanding of the early Universe, particularly concerning the growth of supermassive black holes and the formation of large-scale structures.

3.4 Alternatives to the ΛCDM model

The previous sections have made it increasingly evident that the standard ΛCDM framework may be incomplete. The number of persistent and significant tensions and anomalies is nowadays a *challenge* for the cosmological community, which is motivated to the exploration of alternative scenarios in which new physical ingredients — ranging from modifications in the early Universe to changes in the late-time cosmic expansion or structure formation — play a role. This common effort can be visualized in Fig. 3.4, where a "summary" of alternative proposed theories is shown. In this section, we briefly discuss those most relevant to the present work, while noting that a comprehensive treatment falls beyond the scope of this thesis.

In Chapter 1, we have seen that a component with negative pressure, termed dark energy, was introduced to explain the observed accelerated expansion of the Universe [13, 14]. While its simplest form, the cosmological constant Λ, fits a broad range of data, it faces significant theoretical challenges, such as the coincidence problem, further complicated by current observational tensions.

Figure 3.4. A sketch of fundamental physics theories beyond the standard framework of ΛCDM proposed to address the current cosmological tensions. Figure from [134]

To address these issues, many alternatives to Λ have been explored, including models where the dark energy equation of state parameter $w(z)$ evolves with time (see [40] and references therein). Allowing w to deviate from -1 gives rise to forms of *dynamical dark energy*, which may alleviate some of the theoretical difficulties associated with a rigid cosmological constant. For instance, if the dark energy density gradually decreases from the large value predicted by quantum field theory to the much smaller value observed today, it could provide a partial explanation of the cosmological constant problem. A gradual decrease in the dark energy density can arise naturally in frameworks such as *quintessence* [311, 312, 313, 314], where a minimally coupled scalar field slowly evolves along its potential, or in *running vacuum models* [315, 316, 317, 44, 275], in which the vacuum energy density evolves dynamically with the expansion of the universe, typically as a function of the Hubble rate or its derivatives. In both cases, the dark energy density evolves with time, partially alleviating the fine-tuning problem associated with a constant Λ. However, it is well-known that merely allowing w to vary does not fully resolve the issue, as vacuum quantum fluctuations remain present [42, 26, 43].

A time-varying equation of state for a self-conserved dark energy fluid modifies the Hubble expansion rate through the first Friedmann equation (Eq. (1.11)) as

$$H^2(z) = H_0^2[\Omega_{rel}(1+z)^4 + \Omega_{nr}(1+z)^3 + \Omega_k(1+z)^2 + \Omega_{DE}f(z)]\,, \tag{3.6}$$

where $f(z)$ is given by

$$f(z) \equiv \frac{\epsilon_{DE}(z)}{\epsilon_{DE}(0)} = exp\Big[3\int_0^{\ln(1+z)} d\ln(1+z')(1+w')\Big]\,, \tag{3.7}$$

and the subscript DE denotes quantities associated with the dark energy component. Of course, this is only one example, as many alternative models have been proposed. For the purposes of this thesis, we broadly classify these models according to whether the dark energy dynamics become relevant at late or early cosmological epochs — a distinction that will guide the discussion that follows.

Suppose we do not believe in the presence of systematics in the data. In that case, solutions to the Hubble tension (and, in most cases, its connection to the growth tension) can generally be grouped into two broad categories, distinguished by the requirement of preserving the precisely measured value of θ_* (Eq. (1.71)).

Early-time solutions

This class involves a departure from the standard model before the decoupling of the CMB photons, capable of decreasing the distance traveled by the sound waves in the photo-baryon fluid. This leads to a reduction of the sound horizon to compensate for the smaller angular diameter distance implied by a larger H_0, and can be achieved in different ways: by changing the strength of gravity in early modified gravity models [318, 319, 320, 321, 322, 323, 324, 275, 325], modifying the recombination time with varying atomic constants [326, 327, 328, 329], altering the shape of the primordial power spectrum [330], or by considering different forms of *early dark energy* (EDE) [331, 332, 333, 334, 270, 335, 336, 273, 337].

EDE models, for instance, account for a significant dark energy contribution before recombination, and can be described by, e.g., inhomogeneous dark energy fluids or scalar fields. The scalar field energy density must redshift faster than radiation so that the field becomes a subdominant component at the decoupling time [270, 338]. Several variants of EDE have been explored in the literature. Oscillatory EDE models, often motivated by axion-like fields, involve a scalar field oscillating around the recombination epoch, injecting energy into the expansion rate. For instance, the EDE model by [332] consider scalar-field models (such as oscillating or slowly-rolling) that can produce such a transient energy density contribution. They found that a field accounting for $\sim 5\%$ of the total energy density around $z \sim 5000$ and diluting faster than radiation afterwards yields an H_0 inferred from *Planck* CMB data that agrees with the SH0ES local measurement [94]. Importantly, because the EDE fades away after recombination, it does not affect the late-time dynamics of the Universe or spoil the successful predictions of ΛCDM at low redshifts[8].

[8]Notice that EDE could also help to explain the anomalous population of very massive galaxies at large redshifts observed by JWST [309, 339]. However, this is assuming that σ_8 reliably traces the growth of cosmic structure.

Another proposal falls into the category of *extra relativistic species*. The effective number of neutrino species in the universe is given by the parameter $N_{\rm eff}$, which in standard cosmology is $N_{\rm eff} \simeq 3.043$ [340, 341, 342]. As the contribution of neutrinos to the total radiation energy density ρ_r is proportional to the effective number of neutrinos, variation of $N_{\rm eff}$ modifies the sound horizon at recombination. In particular, larger $N_{\rm eff}$ values decrease the horizon and, consequently, require higher values of H_0 (see, e.g, [343, 344, 345]). This scenario can arise from new light particles, such as sterile neutrinos or dark radiation. The same dynamics occur for EDE, since these models also increase the total energy density before recombination. As a consequence, this mechanism leads to an apparent increase in clustering power when it is quantified through the parameter σ_8, because of the shift in the scale R_8, which depends on h. Correctly treating the problem in terms of σ_{12} does not worsen the growth tension, because a shift towards larger h does not imply a significantly greater clustering in the Universe. Therefore, these candidates cannot be discarded as alternatives to the standard paradigm for alleviating the H_0 tension. More details will be provided in Chapter 11.

Another compelling line of research includes *modified gravity theories*, which propose extensions to GR on cosmological scales by altering the left-hand side of the Einstein equation (Eq. (1.4)), or introducing additional scalar degrees of freedom and altering the underlying geometry, among other alternatives. A similar phenomenology to EDE can be produced by *early* modified gravity models, as they can change the effective strength of gravity before recombination, modifying both the expansion rate and the evolution of perturbations. This can mimic the transient energy injection of EDE, leading to a reduced sound horizon and a larger inferred value of H_0. Concrete realizations include scalar–tensor and Horndeski-type theories with time-dependent kinetic couplings or a running Planck mass, as well as early modifications of $f(R)$ gravity (see, e.g. [322, 323, 275, 346]).

These early-time proposals, though appealing, have limited ability to loosen the tension. Indeed, they could face tight constraints from CMB observations, as the acoustic peak structure is highly sensitive to changes in photon diffusion [347]. Other limitations include the early ISW effect [338], and the requirement of much larger values of the spectral index of the primordial power spectrum of scalar perturbations [332, 320, 338, 325], closer to $n_s \sim 1$. This is welcomed by small-scale CMB experiments as ACT, but not by *Planck* [348, 349, 350], especially when CMB polarization data is included in the fitting analyses, see e.g. [237, 324, 275].

Late-time solutions

The second class consists of late-time solutions that modify the post-recombination expansion history in such a way that the angular diameter distance to recombination remains unchanged.

For instance, *late dark energy* models attempt to address the Hubble tension by modifying the expansion history at low redshifts ($z \lesssim 1$). These models alter the dark energy equation of state, $w(z)$, away from the cosmological constant value $w = -1$. Models of self-conserved dark energy with a transition from negative to positive values of $\rho_{DE}(z)$ require a divergence in $w(z)$.

In a model in which w differs from the cosmological constant value but remains independent of the redshift, i.e. assumes a constant value w_0, Eq. (3.7) takes the form $f(z) = (1+z)^{3(1+w_0)}$. For instance, a likelihood analysis with *Planck* data for this model favors values for $w_0 < -1$ which solve the H_0 tension within 2σ [351]. However, when additional datasets – such as Pantheon and BAO – are considered in the analysis, the tension remains at $\gtrsim 3\sigma$. Such negative values for w_0 are related to phantom-like models [352, 353], in which dark energy density increases over time, leading to an exponential cosmic acceleration so that the scale factor of the Universe would reach infinity in a finite time and the Universe would end in a *"big rip"*. Other scenarios let w vary with the redshift. The Chevallier-Polarski-Linder (CPL) parameterization [354] considers an equation of state

$$w(a) = w_0 + (1+a)w_a \tag{3.8}$$

which represents a Taylor expansion of $w(a)$ around the present epoch up to first order. At a fixed amount of the various cosmic species at present, the growth of large-scale structures is more suppressed in the past if dark energy increases with redshift, exhibiting *quintessence* behavior ($w_0 > -1$), compared to a scenario where dark energy is *phantom* ($w_0 < -1$). The CPL parameterization in terms of a w_0w_aCDM model allows for both behaviors as well as crossing the phantom divide, depending on the values of w_0 and w_a. Recent studies have highlighted strong hints in favor of dynamical dark energy[9]. Current data from CMB, BAO and SNIa prefer a highly non-trivial evolution of the dark energy density at $\sim 3-4\sigma$ CL, depending on the concrete SNIa sample employed [201, 362], with a probability of phantom divide crossing of 96.21% - 99.97% [363, 364]. These dynamical dark energy models lead to values of H_0 at $> 5\sigma$ tension with the SH0ES measurement. However, including SH0ES as a prior with CMB+SNIa+BAO data reduces the preference for dynamical dark energy down to 1.5-2.4σ level [365]. It is thus evident that the assessment of the robustness of SH0ES measurement is crucial not only in light of the Hubble tension but also for a solid quantification of the evidence for dynamical dark energy.

Forms of *interacting dark energy* models have been developed too. They are based on a non-trivial exchange of energy between dark matter and dark energy, thereby modifying both the cosmic expansion history and the growth of structures. Depending on the direction and strength of the coupling between the two components, the expansion rate can be either slowed down or accelerated. For instance, [366] show that a larger value for the Hubble parameter from CMB data can be obtained by including these interactions.

As for modified gravity theories, many of them have been developed so far, such as those embedded in the general class of Horndeski scalar-tensor theories (see, e.g., [367, 368, 303]), which include non-minimally coupled scalar fields with derivative interactions, or the class of $f(R)$ gravity [369], which generalizes GR by replacing the Ricci scalar with a non-linear function of R. These models often require fine-tuning or introduce instabilities in the late Universe and can face difficulties in simultaneously resolving the tension while remaining consistent with solar system tests, CMB lensing and LSS data. Some late-time modified gravity models can also

[9]For some previous hints of dynamical dark energy see, e.g., [355, 356, 357, 358, 315, 316, 359, 317, 360, 262, 361].

be introduced to support an alteration in the calibration of standard candles such as Cepheid variables or SNIa, leading to a biased measurement of H_0. Ultra-late time transition in the effective gravitational coupling G_{eff} and hence in the SNIa absolute magnitude M at $z \approx 0.01$ has been proposed to loosen the tension on H_0 [370, 371, 372, 373, 374, 375]. Indeed, as the local calibration is performed via Cepheid stars at redshifts less than 0.01 (see Sec. 2.1), a solution to this crisis could be the existence of a mechanism that changes the physics of SNIa so that they are dimmer at $z < 0.01$ with respect to their luminosity at higher z. In [370], it has been proposed that a rapid transition in the value of the relative effective gravitational constant,

$$\mu_G \equiv \frac{G_{eff}}{G_N}\,, \tag{3.9}$$

(where G_N is the locally measured Newton constant) at $z \sim 0.01$ could explain the lower luminosity (higher magnitude) of local supernovae, thus solving the H_0 tension. Indeed, a model that features $\mu_G = 1$ for $z = 0.01$ but $\mu_G \simeq 0.9$ for $z \geq 0.01$ would be consistent with local gravitational constraints but also raise the Chandrasekhar mass[10], m_C, and so decrease the absolute magnitude of SNIa at $z \geq 0.01$ by the required value of ~ 0.2 mag needed to compensate for the H_0 – or M – tension (see discussion in Sec. 3.1).

The Chandrasekhar mass depends on both G_{eff} and the mass per electron m' according to $m_C \approx \frac{3}{m'}(\hbar c/G_{eff})^{3/2}$ [376]. In the standard model, this result is independent of the accretion history and the white dwarf progenitor, and yields the well-known value of $1.44 M_\odot$. A decrease in G_{eff} would imply an increase in m_C, which reduces the peak absolute luminosity of SNIa, L. Indeed, assuming a fixed m', this relation can be expressed via $L \sim G_{eff}^{-\alpha}$, where, in the simplest scenario, $\alpha = 3/2$ [377][11]. From Eq. (2.4), it follows that a decrease in G_{eff} would lead to a decrease of the absolute magnitude M. Hence, the ΔM transition, and so the H_0 tension, could be explained by the following evolution of the effective gravitational constant [370]: from Eq. (3.9),

$$\mu_G \equiv G_{eff}/G_N = \begin{cases} 1 \equiv \mu_G^< & if z \leq z_t \\ 1 + \Delta\mu_G \equiv \mu_G^> & if z > z_t\,, \end{cases} \tag{3.10}$$

where $z \sim 0.01 \equiv z_t$ and in which the change in μ_G is related to the change in M according to

$$\Delta M = M(z < z_t) - M(z > z_t) = -\frac{5}{2}\log_{10}\frac{L^P}{L^R} = \frac{15}{4}\log_{10}\mu_G\,, \tag{3.11}$$

where L^P and L^R are the CMB-calibrated and Cepheid-calibrated SNIa luminosities, respectively. In [370], it has been shown that a rapid 10% increase of the effective gravitational constant roughly at z_t would not only resolve the Hubble tension but it would also help resolve the growth tension as it would reduce the growth of

[10] SNIa explosion occurs when the white dwarf mass reaches the critical Chandrasekhar mass, by accreting matter from a companion (see Sec. 4.2).

[11] See, however, [375] for a slightly different value of α which follows from changes in the light curve shape of SNIa affecting their luminosity, and [378] for careful reconsideration of the relation between the SNIa luminosity and the gravitational coupling.

density perturbations without affecting the *Planck*/ΛCDM background expansion[12]. However, these models do not address why a transition in G_{eff} would occur precisely at $z_t \simeq 0.01$. In addition, any rapid change in G_{eff} must be embedded within a consistent theoretical framework that explains its triggering at ultra-late times and that provides a viable screening mechanism to satisfy local gravitational constraints. These considerations underline that, although this model is intriguing, its origin and consistency with other cosmological observables remain open questions.

In the context of a modified theory of gravity, G_{eff} is the "effective strength of gravity" and allows one to obtain the equation of matter perturbations at small scales. Subsequently, the growth of matter perturbations becomes scale-dependent and one can discriminate between proposed models of modified gravity [379]. This change of the gravitational coupling is a scenario in which perturbations are suppressed but the background expansion does not deviate from that of the standard model. In general, modifications to the linear growth of matter overdensities δ can be encoded in $G_{eff}(z,k)$, so that Eq. (1.45) is modified through

$$\ddot{\delta}_k + 2\frac{\dot{a}}{a}\dot{\delta}_k = 4\pi G_{eff}(z,k)\bar{\rho}\delta_k \,. \tag{3.12}$$

These effects can be probed with large-scale structure surveys, RSD, WL, and CMB lensing. Modified gravity can thus be constrained not only by background expansion (SNIa, BAO, H_0) but also by the growth of structure (σ_8, $f\sigma_8$).

Both early- and late-time solutions to the current tensions come with strengths and limitations. Early-time scenarios can alter the detailed expansion history probed by BAO and SNIa, extending beyond a "simple" shift in H_0, but they are strongly constrained by CMB data. Conversely, late-time scenarios more easily preserve CMB consistency through geometrical degeneracies, yet they face tight bounds from low-redshift measurements [223].

As we have seen throughout this section, many of these alternative models inevitably call for a modification in the calibrators of the ladder, M and r_d[13]. Part of the work presented in this thesis (see, in particular, Chapter 6) focuses on studying and estimating both in a model-independent manner. Having an estimation of the ladder calibrators not affected by the main drivers of the current tensions is therefore particularly relevant, as the results can be used to test the viability of these models beyond ΛCDM, helping to clarify the discussion and potentially shed light on the Hubble – and, where possible, growth – tension.

[12]However, $\alpha \neq 3/2$ would imply that SNIa were intrinsically brighter in the past, corresponding to larger values of G_{eff}. The requirement of stronger gravity in the past would make these models unable to resolve the growth tension [378].

[13]Other proposals not discussed include, e.g., coupled dark energy models [380, 381, 382, 383, 384], models with primordial magnetic fields [385], running vacuum models with interaction between the vacuum and cold dark matter [386] or a simultaneous running of the effective gravitational coupling and Λ [324]. We refer the reader to [224] for a review and a more complete list of references.

Chapter 4

Observables

The current transition to a data-driven cosmology has fueled an increasingly high amount of data, largely accessible to the community, which can benefit from high-volume and high-quality observations spanning from the high-redshift measurements of the CMB to the late-Universe probes. In the last decades, many advances in cosmology have been made through this exponential increase in available data, and many more will be collected with future planned surveys. In light of the great abundance of unsolved questions that affect the community and the stability of the standard model as we know it, these measurements can help shed light on the fundamental assumptions behind ΛCDM or support alternative scenarios (see Chapter 3). The research carried out in this thesis is largely based on data-driven approaches. Particularly, we are interested in those observables which are not involved in the current mismatches within the standard cosmology, thereby providing unbiased results in testing its fundamental assumptions. However, we deem it interesting also to assess the consistency of these probes to further validate the analyses which employed such data.

We dedicate this Chapter to illustrate and describe all these observables. In particular, we start from presenting the cosmic clocks named Cosmic Chronometers (Sec. 4.1), the Supernovae of Type Ia standard candles (Sec. 4.2) and the cosmic rulers in the form of the Baryon Acoustic Oscillations (Sec. 4.3). We continue by providing a brief overview of the Cosmic Microwave Background data in Sec. 4.4, concluding the Chapter with two other potentially standardizable candles observed at higher redshifts, i.e. Gamma-Ray Bursts and Quasars, in Secs. 4.5 and 4.6, respectively. While most of these probes have been presented in the preceding Chapters, the focus now shifts to a deeper analysis of their measurements, with the aim of understanding both their methodological underpinnings and their role in the research of this thesis.

In the case of CCH, SNIa, and BAO, we also outline the expectations from ongoing and forthcoming dedicated surveys. This discussion will be further developed in Sec. 6.3.3 of Chapter 6, where we present the corresponding forecast analyses.

4.1 Cosmic Chronometers

The drive to determine the expansion rate of the Universe independently of cosmological assumptions has intensified over the past two decades, leading to the development of novel observational probes. The need for direct measurements of $H(z)$, rather than those inferred from integrated quantities such as cosmic distances, arises from the fact that the latter cannot by themselves provide immediate cosmological information—such as the energy content of the Universe (see Eq. (1.11))—which is essential for testing model assumptions in a fully agnostic framework.

The pioneers of the idea were Jimenez & Loeb [387], which aimed to directly express $H(z)$ only as a function of the differential time evolution of the Universe[1], dt, in a given redshift interval, dz. Indeed, under the minimal assumption that the Universe is described by a FLRW metric, where the scale factor $a(t)$ is directly related to the redshift as in Eq. (1.10), the Hubble function can be expressed as

$$H(z) = \frac{\dot{a}}{a} = \frac{-1}{1+z}\frac{dz}{dt}\,. \tag{4.1}$$

The ratio dz/dt incorporates the time dependence and can be taken to be the look-back time differential change with redshift. Since this quantity is not a direct observable, one needs to identify objects in the Universe whose time evolution across redshift ranges can be properly determined with the aid of *differential age techniques*. These objects are called *cosmic chronometers*.

The best candidates are galaxies, since they can be observed with reasonably high signal-to-noise over a wide range of cosmic times. Moreover, they have to be massive ($\log(M/M_\odot) \gtrsim 11$) and passively-evolving, characterised by old stellar populations, which have exhausted their gas reservoir and have very minimal star formation rates. This ensures low contamination from young components. These galaxies have formed at $z \sim$2-3 over a brief period, typically over timescales of $t \sim 0.3$ Gyr, and are homogeneous over cosmic time, meaning that they have formed at the same time independently of the redshift at which they are observed. Indeed, they evolve on timescales much longer than their differential ages. The homogeneity property relies on the Copernican principle and underpins the rationale for this method, demonstrating its practical utility: comparing two ensemble of galaxies that have formed at the same time but are at different (but suitably narrow) redshifts, the difference in their evolution state traces the time elapsed between the redshifts — how much time has passed since they have run out of their gas and stopped star formation — effectively mapping the expansion history of the universe. Since blue stars die earlier than red stars, and so the galaxies become redder with time, by analyzing their spectral energy distributions (SED) we are able to know how much time has passed since they have run out of their gas and stopped star

[1]Another interesting model-independent tracer of the Universe expansion history is the *redshift drift*. First proposed by Sandage in 1962 [388] and later explored by Loeb in 1998 [389], this alternative probe is based on the fact that the redshift of a distant source slowly changes over time due to the evolving Hubble flow. It is simply given by the relation $\dot{z} = H_0(1+z) - H(z)$, and it can be measured, for instance, by observing spectral lines of distant QSOs and tracking their subtle changes over decades (see, e.g. [390]). However, because detecting such small changes requires high spectral resolution and long-term observational campaign, direct measurements of the redshift drift are not yet feasible [391].

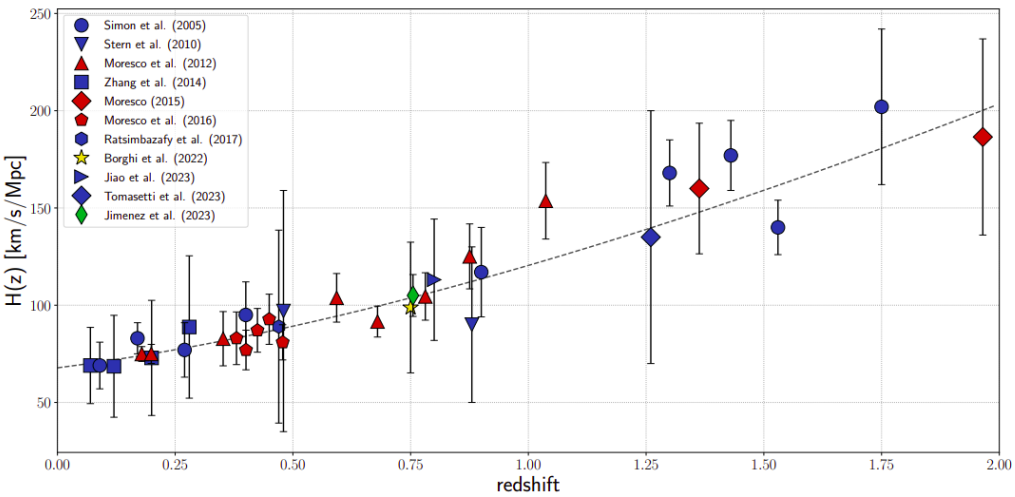

Figure 4.1. Latest compilation of CCH measurements obtained with different methodologies. Figure from [401].

formation. This is done assuming an underlying stellar population synthesis (SPS). While redshift can be accurately determined through spectral line analysis, ages are not direct observables and techniques such as photometry or single spectral regions (e.g., the D4000 break [392]) or the entire spectrum features (full-spectral fitting) have to be adopted. This way, the CCH method enables measurements of $H(z)$ via Eq. 4.1, under the assumption that GR and standard physics hold in the environment of the stars. Apart from that and the CP, CCH are devoid of additional cosmological assumptions, which makes these data stand out as one of the ideal probes for model-independent analyses, like those we will carry out in this thesis.

This is contrary to other probes, which use model-dependent or integrated quantities for $H(z)$ (see, e.g., Eq. (1.78)). As a consequence, the CCH measurement is more sensitive to cosmological parameters that affect the evolution of the expansion history, since a difference in luminosity distance of 5% corresponds to a difference in $H(z)$ of 10% [393]. These cosmic clocks can be employed to calibrate the ladders, e.g. BAO and SNIa [394, 395, 396, 397, 398, 241, 399, 400] or GRBs and QSOs [148, 174, 175, 176, 399, 164].

Throughout the analyses of this thesis, we use state-of-the-art data on CCH, consisting of 33 data points in the redshift range $0.07 < z < 1.965$. The complete list of these measurements of $H(z)$ obtained with the CCH method and the corresponding references can be found in Appendix A and is plotted in Fig. 4.1, taken from [401]. Correlations among these data are incorporated via the covariance matrix. In the following, we describe the systematics affecting the CCH method and examine how they propagate into the covariance matrix.

In the last years, important efforts have been dedicated in building the error budget of the CCH data [392]. Different criteria are taken into account to minimize as much as possible the contamination from, e.g., photometry, spectroscopy, stellar velocity and mass dispersion. Potential degeneracies between physical parameters of the galaxy SED (e.g., age-metallicity) also contribute to the error budget. The reconstruction of the star formation history (SFH) of age-dating galaxies is very

challenging. Nevertheless, a strength of CCH lies in estimating the quantity dt rather than the absolute age t, so any systematic offset in the absolute age estimation will be minimised in the measurement of the differential age. There are some alternative methods to compute the latter, which depend, e.g., on the galaxy spectral features used in the analysis. One of the most common methods, proposed by Moresco et al. [402], uses the spectral break at 4000Å rest frame, also known as D4000, which is one of the main characteristic observables of the spectrum of passive galaxies. The 4000Å break is linearly related (at fixed metallicity) with the age of the stellar population. This allows one to rewrite Eq. (4.1) in the form

$$H(z) = -A(Z, SFH)(1+z)dz/d(D4000)\,, \tag{4.2}$$

where $A(Z, SFH)$ is a function of the metallicity and the SFH, and can be calibrated on SPS models. This technique has the advantage of decoupling systematic and statistical effects and is more robust against the models assumed to calibrate the relation [402]. Different independent works (see Table A.1) compute the value of $H(z)$ mainly with this procedure, but other techniques are also available (e.g. analyzing the ages of luminous red galaxies with the full spectral fitting technique). For more details, we refer the reader to Sec. 3.1 of the review in [403].

In general, with the CCH method, it is possible to reach an accuracy on the determination of the expansion history of the Universe around 5% at $z \sim 0.5$ up to 10-20% at $z \sim 2$ [404]. All the possible sources of errors discussed above are taken into account in the covariance matrix built upon recipes in [392] and computed following [2] as

$$Cov_{ij} = Cov_{ij}^{stat} + Cov_{ij}^{sys}\,. \tag{4.3}$$

C^{stat} contains the statistical errors and is diagonal. The systematic uncertainties contained in C^{sys} account for several effects. The intrinsic physical properties of the galaxies introduce diagonal errors, given that these uncertainties are uncorrelated between galaxies at different redshifts. This is the case, for example, of possible contamination by younger stars, which can cause the measurement of younger ages and stellar metallicity, currently resulting in errors of $< 0.5\%$ and 4% on $H(z)$, respectively. However, this is bound to be kept under control with high spectral resolution and high-S/N data [392]. Contributions from progenitor bias and mass dependence are already considered negligible. On the other hand, other sources of uncertainty, like those primarily due to the choice of initial mass function (IMF), stellar library, etc., rely on the common SPS model used to study the evolution of galaxies, thereby providing a certain degree of correlation between the redshifts, which is represented by C_{ij}^{model} (see Eq. (4.5). We base our treatment of systematic uncertainties that will enter Eq. (4.3) on the recipes described in [405]. In conclusion, the total systematic contribution is included as

$$Cov_{ij}^{sys} = C_{ij}^{met} + C_{ij}^{young} + C_{ij}^{model}\,, \tag{4.4}$$

where

$$C_{ij}^{model} = C_{ij}^{SFH} + C_{ij}^{IMF} + C_{ij}^{st.lib.} + C_{ij}^{SPS}\,. \tag{4.5}$$

[2] `https://gitlab.com/mmoresco/CCcovariance`

The error introduced on $H(z)$ is, on average, of 2-3% for the SFH contribution and 0.4% for the IMF. The effect of considering different SPS models impacts the $H(z)$ measurement with a 9% error on average, with a decreasing trend with increasing redshift in $0 < z < 1.5$. In this region, SPS model choice dominates the total error budget, with a contribution of $\sim 4.5\%$. This different trend is related to the behavior of the slopes of the D4000-age relations for the different models [392]. These errors are highly correlated across different spectra.

As suggested in [405] and [404], advancements in future spectroscopic analyses and observations are expected to aid in identifying and narrowing down the set of SPS models that best reproduce the data. As a result, in an optimistic scenario, the associated systematic uncertainty is assumed to be resolved for future data, and the IMF-related uncertainty is the only systematic contribution considered. The treatment of future CCH systematics will be important for the analysis presented in Sec. 6.3.3, where we will explain how to build mock CCH data sets expected from surveys like Euclid [406], the Wide-field Spectroscopic Telescope (WST) [407] or the Astrophysics Telescope for Large Area Spectroscopy Probe (ATLAS) [408].

For a more detailed review of the origin and modelling of systematic errors in the CCH data, we refer the reader to [392].

4.2 Supernovae of Type Ia

Supernovae are stellar explosions marking the final stages of stellar evolution, often outshining their host galaxy for weeks. Among them, Type Ia supernovae are particularly luminous and can be distinguished from core-collapse (Type II) supernovae by the absence of hydrogen lines in their spectra. In particular, SNIa are thermonuclear explosions of carbon–oxygen white dwarfs in binary systems, triggered when the white dwarf approaches the Chandrasekhar mass of $1.44 M_\odot$ through accretion or merger. Their remarkable utility in cosmology stems from the homogeneity of their peak luminosities, which, after empirical corrections for light-curve shape and color, exhibit a small intrinsic scatter ($\approx$ 0.1–0.15 mag)[3]. This makes them excellent standardizable candles. Indeed, as discussed in Sec. 2.1, SNIa are bright enough to be observed across cosmological distances, bridging the local and distant Universe. They occupy a central role in the cosmic distance ladder, providing one of the most direct and precise routes to determine the Hubble parameter. Beyond this role, which is occupied by low-z SNIa, large samples in the high-redshift regime have also been pivotal for cosmology. Their use as standard candles led to the discovery of the accelerated expansion of the Universe in the late 1990s, providing the first direct evidence for dark energy [13] (see Fig. 2.1).

Their utility in probing cosmic expansion has been firmly established through extensive surveys over the past decade.

[3]SNIa are not perfectly standard: the peak luminosity varies by about 0.3 mag. This dispersion can be reduced using empirical correlations, such as the Phillips relation [409], which links peak luminosity to the decline rate of the light curve over the first 15 days after maximum (faster-declining supernovae are intrinsically dimmer and redder). Also, color–luminosity corrections are applied to account for intrinsic color variations and dust extinction in host galaxies [410].

In this thesis, we make use of two of the most recent SNIa compilations, which collect thousands of lightcurves obtained from different surveys. In the following, we outline their main features.

Pantheon+ compilation [95]: this sample includes 1701 light curves of 1550 unique, spectroscopically confirmed SNIa, ranging in redshift from $z = 0.001$ to 2.26 and coming from 18 different surveys. For the majority of our analyses, we exclude the SNIa data points belonging to the host galaxies used by SH0ES [94, 192], in order to obtain results independent of their calibration. The remaining sample then consists of 1624 SNIa. Nevertheless, we will also consider the full data set, including the SH0ES host-galaxy distances from the first rungs of the distance ladder, to evaluate their impact on our model-independent estimation of the quantities M, r_d and Ω_k (see Chapter 6 for more details).

The SNIa data in the Pantheon+ compilation are given as follows. For each lightcurve, we have the apparent magnitude as measured on Earth, $\tilde{m}$, together with the heliocentric and Hubble diagram redshifts, denoted as $z_{\rm hel}$ and $z_{\rm HD}$ [411], respectively. Following Eq. (2.2), if M is the standardized absolute magnitude of the SNIa and $\tilde{D}_L$ is the luminosity distance inferred from the measurements for a fixed M, we have the following relation,

$$\tilde{m}(z_{\rm hel}, z_{\rm HD}) = M + 25 + 5\log_{10}\left(\frac{\tilde{D}_L(z_{\rm hel}, z_{\rm HD})}{1\,{\rm Mpc}}\right)\,, \tag{4.6}$$

with

$$\tilde{D}_L(z_{\rm hel}, z_{\rm HD}) = \left(\frac{1+z_{\rm hel}}{1+z_{\rm HD}}\right) D_L(z_{\rm HD})\,, \tag{4.7}$$

and $D_L(z)$ is given in Eq. (1.78). Using these relations, it is possible to rewrite the expression of the apparent magnitude in the most usual form, only in terms of the redshift $z_{\rm HD}$,

$$\begin{aligned} m(z_{\rm HD}) &= \tilde{m}(z_{\rm hel}, z_{\rm HD}) - 5\log_{10}\left(\frac{1+z_{\rm hel}}{1+z_{\rm HD}}\right) \\ &= M + 25 + 5\log_{10}\left(\frac{D_L(z_{\rm HD})}{1\,{\rm Mpc}}\right)\,. \end{aligned} \tag{4.8}$$

This is the apparent magnitude that would be measured in the absence of peculiar motions, and is the quantity that we use in our analyses, together with the corresponding non-diagonal covariance matrix, which includes the effect of statistical and systematic uncertainties (e.g. intrinsic scatter modeling or host galaxy properties). All these quantities are available at [4].

DESY5 [412]: this is currently the most recent SNIa compilation, which has been released by the DES collaboration. Consisting of 1829 objects, it is the largest single sample survey to date (1635 DES SNIa), although it covers a smaller redshift range than Pantheon+, up to $z \sim 1.12$. At low redshifts, $z < 0.1$, the data set is complemented by 194 spectroscopically confirmed low-z SNIa from external samples,

[4] `https://github.com/PantheonPlusSH0ES/DataRelease`

90% of which are in common with the Pantheon+ compilation. Indeed, the latter includes ∼500 low-z SNIa, which are not in DESY5 in order to minimize low-z systematics due to calibration [169]. For instance, SNIa at $z < 0.025$ have been removed to reduce the impact of peculiar velocity uncertainties. At higher redshifts ($z > 0.1$), the overlap between the two samples consists of 145 DES SNIa events and in particular, for $z > 0.5$, the number of high-quality SNIa is ~ 5 times higher in DESY5 [412][5].

There are several ongoing debates on systematics affecting the low-z SNIa of Pantheon+ or DESY5 [166, 167, 168, 169, 170]. However, the DES collaboration have provided arguments against these concerns [169]. Without delving into the merits of these debates, in this thesis, some of the results will be provided in terms of both data sets, allowing us to assess their impact on the results.

As for the DESY5 sample, we employ the corrected apparent magnitudes $m(z)$ along with the corresponding covariance matrix, $C_{\rm DES}$, from[6], which accounts for both statistical and systematic uncertainty.

Looking ahead, a new generation of wide-field surveys is poised to dramatically expand the available SNIa samples, both in redshift coverage and statistical precision. Projects such as the Vera C. Rubin Observatory's Legacy Survey of Space and Time (LSST) [413] and the Nancy Grace Roman Space Telescope [414] are expected to deliver thousands to tens of thousands of well-measured SNIa over the coming decade. Already with an early data release corresponding to roughly half of its final mission target, LSST is expected to be able to constrain a constant dark energy equation of state w at the sub-5% level and to obtain a precision of 0.05 on w_0 for a time-varying equation of state [415]. The survey is projected to increase the SNIa sample size by up to a factor of 100 compared to previous samples [416], using a single instrument, which may help mitigate calibration issues present in samples built from different telescopes. A good-enough photometry will enable sufficiently well-sampled and accurate light curves, host galaxy redshifts, whose distribution mean will be around $z \sim 0.4$ [417]. However, the detectable universe for LSST will most likely be limited to $z \sim 1.2$. That is, the redshift distribution is predicted to be the same as that of DESY5. For a more extensive volume, we may have to wait until the Roman Space Telescope, which is expected to detect SNIa up to $z \sim 3$.

In Sec. 6.3.3, we will outline the strategy followed to build a mock SNIa data set representative of an LSST-like survey for forecast analyses.

4.3 Baryon Acoustic Oscillations

Galaxy surveys provide measurements of both the angular positions and the redshift distributions of galaxies across the sky. These data sets can be transformed, through appropriate modeling, into an estimate of the matter power spectrum $P(k, z)$ in redshift space. The process requires two key steps: modeling the galaxy bias and

[5]The broader redshift coverage of Pantheon+ ($z \lesssim 2.3$) compensates for its larger distance errors when these SNIa are used to obtain cosmological constraints, whose uncertainties are smaller than those obtained using DESY5, also because the latter include additional systematic uncertainties [169].

[6]`https://github.com/des-science/DES-SN5YR`

converting the observed angular coordinates and redshifts into comoving distances. The latter transformation is inherently cosmology-dependent.

Along the line of sight, the comoving separation between two sources is related to their redshift difference, Δz, via the relation

$$\Delta z = \frac{r_d H(z)}{c}\,, \tag{4.9}$$

while in the transverse direction, the separation is determined from the observed angular distance $\Delta\theta$ as

$$\Delta\theta = \frac{r_d}{(1+z)D_A(z)}\,. \tag{4.10}$$

In both cases, the conversion depends on the assumed background cosmology. For this reason, analyses typically adopt a fiducial cosmological model — most often a ΛCDM model with fixed parameter values — as a reference framework. The results from other cosmological models are then expressed relative to this fiducial choice[7].

If the assumed model is incorrect, isotropic features in the clustering of galaxies appear distorted along or across the line of sight. This phenomenon is called the *Alcock-Paczyński effect* (AP) [418, 419]. The AP effect is captured by two scaling parameters:

$$\alpha_\perp = \frac{D_M(z)/r_d}{D_M^{\rm fid}(z)/r_d^{\rm fid}}\,, \tag{4.11}$$

$$\alpha_\parallel = \frac{D_H(z)/r_d}{D_H^{\rm fid}(z)/r_d^{\rm fid}}\,, \tag{4.12}$$

where $D_M(z)$ is the comoving transverse distance defined in Eq. (1.82) and $D_H(z) = c/H(z)$ is the Hubble distance along the line of sight. The anisotropic BAO signal carries crucial cosmological information, since it allows a simultaneous measurement of the angular diameter distance and the expansion rate at the effective redshift of the survey.

For redshift bins with low signal-to-noise ratio, galaxy surveys can only compute a volume-averaged spectrum and obtain a measurement of the *isotropic* BAO estimator given as follows[8]

$$\frac{D_V(z)}{r_d} = \frac{\left[zD_M^2(z)D_H(z)\right]^{1/3}}{r_d}\,, \tag{4.13}$$

where $D_V(z)$ is the so-called *dilation scale*. Notice that, in this case, the isotropic dilation parameter is defined as

$$\alpha \equiv \frac{D_V(z)/r_d}{D_V^{\rm fid}(z)/r_d^{\rm fid}}\,, \tag{4.14}$$

[7]It is important to note that different studies may employ slightly different fiducial parameter sets, which can lead to small but non-negligible differences in derived quantities and must be handled with care.

[8]Notice that when it is possible to split the angular and radial BAO information, providing data on $D_M(z)/r_d$ and $H(z)r_d$ separately, they carry some degree of correlation.

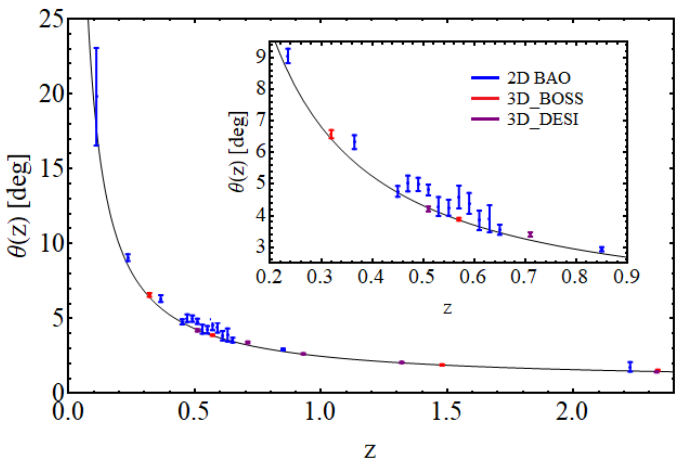

Figure 4.2. 2D and 3D BAO measurements of $\theta(z) = r_d/D_M(z)$. The black curve is the theoretical prediction obtained with the best-fit *Planck*/ΛCDM model (TT,TE,EE+lowE+lensing analysis [11]). The inner plot shows a zoom in the redshift range $z \in [0.2, 0.9]$.

and is linked to the anisotropic scaling parameters as $\alpha = \alpha_\perp^{2/3}\alpha_\parallel^{1/3}$. This quantity measures the average isotropic scaling of distances relative to the fiducial cosmology and is directly constrained by spherically averaged BAO measurements. Thus, the AP effect allows BAO to be used not only as a standard ruler but also as a geometrical probe of cosmology.

To summarize, all these *"3D"* BAO exploit the radial and angular clustering signal imprinted on the LSS of the Universe by assuming a *fiducial* cosmology to convert redshift and angles into comoving distances to build the three-dimensional tracers map [420].

On the other hand, the analysis can be carried out in the two-dimensional parameter space by making use of the two-point angular correlation function or the angular power spectrum. In this case, the *"2D"* BAO signal comes from the angular position of the BAO peak. A fiducial cosmology is not required and, for this reason, these measurements are claimed to be less affected by model dependencies than the standard 3D approach [421, 422, 420].

2D analysis is particularly useful in photometric surveys or when redshift precision is limited. Indeed, the galaxy sample is divided into narrow redshift shells, each spanning a small range of Δz. Within each shell, the galaxy distribution is projected onto the 2D sky sphere, essentially collapsing the radial dimension inside that shell. The BAO signal is then extracted as an angular correlation function or angular power spectrum on the sky for each redshift shell separately. Since the analysis integrates over radial distances within each shell, information about the radial BAO scale and thus $H(z)$ is largely lost. The provided information is given in terms of the angular (transversal) scale $\theta(z)$.

We deem it interesting to give here the reader a visual representation of the difference between 2D and 3D BAO. In Fig. 4.2, we plot the quantity $\theta(z) = r_d/D_M(z)$. One can already notice the discrepancy affecting the two distinct methodologies used to extract the BAO signal. The agreement between the ΛCDM prediction

and the vast majority of the 3D BAO data is clear, whereas there is an obvious tension between the fiducial cosmology and the 2D BAO data in the redshift range $0.4 \lesssim z \lesssim 0.7$, since all the data in that redshift range fall above the ΛCDM best-fit curve. This implies that 2D BAO angular diameter distances are smaller than those preferred by the standard model. Whether this discrepancy is due to the existence of unaccounted systematic errors affecting one or both BAO data sets, or to an underestimation of their uncertainties, is still unknown. The impact of the fiducial cosmology on the 3D BAO analysis has been demonstrated to induce only small shifts in the inferred cosmological distances when it does not differ significantly from the true model [205, 423, 206, 424, 425, 426]. However, [427] argued that these works do not explore a wide enough range of the fiducial parameter values allowed by the measured BAO distances, which are quite far away from the *Planck*/ΛCDM best-fit model. In fact, [428] showed that fitting the two-point correlation function while fixing the cosmological and the non-linear-damping parameters at fiducial values leads to an underestimation of the errors by a factor of two. We will study in detail the implications of these two BAO data sets in Chapters 9 and 10.

In this thesis, we make use of both 2D and 3D BAO data sets as provided by several recent galaxy surveys. These encompass measurements from 6dFGS, BOSS, eBOSS, WiggleZ, DES and DESI surveys. As new measurements have become available over time, different combinations of BAO data have been employed in the analyses presented in this thesis. We refer the reader to Tables A.2, A.3 and A.4 for a complete list of the specific samples used. In the following, we present additional details on the recent DESI data, as these will serve as a key input for the forecast analysis discussed in Sec. 6.3.3.

DESI BAO measurements represent the most recent available data. The DESI collaboration released anisotropic BAO data from galaxy, quasar and Lyman forest tracers from the first year (DR1) and three years (DR2) of observations. In this thesis, we make of data points from the following galaxy tracers: the Bright Galaxy Sample (BGS) in $0.1 < z < 0.4$, the Luminous Red Galaxy Sample (LRG) in $0.4 < z < 0.6$ and $0.6 < z < 0.8$, LRG + Emission Line Galaxy Sample (ELG) in $0.8 < z < 1.1$ and ELG data in $1.1 < z < 1.6$. Specifically, we have data in $0.30 \leq z \leq 1.32$, along with the QSO result at $z = 1.49$ and the Lyman-α result at $z = 2.33$. DESI BAO given in terms of D_M/r_d and D_H/r_d are measured at the same redshift and therefore have some degree of correlation. For the analysis in Sec. 6.3.1, which makes use of both the observables, we account for these correlations through the corresponding covariance matrix. Moreover, for completeness, we perform the analysis using both DESI-DR1 and DESI-DR2 BAO data, which are listed in [300] and [201], respectively.

In [269], the DESI collaboration reported BAO and RSD forecasts that represent the expected final target of the mission. They account for a predicted full footprint of 14,000 deg2 for each tracer. This area is used for cosmological forecasts, which set DESI as a Stage-IV dark energy experiment. Indeed, the precision on the isotropic BAO distance scale from BGS and LRG at redshifts $z < 1.1$ is expected to be of 0.28%, while the ELG and quasar sample in $1.1 < z < 1.9$ will provide BAO measurements at 0.37% precision. For the forecast analysis in Sec. 6.3.3, we employ the predicted D_A/r_d and $H(z)r_d$ measurements provided in Table 7 of [269], for a

total of 42 points between $0.05 \leq z \leq 2.05$. Predicted redshifts and the corresponding covariance matrix that we use are available as supplementary materials at [9].

4.4 Cosmic Microwave Background

In Sec. 1.2, we extensively discussed the main features of the CMB and the cosmological insights that can be drawn from the analysis of its anisotropies. In what follows, we summarize the key pieces of information extracted from CMB measurements that we employ in this thesis. Specifically, we adopt constraints derived from the *Planck* mission, which currently provides the most precise determination of several key cosmological parameters within the ΛCDM framework and its extensions. Notice that using the full CMB likelihood is always necessary when using CMB to constrain models that introduce new physics before recombination, as such modifications can affect the detailed structure of the temperature and polarization spectra. In contrast, for models that introduce new physics at low redshift, although small imprints on the spectra may still appear, the main constraints on the background evolution can typically be captured using a compressed likelihood, with minimal loss of statistical information on the cosmological parameters. This justifies our use of CMB information as provided below.

In Chapter 11, we will investigate the bias introduced by the σ_8 parameter in cosmological analyses. As explained in Sec. 3.2, the growth tension arises as a mismatch between the late-time measurements of the matter clustering and the *Planck* data. Additionally, the discussion around the interpretability of σ_8 is inevitably intertwined with the ongoing issue of the Hubble tension, in which the *Planck* analysis plays a pivotal role. As a consequence, we will use the CMB temperature and polarization power spectra plikTTTEEE + low$l$ + lowE from the legacy *Planck* release as a reference for CMB observations [11, 429].

On the other hand, Gaussian priors on specific cosmological parameters allow the incorporation of CMB information without using the full temperature and polarization data. In Chapter 9, we will study late-time solutions to the Hubble tension, and for this reason, we need to rely on standard pre-recombination physics. This can be done by leveraging the TT,TE,EE+lowE+lensing ΛCDM best-fit values on the quantities $\{D_A(z_*), r_d, \Omega_m, H_0\}$, including the corresponding covariance matrix, C_{cmb}. This information can be obtained from the Planck Legacy Archive[10]. They read, respectively,

$$\begin{pmatrix} D_A(z_*)\,[\text{Gpc}] \\ r_d\,[\text{Mpc}] \\ \Omega_m \\ H_0\,[\text{Mpc/km/s}] \end{pmatrix} = \begin{pmatrix} 13.872 \\ 147.09 \\ 0.3153 \\ 67.36 \end{pmatrix}, \tag{4.15}$$

$$C_{cmb} = \begin{pmatrix} 6.11 \cdot 10^{-4} & 6.42 \cdot 10^{-3} & -1.49 \cdot 10^{-4} & 9.84 \cdot 10^{-3} \\ - & 7.04 \cdot 10^{-2} & -1.51 \cdot 10^{-3} & 9.85 \cdot 10^{-2} \\ - & - & 5.44 \cdot 10^{-5} & -3.94 \cdot 10^{-3} \\ - & - & - & 2.90 \cdot 10^{-1} \end{pmatrix}, \tag{4.16}$$

[9] `https://doi.org/10.5281/zenodo.10063934`
[10] http://pla.esac.esa.int/pla/#home

where the units of the elements of C_{cmb} are set by those employed in Eq. (4.15), and we omit the lower half of the covariance matrix, since it is symmetric. Furthermore, we employ a CMB prior on the radiation parameter, which reads $\Omega_r = 4.18343 \cdot 10^{-5}/h^2$. The numerical coefficient is fixed by the current CMB temperature [430], assuming for the sake of simplicity three relativistic neutrino species.

The CMB constraints play a dual role: they break degeneracies inherent in BAO-only analyses, and they anchor the absolute scale of the BAO ruler via the determination of the sound horizon at the drag epoch. Unless otherwise stated, all *Planck*-derived values correspond to the 2018 baseline results [11].

4.5 Gamma-Ray Bursts

Gamma-Ray Bursts are transient, extremely energetic phenomena that have been detected up to $z \sim 9.4$ [113]. As already noted in Sec. 2.1, they exhibit characteristics that suggest they are potentially standardizable candles, allowing their use to extend the distance ladder beyond SNIa. This requires identifying robust, intrinsic correlations, unaffected by selection biases, linking their light-curve or spectral parameters to their luminosity or energy.

In this thesis (see Chapter 7), we make use of the three-dimensional fundamental plane correlation, also known as 3D Dainotti correlation, which reads [138, 139, 431]

$$\log L_{\rm X} = C_o + a \log T^*_{\rm X} + b \log L_{\rm peak}\,, \tag{4.17}$$

where

$$L_{\rm X} = 4\pi D_L^2 F_{\rm X} K_{\rm plateau} \tag{4.18}$$

is the X-ray source rest-frame luminosity,

$$L_{\rm peak} = 4\pi D_L^2 F_{\rm peak} K_{\rm prompt} \tag{4.19}$$

is the peak prompt luminosity (both luminosities are in units of $erg\ s^{-1}$) and $T^*_{\rm X}$ is the characteristic time scale which marks the end of the plateau emission (in units of s) [11]. In the above equations, $F_{\rm X}$ is the measured X-ray energy flux at $T^*_{\rm X}$, $F_{\rm peak}$ is the measured gamma-ray energy flux at the peak of the prompt emission over a $1s$ interval (both fluxes are in units of $erg\ cm^{-2}\ s^{-1}$), $K_{\rm plateau} = (1+z)^{\alpha_{\rm plateau}-2}$ is the power-law plateau K-correction with $\alpha_{\rm plateau}$ being the X-ray photon index of the plateau phase. The K-correction for the prompt emission, $K_{\rm prompt}$, depends instead on the X-ray photon index ($\alpha_{\rm prompt}$), energy and differential spectrum.

The correlation parameters in Eq. (4.17) are identified by a, b, and C_o. The a parameter denotes the anti-correlation between $\log L_X$ and $\log T^*_{\rm X}$, thus identifying the slope of the correlation; b is the parameter that controls the relation between $\log L_{\rm peak}$ and $\log L_X$; C_o is the normalization of the plane. When dealing with GRBs, one has also to consider that these data suffer from an unknown source of scatter on the plane, σ_{int}, which cannot be neglected since it specifies the tightness of the relation. This tightness relies on the spin period and magnetic field variations of

[11] All the quantities appearing in the logs of Eq. (4.17) are made dimensionless, dividing them by their corresponding units.

a fast millisecond magnetar. Indeed, the plateau emission can be ascribed to the magnetar model [432, 140, 142, 143], which describes that the X-ray plateaus are caused by a fast-spinning neutron star. In this case, the slope of the correlation is $a = -1$.

Neglecting b in Eq. (4.17) leads to a X-ray time-luminosity relation, i.e. the *2D Dainotti correlation* [127]:

$$\log L_{\rm X} = C_o + a \log T^*_{\rm X} \,. \tag{4.20}$$

While $T^*_{\rm X}, F_{\rm X}, \alpha_{\rm plateau}, F_{\rm peak}, \alpha_{\rm prompt}$ are measurable quantities, a, b, C_o, and σ_{int} can only be determined through a proper calibration, which, as evident from Eqs. (4.18), (4.19) requires the use of cosmological luminosity distances. To perform this calibration in an agnostic way, we can leverage low-redshift probes, such as CCH, which allow the reconstruction of GRB luminosity distances without relying on a specific cosmological model. We will apply this methodology to the calibration of both the 3D and 2D Dainotti relations. For other works related to the application of the Dainotti relations as a cosmological tool, see [151, 159, 110, 111].

Redshift evolution corrections. Each physical feature of the three-dimensional GRB fundamental plane, $L_{\rm X}$, $T^*_{\rm X}$ and $L_{\rm peak}$, is affected by selection biases due to instrumental thresholds and redshift evolution of the variables involved in the correlations. It was shown in [130, 433, 434, 431, 147, 435] that in order to correct for these effects, one can employ the Efron & Petrosian method [436], which tests the statistical dependence among $L_{\rm X}$, $T^*_{\rm X}$ and $L_{\rm peak}$ (for further details, see [131, 159]). Once one introduces this correction, the expression for the GRB fundamental plane in Eq. (4.17) takes the following form:

$$\begin{aligned} \log L_{\rm X} - k_{L_x} \log(1+z) =& a_{ev}(\log T^*_{\rm X} - k_{T^*_{\rm X}} \log(1+z)) + \\ &+ b_{ev}(\log L_{\rm peak} - k_{L_{\rm peak}} \log(1+z)) + \\ &+ C_{o,ev} \,. \end{aligned} \tag{4.21}$$

The subscript ev is used to distinguish the relation parameters from those adopted in the non-evolutionary case, while $k_{L_x}, k_{T^*_{\rm X}}$ and $k_{L_{\rm peak}}$ represent the evolutionary coefficients related to each physical feature.

In this thesis, we make use of observations of 50 long GRBs (i.e., with a burst phase that lasts $> 2s$) in the redshift range $0.553 \leq z \leq 5.0$. These objects constitute the so-called *Platinum sample*, defined for the first time in [431] and being a subsample of the larger Gold Sample [138]. The latter is based on the requirements for the plateau phase, including strict data quality and morphology criteria. Two selection criteria guarantee that the light curves present the transition from the steep decay after the prompt emission to the plateau (its inclination must be < 41 deg). To build the Platinum Sample, the following additional requirements for the GRBs plateau were added[12]: it should last at least 500 s — to avoid that the plateau phase is longer than the one observed — and it should not present flares at its start or

[12]The GRB lightcurves used to build the Platinum sample in [431] are gathered from the official Swift web page repository (The Swift Burst Analyser [439, 440]).

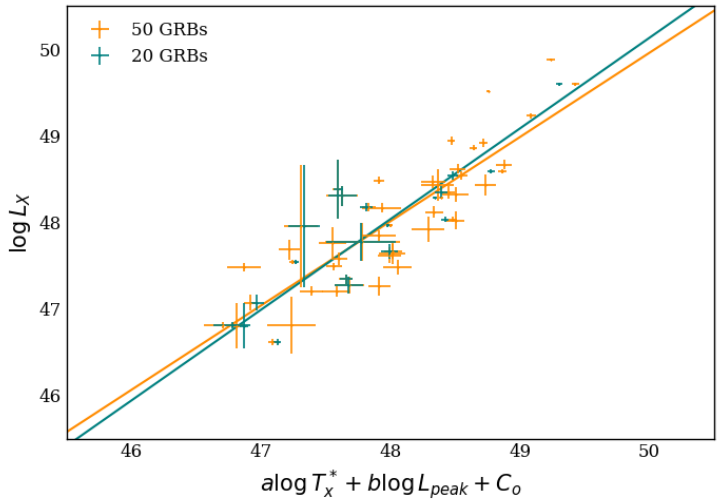

Figure 4.3. 2D projections of the fundamental plane for the Platinum sample (in orange) and for the sub-sample of 20 GRBs used for the calibration (in green), both obtained taking the mean values of a, b, and C_o from the related fundamental plane fitting analyses. This is the standard procedure, widely used in the context of GRB cosmology. The likelihood is built by making use of the D'Agostini and Kelly method [437, 438], and an underlying cosmological model is assumed to compute the luminosity distances entering Eqs. (4.18) and (4.19) (see, e.g., [147]). We follow this approach only to map the positions of the GRBs from the Platinum sample within the plane defined by the 3D Dainotti relation. The error bars represent the 1σ uncertainty. See Chapter 7 for more details.

during its duration. The construction of the sample relies on the limiting luminosity and times, which depend on instrumental selection thresholds. These effects have been accounted for in [431] by applying the Efron & Petrosian method [436], as discussed above. The Platinum sample collects well-defined morphological features of GRBs which, at a given redshift z, are identified by the following five quantities: $T_{\rm X}^*$, $F_{\rm X}$, $K_{\rm plateau}$, $F_{\rm peak}$, $K_{\rm prompt}$. For the sake of visualization, in Fig. 4.3, we present the 2D projection of the fundamental plane for both the full Platinum sample (50 GRBs) and the sub-set of 20 GRBs at $z \lesssim 2$, which are used in the calibration of the Dainotti relations (see Sec. 7.1). These data are listed in Table A.5.

4.6 Quasars

Being among the most luminous persistent objects in the Universe, visible up to redshifts $z \sim 7$, QSOs have an extreme brightness that allows us to probe cosmological distances far beyond the reach of SNIa, providing a unique window into the high-redshift Universe.

The potential of QSOs as cosmological probes relies on empirical correlations between their multi-wavelength emissions, such as the non-linear relation between the UV and X-ray luminosities. This relation enables the estimation of quasar distances independently of the traditional cosmic distance ladder, effectively turning QSOs into standardizable candles.

Building on Eq. (2.9), the Risaliti-Lusso relation is given as follows [179]

$$\log L_X = \gamma \log(L_{UV}) - \beta \tag{4.22}$$

where

$$\log L_{UV} = \log(F_{UV} 4\pi D_L^2) \tag{4.23}$$
$$\log L_X = \log(F_X 4\pi D_L^2) \tag{4.24}$$

are the logarithm of the rest-frame UV luminosity at 2500Å(L_{UV}) and the X-ray luminosity at 2 keV (L_X), respectively, and F_X and F_{UV} represent the relative flux densities (in $erg\ cm^{-2}\ s^{-1}\ Hz^{-1}$). The slope of the relation, γ, is a free parameter, and so is the intercept β. The parameters of this relation determine the amount of energy transfer from the X-ray to UV bands. Analogously to SNIa and GRBs, also QSOs suffer from a source of scatter, δ_{int}, which can be considered a proxy of the intrinsic dispersion of the relation, under the assumption that all the systematics have been taken into account. Indeed, most of the observed dispersion in the L_X–$L_{\rm UV}$ relation is not intrinsic, but arises from observational effects such as X-ray absorption, UV dust extinction, X-ray calibration uncertainties, variability, and selection biases due to flux limits. By carefully selecting a clean sample of sources, where the intrinsic UV and X-ray emission can be reliably measured, the observed dispersion decreases from ~ 0.4 dex to ~ 0.2 dex [441]. For further details on sample selection, the reader is referred to [179, 106].

To build a quasar sample, both X-ray and UV data are required to cover the rest-frame 2 keV and 2500Å. The most up-to-date broad-line quasar sample considered for cosmological purposes has been assembled by combining seven different samples from both the literature and the public archives, which culminate in the sample by [106], constituting a collection of 2421 quasars spanning a redshift interval $0.009 \leq z \leq 7.52$. Using this sample to analyze Eq. (4.22), studies typically find $\gamma \sim 0.6$ and $\beta \sim 8$ (see, e.g., [106]). In [186], a binning method for QSOs data was proposed to identify a *Golden sample* suitable for use as standard candles. Applying this method to the full sample in [106], yields a sub-sample of 1253 quasars up to $z = 7.54$, with a significantly reduced intrinsic dispersion in the UV–X-ray flux relation, $\delta_{int} = 0.096 \pm 0.003$ - a 56% improvement over the original sample, where $\delta_{int} = 0.22$. This approach also avoids the circularity problem (discussed in Sec. 2.1), as it is based on a flux–flux relation, while accounting for selection biases and possible redshift evolution.

In Chapter 8, we will apply the calibration methodology already mentioned for GRBs in Sec. 4.5 to both the full sample and the sub-sample of QSOs, while testing the impact of redshift evolution correction. Indeed, we deem it particularly interesting to study these objects in light of the reported $\gtrsim 4\sigma$ tension between the high-redshift QSO Hubble diagram and ΛCDM predictions in recent studies [100, 101, 102, 103].

Part II

Statistical methods

Chapter 5

Bayesian Inference

Building on the theoretical and observational challenges in modern cosmology outlined in Chapter 3, this thesis seeks to tackle several of these open questions and to investigate approaches that extend beyond the standard ΛCDM framework. In recent years, such investigations have generally followed two complementary strategies. In broad terms, the *model-dependent* approach tests specific cosmological models against observational data and directly compares their predictions with those of ΛCDM. By contrast, the *model-independent* approach seeks to extract information from the data without assuming a particular model, allowing cosmological trends to emerge directly from observations. Both types of analyses are naturally implemented within a Bayesian framework.

Bayesian inference provides a consistent methodology to combine prior knowledge with observational evidence, yielding a posterior probability distribution that captures both the uncertainty and the correlations among parameters. By working in this probabilistic framework, we can rigorously propagate observational errors and also quantify the degree of agreement between data sets and theoretical predictions. This is particularly important in cosmology, where multiple, sometimes partially independent, probes must be analyzed together. By highlighting potential systematic differences or tensions between measurements, these techniques can uncover subtle discrepancies that might otherwise be obscured in model-dependent analyses.

This thesis is primarily guided by a model-independent perspective. Accordingly, in the following Sections of this Chapter, we present the Bayesian framework underlying the two main techniques employed in our analysis to pursue this objective. These techniques are the Gaussian Processes and the Markov Chain Monte Carlo, which will be described in Secs. 5.1 and 5.2, respectively.

The Bayes Theorem

Unlike the frequentist approach, which interprets probabilities as long-term frequencies of outcomes and assumes an underlying "true" value of the parameters, the Bayesian perspective treats probabilities as measures of our *degree of belief* in a hypothesis given the available information. In Bayesian inference, prior knowledge is encoded in a *prior* distribution. This prior is then combined with the likelihood of observing the current data to update our beliefs about a hypothesis as more evidence

becomes available.

Let θ denote the set of parameters of a model and $\mathcal{D}$ the observed data. The *Bayes theorem* states that the posterior probability distribution of the parameters, given the data, is

$$P(\theta|\mathcal{D}) = \frac{P(\mathcal{D}|\theta)P(\theta)}{P(\mathcal{D})}\,, \tag{5.1}$$

where

- $P(\theta|\mathcal{D})$ is the *posterior*, representing the updated knowledge of θ after observing the data,
- $P(\mathcal{D}|\theta)$ is the *likelihood*, giving the probability of observing the data for a given choice of parameters, often denoted as $\mathcal{L}(\theta) \equiv P(\mathcal{D}|\theta)$,
- $P(\theta)$ is the *prior*, encoding information about θ before observing the current data, and
- $P(\mathcal{D})$ is the *evidence* or marginal likelihood, defined as

$$P(\mathcal{D}) = \int P(\mathcal{D}|\theta)P(\theta)d\theta\,, \tag{5.2}$$

  which corresponds to the probability of observing the data averaged over all possible values of the parameters under the prior. The evidence ensures that the posterior is properly normalized, i.e. $\int P(\theta|\mathcal{D})d\theta = 1$.

A shorthand often used in practice is

$$P(\theta|\mathcal{D}) \propto P(\mathcal{D}|\theta)P(\theta)\,, \tag{5.3}$$

where the proportionality hides the evidence term that only serves as a normalization constant.

For a Bayesian, no inference can be made without specifying a hypothesis. The choice of prior reflects the state of knowledge about the problem before collecting the data. Priors can be informed, for instance, by previous analyses (in which case the prior may coincide with the posterior of those studies), or non-informative if such information is unavailable. In cosmology, it is common practice to adopt flat (uniform) priors, assigning equal probability to all parameter values within a specified range. Even a flat prior can become informative under a nonlinear transformation of parameters, so care must be taken in its definition. More refined options include Jeffreys priors, which are invariant under reparameterizations, while Gaussian priors are useful when prior knowledge exists or when parameters are expected to be constrained around certain values.

If the observational data $\{(x_i, y_i)\}_{i=1}^n$ are Gaussian-distributed and uncorrelated, the likelihood function is directly related to the familiar χ^2 statistics as follows

$$\mathcal{L}(\theta) = P(\mathbf{y}|\mathbf{x},\theta) \propto \exp\left(-\frac{1}{2}\,\chi^2(\theta)\right) = \exp\left[-\frac{1}{2}\sum_{i=1}^{n}\left(\frac{y_i - f(x_i,\theta)}{\sigma_i}\right)^2\right]\,, \tag{5.4}$$

where $f(x_i, \theta)$ is the model prediction for input x_i, and σ_i is the measurement uncertainty. So, minimizing χ^2 corresponds to maximizing the likelihood. This form of the likelihood is widely used in cosmology for regression, parameter estimation, and model comparison. The combination of the likelihood function in Eq. (5.4) and the prior $P(\theta)$ constitutes the full posterior distribution, up to a multiplicative constant.

In case of correlated data, one has to take into account a covariance matrix C, therefore the likelihood in Eq. (5.4) can be written as

$$\mathcal{L}(\theta) = \frac{1}{\sqrt{(2\pi)^n \det C}} \exp\left[-\frac{1}{2}\sum_{i,j=1}^{n}(y_i - f(x_i,\theta))C_{ij}^{-1}(y_j - f(x_j,\theta))\right]. \tag{5.5}$$

For most realistic problems, the posterior distribution cannot be computed analytically due to high dimensionality or complex likelihoods. In such cases, numerical methods are required to explore the posterior distribution. A widely used approach is *Markov Chain Monte Carlo* (MCMC) sampling, which generates representative samples from the posterior in order to estimate summary statistics such as means, credible intervals, and parameter correlations. We will detail the method in Sec. 5.2.

Bayesian inference also provides a natural framework for model comparison. The ratio of posterior probabilities for two models M_1 and M_2 is given by the *Bayes factor*:

$$B_{12} = \frac{P(\mathcal{D}|M_1)}{P(\mathcal{D}|M_2)}, \tag{5.6}$$

where $P(\mathcal{D}|M_i)$ is the evidence for model M_i. The Bayes factor quantifies how strongly the data support one model over another, naturally incorporating the *Occam's razor* by penalizing models with excessive complexity.[1] Computing the evidence exactly can be computationally demanding, which is why approximate criteria are sometimes used to compare models. Two commonly used alternatives are the Bayesian Information Criterion (BIC) [442] and the Akaike Information Criterion (AIC) [443]. The former is defined as

$$\mathrm{BIC} = k \ln n - 2 \ln \hat{\mathcal{L}}, \tag{5.7}$$

where k is the number of fitting parameters, n is the number of data points, and $\hat{\mathcal{L}}$ is the maximum likelihood of the model. Lower BIC values indicate a preferred model. The BIC tends to penalize model complexity more strongly than the AIC, favoring simpler models when the data set is large.

The AIC balances goodness-of-fit and model complexity differently. It is given by

$$\mathrm{AIC} = 2k - 2 \ln \hat{\mathcal{L}}. \tag{5.8}$$

Like the BIC, lower AIC values indicate preferred models, but the AIC does not explicitly account for sample size, and thus tends to be less conservative in penalizing extra parameters, making it more suitable for smaller data sets.

[1] The Occam's razor is a rule of thumb for reasoning and model selection and states that among competing explanations that fit the data equally well, the simplest one is usually preferred.

In cosmology, BIC and AIC are often used to quickly assess the relative performance of models with different numbers of parameters, such as dynamical dark energy models or extensions to the standard ΛCDM framework. In such a case, AIC (or BIC) values of the non-standard models to that of ΛCDM can be computed by evaluating the difference $\Delta\mathrm{AIC} = \mathrm{AIC}_{\Lambda\mathrm{CDM}} - \mathrm{AIC}_i$, i.e., using the standard model as the benchmark. A positive difference of ΔAIC signals a preference for the non-standard model. More concretely, one can adopt the Jeffreys' scale [444] which states that: if $0 \leq \Delta\mathrm{AIC} < 2$, there exists *weak evidence* in favor of the new model i, compared to the standard model. If $2 \leq \Delta\mathrm{AIC} < 6$, we speak instead of *positive evidence*. If $6 \leq \Delta\mathrm{AIC} < 10$, there is *strong evidence*, and if $\Delta\mathrm{AIC} > 10$ we conclude that there is *very strong evidence* supporting the model i against ΛCDM.

In summary, Bayesian methods offer a rigorous framework for quantifying uncertainties, incorporating prior knowledge, and updating our understanding as new data become available, while also enabling principled model comparison. Building on this framework, we employ MCMC and Gaussian Process regression to reconstruct cosmological trends and estimate parameters in a fully probabilistic, data-driven way. These techniques provide a robust foundation for model-independent inference, setting the stage for the analyses presented in the following Chapters.

5.1 Gaussian Processes

Cosmological functions can be reconstructed with minimal model assumptions using *Gaussian Processes* (GPs). Based on Bayesian statistics, this machine learning algorithm has become in recent years one of the most widely used model-independent regression techniques in cosmology (see, e.g., [445, 396, 397, 398, 446, 447, 448, 449, 450, 451, 452, 447, 453, 454, 455, 173, 164]).

A Gaussian Process is commonly referred to as a generalization of a multivariate Gaussian [456],

$$f(x) \sim \mathrm{GP}(\mu(x), D(x, \tilde{x}))\,, \tag{5.9}$$

defined by the mean function $\mu(x)$ and the covariance matrix $D(x, \tilde{x})$. Let us denote the collection of n data points used to train the GP as Y, located at input positions X. The covariance matrix D takes the following form

$$D(x, \tilde{x}) \equiv \begin{cases} K(x, \tilde{x}) + C & \text{if } x \text{ and } \tilde{x} \in X \\ K(x, \tilde{x}) & \text{otherwise} \end{cases}\,, \tag{5.10}$$

where C is the covariance matrix of the data and $K(x, \tilde{x})$ contains the covariances between all pairs of training points according to the chosen *kernel* function. Suppose we want to reconstruct the function at a set of locations $X^\star$. By computing the probability of finding a given realization of the GP under the condition $f(X) = Y$ we find that the resulting GP is characterized by the mean function

$$\bar{f}^\star = \mu^\star + K(X^\star, X)[K(X, X) + C(X, X)]^{-1}(Y - \mu)\,, \tag{5.11}$$

and the covariance

$$cov(f^\star) = K(X^\star, X^\star) - K(X^\star, X)[K(X, X) + C]^{-1}K(X, X^\star)\,. \tag{5.12}$$

$\mu^\star \equiv \mu(X^\star)$ is the a priori assumed mean of the reconstructed function at $X^\star$. The kernel K, which encodes the assumptions on the covariance between points at which we do not have data, plays a central role. The simplest choice falls into the category of *stationary* kernels, which depend only on the distance between the input data points, that is, on $|x - \tilde{x}|$, and not on their individual values x and $\tilde{x}$, being thus invariant to translations in the input space. This means that the kernel function is able to build a correlation matrix that is symmetrical and positive definite.

Although the GP is regarded as a non-parametric method, the kernels introduce some *hyperparameters* that are typically in charge of controlling the strength and size of the correlations between two separate points. Typically, they are identified by ℓ and σ_f. The former can be thought of as the distance one has to travel in the x-direction to get a significant change in $f(x)$, whereas the latter denotes the typical change in the y-direction, so the size of these changes. This set of hyperparameters follows a likelihood that is set by the probability of the GP to produce a given data set at every point of the hyperparameter space. Before the reconstruction can take place, these hyperparameters can be trained by maximizing the marginal likelihood, which is the marginalization over function values f at locations X:

$$P(y|X, \sigma_f, \ell) = \int P(y|f, X) P(f|X, \sigma_f, \ell) df \,. \tag{5.13}$$

The integral in Eq. (5.13) can be performed analytically if one sets a Gaussian prior $P(f|X, \sigma_f, \ell) \sim \mathcal{N}(\mu, K(X, X))$ and with $P(y|f) \sim \mathcal{N}(f, C)$. This yields the following log marginal likelihood [448]:

$$\begin{aligned} \ln \mathcal{L} &= \ln P(y|X, \sigma_f, \ell) \\ &= -\frac{1}{2}(y-\mu)^{\mathrm{T}} \left[K(X,X) + C\right]^{-1} (y-\mu) - \frac{1}{2} \ln |K(X,X) + C| - \frac{n}{2} \ln 2\pi \,. \end{aligned} \tag{5.14}$$

The hyperparameters of the kernel can be optimized by maximizing this equation. In many cases, this likelihood is sharply peaked and using the best-fit values of the hyperparameters becomes a good approximation [448]. However, from a Bayesian perspective, the correct approach involves obtaining the complete distribution of the hyperparameters to account for their correlations and propagate their uncertainties to the final reconstructed function [397, 457]. This requires the sampling of the likelihood in Eq. (5.14). Since it is important to properly assess their impact on the final results, in this thesis, we train the hyperparameters using both optimization and marginalization procedures (see Sec. 6.1).

Just to give an idea of the role of the kernel hyperparameters, let us study the simple case of a one-dimensional Gaussian kernel:

$$K(x, \tilde{x}) = \exp\Big(-\theta (x - \tilde{x})^2\Big) \,, \tag{5.15}$$

where θ is the parameter that governs the correlations between points. When θ is small, two distant points are still highly correlated and therefore the resulting underlying function will have similar outputs in these two points as long as $\theta^{-1} \gg (x - \tilde{x})^2$. Due to the shift symmetry, this is true regardless of the position we consider on the x axis when we move along it. Indeed, for $\theta \to 0$ the kernel value

approaches 1, thus our model believes that any two random variables are 100% correlated, no matter how far away they are. That is, in this case, the x feature is not that significant for the predictions. As a practical visualization, the stationary nature of these kernels can be observed in the banding around the diagonal of the kernel covariance matrix. Increasing the length parameter ℓ increases the banding, as points further away from each other become more correlated.

Specifying ℓ and σ_f in Eq. (5.15) yield to the definition of the *Squared Exponential* (SE) kernel:

$$K(x, \tilde{x}) = \sigma_f^2 \exp\Big(-\frac{(x-\tilde{x})^2}{2\ell^2}\Big) . \tag{5.16}$$

The sum of two SE kernels defines the so-called *Double Squared Exponential* (DSE) kernel, characterized by four hyperparameters. Also, *Matérn* family covariance functions can be employed. The Matérn covariance between two points separated by the distance $d = |x - \tilde{x}|$ is given by

$$K_\nu(d) = \sigma_f^2 \frac{2^{1-\nu}}{\Gamma(\nu)} \left(\sqrt{2\nu}\frac{d}{\ell}\right)^\nu Y_\nu\left(\sqrt{2\nu}\frac{d}{\ell}\right) , \tag{5.17}$$

where Γ as the gamma function, Y_ν the modified Bessel function of the second kind and $\nu = p + 1/2,\ p \in \mathbb{N}^+$. In the limit $\nu \to \infty$ we recover the SE kernel. The Matérn covariance family is m times differentiable in the mean-square sense, i.e. the derivative $\delta^{2m}K(x, \tilde{x})/\delta z^m \delta \tilde{z}^m$ exists and is finite if $\nu > m$. Higher values of ν translate into wider peaks and smoother reconstructed functions due to the stronger correlation between points.

The aforementioned kernels are included in the public package *Gaussian Processes in Python* (`GaPP`) [2], first developed by Seikel et al. [448]. We employ this tool in all our GP analyses. In particular, `GaPP` is implemented with the definition of four Mátern kernels with $\nu = 3/2, 5/2, 7/2, 9/2$. Hereafter, we will denote them as M32, M52, M72 and M92, respectively.

Before concluding this Section, we want to provide the reader with a summary on how to train a basic GP:

1. Choose the data set;
2. Choose points X^* where to estimate the function f^*;
3. Choose a kernel covariance function $K(x, \tilde{x})$;
4. Decide the a priori mean function $\mu(x)$. A constant μ is a safe choice.
5. Train the hyperparameters:
   - Maximization: maximize the likelihood function in Eq. (5.14) to find the best-fit hyperparameters.
   - Sampling: sample the posterior of the hyperparameters to generate a chain of hyperparameter values.

[2] `https://github.com/carlosandrepaes/GaPP`

6. Compute the reconstructed function and its uncertainty:
   - Maximization:
     - Calculate the mean function $\bar{f}^*$ using Eq. (5.11).
     - Compute the covariance matrix $cov(f^*)$ using Eq. (5.12). The diagonal gives the variance of f^*.
   - Sampling: for each hyperparameter set in the chain, produce a random value of f^*, considering a Gaussian centered in the corresponding $\bar{f}^*$ with covariance $cov(f^*)$.

A comment on point 4. In practice, it is generally recommended to adopt a constant a priori mean function μ, since the data themselves should contain sufficient information to guide the reconstruction of the underlying function but mostly because setting μ equal to a specific theoretical prediction can introduce strong model-dependent biases. This occurs because the hyperparameter σ_f (which controls the typical amplitude of deviations from the mean) tends to become small, effectively forcing the reconstructed function to remain close to the assumed mean. As a consequence, the GP reconstruction exhibits artificially small uncertainties that are insensitive to the observational error bars or to the density of data points across redshift. This behavior arises because the prior mean is already very close to the data, leaving little flexibility for the GP to adjust. This is easy to understand. Let us consider an extreme case, in which we use a prior mean with an arbitrary shape, but passing exactly through the central values of the data. In the standard GP the hyperparameters are determined by demanding the GP to maximize the probability of producing the central values of the data Y. If we set $\mu = Y$ at the locations of the data points, the marginal likelihood in Eq. (5.14) reduces to

$$\ln \mathcal{L} = \ln\left(\frac{1}{|K(X,X)+C|^{1/2}}\right) - \frac{n}{2}\ln(2\pi)\,. \tag{5.18}$$

This quantity is maximized when the kernel contribution vanishes, i.e. when $\sigma_f = 0$, independently of the value of ℓ. In this case, the predictive mean becomes $\bar{f}_\star = \mu_\star$ and zero covariance. The interpretation is straightforward: since the prior mean already coincides with the central values of the data, the GP maximizes the likelihood by minimizing the scatter around the mean. As a result, the reconstruction simply reproduces the prior mean with vanishing uncertainty. From a Bayesian perspective, this situation reflects an overconfident prior: the GP attributes excessive credibility to the chosen mean function, thereby underestimating posterior uncertainty. Therefore, the standard GP framework does not provide a reliable reconstruction of the underlying function when the prior mean is too close to the observed data, which is not the behavior one would expect from an optimal, data-driven reconstruction method. Strictly speaking, a rule of thumb for a "safe" approach in standard GP is to use a constant mean (often set to zero without loss of generality, as the kernel can account for deviations).

However, another possibility can also arise by noting that a more robust cosmological inference requires treating *all* the kernel parameters as free variables and implementing full Bayesian marginalization, something that we have explored in

[458]. In this work, a generalized framework for GP, called *Gen GP*, is proposed to highlight some limitations of traditional GP approaches, especially when using an informed a priori mean function. Gen GP extends the standard formulation by treating the Matérn smoothness parameter ν as a free parameter, together with the set $\{\sigma_f, \ell\}$ (see Eq. (5.17)). Some key findings of this work demonstrate that the choice of kernel introduces systematic variations comparable to those arising from different cosmological models and that Gen GP demonstrates improved consistency between reconstructions obtained via hyperparameter optimization and marginalization, relative to standard GP. These improvements are most notable in regions with sparse data and when using a ΛCDM-based mean function, highlighting flexibility gains that provide more realistic uncertainty estimates without compromising data fidelity. Without delving into the details of this alternative approach, in this thesis, we restrict the discussion to illustrating the impact of the shortcomings of the standard GP method, which have been discussed throughout this section.

In particular, in Sec. 6.1, we will perform a series of tests focusing on the choice of the a priori mean function and the kernel, as well as on the marginalization over the kernel hyperparameters, in the reconstruction of the Hubble function. One of the `GaPP` modules is designed to perform the MCMC sampling of the kernel hyperparameters. It relies on the public package `emcee`[3] [459], which is a Python implementation of the affine invariant MCMC ensemble sampler by [460]. The MCMC method will be the subject of the following section.

5.2 Markov Chain Monte Carlo

Probabilistic data analysis often relies on computational techniques that enable the sampling of the posterior probability density function (PDF) of interest. A straightforward approach to parameter estimation is the so-called *grid-based* approach, where the posterior is mapped by constructing a grid in parameter space. Each grid point, or *knot*, corresponds to a specific set of parameter values, and by exhaustively evaluating the posterior on the grid one can reconstruct its shape. A gridded minimization of the total χ^2 function identifies the best-fit parameter values. In Sec. 6.3, we make use of a grid-search approach to simultaneously constrain the calibrators of the local distance ladder, M and r_d, and Ω_k. However, this method quickly becomes infeasible in high-dimensional parameter spaces, as the computational cost grows exponentially with the number of parameters. In practice, grid-based approaches become inefficient beyond ~ 4 parameters, as reducing the step size to save time severely degrades the resolution, while much of the computational effort is wasted in regions with negligible probability.

For models with high-dimensional parameter space, stochastic sampling methods provide a more efficient alternative. Rather than evaluating the posterior on a full grid, these methods explore parameter space through random samples drawn according to a probabilistic algorithm. Among them, the MCMC method has become the standard in cosmological data analysis.

A Markov chain is defined as a sequence of random variables $\{X(t)\}_{t=0}^{\infty}$[4] such that

[3] `https://emcee.readthedocs.io/en/stable/`

[4] Defining a Markov chain as an infinite sequence of random variables is in principle correct, as it

the conditional probability of the current state $X(t)$ depends only on the previous state $X(t-1)$:

$$P\big(X(t) \mid X(t-1), X(t-2), \ldots, X(0)\big) = P\big(X(t) \mid X(t-1)\big)\,. \tag{5.19}$$

The key property of such processes is their convergence to a stationary distribution $\pi(X)$, which no longer depends on t, satisfying

$$\pi(X') = \sum_X \pi(X)\, P(X \to X')\,, \tag{5.20}$$

where $P(X \to X')$ denotes the transition probability between states. In Bayesian inference, this stationary distribution corresponds to the posterior,

$$\pi(\theta) \propto P(\theta|\mathcal{D}) \propto \mathcal{L}(\theta)P(\theta)\,, \tag{5.21}$$

which follows from Eq. (5.3). Thus, each state in the chain corresponds to a parameter vector θ, for which the posterior is evaluated.

To explore the posterior efficiently, various sampling algorithms have been developed. The most widely used is the *Metropolis-Hastings* (M-H) algorithm [461]. It requires the choice of a proposal — or transition distribution — $q(Y \mid X(t))$, which generates a candidate position Y given the current position $X(t)$. A common choice is a multivariate Gaussian centered on $X(t)$. The candidate is then accepted with probability

$$\min\left(1, \frac{P(Y|\mathcal{D})}{P(X(t)|\mathcal{D})}\frac{q(X(t)|Y)}{q(Y|X(t))}\right). \tag{5.22}$$

If the candidate is accepted, the chain moves to $X(t+1) = Y$; otherwise, it remains at $X(t+1) = X(t)$.

Despite its simplicity, the M-H algorithm has limitations. In particular, the covariance matrix of the proposal distribution requires careful tuning of $\sim N^2$ parameters in an N-dimensional space. The efficiency of the sampler is highly sensitive to these parameters, and there is no a priori method for choosing the values correctly. As a result, convergence can be slow if the proposal is not well calibrated.

To overcome these difficulties, Goodman & Weare (2010) [462] proposed an *affine-invariant ensemble sampler*, later implemented in the `emcee` Python package by Foreman & Mackey [459]. An affine-invariant algorithm performs equally well under any linear transformation of the parameter space, making it insensitive to parameter covariances. This property is particularly useful for efficiently sampling highly anisotropic posteriors, since the algorithm automatically adapts to correlations between parameters.

The efficiency of the sampler can be quantified through the *autocorrelation time* τ, which measures how many steps are required before successive samples can be considered effectively independent. A chain with shorter autocorrelation time is more efficient. The effective number of independent samples is N/τ, where N is the

allows us to study properties like convergence and stationarity. However, in practice, one only runs the chain for a finite number of steps, say $t = 0, 1, \ldots, T$, with T large enough to approximate the stationary distribution.

total number of samples. The sampling variance of an estimator $f(\theta)$ can then be written as

$$\sigma^2 = \frac{\tau}{N} \mathrm{Var}_{p(\theta)}[f(\theta)] \,, \tag{5.23}$$

so that estimating τ directly informs how many samples are needed to reduce Monte Carlo error and avoid oversampling redundant, correlated states. The affine-invariant ensemble sampler is based on the so-called *stretch move*. The method evolves an ensemble of k walkers, each representing a parameter vector in the N-dimensional space. These walkers explore the parameter space in parallel, beginning from initial guesses, such as a uniform distribution around the priors[5]. The stretch move involves two different ensembles of k walkers. The first ensemble, $S = \{X_k\}$, incorporates for each k a transition distribution q which is based on the current positions of the $k-1$ walkers in the second, complementary, ensemble $S[k] = \{X_j, \forall j \neq k\}$. Each position is defined by a vector in the N-dimensional parameter space and its update from X_k is driven by a randomly drawing $X_j \in S[k]$:

$$X_k(t) \to Y = X_j + Z\,[X_k(t) - X_j] \,, \tag{5.24}$$

where Z is a random variable drawn from a distribution $g(Z = z)$ which is defined by

$$g(z) = \begin{cases} \dfrac{1}{\sqrt{z}} & \text{if } z \in [1/a,\, a], \\ 0 & \text{otherwise}\,, \end{cases} \tag{5.25}$$

with a an adjustable scale parameter. The proposed position is accepted with probability

$$q = \min\left(1,\, Z^{N-1}\, \frac{P(Y)}{P(X_k(t))}\right). \tag{5.26}$$

During this iterative process, each walker takes a step to a new point in parameter space and generates the corresponding model. As the chain progresses, the walker produces a sequence of accepted parameter vectors, together with their likelihood values. Once the walk is complete, this sequence forms the Markov chain, which approximates samples from the posterior distribution.

The affine-invariant ensemble sampler introduced by [462] and implemented in `emcee` [459] has become one of the most widely used tools in cosmology and astrophysics, owing to its efficiency, simplicity of use, and robustness in high-dimensional spaces. We will employ this sampler for most of our analyses, except for those in Chapter 11, where we make use of a different tool specifically designed for cosmological model fitting. This package is called `Cobaya` [463]. In particular, we explore the parameter space of the various models using the MCMC sampler developed for `CosmoMC` [464, 465]. The convergence of the chains obtained with this procedure is tested using the Gelman-Rubin statistics ($\hat{R}$) [466]. This diagnostic compares the variance within each chain to the variance between multiple chains initialized from different starting points, providing a measure of how close the chains are to sampling the same stationary distribution. A value of $\hat{R}$ close to 1

[5] To confine the walkers to a finite parameter volume, the prior probability is set to zero outside the allowed range, i.e. its logarithm returns $-\infty$.

indicates convergence. We adopt a conservative threshold for convergence, requiring $\hat{R} - 1 \lesssim 0.02$.

All the posterior distributions are analyzed using the `GetDist` package [467].

With the theoretical framework, relevant observables, and methodology now established, we turn to the core of this dissertation. The following chapters present the research conducted to address some of the most pressing open questions in cosmology.

Part III

Model-independent calibration of the cosmic distance ladder

Chapter 6

Calibrating the ladders and measuring Ω_k

The content of this Chapter is based on our work published in [468] and the follow-up analysis in [469].

The calibrators of the direct and inverse distance ladders - the SNIa absolute magnitude and the sound horizon at the baryon-drag epoch - play a crucial role in the Hubble tension (see Chapters 2, 3). The latter can indeed be reframed as a tension in the values of M and r_d, as it is clear from Fig. 3.2. For this reason, it is crucial to measure these distance calibrators independently of CMB observations and the first rungs of the direct distance ladder, as a means of cross-checking the results obtained with the standard methods that contribute to the discrepancy in H_0.

Apart from that, it is also interesting to perform these calibrations in a model-independent way to assess the viability of models beyond ΛCDM that have been proposed in recent years to address the tension (see Sec. 3.4).

Building on these arguments, we propose a methodology for calibrating the cosmic ladders in a model-independent framework that simultaneously constrains the spatial curvature of the Universe. The original idea of this calibration technique was presented in [470]. It was applied for the first time by [394] and several subsequent works in the literature developed the method through alternative data sets and statistical tools, see, e.g., [395, 398, 451, 471, 241, 472, 473, 474]. It assumes that gravity can be described by a metric theory, together with the CP and the validity of CCH as reliable cosmic clocks, and SNIa and BAO as optimal standard candles and standard rulers, respectively (see Secs. 4.1-4.3).

To perform this calibration, we first need to ensure that M, r_d and Ω_k can be safely treated as constants, in order to constrain them. For this purpose, we begin with preliminary analyses: we reconstruct the shape of $H(z)$ from CCH and of the apparent magnitude of SNIa $m(z)$ with GPs. We use these shapes to test some of these basic assumptions, which are usually taken for granted in other works. In particular, we reconstruct $\Omega_k(z)$ applying the method proposed by [475] to test the homogeneity property of the Universe by checking that this function is compatible

with a constant for $z \lesssim 2$. See [449, 450, 476] for similar studies along this direction. We also reconstruct the absolute magnitude of SNIa as a function of the redshift, $M(z)$, and check that no evolution is preferred by current data. This analysis is on the lines of the one by [477], but we use different data sets, have better control of the effect of correlations and get rid of double-counting issues in the data. Finally, we perform a consistency test among the 3D BAO data points employed in this work, and show that according to the low-redshift data sets under consideration, there is no significant statistical internal tension between them. These preliminary tests legitimize the final part of the analysis, in which we obtain model-independent constraints on Ω_k and the calibrators M and r_d. This independent calibration of the ladders is obviously relevant for the discussion of the H_0 tension for the reasons already explained. On the other hand, the spatial curvature Ω_k, which enters the geometrical pre-factor in the definition of the luminosity distance (see Eq. (1.79)), provides us with information about the early Universe and the period of inflation. Within the ΛCDM framework, CMB data from *Planck* prefer a closed Universe at $< 2\sigma$ C.L. for the *Planck* 2018 TT,TE,EE + lensing likelihood, $\Omega_k = -0.0106 \pm 0.0065$ [11, 28, 29]. However, the compatibility with a flat Universe is recovered as soon as data on BAO, SNIa, the full-shape galaxy power spectrum or CCH are added on top of CMB [11, 30, 31, 32], or when using only CMB data from the ACT [34]. Moreover, the final (PR4) *Planck* data release leads to $\Omega_k = -0.012 \pm 0.010$ [35], again compatible with the flat scenario. Within the CCH calibration technique, here, we constrain Ω_k using a quite model-independent approach, which relies on the validity of the CP and a metric description of gravity.

This Chapter is organized as follows. In Sec. 6.1, we apply GPs to reconstruct the shape of $H(z)$ and $m(z)$, alongside testing some technical aspects of this tool, e.g. on how to select a kernel applying an objective mathematical criterion. The shape of $H(z)$ provide us the background history from which SNIa and BAO cosmic distances can be inferred. This, together with $m(z)$, allows us to test some basic assumptions behind ΛCDM, such as the constancy of $M(z)$ and $\Omega_k(z)$. We will do that in Sec. 6.2. A joint analysis using CCH, SNIa and BAO enables us not only to put constraints on the triad (M, Ω_k, r_d) but also to obtain an estimate of the Hubble parameter, H_0, through a cosmographic approach. This last part of the analysis will be addressed in Sec. 6.3, in particular

- Sec. 6.3.1, using SNIa from Pantheon+ (see Sec. 4.2) and 3D BAO from different galaxy surveys: 6dFGS, BOSS, eBOSS, WiggleZ and DES Y3 (see Table A.2). This is still part of our work in [468].

- Sec. 6.3.2; having established the whole framework, we update our results in the follow-up analysis in [469]. We use here the most recent DESY5 SNIa sample [412] and the BAO data from the data releases DR1 and DR2 of DESI [300, 362]. We will also employ angular (2D) BAO data (see Table A.4). Assessing the impact of these new data is crucial in light of the current claims and ongoing debates (see discussion in Sec. 3.1).

- Sec. 6.3.3; we take a step forward and look at the constraining power that future data will have in the context of this model-independent methodology.

Upcoming generation of surveys – such as the Euclid ESA mission [406] and LSST [413] – is expected to deliver transformative improvements in both statistical precision and control of systematics. It is therefore timely to assess the performance of this methodology in light of forthcoming data. To this end, we present here a forecast analysis, conducted as part of our follow-up work in [469].

Final discussion and conclusion are presented in Sec. 6.4.

6.1 Reconstructing background quantities: the role of GPs

We start our analysis by reconstructing the Universe background history, employing 32 $H(z)$ measurements from CCH, which are listed in Table A.1[1] with the GP method. First, to ensure the robustness of our results, we assess the impact of different GP kernels available in the `GaPP` package. We recall the reader that these kernels are six different covariance functions, see Eqs. (5.16),(5.17). To this end, we perform the reconstruction in the redshift range $0 \leq z \leq 1.965$ and assuming a zero mean function μ. To evaluate the performance of the kernels in the reconstruction of $H(z)$, we proceed as follows. We draw with each kernel $N_{real} = 10^4$ GP random realizations, $H_{rec_\mu}(z)$ with $\mu = 1, ..., N_{real}$, accounting for both the covariance of the data points and that of the reconstruction. For each realization we compute the χ^2 statistics, using the following expression,

$$\chi^2_\mu = \sum_{i,j=1}^{32} [H(z_i) - H_{rec,\mu}(z_i)]\tilde{C}^{-1}_{ij}[H(z_j) - H_{rec,\mu}(z_j)] \,, \tag{6.1}$$

where $\tilde{C}$ is the covariance matrix of the CCH data and the Latin indices label the $n_p = 32$ redshifts at which we have data. Thus, the N_{real} realizations of the Hubble function lead to N_{real} values of χ^2_μ. More concretely, in order to penalize the use of additional hyperparameters, we compute the reduced χ^2, $\tilde{\chi}^2_\mu = \chi^2_\mu/\text{dof}$, with dof being the number of degrees of freedom, i.e. the number of data points minus the number of kernels hyperparameters. We then build a histogram of $\tilde{\chi}^2_\mu$ for each kernel, shown in Fig. 6.1. As one can see, the mean values of $\tilde{\chi}^2$ lie below and quite far from 1, regardless of the kernel. This might be due to an overestimation of the CCH uncertainties. We will speculate about this possibility and see how our results change when we allow the CCH data to have smaller errors. Moreover, the kernel Matérn 32 is the one with the lowest mean $\tilde{\chi}^2$. However, we need to estimate more quantitatively the relative ability of the kernels to describe the data. Let us consider two kernels K_i and K_j. The probability that the reduced $\tilde{\chi}^2_\mu$ associated to K_i is lower than the one associated to K_j reads,

$$P_{\tilde{\chi}^2_{K_i} < \tilde{\chi}^2_{K_j}} = \frac{1}{1 + P_j/P_i} \,, \tag{6.2}$$

[1]Here, we do not employ the point at $z = 1.26$ from [478] as it was not yet available when we wrote the paper on which this section is based.

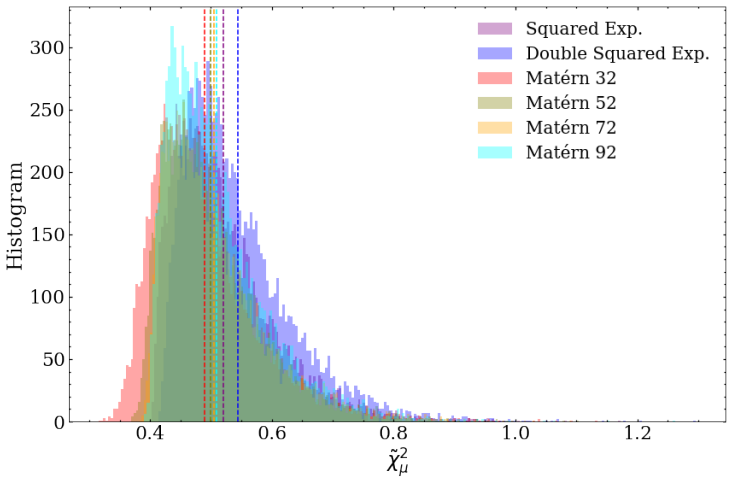

Figure 6.1. Histograms of the $\tilde{\chi}^2_\mu$ obtained for the reconstruction of $H(z)$ for the six kernels employed in the GP training (see Sec. 6.1 for more details). The vertical dotted lines are located at the corresponding mean values.

Table 6.1. Results of the test based on the $\tilde{\chi}^2_\mu$ analysis to determine the kernel that performs the best for the reconstruction of $H(z)$. In the first column we indicate the pairs of kernels under comparison, taking in all cases the Squared Exponential as reference. The second column shows the relative weight of the kernels. The best-performing kernel is Matérn 32, cf. the line in bold.

Kernels	$P_{\rm SE}/P_j$
SE vs DSE	1.42
SE vs M32	**0.62**
SE vs M52	0.72
SE vs M72	0.82
SE vs M92	0.83

where P_j/P_i in the right-hand side is the ratio of their statistical weights. In practice, if we use a sufficiently large number of realizations, N_{real}, we can estimate $P_j/P_i \sim N_j/N_i$, with N_i being the number of realizations in which $\tilde{\chi}^2_{K_i} < \tilde{\chi}^2_{K_j}$ and $N_j = N_{real} - N_i$. As we are computing relative weights, we can set e.g. $j = 1$, and compute its relative performance with respect to the Kernels $K_2, .., K_6$. In the analysis presented in Table 6.1 K_1 stands for the Squared Exponential kernel. It is clear from that table that Matérn 32 is the best-performing kernel regarding the reconstruction of $H(z)$[2].

We can now reconstruct the shape of the Hubble function $H(z)$ and the apparent magnitude of SNIa $m(z)$ in the common redshift range of interest. As anticipated, the aim of obtaining these model-independent reconstructions is to use them (among other things) to reconstruct first the absolute magnitude of SNIa and the curvature

[2]For completeness, we also check whether this result is sensitive to the ordering of the vectors containing the values of $\tilde{\chi}^2_\mu$. The results are very stable. Indeed, the ratios $P_{\rm SE}/P_i$ differ only by a tiny percentage, which is only due to numerical noise, i.e. it becomes smaller and smaller for increasing values of N_{real}.

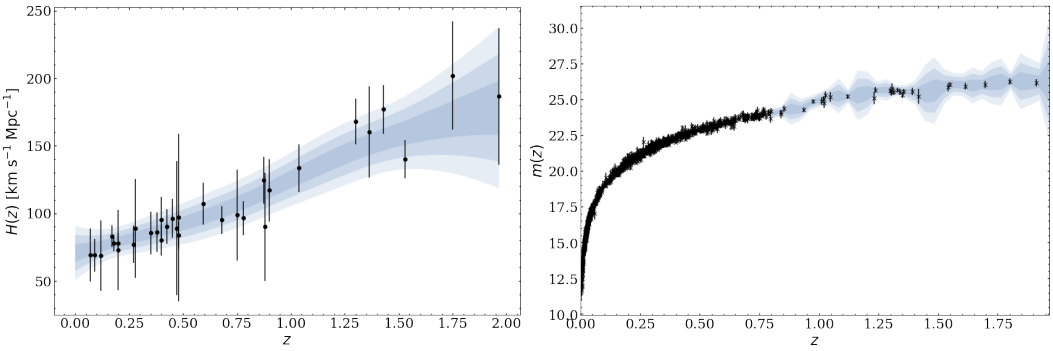

Figure 6.2. Reconstructed shapes of the Hubble function $H(z)$ (left plot) and the apparent magnitude of SNIa $m(z)$ (right plot), at 1σ, 2σ and 3σ obtained from GPs. See main text for details.

parameter as a function of the redshift, see Sec. 6.2.

We obtain $H(z)$ from CCH following the method and the prescriptions derived from previous results. That is, we use the M32 kernel, a zero mean function μ, and taking into account the full distribution of the hyperparameters σ_f and l, so as to conduct a fully Bayesian analysis (see discussion in Sec. 5.1). This, in particular, only has a modest impact on the final reconstruction. The mean in the marginalization procedure differs by 5% at most from the optimized result and the errors are 8% larger. Moreover, we have explicitly checked that we obtain very similar results using $\mu = 0, 10, 100$. They differ only by $\lesssim 0.1\sigma$. Hence, a full marginalization process that includes also the marginalization over a constant μ (together with the hyperparameters) leads essentially to the same final reconstructed shape of $H(z)$. In addition, we have also studied what happens if we assume a prior mean based on the ΛCDM prediction, marginalizing also over the parameters H_0 and Ω_m. We find that this introduces very strong model dependencies, basically yielding the same output as in a pure ΛCDM fit. This is consistent with the discussion in Sec. 5.1 regarding the behaviour of the hyperparameter σ_f: in such cases it tends to become small and, since it controls the typical amplitude of deviations from the mean, the reconstructed function is forced to remain close to it. For this reason, we proceed by adopting a zero mean function in all our main GP analyses.

The SNIa apparent magnitude $m(z)$ is obtained using the Pantheon+ compilation. However, due to the large covariance matrix of the sample, it is very expensive from the computational point of view to perform the marginalization over the hyperparameters, so we opt to use also in this case the M32 kernel and the best-fit values obtained from the maximization of the marginalized likelihood Eq. (5.14). Using the binned Pantheon data from [479], we have checked that the results are not very sensitive to these choices. In addition, we employ the reconstruction of $m(z)$ only in some of the tests of Sec. 6.2. The conclusions of these tests do not depend on these subtleties. To obtain the final constraints on the triad of parameters (M, Ω_k, r_d) in Sec. 6.3, we only make use of the reconstruction of the Hubble rate, which duly incorporates the uncertainties of the hyperparameters.

We show the reconstructed shapes of $H(z)$ and $m(z)$ in Fig. 6.2[3]. From the GP

[3]For previous reconstructions of the Hubble rate with GPs and CCH see e.g. [445, 396, 397, 398,

reconstruction, the extrapolated value of the Hubble parameter at $z = 0$ is found to be $H_0 = (70.7 \pm 6.7)$ km/s/Mpc.

6.2 Consistency tests for low-z data and tests of some theoretical assumptions behind ΛCDM

In this Section, we show how to use the reconstructed shapes of $H(z)$ and $m(z)$ obtained in Sec. 6.1 to get the trend of the absolute magnitude of SNIa, $M(z)$, at $z \lesssim 2$. The Hubble function will be also used to obtain the shapes of $\Omega_k(z)$ and $r_d(z)$. The assessment of their constant value throughout the considered redshift range is crucial for the last part of the analysis, presented in Sec. 6.3.

6.2.1 Testing the constancy of M

$M(z)$ can be reconstructed using formula (4.8). First, we draw $N_{real} = 5 \cdot 10^5$ realizations (curves) of the Hubble function and the apparent magnitude from their corresponding GP. In order to compute the reconstructed shape of the luminosity distance using Eq. (1.78) we have to employ a prior for the curvature parameter. For this first analysis we fix $\Omega_k = 0$, while then we will study also other values to assess the impact of this prior on our result. For each realization in the sample, we compute $M(z_i)$ at $n_p = 50$ equispaced knots. We present the reconstructed shape of $M(z)$ and its first derivative, dM/dz, in Fig. 6.3. From these plots it is evident that the resulting function is fully compatible with a constant at $\lesssim 1\sigma$. We have checked that this statement actually holds for a wide range of values of the curvature parameter $\Omega_k \in [-1, 1]$.

In view of these results, it is natural to estimate the value of the constant M from the reconstructed shape of $M(z)$. As we have n_p knots we have n_p distributions of M, i.e. one for each knot. These samples are correlated, of course. Assuming that they are Gaussianly distributed, we can construct a probability distribution that takes the following form,

$$\mathcal{L}(M) = \mathcal{N} \exp\left[-\frac{1}{2}\sum_{i,j=1}^{n_p}(M - \bar{M}_i)(M - \bar{M}_j)(C_M^{-1})_{ij}\right], \tag{6.3}$$

with $\mathcal{N}$ the normalization constant and $\bar{M}_i$ the mean value in the i-th knot. Let us define now $A_{ij} \equiv (C_M^{-1})_{ij}$ to simplify the notation. It is easy to show that Eq. (6.3) can be rewritten as follows

$$\mathcal{L}(M) = \tilde{\mathcal{N}} \exp\left[-\frac{1}{2}\left(\sum_{i,j=1}^{n_p} A_{ij}\right)\left(M - \frac{\sum_{i,j=1}^{n_p}\bar{M}_i A_{ij}}{\sum_{i,j=1}^{n_p} A_{ij}}\right)^2\right]. \tag{6.4}$$

This means that the distribution of M is a Gaussian with mean and deviance

446, 447], and for previous reconstructions of $m(z)$ or the distance modulus from SNIa data see e.g. [448, 449, 450, 451, 452, 447].

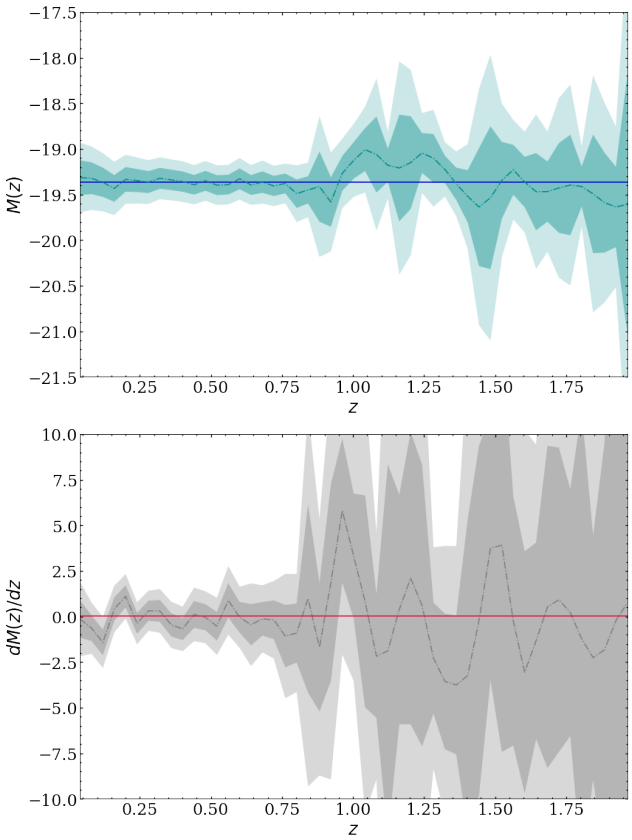

Figure 6.3. Reconstruction of $M(z)$ and its derivative dM/dz at 68% and 95% C.L., obtained by fixing $\Omega_k = 0$ and using the method described in Sec. 6.2. The constant lines appearing in the plots (in blue and red, respectively) are the corresponding weighted means, computed with formula (6.5).

$$\bar{M} = \frac{\sum_{i,j=1}^{n_p} \bar{M}_i A_{ij}}{\sum_{i,j=1}^{n_p} A_{ij}} \quad ; \quad \sigma^2 = \frac{1}{\sum_{i,j=1}^{n_p} A_{ij}} \,, \tag{6.5}$$

respectively. We estimate the covariance matrix from our sample as follows,

$$C_{M,ij} = \frac{1}{N_{real}} \sum_{\mu=1}^{N_{real}} (M_{\mu,i} - \bar{M}_i)(M_{\mu,j} - \bar{M}_j) \,, \tag{6.6}$$

where $M_{\mu,i}$ is the value of the absolute magnitude at the i-th knot for each realization $\mu = 1, ..., N_{real}$.

Applying these formulas, we find $\bar{M} = (-19.368 \pm 0.092)$ mag in the case in which we set $\Omega_k = 0$. However, this result can only be considered as a first approximation for two reasons: (i) non-Gaussian features, despite being small, can introduce some mild changes, which are not captured by the distribution Eq. (6.3). However, we have performed a sanity check to verify that the n_p distributions of M are Gaussian in very good approximation. At each redshift point where we reconstruct $M(z)$, we

build a histogram from its N_{real} realizations and check that the skewness of each of them is compatible with zero. Hence, the bias introduced by this fact is certainly very small; and (ii) in this calculation all the redshift range is equally weighted, but in reality the data points are not uniformly distributed and this might also have an impact on the estimation of the weighted mean and its uncertainty.

At this stage, the test performed in this Section indicates that, based on CCH and Pantheon+ data, there is no significant statistical evidence for an evolution of $M(z)$ at $z \lesssim 2$[4].

6.2.2 Testing the homogeneity property of the Universe

Now, we reconstruct $\Omega_k(z)$. The result can be employed to test the Cosmological Principle without specifying the energy content of the Universe nor the gravity action. As a diagnostic of the homogeneity of the Universe, one can use [475]

$$\Omega_k(z) = \frac{[H(z)D'_M(z)/c]^2 - 1}{[H_0 D_M(z)/c]^2}\,, \tag{6.7}$$

with the prime denoting a derivative with respect to the redshift. This expression is obtained straightforwardly from Eq. (1.78) (and recalling Eq. (1.82)). Any of its deviations from a constant value at any redshift can be considered to be a hint of the breaking of the CP. The function (6.7) can be reconstructed from measurements of $H(z)$ and the luminosity distance. Hence, one can build it from CCH and calibrated SNIa data. However, here, we reconstruct $\Omega_k(z)$ in an alternative way, which allows us to skip the numerical computation of the derivatives $D'_M(z)$ appearing in Eq. (6.7). It works as follows. We use the GP of $H(z)$ to generate N samples of the Hubble function. On the other hand, we draw N values of M from the SH0ES Gaussian prior on the absolute magnitude of SNIa, $M^{R22} = (-19.253 \pm 0.027)$ mag [94]. With the latter and N GP-realizations of $m(z)$, we can reconstruct $D_L(z)$ from formula (4.8), and also the angular diameter distance through the Etherington relation in Eq. (1.81). We employ all these ingredients to solve Eq. (1.78) numerically for every redshift and find N realizations of $\Omega_k(z)$. Our results are presented in Fig. 6.4. The reconstructed function is compatible with a constant, so there is no hint of a violation of the homogeneity property of the Universe at $z \lesssim 2$. This resonates well with previous results in the literature obtained with older data sets and applying a different methodology, see e.g. [449, 450, 451]. We have verified that this finding is again independent of the prior on M employed in the analysis, although the constraint we get on the constant value of Ω_k does depend on it. This is evident from Fig. 6.4. To get rid of the ambiguity introduced by the subjective choice of the priors, in Sec. 6.3, we will provide joint constraints on these parameters.

6.2.3 Internal consistency of 3D BAO data

We proceed now by testing the internal robustness of the BAO data from the galaxy surveys 6dFGS, BOSS, eBOSS, WiggleZ and DES Y3 (listed in Table A.2) in the

[4] Although CCH+SNIa do not favor a variation of M, they do not exclude it either, given the large error bars. In Chapter 9, we reconstruct the shape of $M(z)$, not only in light of CCH and Pantheon+, but also using different types of BAO data, the CMB, and the SH0ES prior on H_0, to explore how a variation of M could help alleviate the Hubble tension.

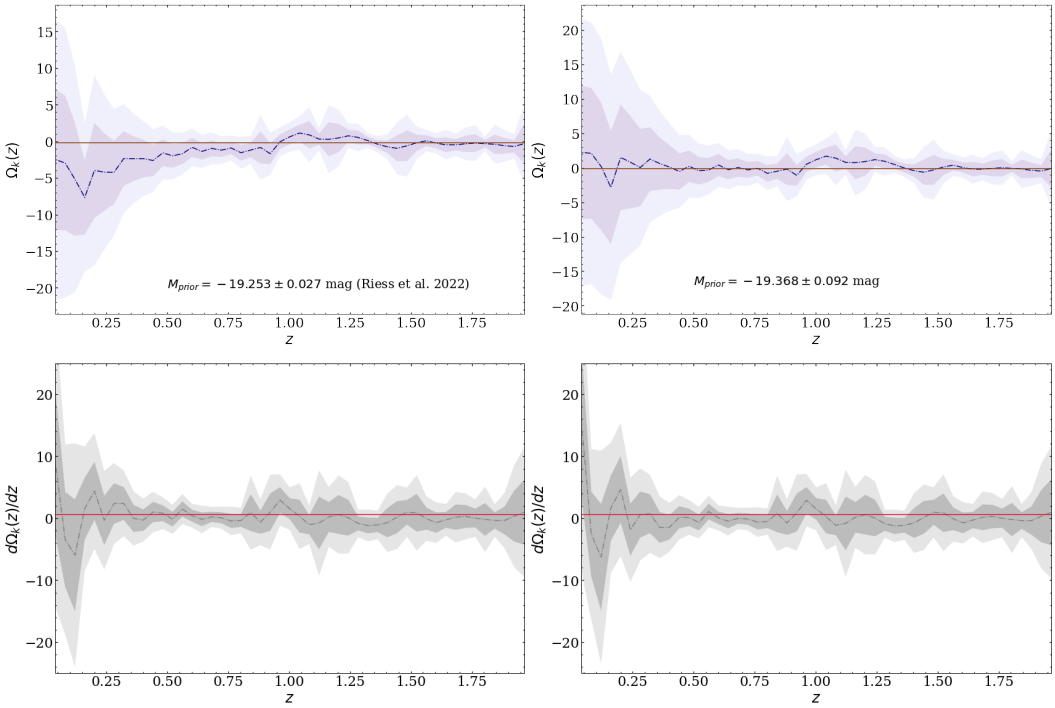

Figure 6.4. *Left panels:* Reconstructed shape of $\Omega_k(z)$ and $d\Omega_k(z)/dz$ at 1σ and 2σ C.L. obtained as explained in Sec. 6.2.2, assuming the SH0ES prior M^{R22} [94]. *Right panels:* The same, but using the Gaussian prior for M obtained from the analysis presented in Fig. 6.3, $M = (-19.368 \pm 0.092)$ mag. In all the plots the dot-dashed lines correspond to the mean curves of $\Omega_k(z)$ and $d\Omega_k(z)/dz$, while the constant solid lines are their overall weighted mean, computed again with formula (6.5). We get the mean values $\bar{\Omega}_k = -0.21$ and $\bar{\Omega}_k = -0.17$ in the upper and lower plots, respectively.

light of the CCH data. The rationale is simple. Given the reconstructed expansion rate derived from CCH, we would expect the values of r_d obtained from the various BAO data points to be statistically consistent with each other. Otherwise, this could signal the presence of uncorrected systematic effects in the data.

We apply a method that is completely analogous to the one performed to obtain $M(z)$ and $\Omega_k(z)$ in Secs. 6.2.1 and 6.2.2, respectively. We use the GP for $H(z)$ to generate curves of the Hubble function. From them we can also reconstruct $D_A(z)$ for a fixed curvature parameter (we first consider the case of a flat Universe, i.e. $\Omega_k = 0$). We compute the angular diameter distances and $H(z)$ at the redshifts of the BAO data points. Finally, we draw Gaussian-distributed vectors of BAO data and combine this information to obtain 11 distributions of r_d, i.e. one for each BAO data point.

We present our results in Fig. 6.5. For those redshifts with two BAO data points (at $z = 0.32, 0.57, 1.48$, cf. Table A.2) we use the weighted mean and uncertainty as provided in Eq. (6.5) to obtain a single value of r_d. It is clear from that plot that the values of r_d at the various redshift values are consistent with each other. This result still holds (at 68% C.L.) if we allow the Universe to take closed or open geometries, as we have explicitly checked by exploring values of $\Omega_k \in [-0.8, +0.5]$. The same applies to $M(z)$, as mentioned in Sec. 6.2.1. Its shape is indeed compatible with a

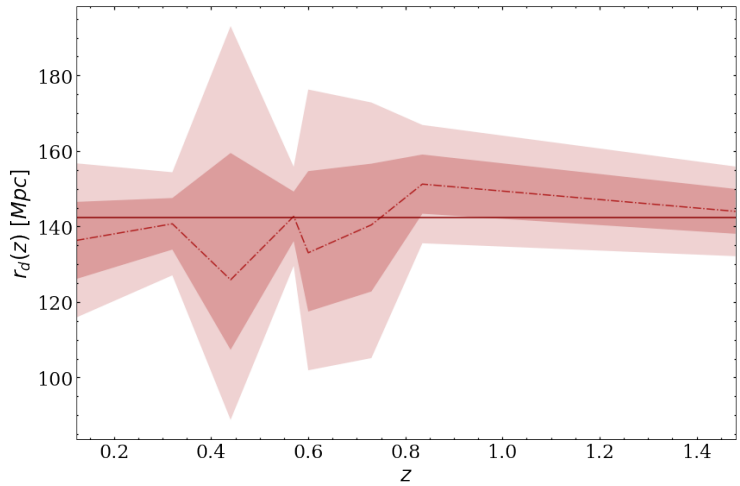

Figure 6.5. Result of the consistency test of the BAO data listed in Table A.2, as described in Sec. 6.2.3. The plot shows measurements of r_d (at 68% and 95% C.L.) as a function of the redshift, fixing $\Omega_k = 0$. The dot-dashed line passes through the peak values of the individual histograms of $r_d(z)$ at each redshift, while the solid line represents the weighted mean obtained from formula (6.5), which reads: $\bar{r}_d = (142.5 \pm 5.3)$ Mpc.

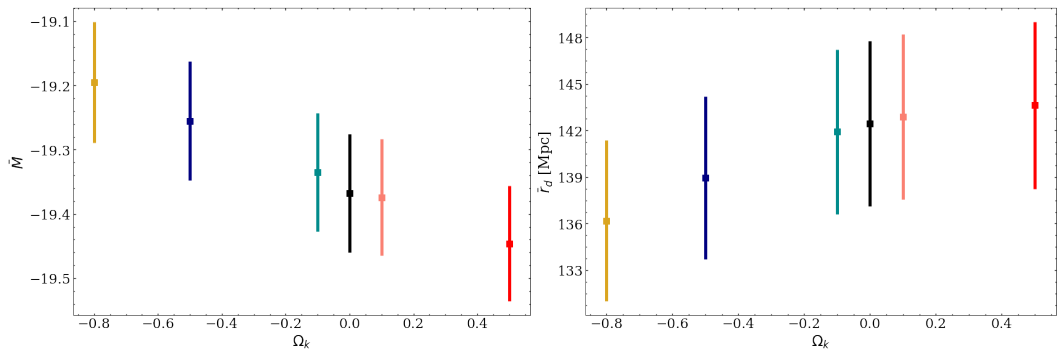

Figure 6.6. Dependence of the weighted mean $\bar{M}$ and $\bar{r}_d$ (at 1σ C.L.) on the prior value of Ω_k employed in the analysis, cf. Secs. 6.2.1 and 6.2.3.

constant regardless of the value of Ω_k chosen to carry out the analysis. Nevertheless, it is important to notice that the value of that constant for both $\bar{M}$ and $\bar{r_d}$ depends a lot on the prior. In Fig. 6.6 we show how the constraints on the ladder calibrators change with Ω_k[5].

[5]The range of values of Ω_k explored here is much broader than what is allowed by the ΛCDM constraints from *Planck* [11]. This has to be consistent with our model-independent approach. As we will see in Sec. 6.3, large absolute values of the curvature are not excluded by the low-redshift data sets employed in this work.

6.3 Simultaneous calibration of the ladders and measurement of Ω_k

The analyses carried out in Sec. 6.2 show no evidence for an evolution of the absolute magnitude of SNIa with redshift nor a departure from homogeneity at large scales. Moreover, we have checked that the 3D BAO data employed are consistent and lead to values of r_d that are fully compatible with each other. Hence, we are legitimated to perform an analysis to jointly constrain the curvature parameter and the calibrators of the distance ladders by treating them simply as constants[6].

Our approach works as follows. We employ the GP-reconstructed functions in a grid-search method. First, CCH and SNIa data sets are used to obtain joint constraints in the plane (M, Ω_k). The same for CCH and BAO in the plane (Ω_k, r_d). These two-dimensional joint analyses are then combined to exploit the full three-dimensional parameter space of (M, Ω_k, r_d). We remark here that in our analyses we constrain Ω_k through its effect on the geometrical pre-factor of the luminosity distance (cf. Eq. (1.79)) and not on $H(z)$, since we reconstruct the Hubble function directly with GP+CCH. The size and resolution of each grid can vary depending on the data set employed. We always assume flat priors for M, Ω_k, r_d, much wider than the uncertainties obtained in our analyses.

For each point of the grid, which is characterized by the pair (M, Ω_k) or (Ω_k, r_d), we generate N realizations of $H(z)$, which are then employed to obtain N realizations containing the values of the luminosity distances (Eq. 1.78) at the SNIa redshifts, or angular diameter distances and dilation scales (Eqs. (1.81), (4.13)) and values of $H(z)$ at the BAO redshifts. These N realizations are easily converted into N realizations of reconstructed SNIa and BAO observables at the corresponding redshifts. This information is then used to perform a χ^2 analysis using the SNIa or BAO data. For each realization $I = 1, .., N$ in the μ-th knot, we have

$$\chi^2_{X,\mu,I} = \sum_{k,l=1}^{D_X} [f_k - f^{rec}_{\mu,I,k}](C_X^{-1})_{kl}[f_l - f^{rec}_{\mu,I,l}] \,, \tag{6.8}$$

where C_X is here the covariance matrix of the data set X employed – either SNIa or BAO –, and D_X the corresponding total number of data points. Notice that each index k, l labels an individual data point in the data set X, as the latter can include multiple measurements at the same redshift z. Each knot of the grid is weighted by

$$w_\mu \propto B_\mu \sum_{I=1}^{N} \exp(-\chi^2_{X,\mu,I}/2) \,, \tag{6.9}$$

where the prefactor B_μ accounts for the bins size at the μ-th knot. If we denote with P_{AB} the two-dimensional probability for the parameters A and B, then its evaluation will be as follows

$$P_{AB}(a, b) = \frac{w_{\mu\to(a,b)}}{\sum_\beta w_\beta} \,. \tag{6.10}$$

[6]We still assume cosmological isotropy, even though this symmetry of the CP has not been tested by us. See [23] for a review of the CP and hints for deviations from it.

While the denominator accounts for contributions from all knots, the numerator is restricted to the knot corresponding to the parameter values a and b of A and B, respectively. Analogously, the one-dimensional posterior probability for each parameter A, P_A, is

$$P_A(a) = \frac{\sum\limits_{\mu \to a} w_\mu}{\sum\limits_{\beta} w_\beta} \,. \tag{6.11}$$

The sum in the numerator is now limited to the knots associated with the value a of A. Best-fit values for each parameter are therefore obtained by maximizing Eq. (6.9).

Notice that, as mentioned before, the 2D analyses are combined together to explore the full parameter space. From Eq. (6.8), this simply translates in computing

$$\chi^2_{X\tilde{X}} = \chi^2_X + \chi^2_{\tilde{X}} \,, \tag{6.12}$$

as the BAO and SNIa data are independent. To summarize, both, uncalibrated SNIa and BAO, are relative distance indicators. In practice, we use CCH to calibrate the standard candles and the standard rulers. Finally, we combine the three data sets CCH+SNIa+BAO to constrain the full parameter space (M, r_d, Ω_k).

An estimate of H_0 from the CCH-calibrated ladders

It is natural to ask what value of the Hubble parameter is favored by the CCH ladder calibration, as this provides a crucial benchmark for assessing where model-independent estimates of H_0 lie within the current (and future) cosmological landscape. To do so, as done within the context of the local distance ladder analyses (see Sec. 2.1), we apply the following cosmographical expansion for the luminosity distance, which follows from Eqs. (2.6)-(2.8)[7]:

$$D_L(z) = czH_0^{-1}\left[1 + \frac{z}{2}\left(1 - q_0\right)\right] + \mathcal{O}(z^3) \,, \tag{6.13}$$

with q_0 the deceleration parameter defined in Eq. (2.7). The luminosity distance is computed using the SNIa apparent magnitudes in the Hubble flow ($0.023 < z < 0.15$) and the constraint on M we obtain from the final 3D joint analysis. This is analogous to the analysis performed by the SH0ES collaboration, which uses the Cepheid-calibrated value of M and a fixed value for the deceleration parameter, $q_0 = -0.55$ [93, 94]. At very low redshifts ($z \lesssim 0.1$), the impact of the first-order correction in q_0 is small, since $z^2 \ll 1$. Although this makes q_0 estimation challenging from low-redshift data alone (especially if one has a large uncertainty on M that dominates the error budget), we opt to fit both parameters simultaneously. This way, uncertainties in q_0 can be propagated into uncertainties (or potential biases) on the estimation of H_0.

[7]We can neglect here curvature corrections as they are of third order in z, therefore playing a negligible role within the Hubble flow.

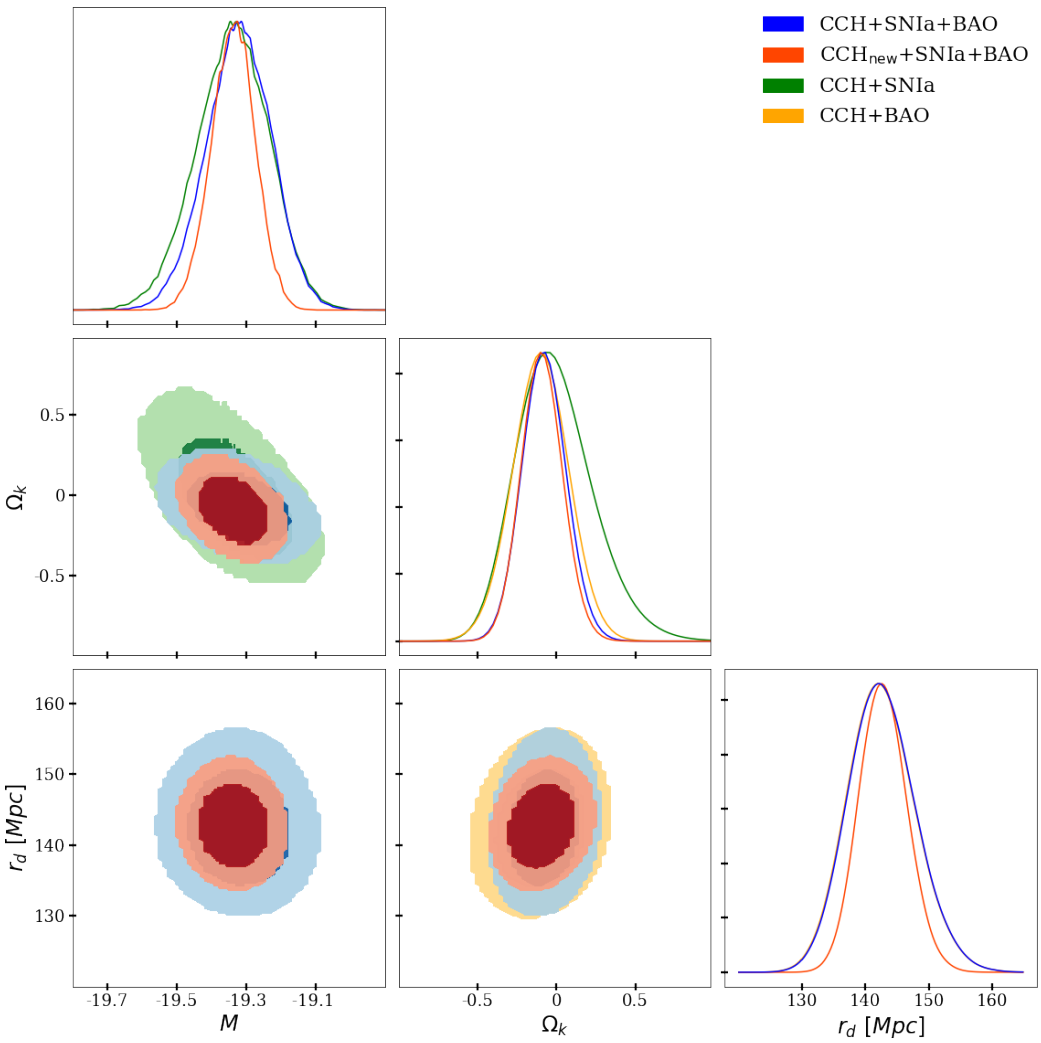

Figure 6.7. Two-dimensional contour plots in all the planes of the parameter space (M, Ω_k, r_d) and the corresponding one-dimensional posterior probability distributions obtained from the joint analyses described in Sec. 6.3.1. The 2D contours are evaluated at 68% and 95% C.L. As expected, the combination of the three data sets (CCH+SNIa+BAO) allows for obtaining tighter constraints with respect to the CCH+SNIa and CCH+BAO analyses (see the estimated values in Table 6.2). This trend is even more remarkable if we allow uncertainties on the CCH data to decrease by a factor $\sim 3/2$ (in red). See main text for more details.

6.3.1 Constraints from current data

We now present the results obtained with the methodology described above, employing the following data: CCH, Pantheon+ SNIa, and the BAO measurements listed in Table A.2. This analysis is still part of our work in [468].

The one-dimensional posteriors and the confidence regions at 68% and 95% C.L. in all the planes of parameter space are provided in Fig. 6.7 and the derived constraints on the various parameters are presented in Table 6.2. By evaluating for each parameter the maximum of the probability Eq. (6.11) and the 68% confidence

Table 6.2. Constraints on M, Ω_k and r_d obtained from the joint analyses presented in Sec. 6.3.1, see also Fig. 6.7. We remind the reader that these results are obtained with Pantheon+ SNIa and the BAO in Table A.2, and are independent of the SNIa calibration with Cepheids in the first rungs of the cosmic distance ladder, since we exclude the SNIa contained in the host galaxies employed by SH0ES in their analysis [94, 95]. Notice that the central values for Ω_k obtained with CCH+SNIa and CCH+SNIa+BAO are the same and a bit larger than the one obtained with CCH+BAO. In reality, the CCH+SNIa+BAO constraint for Ω_k falls somewhere in the middle between the CCH+SNIa and CCH+BAO results, as expected, but we are limited by the resolution of our grid, since we use a step $\Delta\Omega_k = 0.03$. In any case, this step is much lower than the uncertainty of Ω_k, so this fact has no impact on our conclusions.

	CCH+SNIa	CCH+BAO	CCH+SNIa+BAO
M [mag]	$-19.344^{+0.116}_{-0.090}$		$-19.314^{+0.086}_{-0.108}$
Ω_k	$-0.07^{+0.27}_{-0.21}$	-0.10 ± 0.18	$-0.07^{+0.12}_{-0.15}$
r_d [Mpc]		$141.9^{+5.6}_{-4.9}$	142.3 ± 5.3

intervals, we obtain the following results:

- From CCH+SNIa: $M = (-19.344^{+0.116}_{-0.090})$ mag and $\Omega_k = -0.07^{+0.27}_{-0.21}$. The constraint on Ω_k is similar to the one found by [471] using the Pantheon compilation of SNIa (instead of the most updated Pantheon+) and without considering the correlations between the CCH data nor the data point from [480], $\Omega_k = -0.03 \pm 0.26$. In addition, we also provide a constraint on M, which is not reported by [471], since they marginalize their result over it.

- From CCH+BAO: $\Omega_k = -0.10 \pm 0.18$ and $r_d = (141.9^{+5.6}_{-4.9})$ Mpc. The combination of the CCH data set with the BAO measurements still favors a negative central value for the curvature parameter, although it is compatible with a flat geometry within only $\sim 0.6\sigma$. The uncertainty of Ω_k is $\sim 25\%$ smaller than in the analysis with CCH+SNIa. This is clear from the comparison of the green and yellow one-dimensional posteriors of the curvature parameter in Fig. 6.7.

  The posterior of r_d peaks $\sim 1\sigma$ below the preferred *Planck*/ΛCDM value, $r_d = (147.09 \pm 0.26)$ Mpc, closer to the region preferred by EDE and modified gravity models proposed to alleviate the H_0 tension (see Sec. 3.4). However, this deviation is not statistically significant.

- From CCH+SNIa+BAO: $M = (-19.314^{+0.086}_{-0.108})$ mag, $\Omega_k = -0.07^{+0.12}_{-0.15}$ and $r_d = (142.3 \pm 5.3)$ Mpc. As expected, the combination of all the low-z data sets employed in this work leads to smaller uncertainties (see Table 6.2 and Fig. 6.7), especially in the case of Ω_k, since this is the only parameter that is constrained from both the CCH+SNIa and CCH+BAO data sets. If we set $\Omega_k = 0$ we find $M = (-19.346^{+0.094}_{-0.088})$ mag and $r_d = (142.6 \pm 5.3)$ Mpc, which remain extremely close to the main results, but with slightly smaller errors[8].

  Our result for the absolute magnitude is independent of the SNIa distance ladder calibration. It is compatible within 1σ with M^{R22}, but our method

[8]We take the arithmetic mean of the upper and lower uncertainties to make this comparison.

Table 6.3. The same as in Table 6.2, but including the SNIa in the host galaxies [95] and their distances to calibrate the SNIa as SH0ES [94]. This has a very little impact on our constraints on Ω_k and r_d.

	CCH+SNIa_host	CCH+BAO	CCH+SNIa_host+BAO
M [mag]	$-19.252^{+0.024}_{-0.036}$		$-19.252^{+0.024}_{-0.036}$
Ω_k	$-0.13^{+0.18}_{-0.21}$	-0.10 ± 0.18	$-0.10^{+0.12}_{-0.15}$
r_d [Mpc]		$141.9^{+5.6}_{-4.9}$	$141.9^{+5.6}_{-4.9}$

cannot achieve the precision attained by SH0ES [94]. Our constraint is also in agreement with the one in [241], obtained using a different method based on the index of inconsistency by [243], the Pantheon data set and less CCH data points, but still making use of the combination CCH+BAO+SNIa. We find a 1σ-compatibility also with the ΛCDM result $M = (-19.403 \pm 0.010)$ mag [235], although we remark again that our results have been obtained in a model-independent way.

Our measurement of Ω_k points very mildly to a closed Universe, being compatible with the flatness assumption within only $\sim 0.5\sigma$. In contrast to the previous work [241], which reports $\Omega_k = -0.01 \pm 0.1$, here we do not make use of any cosmological prior inspired by the *Planck*/ΛCDM results. The latter would dominate the final constraint on the curvature parameter over the low-z data sets, something that we wanted to avoid here. The uncertainty of Ω_k is much larger than the one obtained in model-dependent analyses like the one by [11] or [32]. The latter obtain $\Omega_k = -0.0054 \pm 0.0055$ in the context of the non-flat ΛCDM by combining the CMB data from *Planck* with CCH.

The calibration of the standard ruler with CCH+SNIa+BAO leads to a value which is $\sim 1\sigma$ smaller than the ΛCDM value preferred by *Planck* [11], similar to the one obtained from the CCH+BAO analysis, and again peaks at values more in accordance with theoretical scenarios that alleviate the Hubble tension. Our value of the sound horizon at the drag epoch is also compatible with other model-independent analyses, as those by [398], $r_d = (145.6 \pm 5)$ Mpc, and [241], $r_d = (146.0^{+4.2}_{-5.1})$ Mpc.

By employing as a prior our CCH+SNIa+BAO constraint on M and the apparent magnitudes of the Pantheon+ SNIa in the Hubble flow, from Eq. (6.13) we obtain $H_0 = (71.5 \pm 3.1)$ km/s/Mpc. The uncertainty is roughly a factor 1/2 smaller than the one obtained using only CCH, see Sec. 6.1. As a byproduct, we also constrain the deceleration parameter $q_0 = -0.44 \pm 0.19$. This result is fully compatible with the model-independent measurements extracted from CCH+SNIa+BAO [398, 481], but with an uncertainty a factor of two larger, since here q_0 is fixed only by the SNIa in the Hubble flow.

To complement the analysis, we also provide two additional tests, which we anticipated in this Section: a possible overestimation of CCH uncertainties, and the impact of SNIa in the host galaxies employed by SH0ES to estimate H_0.

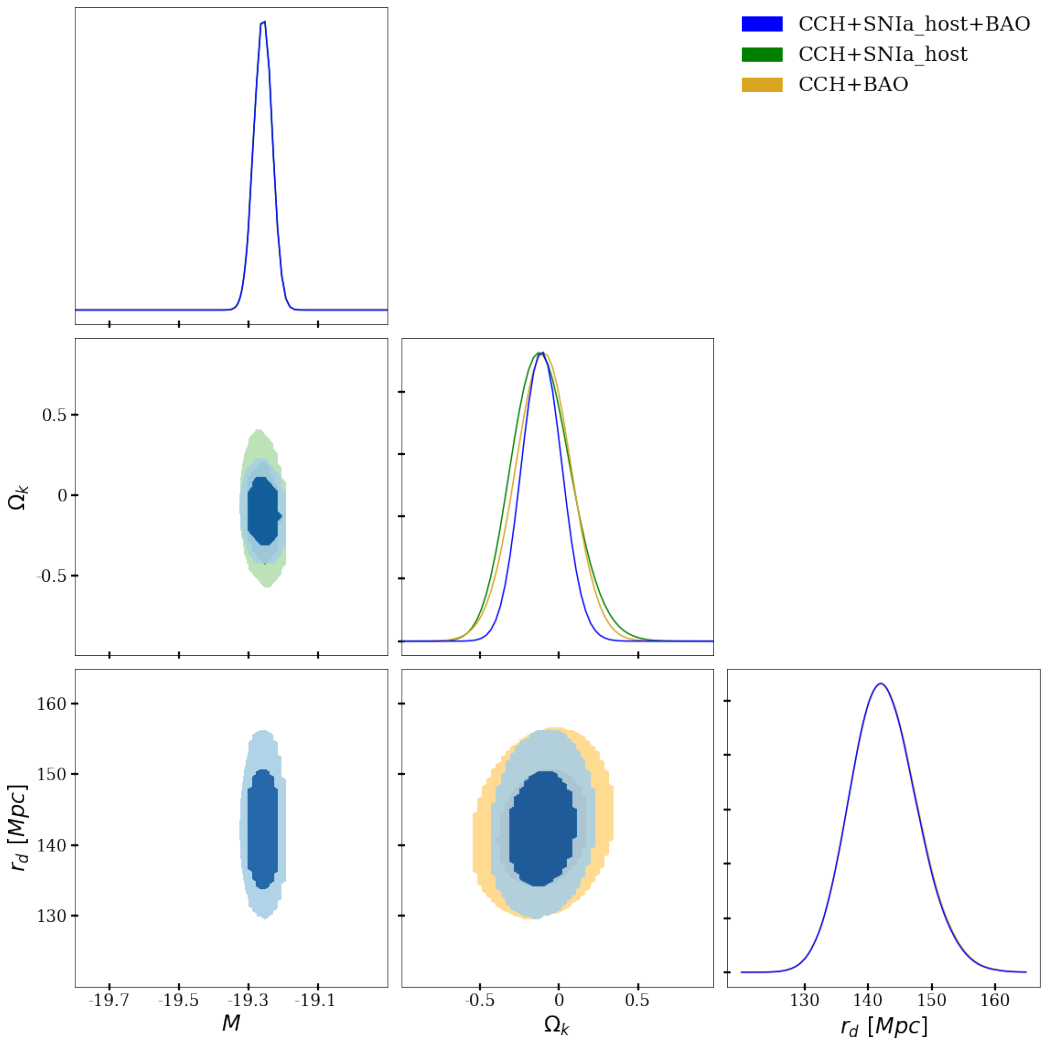

Figure 6.8. As in Fig. 6.7, but including the information from the SNIa in the host galaxies [95] and their distances employed by SH0ES [94].

Considering smaller uncertainties in the CCH data

The GPs kernel performance test done in Sec. 6.1 shows that the mean values of the reduced chi-square, $\tilde{\chi}^2_\mu$ in Eq. (6.1), associated to the reconstruction of $H(z)$ with the CCH data points listed in Table A.1 are all much smaller than 1 (see also Fig. 6.1). This result is not expected to be due to an overfitting of the GP, since similar values of the $\tilde{\chi}^2$ are also found in fitting analyses with a simple straight line or a parabola [397]. As already mentioned, the small values of $\tilde{\chi}^2_\mu$ could instead be a hint of an overestimation of the errors in the covariance matrix of the CCH data, $\tilde{C}_{ij}$. We deem it interesting to explore this possibility by studying how the results on (M, Ω_k, r_d) change if we allow for smaller uncertainties in $\tilde{C}_{ij}$. With this aim we build the new CCH covariance matrix $\tilde{C}_{ij,new} = \tilde{C}_{ij}/N^2$, with N a positive factor. This is equivalent to decrease all the individual CCH uncertainties by a common factor N, while leaving the previous correlation coefficients intact. For this purpose,

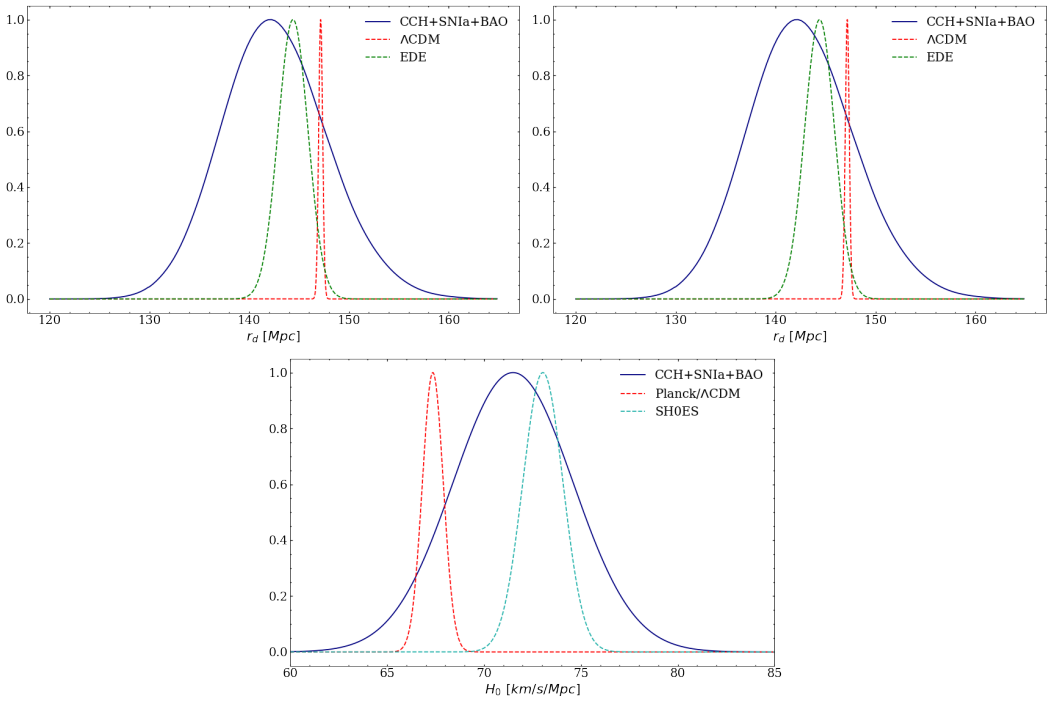

Figure 6.9. *Upper left plot:* Model-independent constraint on M obtained from the analysis of Sec. 6.3.1, compared with the SH0ES posterior $M^{R22} = (-19.253 \pm 0.027)$ mag [94] and the constraint obtained in the ΛCDM from the fitting analysis with Planck2018+SNIa+BAO data, $M = (-19.403 \pm 0.010)$ mag [235]. *Upper right plot:* The same, but for r_d. Here, our result is compared with the posterior obtained from the Planck2018+SNIa+BAO analyses in the context of ΛCDM, $r_d = (147.17 \pm 0.20)$ Mpc, and the ultra-light axion-like model of EDE, $r_d = (144.4 \pm 1.5)$ Mpc [235]. *Lower plot:* Constraint on H_0 obtained from our CCH+SNIa+BAO prior on M (cf. the upper left plot and Table 6.2) and the apparent magnitudes of the SNIa in the Hubble flow. This result is compared with the SH0ES [94] and *Planck*/ΛCDM [11] values.

we first repeat the χ^2 test of Sec. 6.1 with the M32 kernel, but increasing the values of $N > 1$ until the mean of the corresponding reduced chi-squared equals one, i.e. until $\tilde{\chi}^2_\mu = 1$. We find that this happens when the CCH uncertainties decrease by a factor $N = 1.579 \sim 3/2$. We denote the resulting CCH data set with the new covariance matrix simply as $\mathrm{CCH_{new}}$ to distinguish it from the original one (CCH).

We can now repeat the analyses explained in Sec. 6.3 with $\mathrm{CCH_{new}}$ to study the impact of this change on the data uncertainties, bearing in mind that this is only a first (naive) attempt to estimate the impact of a possible overestimation of the uncertainties of the CCH data[9]. This leads to the following $\mathrm{CCH_{new}}$+SNIa+BAO constraints: $M = (-19.326^{+0.050}_{-0.068})$ mag, $\Omega_k = 0.10^{+0.12}_{-0.15}$ and $r_d = (142.6^{+3.9}_{-3.5})$ Mpc. The uncertainties of r_d and M decrease by a ∼30%-40% with respect to those found in the CCH+SNIa+BAO analysis (see red contours in Fig. 6.7). We do not find, however, the same decrease in the uncertainty of Ω_k. The reason is simple. Let us

[9]A more refined analysis would probably require a better understanding of the systematics in the data and/or the application of an improved statistical method, on the lines of what was done by [482].

Table 6.4. Constraints at 68% C.L. on the ladder calibrators, M and r_d (in Mpc), and on the curvature parameter Ω_k, from the joint analyses presented in Sec. 6.3.2. In the last two columns, we report the cosmographical constraints on H_0 (in km/s/Mpc) and q_0, cf. Eq. (6.13), while the last two rows include the results in which we test the impact of changing SNIa data (Pantheon+) or the type of BAO (2D, angular).

	M	Ω_k	r_d	H_0	q_0
CCH+DESY5	$-19.277^{+0.104}_{-0.106}$	$-0.48^{+0.32}_{-0.27}$	-	-	-
CCH+DESI DR1	-	$-0.03^{+0.17}_{-0.16}$	$146.10^{+5.38}_{-5.18}$	-	-
CCH+DESI DR2	-	-0.12 ± 0.09	$144.20^{+5.18}_{-4.88}$	-	-
CCH+DESY5+DESI DR1	$-19.330^{+0.095}_{-0.099}$	$-0.113^{+0.150}_{-0.155}$	$145.30^{+5.28}_{-5.08}$	$68.60^{+2.90}_{-3.30}$	$-0.06^{+0.34}_{-0.33}$
CCH+DESY5+DESI DR2	$-19.324^{+0.092}_{-0.095}$	-0.143 ± 0.085	$144.00^{+5.08}_{-4.88}$	$68.83^{+3.03}_{-3.07}$	$-0.05^{+0.34}_{-0.32}$
CCH+PAN+DESI DR2	-19.309 ± 0.088	$-0.107^{+0.079}_{-0.083}$	$144.00^{+5.38}_{-4.68}$	$72.12^{+2.97}_{-2.95}$	-0.45 ± 0.19
CCH+DESY5+2D_BAO	$-19.294^{+0.101}_{-0.106}$	$-0.362^{+0.259}_{-0.240}$	$147.95^{+7.32}_{-6.84}$	$69.85^{+3.19}_{-3.58}$	$-0.04^{+0.34}_{-0.31}$

focus on the combination CCH_{new}+SNIa. The low-redshift data at $z \ll 1$ basically constraints M and is insensitive to the curvature parameter. At larger redshifts, though, we can get constraints on Ω_k, which depend on the reconstruction of the ratio $E(z) = H(z)/H_0$, see Eq. (1.78). The point is that the correlation coefficients employed in the new CCH data set are exactly the same as those used in the original analysis, what makes the reconstructed shape of $E(z)$ to remain the same. This fact, in turn, explains why we find the same constraint on Ω_k as well.

Inclusion of the SNIa in the host galaxies and their distances

In our main analyses, we have excluded the SNIa located in the host galaxies and the information of their distances inferred from calibrated Cepheids, i.e. those employed by SH0ES in the second rung of the cosmic distance ladder [94, 95]. We do so to obtain results that are independent of the main drivers of the Hubble tension. Nevertheless, we may ask ourselves which is the impact of considering this additional information, which is actually included in the full Pantheon+ compilation. We call this SNIa data set SNIa_host, in short. The results of this analysis are shown in Fig. 6.8 and listed in Table 6.3. The output from the analysis with CCH+BAO is not sensitive to the changes in the SNIa data set, for obvious reasons. As expected, the constraints on M are fully dominated by the calibration of the SNIa at the host galaxies. In particular, for the CCH+SNIa_host+BAO analysis we obtain: $M = (-19.252^{+0.024}_{-0.036})$ mag, $\Omega_k = -0.10^{+0.12}_{-0.15}$ and $r_d = (141.9^{+5.6}_{-4.9})$ Mpc, with $H_0 = (74.0^{+1.0}_{-0.9})$ km/s/Mpc. No important differences are found in the curvature parameter and r_d with respect to the 3D results presented in Table 6.2.

A summary of the relevant results presented in this first part of Sec. 6.3 based on CCH, Pantheon+ SNIa, and 3D BAO data – which are collected in [468] – is shown in Fig. 6.9.

6.3.2 Constraints from current data: an updated analysis

We now proceed to the follow-up analysis of our previous work, detailed in Sec. 6.3.1, which extends the study of [468]. We do so by substituting Pantheon+ SNIa with the most recent DESY5 sample and using the BAO data from the data releases

DR1 and DR2 of DESI, as well as 2D BAO. We refer the reader to Secs. 4.2 and 4.3 for descriptions of these samples. As already stressed, assessing the impact of these new data is crucial in light of the current claims and ongoing debates, which we extensively discussed in Chapter 3. In extending our previous work, in [469] we also assess the level of methodological bias that might arise from our calibration technique, which is based on the GP approach. Indeed, as already seen in Section 5.1, the GP posterior mean function in Eq. (5.11) explicitly depends on the data uncertainties. For a zero prior mean function ($\mu = 0$), the expectation value of the posterior mean at the data location ($z^\star = z$) generally differs from the input data vector Y, except in the limit of vanishing noise. For $\mu \neq 0$, instead, the only way to force the proposed mean function to pass exactly through the data points would be to set $\mu = Y$, so that $f^\star \equiv \mu(z^\star)$. However, in realistic applications, the true underlying function is unknown, and such a choice is not possible. Moreover, our method is designed to remain model-agnostic: by setting $\mu = 0$, we assume no prior knowledge of the functional form behind the data. As a result, an offset might arise as an intrinsic feature of the GP reconstruction (see also [448, 483, 484]). Because this offset propagates through the analysis and can ultimately induce a bias on the inferred parameters (M, Ω_k, r_d), we find it necessary to quantify this effect using mock data, for which the fiducial values of the parameters are known. Indeed, even for these mocks, the GP posterior mean does not exactly recover the fiducial $H(z)$, because it sees only discrete samples with associated uncertainties. Realizations drawn from the GP posterior fluctuate around this biased mean, and averaging them simply reproduces it. As a result, any bias encoded in the posterior mean persists in all reconstructed quantities. We estimate this effect as the difference between the recovered and the fiducial value of each parameter A, $\tilde{b} = A_{\rm rec} - A_{\rm fid}$. Accounting for the sign of $\tilde{b}$ is essential, as the direction of the offset is physically informative: a systematic shift, for instance towards higher values of $H(z)$, implies a smaller sound horizon and higher absolute magnitude. The sign of $\tilde{b}$ thus verifies that the parameter recovery aligns with the expected physical trend.

In Table 6.4 we present the constraints at 68% C.L. on M, Ω_k, r_d and H_0 obtained with the most recent data from current surveys. The one-dimensional posteriors and the confidence regions at 68% and 95% C.L. in all the planes of the parameter space for M, Ω_k and r_d are shown in Fig. 6.10, in particular for the combination of CCH with DESY5 and DESI DR2 data. Again, we can draw some conclusions from each separate analysis:

- From CCH+SNIa: the analysis with CCH and DESY5 constrains the SNIa absolute magnitude as $M = -19.277^{+0.104}_{-0.106}$ and the curvature parameter as $\Omega_k = -0.48^{+0.33}_{-0.27}$. In Sec. 6.3.1, using CCH data and SNIa from Pantheon+ (hereafter PAN), we obtained $M = -19.344^{+0.116}_{-0.090}$ and $\Omega_k = -0.07^{+0.27}_{-0.21}$. The new constraint for M remains quite stable. Its uncertainty is driven by the errors on $m(z)$ and $\log D_L(z)$ (see Eq. (2.2)). However, the dominant contribution arises from the luminosity distance, as it is the quantity derived from the GP reconstruction with CCH, which are not as precise as SNIa measurements. Since the CCH data set is the same between the analyses performed with DESY5 and Pantheon+, the determination of M appears largely unaffected. On the other hand, Ω_k from Pantheon+ is more precise

than that obtained here with DESY5, and this can be attributed mainly to the following reason. Ω_k is more sensitive to higher redshifts. The Pantheon+ SNIa span the redshift range $[0.001, 2.26]$, compared to the region $[0.025, 1.12]$ of DESY5. As a result, the current 2D analysis yields relatively weaker constraints on the curvature parameter. We have checked that, if we cut the Pantheon+ sample at $z < 1.12$, i.e., taking the largest redshift as in DESY5, and perform the CCH+PAN analysis, we indeed obtain a 40% increase in the uncertainty of Ω_k compared to the one obtained exploiting all the SNIa up to $z = 2.26$, hence obtaining an uncertainty closer to that of DESY5. It should be noted that the broader redshift coverage of Pantheon+ compensates for its larger distance errors when these SNIa are used to obtain cosmological constraints, whose uncertainties are smaller than those obtained using DESY5, also because the latter include additional systematic uncertainties [169].

- From CCH+BAO: The DESY5 mild preference at 1.6σ for a negative Ω_k is erased by DESI DR1 data in the CCH+DESI DR1 analysis, while the most stringent result with DESI DR2 partially recovers it at 1.3σ. The second data release improved upon the constraining power of the BAO measurements from DR1; therefore, the most precise results are expected from the former. Nonetheless, we find it valuable to assess the effect of both data releases in this work. The impact of DESI DR2 on Ω_k is substantial, reducing its uncertainty by a factor $\sim$2. On the other hand, the constraint on r_d decreases only by 4%.

- From CCH+SNIa+BAO: The 3D joint analysis performed with DESI DR2 leads to $M = -19.324^{+0.092}_{-0.095}$, $\Omega_k = -0.143 \pm 0.085$ and $r_d = (144.00^{+5.08}_{-4.88})$ Mpc. Again, we can compare these updated constraints with those obtained in Sec. 6.3.1 with SNIa from Pantheon+ and BAO from 6dFGS, BOSS, eBOSS, WiggleZ and DES Y3, which read: $M = -19.314^{+0.086}_{-0.108}$, $\Omega_k = -0.07^{+0.12}_{-0.15}$ and $r_d = (142.3 \pm 5.3)$ Mpc. The addition of DESI DR2 data clearly balances the increase in the error bars given by DESY5 SNIa, which we discussed above. This makes the updated constraints with current late-time data tighter than those obtained in the previous analysis. The value of the Hubble constant stands at $H_0 = 68.83^{+3.03}_{-3.07}$ km/s/Mpc using the value of M obtained within the CCH+DESY5+DESI DR2 analysis. In Sec. 6.3.1, we obtained $H_0 = (71.5 \pm 3.1)$ km/s/Mpc. While the error does not move significantly, the central value points now to the ballpark of H_0 values obtained with CMB probes under the assumption of ΛCDM. We deem it interesting to study what happens if we still use the DESY5 SNIa in the Hubble flow but considering the SH0ES prior on M obtained from the SH0ES collaboration via the local distance ladder method, $M^{R22} = -19.253 \pm 0.027$ [94]. Remarkably, this leads to $H_0 = (70.84 \pm 1.16)$ km/s/Mpc. This value is compatible at $< 1\sigma$ with those obtained with CCH+DESY5+DESI DR1/DR2 (see Table 6.4) and, above all, it is lower than that obtained with the local distance ladder using SNIa from Pantheon+, $H_0 = (73.04 \pm 1.04)$ km/s/Mpc [94], bringing the tension with the *Planck* result, $H_0 = (67.36 \pm 0.54)$ km/s/Mpc [11], below 3σ. This is true even considering the tightest CMB-based constraint on H_0 obtained from the combination of *Planck*+ACT+SPT, $H_0 = (67.24 \pm 0.35)$ km/s/Mpc [485]. It

is important to highlight this result since, as already mentioned in Sec. 4.2, there are several ongoing debates on systematics affecting the low-z SNIa of Pantheon+ or DESY5 [166, 167, 168, 169, 170]. For this reason, we also study the case in which the Hubble flow of Pantheon+ is used together with the value of M obtained in the CCH+PAN+DESI DR2 analysis, $M = -19.309 \pm 0.088$. Again, we observe that Pantheon+ prefers a higher value of H_0, but with the smallest uncertainty, being $H_0 = 72.12^{+2.97}_{-2.95}$ km/s/Mpc, for the reasons explained throughout this Section.

Replacing DESI with angular BAO does not significantly change our conclusions regarding the ladder calibrators, as the larger uncertainties prevent drawing robust inferences. This is expected, since these data, being subject to minimal model assumptions, are less precise than the 3D BAO measurements. Consequently, the CCH+DESY5+2D_BAO combination is the least constraining, cf. Table 6.4. For instance, while 2D BAO slightly favors a more closed universe than DESI BAO, with $\Omega_k = -0.362^{+0.259}_{-0.240}$, the uncertainty remains too large for a definitive conclusion. 2D BAO prefer a slightly higher value of the Hubble parameter, $H_0 = 69.85^{+3.19}_{-3.58}$ km/s/Mpc, than the result obtained with anisotropic BAO using the same SNIa sample (DESY5). This is consistent with previous findings in the literature. Indeed, it is already known that angular BAO show a better agreement with the SH0ES estimate [240, 486, 487, 242, 276, 277].[10]

As expected, the resulting constraints on the deceleration parameter q_0 are very loose for all the cases under study, with the exception of CCH+PAN+DESI DR2 analysis. This is driven by the smaller uncertainty on the corresponding M but especially by the larger number of Pantheon+ SNIa in the Hubble flow, which is more than twice that of DESY5. Our q_0 obtained with Pantheon+, $q_0 = -0.45 \pm 0.19$, is fully compatible with the value employed by SH0ES to estimate H_0, $q_0 = -0.55$ [93, 94][11]. With DESY5, instead, we obtain $q_0 = -0.05^{+0.34}_{-0.32}$. In this case the lack of a strong low-z anchor leaves the fit poorly constrained, compatible with a decelerated universe, but still in full agreement with the value obtained from the model-agnostic reconstruction of $q(z)$ using CMB data from Planck, BAO from DESI DR2 and the SNIa from DESY5, $q_0 = -0.28^{+0.09}_{-0.08}$ [363] – see also [362]. Our results are therefore consistent with previous results in the literature.

Lastly, we briefly comment on the methodological bias $\tilde{b}$ introduced by the GP. We recall that, while this bias pertains to the parameters being analyzed, it is quantified via a separate analysis which makes use of mock data vectors generated assuming the ΛCDM model and current data uncertainty. We focus on the combination of CCH, DESY5 and DESI DR2 as a representative test case. Our results show that the $|\tilde{b}|$ values for all parameters are well below

[10] Because 2D BAO angular diameter distances are smaller than expected within the standard model, these data tend to favor higher values of the Hubble function, bringing them into closer alignment with the SH0ES measurement.

[11] As stated in [94], the choice of $q_0 = -0.55$ relies on the fact that it has historically provided a good fit to high-redshift SNIa and matches the expectation from the flat ΛCDM model with $\Omega_m = 0.3$ and $\Omega_\Lambda = 0.7$. Independent works find consistent results, see, e.g., [398, 481].

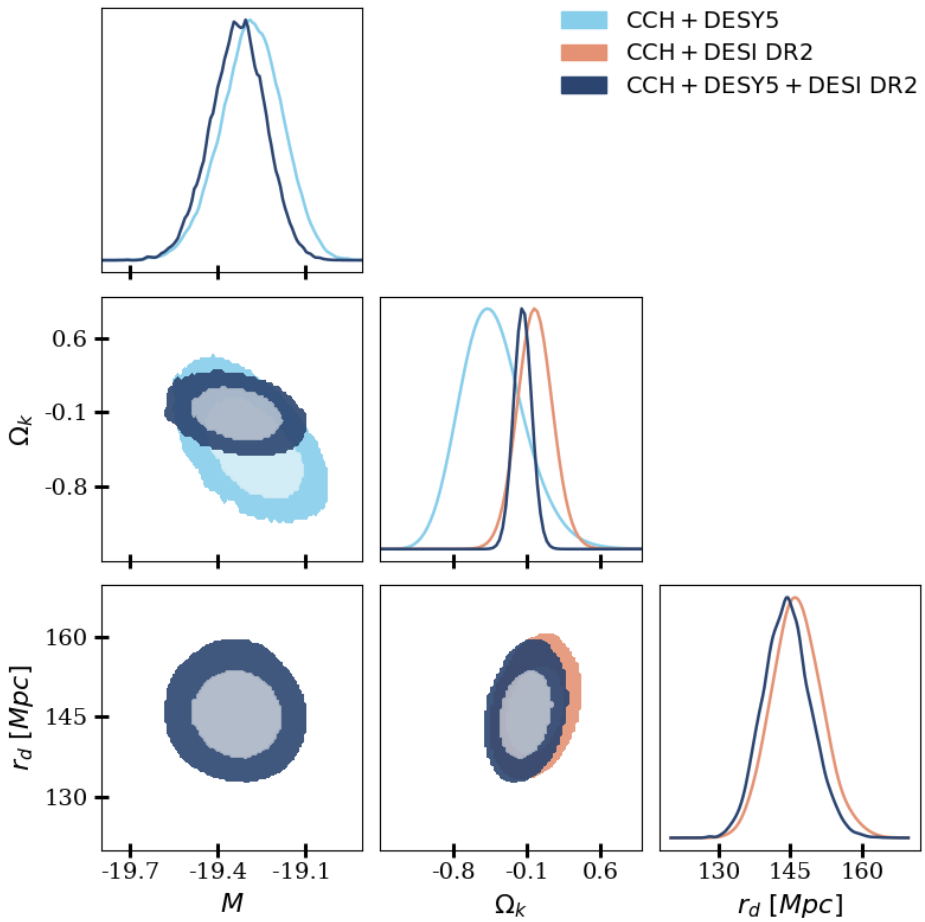

Figure 6.10. Two-dimensional contour plots in all the planes of the parameter space (M, Ω_k, r_d) and the corresponding one-dimensional posterior probability distributions obtained from the analyses described in Sec. 6.3.2. The 2D contours are evaluated at 68% and 95% C.L.

the 1σ uncertainty on the parameter, being generally $\lesssim 0.1\sigma$ and at most 0.3σ for M. For the 3D analysis, they read, $\tilde{b} = (+0.029, -0.007, -0.57 \text{ Mpc})$ for M, Ω_k and r_d, respectively. In Sec. 6.3.3, we show that this bias is reduced as data quality improves, as expected, providing further evidence that it stems from the GP reconstruction itself.

The results presented here and in the previous Section exhibit several noteworthy features. They are independent of both the direct and inverse distance ladders, largely model-independent, and remain robust under the choice of alternative GP kernels. This is interesting *per se*. However, they cannot arbitrate the H_0 tension yet. Current observations still limit the precision on these quantities and the conclusions that can be drawn from them. The low-redshift data sets under consideration give still room to new physics both in the pre- and post-recombination eras. For instance, the uncertainties that we have found are still one order of magnitude larger compared to the determinations by *Planck* under the assumption of ΛCDM [11]. Future data

will not only decrease the uncertainties of the curvature parameter through the model-independent analyses of standard candles and large-scale structure data [488, 489], but also improve the constraints we get for the calibrators M and r_d, which is obviously important for the discussion of the H_0 tension. As shown in Fig. 6.9, in the light of the current low-redshift data our method does not let us arbitrate the tension yet, but we might be able to do so with the advent of upcoming telescopes and surveys. We have seen in Sec. 6.3.1 that a decrease by a factor 3/2 of the uncertainties of the CCH data produces a $30\% - 40\%$ decrease of the uncertainties of the calibrators. Thus, an improvement in the CCH data, either in terms of quality or quantity, can also have a non-negligible impact on the outcome of this method. For all these reasons, we find it instructive and timely to explore the constraining power of our methodology with future SNIa, CCH, and BAO observations. This will be addressed over the next Section.

6.3.3 Forecasts

We start by detailing the mock data sets that we build to perform forecasts for future surveys. For all observables of our interest - namely $H(z)$, $m(z)$ and the BAO distances - we adopt as fiducial data vector the corresponding ΛCDM prediction based on the *Planck* TT,TE,EE+lowE+lensing best-fit parameters from [11], and $M = -19.4$.

- **CCH**: We generate data on $H(z)$ following the recipes for the error budget and the redshift range provided in [405, 404]. Specifically, the redshift range is adopted from [404], which selects 20 points at low-redshifts ($z < 1.5$) that will be provided by future surveys, such as the WST [407] or ATLAS [408]), along with 5 high-redshift points ($1.5 < z < 2$), from the Euclid mission, for a total of 25 data points[12]. A statistical uncertainty of 5% is assumed for measurements of $H(z)$ throughout the redshift range, as expected for WST over $z < 1.5$ [407], and for Euclid. The ESA mission is likely to provide up to a few thousand passively evolving galaxies at $1.5 < z < 2$, increasing the current statistical sample by two orders of magnitude [490]. This would enable measurements of the Hubble function to improve upon the current precision, which ranges between 10% and 25% [478].

  We base our treatment of systematic uncertainties that will enter Eq. (4.3) on the recipes provided in [405].

  When massive and passively evolving galaxies are employed as CCH candidates, their intrinsic physical properties introduce diagonal errors, given that these uncertainties are uncorrelated between galaxies at different redshifts. This is the case of, e.g. possible contamination by younger stars which causes the measurement of younger ages, and stellar metallicity, currently resulting in a $< 0.5\%$ and 4% level error on $H(z)$, respectively. However, this is bound to be

[12]To be consistent across all the forecasts presented for SNIa, BAO and CCH data, we choose not to combine current and future CCH data in this work. For cosmological constraints derived from such a combination, we refer the reader to [405, 404]. For instance, in [405], it has been shown that fitting an open wCDM model with future low-z CCH already reduces the H_0 uncertainty to $\approx 4.4\%$, and the combination with current data only marginally improves it, to $\approx 4\%$.

kept under control with high spectral resolution and high-S/N data [392], as those considered in this forecast. For this reason, we regard them as negligible. The same applies to contributions from progenitor bias and mass dependence, which are already considered negligible and therefore not accounted for here. We follow the prescriptions used in [405] and [404], in which the systematic contributions include the impact of the initial mass function (IMF) and SPS models (we call this *pessimistic scenario*). The uncertainty in $H(z)$ due to the IMF is estimated at 0.4%. The effect of considering different SPS models impacts the $H(z)$ measurement with a 9% error on average, with a decreasing trend with increasing redshift in $0 < z < 1.5$. This different trend is related to the behaviour of the slopes of the D4000n-age relations for the different models [392]. By excluding the most discrepant SPS model, the corresponding contribution can be reduced to $\sim 4.5\%$. Nevertheless, the choice of SPS model remains the dominant source of uncertainty in the total error budget, and these errors are highly correlated across different spectra.

As suggested in [405] and [404], we also study an *optimistic scenario* which minimizes the impact of the SPS models. In this case, the associated systematic uncertainty is assumed to be resolved, thanks to advancements in future spectroscopic analyses and observations that are expected to aid in identifying and narrowing down the set of SPS models that best reproduce the data. As a result, the IMF-related uncertainty is the only systematic contribution considered in this scenario.

The covariance matrix in Eq. (4.3) will be

$$C_{\mathrm{CCH}^*,\mathrm{ij}} = C_{ij}^{stat} + C_{ij}^{sys} = C_{ij}^{stat} + C_{ij}^{IMF} + C_{ij}^{SPS}\,, \tag{6.14}$$

where, following the previous discussion, the presence of the last term depends on the scenario considered. Notice that, hereafter, we will call this mock data set **CCH***.

- **SNIa**: LSST will play a pivotal role not only in advancing astrophysical research, but also in driving significant progress in cosmological analyses. Already with an early data release corresponding to roughly half of its final mission target, LSST is expected to be able to constrain a constant dark energy equation of state w at the sub-5% level and to obtain a precision of 0.05 on w_0 for a time-varying w_0w_aCDM equation of state [415]. The survey is projected to increase the SNIa sample size by up to a factor of 100 compared to previous samples [416], with redshifts up to $z \sim 1.2$. It will use a single instrument, which may help mitigate calibration issues present in samples built from different telescopes. A good-enough photometry will enable sufficiently well-sampled and accurate light curves and host galaxy redshifts, whose distribution mean will be around z ~ 0.4 [417].

  According to this framework, we proceed with the SNIa forecast as outlined below. The redshift distribution of the final LSST sample is assumed to be comparable to DESY5 [416]; however, the LSST sample size will be substantially larger. To account for this, we treat the DESY5 data set as a binned proxy

for the final-year LSST data. We rescale the statistical component of the DESY5 covariance matrix by a factor $n = N_{\rm DES}/N_{\rm LSST}$, with $N_{\rm DES} = 1829$ and $N_{\rm LSST} = 10^5$. This number corresponds to the predicted 10-year final sample size (hereafter **LSST-Y10**), which results in a rescaled statistical error $\sigma^{stat}_{\rm LSST-Y10} \approx \sigma^{stat}_{\rm DES}/7$. The increase in sample size N affects only the statistical component of the total uncertainty, which scales as $1/\sqrt{N}$. Reducing the statistical uncertainty enhances the relative contribution of systematics to the overall error budget (see [491]). For the systematic component of the covariance matrix, we keep the estimate from DESY5. This is a conservative choice, as control of systematic uncertainties may improve with the LSST sample. For this reason, we opt to present two distinct scenarios. The one previously discussed will be our conservative approach, and is referred to as the *pessimistic scenario*. In contrast, we also consider an *optimistic scenario*, in which all systematic uncertainties are assumed to be negligible[13].

- **BAO**: as outlined in Sec. 4.3, the DESI collaboration reported BAO forecasts that represent the expected final target of the mission [269]. They account for a predicted full footprint of 14,000 deg2 for each tracer. This area is used for cosmological forecasts, which set DESI as a Stage-IV dark energy experiment. In particular, we employ the predicted D_A/r_d and $H(z)r_d$ measurements provided in Table 7 of [269], for a total of 42 points between $0.05 \leq z \leq 2.05$. Predicted redshifts and the corresponding covariance matrix that we use are available as supplementary materials at [14]. We denote this data set as **DESI***.

We follow the same methodology outlined in Sec. 6.3. However, an additional step is introduced specifically for the forecast analysis. Indeed, given the improved accuracy of the samples considered in this study, we expect that the grid resolution and the number of N realisations needed to obtain well-sampled posteriors for the parameters of interest increase significantly. The effect is even more pronounced when considering the *mixed* cases, which are aimed at illustrating the influence of improvement in a single data set. For instance, the analysis with LSST-Y10+CCH reveals a large difference between the current CCH error bars and the improved statistics achieved by the future SNIa sample. Current CCH measurements exhibit relative uncertainties of 7–60% across the probed redshift range, in contrast to the projected precision of 0.1–0.3% attainable with LSST-Y10. This difference translates into a high computational cost to achieve convergence. For this reason, we opt to fit the mildly noisy posteriors to obtain smoother curves. Thus, accurate constraints on the parameters of interest can still be extracted while preserving the overall shape and width of the original sampled distributions. We refer the reader to Appendix B for details on the approach followed.

For the forecast analysis, we consider different combinations of current and future data sets — e.g., current CCH with future SNIa — to isolate the contribution of each probe to the overall constraints. This approach allows us to quantify how

[13] As we will see, the impact of the DESY5 correlations is derisory when SNIa are combined with CCH in forecast analyses. For this reason, we choose not to analyze an intermediate case for the treatment of systematics in the LSST covariance matrix, as the results would remain unchanged.

[14] `https://doi.org/10.5281/zenodo.10063934`

Table 6.5. Errors at 68% C.L. on the ladder calibrators, M and r_d (in Mpc), on the curvature parameter Ω_k entering Eq. (1.78), and on H_0 (in km/s/Mpc) from the joint analyses presented in Sec. 6.3.3 considering the *pessimistic* scenario for future data on CCH and SNIa. In the last two columns, we report the cosmographical constraints on H_0 and q_0, cf. Eq. (6.13). For each parameter, in the parenthesis we also report the standard deviation (σ) of the corresponding one-dimensional probability posterior.

	M	Ω_k	r_d	H_0	q_0
CCH+**LSST-Y10**	$^{+0.106}_{-0.112}$ (0.110)	$^{+0.254}_{-0.219}$ (0.241)	-	-	-
CCH*+DESY5	$^{+0.087}_{-0.090}$ (0.089)	$^{+0.242}_{-0.222}$ (0.235)	-	-	-
CCH*+DESI DR1	-	±0.150 (0.150)	$^{+5.08}_{-4.78}$ (4.98)	-	-
CCH*+DESI DR2	-	±0.080 (0.082)	$^{+4.68}_{-4.38}$ (4.56)	-	-
CCH+**DESI***	-	±0.047 (0.047)	$^{+5.37}_{-4.95}$ (5.18)	-	-
CCH***+LSST-Y10**	$^{+0.082}_{-0.088}$ (0.086)	$^{+0.130}_{-0.121}$ (0.127)	-	-	-
CCH***+DESI***	-	±0.047 (0.047)	$^{+3.56}_{-3.49}$ (3.57)	-	-
CCH***+LSST-Y10+DESI***	$^{+0.087}_{-0.082}$(0.085)	$^{+0.045}_{-0.043}$ (0.044)	$^{+3.56}_{-3.49}$ (3.57)	$^{+2.54}_{-2.82}$ (2.70)	0.06

Table 6.6. Same as in Table 6.5 but considering the *optimistic* scenario. Notice that the row corresponding to the CCH+DESI* analysis is the same as the previous table, as no distinction between scenarios is adopted for DESI data.

	M	Ω_k	r_d	H_0	q_0
CCH+**LSST-Y10**	$^{+0.095}_{-0.111}$ (0.105)	$^{+0.246}_{-0.203}$ (0.231)	-	-	
CCH*+DESY5	0.056 (0.057)	$^{+0.246}_{-0.226}$ (0.239)	-	-	-
CCH*+DESI DR1	-	$^{+0.145}_{-0.150}$ (0.149)	$^{+2.29}_{-2.39}$ (2.25)	-	-
CCH*+DESI DR2	-	±0.08 (0.082)	$^{+1.89}_{-1.99}$ (1.97)	-	-
CCH+**DESI***	-	±0.047 (0.047)	$^{+5.37}_{-4.95}$ (5.18)	-	-
CCH***+LSST-Y10**	$^{+0.046}_{-0.050}$ (0.049)	$^{+0.132}_{-0.118}$ (0.127)	-	-	-
CCH***+DESI***	-	$^{+0.047}_{-0.045}$ (0.046)	$^{+1.75}_{-1.70}$ (1.73)	-	-
CCH***+LSST-Y10+DESI***	$^{+0.045}_{-0.040}$ (0.043)	$^{+0.043}_{-0.045}$ (0.044)	$^{+1.75}_{-1.70}$ (1.73)	$^{+1.37}_{-1.34}$ (1.35)	0.04

improvements in CCH, SNIa, or BAO individually affect the determination of M, Ω_k, r_d, and H_0, including the role of redshift coverage in each sample. We also investigate the impact of data quality by considering pessimistic and optimistic scenarios for future CCH and SNIa samples, enabling the forecasts to highlight which improvements in the low- or high-redshift regimes are most influential.

We decide to present the forecast results in two separate tables, according to the pessimistic and optimistic scenarios for CCH and SNIa data. Our results are displayed in Tables 6.5 and 6.6, respectively, where we report the upper and lower uncertainties at 68% C.L. on M, Ω_k, r_d and H_0, together with the corresponding standard deviation, σ. A summary of the forecasted constraints obtained with the 2D analyses is provided in Fig. 6.11.

The following comments are in order.

- *Constraints on M*: the CCH+LSST-Y10 analysis shows no improvement in the estimation of M compared to the CCH+DESY5 analysis, under both pessimistic and optimistic scenarios, since all of them lead to $\sigma_M \approx 0.11$. However, this conclusion changes once current CCH data are replaced with the mock data set representing future measurements. In the pessimistic set-up, we obtain $\sigma_M = 0.089$ with CCH*+DESY5 and $\sigma_M = 0.086$ with the full forecast

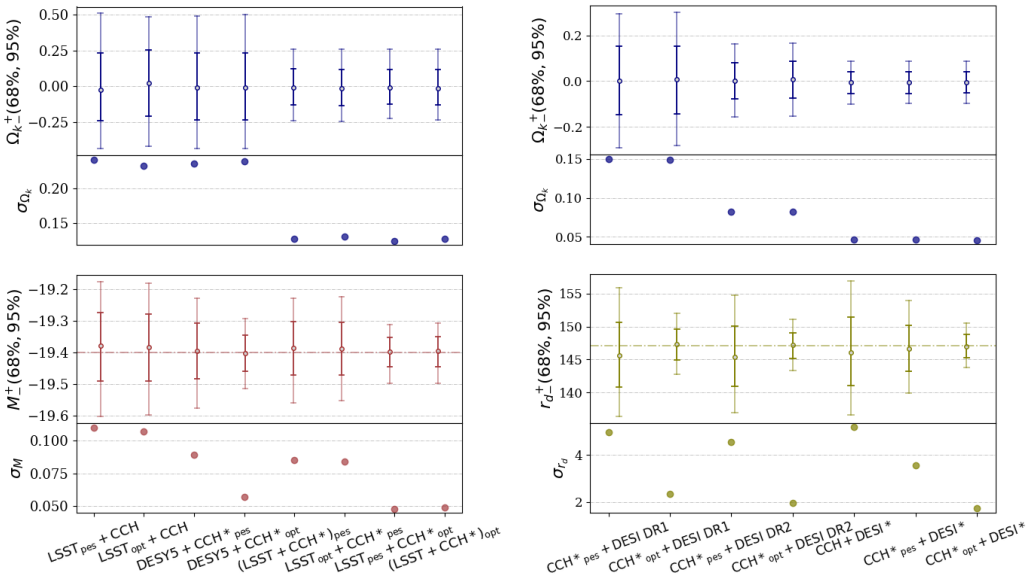

Figure 6.11. *Left panels:* Error bars at 68% and 95% C.L. on the parameters Ω_k and M obtained from the 2D joint analysis presented in Sec. 6.3.3 with different combinations of CCH and SNIa data and under different scenarios (optimistic and/or pessimistic). Central values for each parameter are consistent with the ΛCDM prediction used to build the mock data, $\Omega_k = 0$ and $M = -19.4$ (the latter indicated by the dot-dashed line in the bottom plot). Tiny fluctuations are due to the bias given by the GP reconstruction of the Hubble function (see Sec. 6.3.2). *Right panels:* Same, but for the parameters Ω_k and r_d obtained from the 2D joint analysis with different combinations of CCH and BAO. In the bottom plot, the dot-dashed line represents the value of the sound horizon assumed to generate the mock data, $r_d = 147.09$ Mpc. Lower subplots show the standard deviation, σ_X, of the corresponding one-dimensional marginalized posterior.

CCH*+LSSTY-10. When considering the optimistic scenario, these results change to $\sigma_M = 0.057$ and $\sigma_M = 0.049$, respectively. As already noticed in Sec. 6.3.2, within this approach, one can observe a substantial improvement in M only with a decrease of the CCH error bars. This is why CCH* has such a big impact on the results. Remarkably, the full 3D joint analysis with CCH*+LSST-Y10+DESI* leads to $\sigma_M = 0.043$ in the optimistic scenario, improving by 54% on the result obtained with CCH+DESY5+DESI DR2 (see Fig. 6.12).

- *Constraints on Ω_k:* the curvature parameter is the only parameter constrained by the two 2D analyses, since the luminosity and angular diameter distances entering the SNIa and BAO observables are sensitive to it. The increased statistics of LSST SNIa impact the constraint on Ω_k from the CCH+LSST-Y10 analysis, leading to a decrease of ∼20% of the uncertainty compared to CCH+DESY5 ($\sigma_{\Omega_k} \approx 0.30$), in both pessimistic and optimistic scenarios, for which $\sigma_{\Omega_k} = 0.241$ and $\sigma_{\Omega_k} = 0.231$, respectively. However, when CCH* are used, the improvement increases up to 58% ($\sigma_{\Omega_k} = 0.127$), meaning that a better treatment of the systematics affecting the CCH method will help tighten

constraints on the curvature parameter. Furthermore, extended cosmic-clock galaxies observations up to $z \sim 2.1$ will nearly double the data volume between $1.5 < z < 2.1$, thereby enhancing the constraining power in the regime where Ω_k is most sensitive. The role of CCH data is bypassed once we include in the analysis DESI data on anisotropic BAO (as already seen in Sec. 6.3.2), whose future measurements will be able to constrain Ω_k with $\sigma_{\Omega_k} = 0.046$. The inclusion of SNIa slightly decreases this uncertainty to $\sigma_{\Omega_k} = 0.044$, improving by a factor $\sim 50\%$ on current constraints (see Fig. 6.12). The performance of future data to model-independently constrain the curvature parameter has been recently studied in, e.g., [492, 493, 494, 495]. For instance, our results are fully compatible with [493], where authors obtained a precision of $\mathcal{O}(10^{-2})$ using time-delay distance from strong gravitational lenses, distance modulus measurements from LSST-like SNIa and $H(z)$ from future DESI BAO. With a different forecast analysis with DESI and Euclid data, [494] constrained the spatial curvature with $\sigma_{\Omega_k} = 0.057$, by studying the deviations from statistical isotropy due to the Alcock-Paczyński effect of large-scale galaxy clustering. It will be difficult to constrain Ω_k better than few percent level with future data applying model-independent techniques.

- *Constraints on r_d:* the sound horizon r_d shows the most significant difference between pessimistic and optimistic scenarios concerning the CCH data. Its uncertainty ranges from $\sigma_{r_d} = 4.98$ (4.56) Mpc to $\sigma_{r_d} = 2.25$ (1.97) Mpc when considering CCH*+DESI DR1 (DR2). This is essentially due to the fact that, on average, CCH uncertainties will decrease by a factor $\sim 70 - 80\%$ up to $z \sim 2$, considering the systematics due to SPS models resolved. r_d is the parameter that shows the greatest improvement compared to constraints obtained with current data (see Fig. 6.12). Within CCH*+LSST-Y10+DESI* in the optimistic case, we are able to constrain r_d with $\sigma_{r_d} = 1.73$ Mpc. This result is $\sim$80% less precise than current model-dependent constraints. Indeed, in the context of standard pre-recombination physics, $r_d = (147.09 \pm 0.26)$ Mpc [11]. Thus, our forecast corresponds to a 1.2% precision on the fiducial sound horizon. This result improves upon previous model-independent forecasts, which, however, have been obtained using different combinations of data sets and methodology. In, e.g., [496], a 1.5% precision on r_d is expected with future LISA [497] gravitational waves data as standard sirens and DESI or Euclid angular BAO measurements.

- *Constraints on H_0:* once obtained our model-independent constraint on M, we can break the degeneracy between the latter and H_0 to obtain an estimate of the Hubble parameter using the local distance ladder. By virtue of Eq. (6.13), and using the LSST SNIa in the Hubble flow, we obtain $\sigma_{H_0} = 2.7$ km/s/Mpc and $\sigma_{H_0} = 1.35$ km/s/Mpc for the pessimistic and optimistic scenario, respectively, and the following uncertainities on the deceleration parameter, $\sigma_{q_0} = 0.06$ and $\sigma_{q_0} = 0.04$. Considering having SNIa and CCH systematics well-understood and under control in the next decade, this means constraining H_0 at 2% level without relying on any cosmological model. A very similar result is obtained in forecast analyses performed in [492], although

with a different methodology and combination of probes, which includes, for instance, the use of standard sirens. Future CCH alone will obtain the same level of precision, but in the context of a concrete cosmological model [404]. As for the deceleration parameter, the improvement factor over the typical error obtained with DESY5 in the cosmographical fit, $\sigma_{q_0} \approx 0.32$ (cf. Table 6.4), is ~ 8, essentially driven by the substantial increase in the number of SNIa in the Hubble flow.

For completeness, we also performed all the possible combinations of scenarios between the data set considered, e.g. LSST-Y10$_{\rm opt}$+CCH$^*_{\rm pes}$. Since the conclusions that can be drawn from these intermediate analyses only reinforce those discussed above, we just refer the reader to the results displayed in Fig. 6.11. Essentially, the replacement of LSST-Y10$_{\rm pes}$ with LSST-Y10$_{\rm opt}$ only leads to a very marginal decrease of the uncertainty, which is almost unnoticeable, while the replacement of CCH$^*_{\rm pes}$ with CCH$^*_{\rm opt}$ induce a significant improvement in the constraining power. From these figures, we also observe that the GP reconstruction bias decreases as data precision increases. For a given CCH sample, the offset remains nearly constant across scenarios, further indicating that this systematic shift is an intrinsic methodological feature inherent to the GP approach. We conclude that improving the data quality reduces the magnitude of $|\tilde{b}|$, which tends to vanish in the limit of nearly noise-free data, consistent with the definition of the GP posterior mean. In the optimistic scenario, the offsets observed are typically $\lesssim 0.1\sigma$ in absolute value in all cases. It is worth emphasizing that our framework enables the simultaneous estimation of both statistical uncertainties and the typical level of methodological bias associated with the adopted reconstruction technique.

As a final remark, we expect that all the results presented in this section would benefit from the combination of current and future measurements (see, e.g. [404] concerning CCH data), something that we avoid exploring in this work as it would require a treatment of correlations between samples. Additionally, beyond LSST, the Roman Space Telescope [414] may offer a valuable opportunity to reassess the results of this work, since it will be able to detect SNIa up to $z \sim 3$, which may significantly improve the estimation of Ω_k, in particular.

6.4 Final discussion

In this Chapter, we have first reconstructed the absolute magnitude of SNIa and the curvature of the Universe as a function of the redshift up to $z \approx 2$ making use of Gaussian Processes and data on CCH and the Pantheon+ compilation of SNIa. We have found that these low-redshift data sets do not point to a time evolution of the SNIa intrinsic luminosity nor a breaking of the homogeneity of the universe at large scales. Both, $M(z)$ and $\Omega_k(z)$ are compatible at 68% C.L. with a constant. In addition, we have also tested the consistency of the BAO data from the galaxy surveys 6dFGS, BOSS, eBOSS, WiggleZ and DES Y3, by checking that they are all compatible with a common value of r_d, at least under the precision offered by the CCH data (Sec. 6.2). Motivated by these results, we have then constrained with CCH, SNIa and BAO the constant values of Ω_k and the calibrators of the direct and inverse distance ladders, M and r_d. We have done so by applying a quite

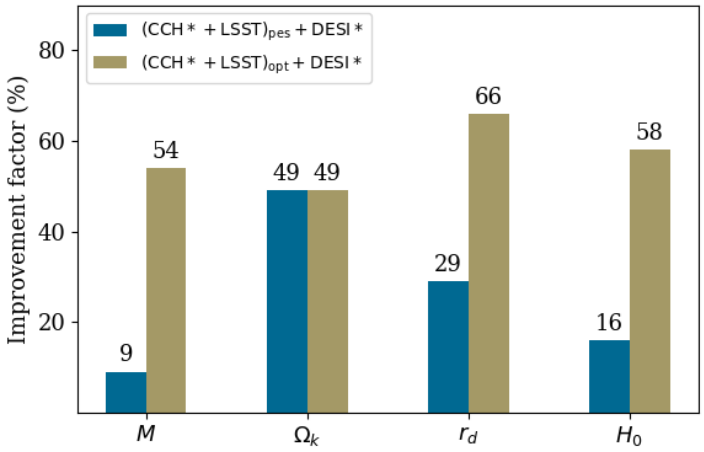

Figure 6.12. Percentage improvement factor on the parameters studied in this work (x-axis) achieved by future surveys in the pessimistic and optimistic scenarios for CCH*+LSST-Y10+DESI* analyses. This is computed over the results obtained with the most recent available data, CCH+DESY5+DESI DR2.

model-independent method (see Sec. 6.3), which is also independent from the first rungs of the cosmic distance ladder employed by SH0ES and the CMB data, i.e. from the main data sets involved in the Hubble tension. Within CCH, Pantheon+ SNIa and anisotropic BAO, we obtain: $\Omega_k = -0.07^{+0.12}_{-0.15}$, $M = (-19.314^{+0.086}_{-0.108})$ mag and $r_d = (142.3 \pm 5.3)$ Mpc. We have checked that the inclusion of the SNIa in the host galaxies and their distances only affects the value of M, making its central value and uncertainties to be very close to those measured by SH0ES. Our results improve previous constraints in the literature obtained also with Gaussian Processes but with slightly different data sets and methodologies. For instance, [477] obtained $M = (-19.42 \pm 0.35)$ mag from data on BAO and SNIa together with a *Planck* prior for r_d. We, instead, have measured M with an uncertainty three times smaller. In addition, we have extracted joint and model-independent constraints for Ω_k and r_d as well, with a more refined BAO data set, which is free from double-counting issues and incorporates the effect of correlations. Our determination of Ω_k is 50% more precise than the one carried out by [471], $\Omega_k = -0.03 \pm 0.26$, thanks mainly to the use of BAO data on top of the CCH and the Pantheon+ compilation of SNIa. The same level of improvement is also obtained compared to the cosmographical analysis of SNIa and strong lensing data by [498], who reported $\Omega_k = 0.12^{+0.27}_{-0.25}$. Our work also improves the analysis of [241], since here we have not used any external prior for the curvature parameter and have employed the SNIa contained in the Pantheon+ compilation, instead of those of Pantheon.

We have then performed a follow-up analysis by incorporating the most recent data on SNIa and BAO as provided by the DES and DESI collaborations (Sec. 6.3.2). Under the umbrella of CCH, SNIa from DESY5 and BAO from DESI DR1, we obtain $M = -19.330^{+0.095}_{-0.099}$, $\Omega_k = -0.113^{+0.150}_{-0.155}$ and $r_d = 145.30^{+5.28}_{-5.08}$ Mpc. Using the most recent and more precise DESI DR2 data, we have been able to place

tighter constraints on these quantities, $M = -19.324^{+0.092}_{-0.095}$, $\Omega_k = -0.143 \pm 0.085$ and $r_d = 144.00^{+5.08}_{-4.88}$ Mpc, which improve those provided previously (Sec. 6.3.1). The CCH+DESY5+DESI DR2 constraint on M and the DESY5 SNIa in the Hubble flow prefer a value closer to the *Planck*-inferred value, being $H_0 = (68.83^{+3.03}_{-3.07})$ km/s/Mpc. Remarkably, substituting M with the SH0ES value (M^{R22}), we obtain $H_0 = (70.84 \pm 1.16)$ km/s/Mpc, reducing the tension with CMB estimates below 3σ. This may have implications for the discussion about possible systematics in low-z SNIa that could bias the local estimate of H_0. We have also studied the case in which DESY5 SNIa are replaced with Pantheon+, i.e. CCH+PAN+DESI DR2. This slightly decreases the uncertainties on M, Ω_k and r_d by 6%, 5% and 1%, respectively, while the corresponding cosmographic estimate of H_0 reads $H_0 = (72.12^{+2.97}_{-2.95})$ km/s/Mpc. However, current observations still limit the precision on these quantities and the conclusions that can be drawn from them. Another example is the result obtained for Ω_k, which points towards a positive curvature. However, with the full combination of data, our constraint is still compatible with the flatness assumption at 1.7σ when using DES SNIa and at 1.2σ when the latter is replaced with Pantheon+.

The robustness of these constraints has been assessed by running the analysis pipeline on mock data that incorporates current observational uncertainties. This allowed us to validate the entire pipeline and test the methodological assumptions. In particular, we quantified the impact of a systematic methodological bias inherent to the GP technique on the inferred parameters, finding the largest offset on M ($\sim 0.3\sigma$), and smaller biases on the remaining parameters ($\lesssim 0.1\sigma$).

Finally, we have extended our analysis with forecasts on future data (Sec. 6.3.3), which will be provided by LSST, Euclid, WST, ATLAS and the final-year DESI observations. Our main results highlight that, in a pessimistic scenario, the combination CCH*+LSST-Y10+DESI* will constrain the SNIa absolute magnitude and the sound horizon with $\sigma_M = 0.085$ and $\sigma_{r_d} = 3.57$ Mpc, respectively. This is mainly driven by the conservative treatment of systematics in the cosmic chronometers method, since CCH act as our calibrator of the ladders. On the curvature parameter, we obtain an error of $\sigma_{\Omega_k} = 0.044$. The optimistic scenario leads instead to $\sigma_M = 0.043$, $\sigma_{r_d} = 1.73$ Mpc and $\sigma_{\Omega_k} = 0.044$. This translates into an improvement by a factor of 54%, 66% and 49%, respectively, on current constraints obtained with the most recent data (CCH+DESY5+DESI DR2). Thus, up to $z \approx 2$, we forecast that the relative precision on the SNIa absolute magnitude will be $\sigma_M/M \sim 0.2\%$, which allows for constraining the Hubble parameter at a 2% level, being $\sigma_{H_0} = 1.35$ km/s/Mpc. The relative precision on the sound horizon, $\sigma_{r_d}/r_d \sim 1.2\%$, will instead be valuable for assessing early-time solutions to the Hubble tension, as those which require new physics prior to recombination that would reduce the value of r_d. The presented results are robust against the intrinsic methodological bias, which remains below 0.1σ for all parameters thanks to the increased precision of future data. In conclusion, this first forecast analysis on the presented methodology, though not yet as precise as model-dependent analyses, is already nearly competitive with current constraints derived from those methods, thereby paving the way for model-independent constraints expected in the coming decade. It provides valuable insight into where improvements are most needed - such as redshift coverage, data volume and assessment of systematics. As already highlighted, future missions beyond those used in this work could prove essential

for a thorough re-evaluation of our findings. This could be the case of the Roman Space Telescope, which is expected to considerably extend the detection of SNIa up to $z \sim 3$. This broader redshift coverage will allow for a more robust anchoring of the Hubble diagram and improved sensitivity to cosmic curvature, enabling tighter tests of the distance ladder and potential deviations from ΛCDM. In this sense, the methodology explored in this work offers a timely and flexible tool to interpret and cross-check future high-precision cosmological data.

Part IV

Extending the distance ladder beyond $z \sim 2.5$

Chapter 7

GRBs calibration

The content of this Chapter is based on our work published in [499].

The cosmic distance ladder finds its main characters in BAO and SNIa. These observables have been extensively investigated in Chapter 6, where their key properties — enabling their use as standard rulers and candles — have been calibrated within a model-independent framework. However, current data on BAO and SNIa cover up to $z \sim 2.5$. As mentioned in Sec. 2.1.1, other standardizable candles can be employed to extend the investigation to higher redshifts. Among them, Gamma-Ray Bursts stand out as one of the most promising observables as they are extremely energetic and can be used to probe the universe up to $z \sim 9.4$. However, the use of GRB correlations is still a challenge due to the spread in their intrinsic properties.

Based on the idea of the low-redshift calibration of the distance ladders that we proposed and applied in Chapter 6, here, we present an innovative method to understand whether low-redshift calibrators can univocally determine the correlation parameters of GRBs, enabling their use as distance indicators. In particular, we can leverage again CCH data at $z \lesssim 2$ and the Gaussian Processes Bayesian reconstruction tool, for a specific data set of GRBs, the *Platinum sample*, which consists of well-defined GRB plateau properties that obey the fundamental plane relation[1]. Both, the relations and the data sample, have been detailed in Sec. 4.5.

The methodology we propose is presented in this Chapter as follows:

- In Sec. 7.1, we apply the calibration of both the 2D and 3D Dainotti relations. To ensure the generality of our method, we verify that the choice of priors on the parameters of the Dainotti relation and the modeling of CCH uncertainties and covariance have a negligible impact on our results.

[1]Recently, the 2D Dainotti relation has been calibrated with GP and OHD by [453] and [454], whose approach has been extended by [455] also for the 3D relation. However, these authors adopt different data sets than those considered in this work. [455], in particular, use a combination of 31 $H(z)$ measurements from CCH (without taking into account their correlations) and 5 from BAO data, after calibrating the latter assuming standard pre-recombination physics. We do not use data on $H(z)$ from BAO to avoid model-dependent assumptions in the calibration process. Moreover, the GRBs they analyze are collected according to a different sample selection (radio plateau phases instead of X-ray plateau phases) and in a different redshift range.

- In Sec. 7.2, we correct the 3D relation for redshift evolution effects and see how this affects the calibration process.
- In Sec. 7.3, we use this result to extend the cosmic distance ladder, presenting a new catalogue of calibrated luminosity distances up to $z = 5$.
- Final discussion and conclusions are presented in Sec. 7.4.

7.1 Calibrating the 3D and 2D Dainotti relations

In Eqs. (4.18) and (4.19), it is immediately noticeable that both $L_{\rm X}$ and $L_{\rm peak}$ depend on the background cosmology since the luminosity distance D_L requires the knowledge of the functional form of the Hubble expansion rate. Therefore, we can leverage GP to reconstruct the shape of $H(z)$ and obtain agnostic estimates of the luminosity distance at the redshifts of the GRB data, $z_{\rm GRB}$. To match the CCH redshift range, we select 20 long GRBs in the range $0.553 \leq z \leq 1.96$ (see Fig. 4.3 and Table A.5). In order to check whether this sub-sample is representative of the full Platinum sample, we perform a Kolmogorov-Smirnov (KS) test [500, 501] for all the variables of the Platinum sample used in this work, i.e. $\log T_X^\star$, $F_{\rm peak}$, $K_{\rm prompt}$, $\log F_X$ and $K_{\rm plateau}$. We also cross-check the results with the Anderson-Darling (AD) test [502]. These statistical analyses allow us to estimate the significance level for rejecting or not rejecting the null hypothesis that the two samples come from the same parent distribution. The results of both tests show that we cannot reject the null hypothesis at 95% C.L., as we find a p value greater than 0.05 in all the tested variables. This supports the choice of the GRBs sub-set used in the calibration analysis and this does not introduce any bias in this choice as no statistical difference in the sample is shown.

As for the GP training with CCH, supported by previous findings in Chapter 6, we adopt the same strategy here[2]. That is, we use the M32 kernel and obtain the full distribution of its hyperparameters, as explained in Sec. 6.1. This is something that has not been done in previous works that employ the GP technique to calibrate GRB correlations (either with SNIa or CCH), and this is certainly important to properly compute the uncertainty of the reconstructed function. This also applies to the use of the CCH covariance matrix. Neglecting the CCH correlations in the GP reconstruction has a modest impact on the final shape of $H(z)$, as we have explicitly checked. The relative difference in units of σ between the correlated and uncorrelated CCH reconstructions is at most 15%, dropping at 1% in the data-poor region, for $z \gtrsim 1$ (with σ being the largest uncertainties of the two reconstructions, i.e. the CCH-correlated one). We reconstruct the Hubble function within the CCH data redshift range, i.e. $z \leq 1.96$. The resulting shape of $H(z)$ is shown in Fig. 7.1, together with the corresponding result for $D_L(z)$, obtained by using the GP-shapes of $H(z)$ and Eq. (1.78)[3].

[2]Since we are reconstructing the same function ($H(z)$) with the same data (CCH), we are legitimate to do so because the GP likelihood does not depend on the points at which the reconstruction is performed.

[3]We ensure that the number of points in which we evaluate the integral in Eq. (1.80) is enough to have an accurate determination of the reconstructed function. This test is especially important

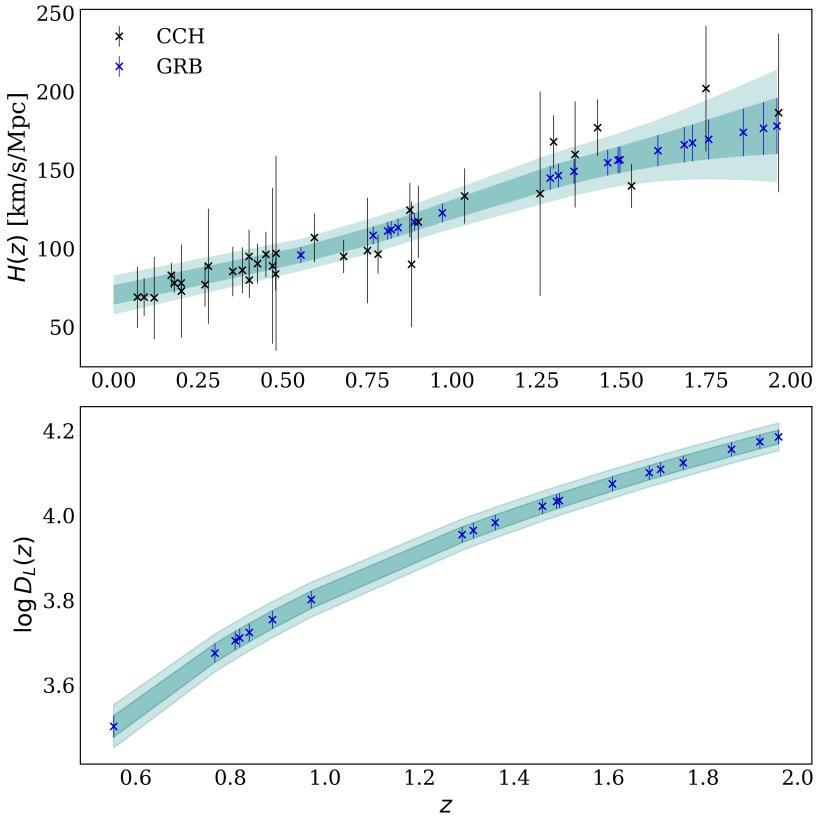

Figure 7.1. *Top panel:* Reconstruction at 2σ C.L. of $H(z)$ with GP. We show the CCH data (in black) and the individual values of $H(z)$ at the various GRB redshifts (in blue), both at 1σ C.L. *Bottom panel:* The corresponding shape of $\log D_L(z)$. The argument of the log is made dimensionless by dividing the luminosity distance by 1 Mpc.

By combining Eqs. (4.17) and (4.19), one can easily obtain the following quantity

$$\log D_L^{\rm th} = a_1 \log T_{\rm X}^* + b_1(\log F_{\rm peak} + \log K_{\rm prompt}) + c_1 + d_1(\log F_{\rm X} + \log K_{\rm plateau})\,, \quad (7.1)$$

which we denote as the theoretical value for the log-luminosity distance, with $D_L^{\rm th}$ written in units of cm. Here, $a_1 = a/2(1-b)$, $b_1 = b/2(1-b)$, $c_1 = ((b-1)\log(4\pi) + C_o)/(2(1-b))$ and $d_1 = -(1-b)/2$.

On the other hand, the GP+CCH result can be used to compute the logarithm of the luminosity distances assuming a flat Universe. This quantity will be our observed value, $\log D_L^{\rm obs}(z)$. We have checked that its distribution is Gaussian in very good approximation. The corresponding covariance matrix can be obtained as follows,

$$C_{\rm obs,ij} = \frac{1}{N_{\rm real}} \sum_{\mu=1}^{N_{\rm real}} (x_{\mu,i} - \bar{x}_i)(x_{\mu,j} - \bar{x}_j)\,, \quad (7.2)$$

in the region of redshifts below the GRB data point with the lowest redshift in our sample. To this purpose, we repeat the GP reconstruction of $H(z)$ by increasing the number of Z^* in $0 < z < 0.553$ and find that the resulting shape of $\log D_L(z)$ remains stable. Thus, we are allowed to use the result obtained at $Z^* = z_{\rm GRB}$ to calibrate the Dainotti relations.

where $x_{\mu,i}$ is the value of $\log D_L^{\rm obs}(z)$ at the i-th redshift for each realization $\mu = 1, ..., N_{\rm real}$.

If we first consider uncorrelated errors, $\sigma_{\rm obs,i}$, i.e., if we consider a diagonal covariance matrix, we can build a chi-squared which takes the following form,

$$\chi^2(a, b, C_o, \sigma_{int}) = \sum_{i=1}^{N} \frac{[\log D_L^{\rm obs}(z_i) - \log D_L^{\rm th}(z_i, a, b, C_o)]^2}{(\sigma^2_{\rm obs,i} + \sigma^2_{int})}\,, \tag{7.3}$$

where $N = n_{\rm GRB}$. We sample the parameters of interest of the Dainotti relations a, b, C_o, and σ_{int} through an MCMC analysis, making use of `emcee` (see Sec. 5.2). The log-likelihood to be evaluated at each step of the Monte Carlo is

$$\begin{aligned}\ln \mathcal{L} &= -\frac{1}{2}\left[\sum_{i=1}^{N} \ln\{2\pi(\sigma^2_{\rm obs,i} + \sigma^2_{int})\} + \chi^2\right] = \\ &= -\frac{1}{2}\sum_{i=1}^{N} \ln\{2\pi(\sigma^2_{\rm obs,i} + \sigma^2_{int})\} - \frac{1}{2}\sum_{i=1}^{N} \frac{[\log D_L^{\rm obs}(z_i) - \log D_L^{\rm th}(z_i, a, b, C_o)]^2}{\sigma^2_{\rm obs,i} + \sigma^2_{int}}\,.\end{aligned} \tag{7.4}$$

In comparison to previous studies, we also allow the five parameters defining the fundamental plane ($\log T^*_{\rm X}, F_{\rm peak}, K_{\rm prompt}, \log F_{\rm X}, K_{\rm plateau}$, cf. Table A.5) to vary freely in the Monte Carlo. We treat them as nuisance parameters. These parameters are specific for each GRB. Thus, for the 3D Dainotti relation (Eq. (4.17)) we have $5 \times n_{\rm GRB} = 100$ nuisance parameters. In the case of the 2D Dainotti relation (Eq. (4.20)), we only sample $\{\log T^*_{\rm X}, \log F_{\rm X},\ K_{\rm plateau}\}$, so we deal with $3 \times n_{\rm GRB} = 60$ nuisance parameters. The constraints for the parameters of interest a, b, C_o, and σ_{int} are then derived after performing the marginalization over the nuisance parameters. Due to the high dimensionality of the problem, to ensure convergence we choose to use a sufficiently large number of walkers (~ 220 for the 3D relation and ~ 140 for the 2D one) as well as a large number of steps in the parameter space $n_{\rm steps} = 6 \cdot 10^5$.

We evaluate the robustness of the proposed methodology by assessing the impact of:

1. The prior choice in the Monte Carlo analyses. Given our aim to develop a method that is as model-independent as possible, we extensively test both Gaussian and flat priors to verify the robustness and compatibility of the results obtained with each. First, we use Gaussian priors on the parameters of interest a, b, C_o, and σ_{int}. To build the priors, we use the mean values and the 1σ uncertainties from the fundamental plane (FP) fitting analysis for the Platinum sample with 20 GRBs (see Fig. 4.3). Their values are listed in Table 7.1. Then, we gradually increase the standard deviation of the Gaussian to 2-, 3- and 5σ, to reduce the informative imprint of the prior. Nonetheless, it is important to mention that to preserve the physical meaning of these parameters, we impose bounds on a, b and σ_{int}. In particular, imposing $a < 0$ ensures that there is an anti-correlation between L_X and T^*_X, and when the value of a is close to -1, this implies that the energy reservoir of the plateau remains constant (see Sec. 4.5). However, we will show that this anti-correlation is indeed

maintained regardless of the physical cut $a < 0$, as positive values of a are consistently distant from the region preferred by the data in all the calibration results presented in this work. Regarding the b parameter, we impose the prior $b > 0$, which is driven by observational evidence and theoretical predictions. A negative b is not physically supported, as it would mean that the higher the peak luminosity, the less bright the plateau. Indeed, as shown in, e.g., [503, 146, 434, 139], there is observational evidence that the more kinetic energy there is in the prompt, the more is transferred in the afterglow phase. Thus, there is a positive correlation between L_X and $L_{\rm peak}$, which supports the choice of the prior. In addition, we will see that the use of this prior is also motivated by the strong degeneracy between b and C_0, which cannot be broken with current data within this model-independent approach. Imposing $b > 0$ allows us to break this degeneracy and thus avoid ending up in unphysical regions of the parameter space. Finally, the intrinsic scatter has to be greater than zero by definition.

Lastly, we adopt flat priors on the parameters of interest, by transforming the previous Gaussian priors into uniform distributions. This conversion can be done in several ways and by applying different definitions. We decided to use the same approach employed by [159][4], which requires

$$\begin{aligned} \mu &= \frac{x_1 + x_2}{2}\,, \\ \sigma &= \sqrt{\frac{(x_2 - x_1)^2}{12}}\,. \end{aligned} \tag{7.5}$$

These are the relations to transform a Gaussian distribution with mean μ and standard deviation σ to a uniform distribution $\mathcal{U}(x_1, x_2)$ with the same mean and standard deviation.

2. The covariance matrix of the reconstructed function $\log D_L^{\rm obs}(z)$ at the GRB redshifts, $C_{\rm obs}$, as defined in Eq. (7.2). The total covariance matrix, $C_{\rm T}$, incorporates also the contribution of the intrinsic scatter $\sigma_{\rm int}$, which is the same for all the GRB data points. Its elements read $C_{\rm T,ij} = C_{\rm obs,ij} + \delta_{ij}\sigma_{int}^2$. Hence, if we define $\Delta_i \equiv \log D_L^{\rm obs}(z_i) - \log D_L^{\rm th}(z_i)$, generalizing Eq. (7.4), we can write the new log-likelihood

$$\ln \mathcal{L} = -\frac{N}{2}\ln(2\pi) - \frac{1}{2}\ln\det(C_{\rm T}) - \frac{1}{2}\sum_{i,j=1}^{N} \Delta_i^T (C_{\rm T}^{-1})_{ij}\Delta_j\,, \tag{7.6}$$

which duly takes into account the correlations.

Once obtained the reconstruction of $\log D_L^{\rm obs}(z)$ together with its uncertainties, we can constrain the correlation parameters in Eq. (4.17) as well as the intrinsic scatter of the plane, by means of the likelihood in Eq. (7.4). As already mentioned, to ensure the efficiency of the method and cross-check the stability of the results,

[4]Therein the authors test the impact of the prior choice in a similar way but to infer cosmological parameters with SNIa and BAO.

Table 7.1. Priors adopted for the 3D relation (first half) and 2D relation (second half) analysis. In the first column, we report the mean values and the corresponding 1σ uncertainties obtained from the GRB fundamental plane fitting ($\mathrm{FP_{BF}}$) analysis, from which we take the Gaussian priors at n-σ. In the second and third columns, we list, respectively, the uniform prior ranges at 3- and 5σ C.L., computed using Eq. (7.5). We impose physical cuts on the parameters ($a < 0$, $b > 0$, $\sigma_{int} > 0$). This is why some of the boundaries in the last two columns coincide.

	$\mathrm{FP_{BF}}$	3σ	5σ
a	-0.81 ± 0.17	(-1.68, 0)	(-2.26, 0)
b	0.50 ± 0.17	(0, 1.37)	(0, 1.95)
C_o	24.65 ± 8.91	(-22,71)	(-53,102)
σ_{int}	0.35 ± 0.07	(0, 0.72)	(0, 0.97)
a	-1.03 ± 0.16	(-1.85, -0.2)	(-2.39, 0)
C_o	51.2 ± 0.52	(48, 54)	(47,56)
σ_{int}	0.43 ± 0.08	(0.01, 0.85)	(0, 1.13)

we need to quantify the impact of the prior choice on the parameters of interest a, b, C_o, and σ_{int} in the Monte Carlo sampling. We thus employ Gaussian priors with a mean equal to that obtained in the fundamental plane fitting analysis and a standard deviation equal to 1, 2, 3 or 5 times the one obtained in the FP analysis (cf. Table 7.1). We present our results in Fig. 7.2. We then repeat the analysis making use of flat priors. We apply the conversion from Gaussian to flat priors of Eq. (7.5). However, in Table 7.1, we only report the results of this conversion for the 3- and 5σ cases since they lead to the most conservative results. We show the corresponding MCMC outcome in Fig. 7.3. Some comments are in order:

- Fig. 7.2 shows that results obtained with different Gaussian priors are all compatible with each other within errors. The largest differences are found with the 1σ prior. This difference can be easily understood. In the 1σ prior case, we only let the walkers explore a very limited region of the parameter space around the fundamental plane mean values.

- Interestingly, as soon as we move away from the 1σ prior and the priors become less informative, the posteriors for a, b, C_o, and σ_{int} do not significantly change between different prior choices. This suggests that the method is stable. This is even more evident if we look at Fig. 7.3, which shows that passing from Gaussian to uniform priors does not alter the posteriors significantly. Given the stability of the results, hereafter, we will consider the set-up with flat priors at 5σ as our *baseline*, being this the most conservative choice. We report the mode and mean values of the one-dimensional marginalized distributions for each of the parameters of interest in Table 7.2.

- We find no preference for a non-zero value of b, suggesting that this parameter is not playing a major role in the evaluation of the cosmological results and hence we can use the 2D relation instead. Actually, its upper bound at 95% C.L. stands around 0.2 in all the analyses presented so far. From a Bayesian

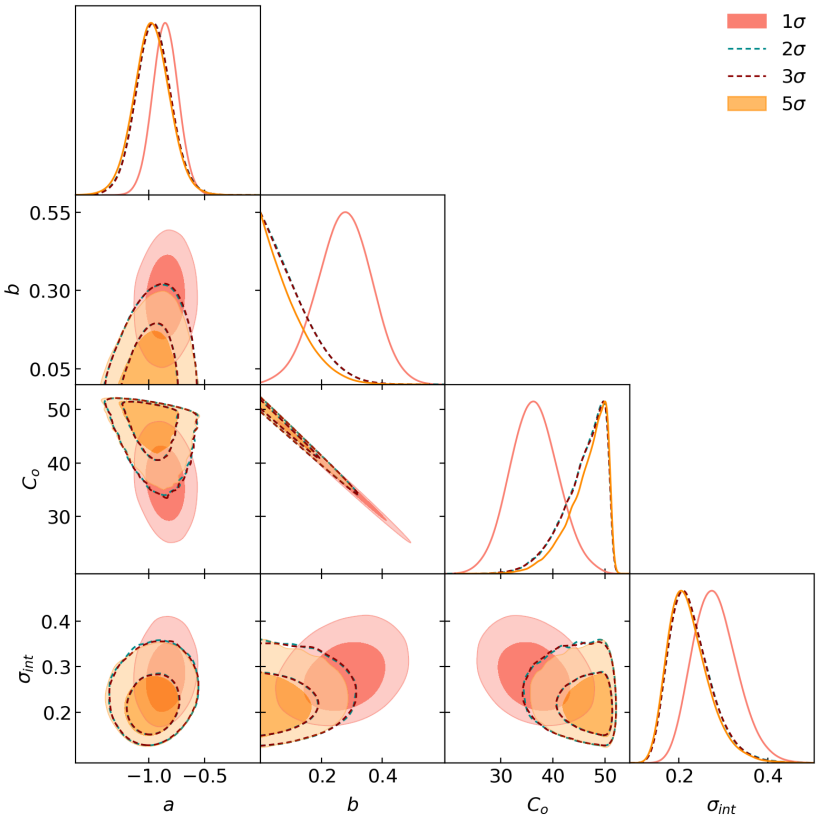

Figure 7.2. 1D posteriors and 2D contours at 68% and 95% C.L. obtained in the analyses of the 3D Dainotti relation, assuming the n-σ progression for Gaussian priors and the physical cuts $a < 0$, $b > 0$, $\sigma_{int} > 0$. Results obtained in the different cases are all consistent with each other. However, the 2σ, 3σ and 5σ priors are more conservative and allow for more model-independent results.

perspective, we are therefore motivated to consider the 2D Dainotti relation, given by Eq. (4.20).

- There is a strong degeneracy between C_o and b. The one-dimensional posterior of the normalization factor exhibits a cut-off around $C_o \sim 52$, which is due to the aforementioned correlations and the physical bound $b > 0$ employed in our analysis of the 3D Dainotti relation. Indeed, in the 2D case we consistently find $C_o \sim 51$ (see Table 7.2), since we are essentially saturating the prior by setting $b = 0$.

To quantify the impact of correlations between different redshifts in $\log D_L^{\rm obs}(z)$ obtained from GP+CCH, we perform an additional analysis in which we also include the contribution of the non-diagonal terms of the covariance matrix $C_{\rm obs}$ (Eq. (7.2)) by making use of the log-likelihood in Eq. (7.6). We compare the results obtained in this new analysis with those discussed above, obtained when we only consider a diagonal covariance matrix. Moreover, we also investigate the scenario in which we neglect the uncertainties of the reconstructed luminosity distances and only consider the effect of the intrinsic scatter, $C_{\rm T,ij} = \delta_{ij}\sigma_{int}^2$. The results are presented in Fig.

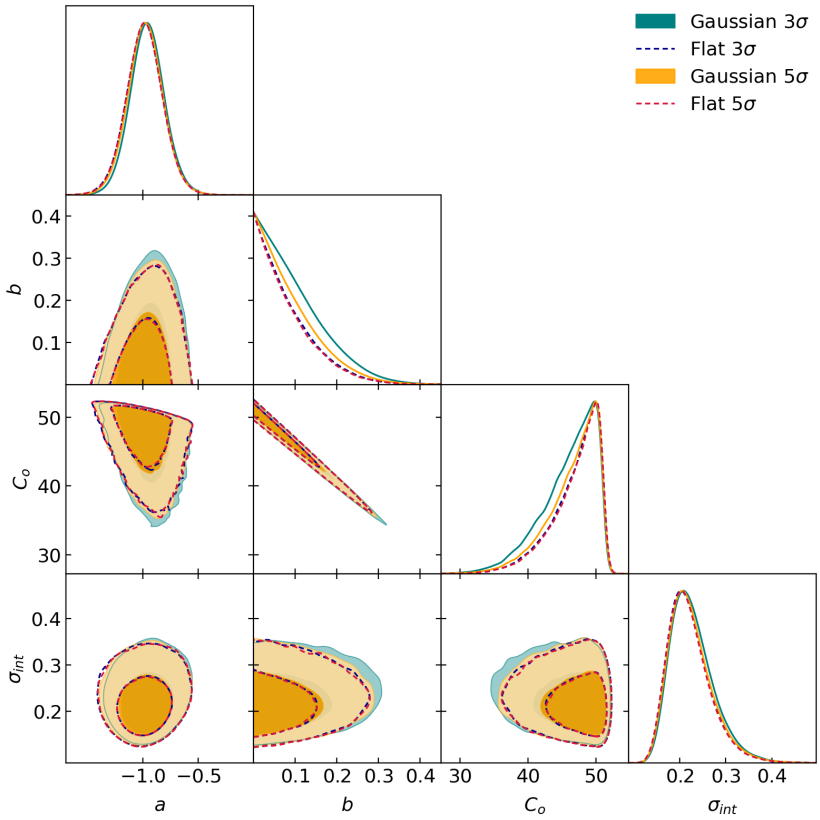

Figure 7.3. 1D posteriors and 2D contour plots at 68% and 95% C.L. obtained in the analysis of the 3D Dainotti relation using Gaussian priors and the corresponding flat priors from Eq. (7.5) at 3- and 5σ. We use dashed lines for the results obtained with flat priors. They match almost perfectly with those obtained with Gaussian priors.

Table 7.2. Constraints on the parameters of interest for the 3D and 2D Dainotti relations sampled assuming the baseline set-up, i.e. uniform priors at 5σ C.L., which leads to the most conservative results (see also Figs. 7.3 and 7.5). We report for each parameter the mode and mean value together with its associated uncertainty at 68% C.L., except for b, for which we give an upper bound at 95% C.L.

		a	b	C_o	$\sigma_{\rm int}$
3D relation	Mode values	-1.03	< 0.21	50.17	0.20
	Mean	-1.00 ± 0.16	< 0.21	$47.05^{+4.21}_{-1.35}$	$0.21^{+0.03}_{-0.05}$
2D relation	Mode values	-1.07		51.19	0.19
	Mean	-1.04 ± 0.16		51.16 ± 0.53	$0.21^{+0.03}_{-0.05}$

7.4, illustrating that the posteriors for the parameters a, b, C_o, and σ_{int} are insensitive to the GP+CCH uncertainties. In Sec. 7.4, we will provide two interpretations of this conclusion.

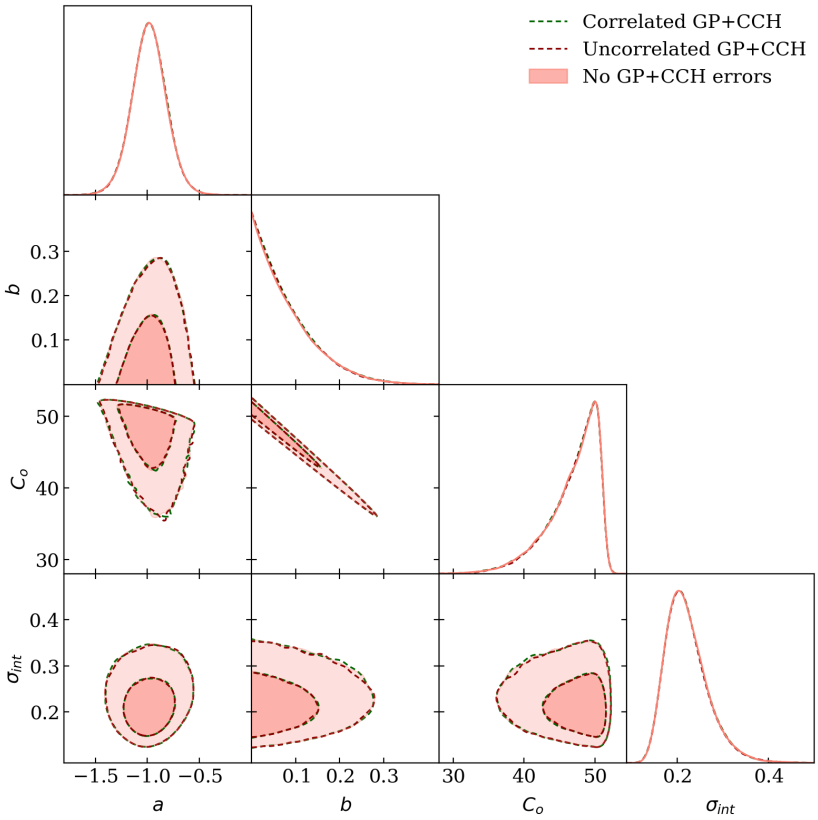

Figure 7.4. 1D posteriors and 2D contour plots at 68% and 95% C.L. for the parameters of the 3D Dainotti relation, obtained assuming flat priors at 5σ. We study the impact of accounting for correlations between redshifts in the luminosity distance estimates reconstructed with GP+CCH (dotted green), neglecting those correlations (dotted red) and completely ignoring the uncertainties in the reconstruction (in pink). Differences are derisory.

As we have seen, the calibration of the 3D Dainotti relation leads to a b parameter that is compatible with 0 at 68% C.L. It is therefore worth analyzing the 2D relation, which incorporates the properties of the end time of the plateau emission and the X-ray luminosity. The parameters to sample are, in this case, a, C_o, and $\sigma_{\rm int}$. Starting from Eq. (4.20), the same reasoning used to obtain the log-luminosity distance in Eq. (7.1) applies here, where we drop the contribution of $\log L_{\rm peak}$. It is straightforward to see that Eq. (7.1) reduces to

$$\log D_L^{\rm th} = a_1 \log T_{\rm X}^* + c_1 + d_1(\log F_{\rm X} + \log K_{\rm plateau})\,, \tag{7.7}$$

where now $a_1 = a/2$, $c_1 = (-\log(4\pi) + C_o)/2$ and $d_1 = -1/2$. On the same line of the 3D relation, we assess the impact of the different priors in the MCMC analysis. Their values are listed in Table 7.1 while the MCMC results are shown in Fig. 7.5.

We report both the mode values and the means of the one-dimensional marginalized distributions in Table 7.2. The constraint we obtain for a resonates well with the expectations: a slope of ≈ -1 implies a constant energy reservoir during the plateau phase [130, 143]. In particular, we can ascribe this phase to energy injection

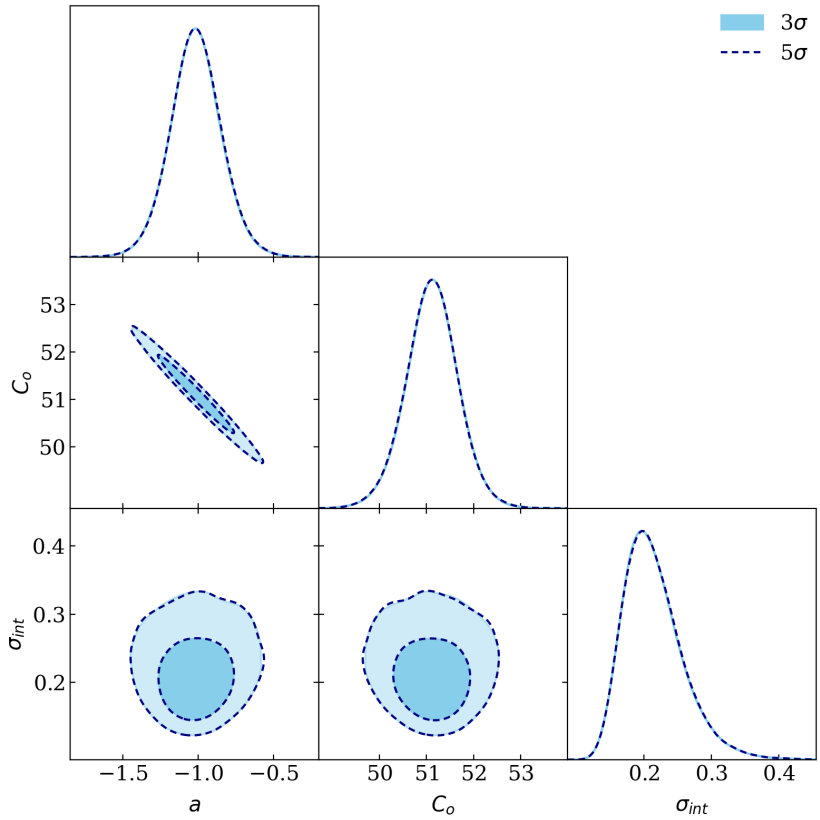

Figure 7.5. 1D posteriors and 2D contour plots at 68% and 95% C.L. from the MCMC carried out for the 2D Dainotti relation assuming flat priors at 3- and 5σ, in cyan and blue, respectively. The results match each other, showing also in the case of the 2D relation the insensitivity of the analysis to the prior choice.

by newly born neutron stars [504, 505], and this result supports that the rotational energy of the latter is constant, indicating that they can be treated as a standard candle [506]. Here, however, we clarify that the construction of the Platinum sample starts from phenomenological choices of the flatness of the plateau, the absence of flares, etc. and therefore, in our approach, we can independently obtain the magnetar-driven parameters. Indeed, the a slope is independent of the initial priors.

In the 2D Dainotti relation, we essentially set $b = 0$, so we break the strong degeneracy between this parameter and C_o (see Fig. 7.6). This explains why the uncertainty on C_o decreases by 80% compared to the baseline constraint obtained for the 3D relation. This fact may enhance our ability to constrain cosmology.

Finally, also for the 2D relation, we assess the impact of the correlations in the values of log $D_L^{\rm obs}$ obtained from the GP reconstruction, finding that our conclusions remain valid within this framework as well.

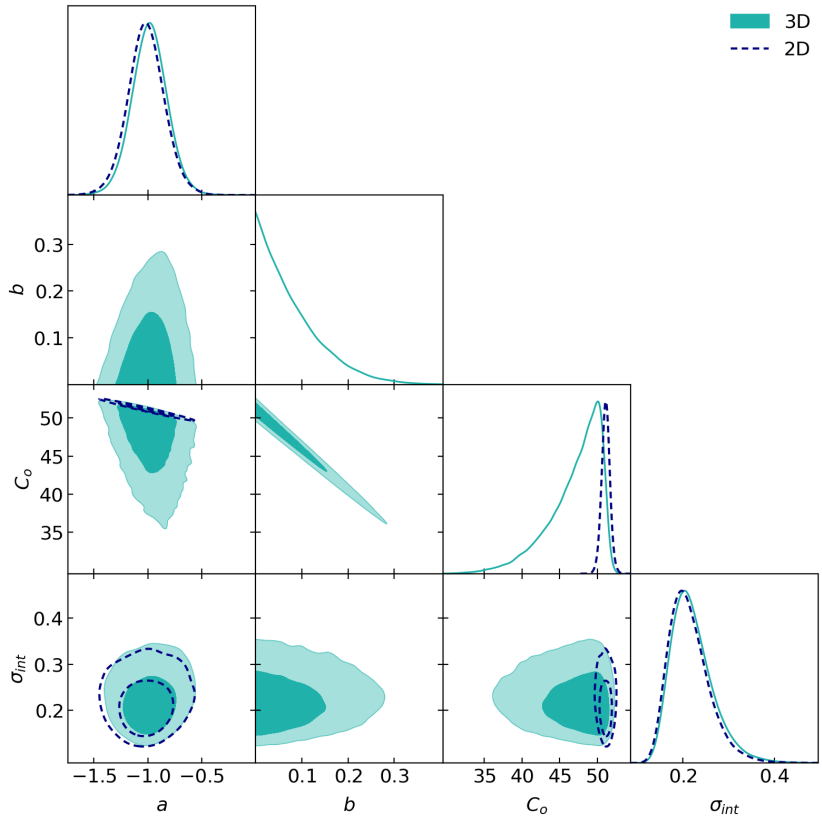

Figure 7.6. Comparison between the MCMC results for the 3D and 2D Dainotti relations obtained with the baseline set-up.

7.2 Redshift evolution corrections

To ensure the generality of our treatment, it is worth discussing the role of the corrections due to evolutionary effects. Indeed, each physical feature of the three-dimensional GRB fundamental plane, $L_{\rm X}$, $T^*_{\rm X}$ and $L_{\rm peak}$, is affected by selection biases due to instrumental thresholds and redshift evolution of the variables involved in the correlations. As already mentioned in Sec. 4.5, it has been shown that in order to correct for these effects, one can employ the Efron & Petrosian method [436], which tests the statistical dependence among $L_{\rm X}$, $T^*_{\rm X}$ and $L_{\rm peak}$ (for details, see [131, 159]). Once one introduces this correction, the expression for the GRB fundamental plane takes the form in Eq. (4.21). We recall that in that formula, we have introduced the subscript ev to distinguish the relation parameters from those employed in the non-evolutionary case, while $k_{L_x}, k_{T^*_{\rm X}}$ and $k_{L_{\rm peak}}$ represent the evolutionary coefficients related to each physical feature.

Starting from Eq. (4.21), one can derive the new likelihood, which now accounts for redshift evolution effects, thus assessing how they can affect the correlation parameters. We evaluate the impact of flat priors on $a_{ev}, b_{ev}, C_{o,ev}, \sigma_{int,ev}$ but only at 3- and 5σ, motivated by our previous results. To use the transformation in Eq. (7.5), we started from the results obtained from the analysis of the Platinum

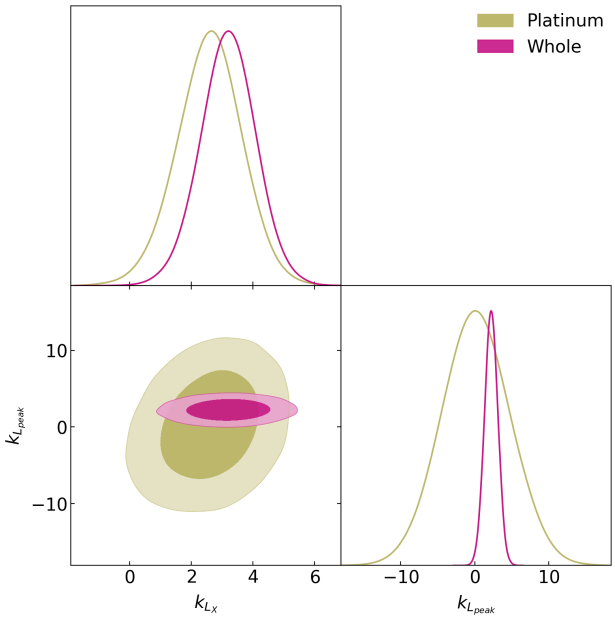

Figure 7.7. 1D posteriors and 2D contour plots at 68% and 95% C.L. for the evolutionary coefficients k_{L_X} and $k_{L_{\rm peak}}$, sampled assuming Gaussian priors at 3σ C.L. from the Platinum sample (in green) or from the Whole sample (in magenta). For the parameters $a_{ev}, b_{ev}, C_{o,ev}$ (not shown here) we impose flat priors at 5σ, cf. the main text and Fig. 7.8 for details.

sample presented in [159], which, at 1σ, read: $a_{ev} = -0.85 \pm 0.12$, $b_{ev} = 0.49 \pm 0.13$, $C_{o,ev} = 25.4 \pm 6.9$, and $\sigma_{\rm int,ev} = 0.18 \pm 0.09$. For the evolutionary coefficients entering Eq. (4.21), we take advantage of two results obtained for the full Platinum sample (50 GRBs) and also for the Whole sample (222 GRBs) in [159]. At 68% C.L. they read, respectively:

$$\begin{aligned} k_{L_x} &= 1.37^{+0.83}_{-0.93}, \quad k_{T^*_{\rm X}} = -0.68^{+0.54}_{-0.82}, \quad k_{L_{\rm peak}} = 0.44^{+1.37}_{-1.76}\,, \\ k_{L_x} &= 2.42^{+0.41}_{-0.74}, \quad k_{T^*_{\rm X}} = -1.25^{+0.28}_{-0.27}, \quad k_{L_{\rm peak}} = 2.24 \pm 0.30\,. \end{aligned} \tag{7.8}$$

The above constraints are obtained assuming a flat ΛCDM model. We decide to proceed in two ways:

- Keep them fixed (Case 1);
- Let them vary in the Monte Carlo analysis, treating them as nuisance parameters (Case 2).

In Case 1), we just fix the k's to the central values reported above. In Case 2), we also use their uncertainties to build the corresponding priors. This is equivalent to propagating them to the parameters of interest in the MCMC analysis. This additional case is indeed performed to coherently reduce the model dependency level with this work's investigation line. Notice, though, that since $k_{T^*_X}$ does not depend on cosmology (being related to a measure of a characteristic time scale for the end of the plateau emission), we keep it fixed while we treat as nuisance parameters $k_{L_{\rm X}}$

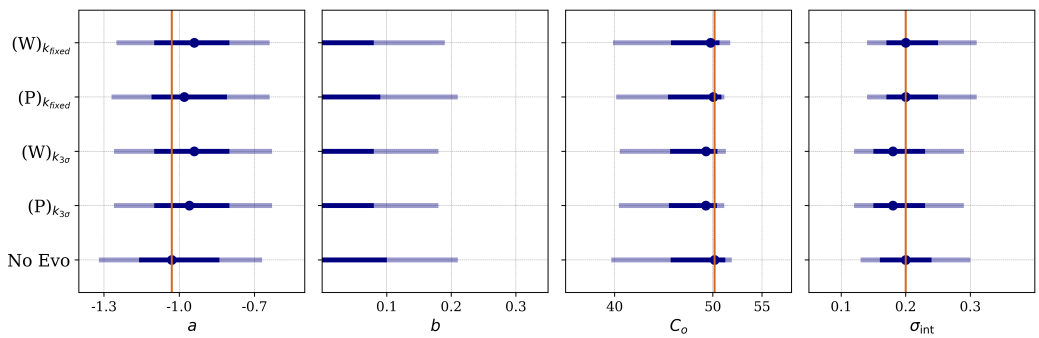

Figure 7.8. Whisker plot for the parameters of interest evaluated at 68% and 95% C.L. (for b we only show its upper bounds), with the dots indicating the mode values of the 1D marginalized distributions. The orange line passes through the *No Evo* (no evolution) mode values, obtained from the analysis with flat priors at 5σ in Sec. 7.1. With W we denote the results obtained considering the evolutionary coefficients from the Whole sample, the Platinum is instead indicated with P. The label k_{fixed} refers to the analyses in which the k's are fixed, whereas $k_{3\sigma}$ refers to those analyses in which the k's are allowed to vary within 3σ. In the cases with evolution, a, b, C_o, σ_{int} become, respectively, $a_{ev}, b_{ev}, C_{o,ev}, \sigma_{int,ev}$.

and $k_{L_{\rm peak}}$. Since, as one can appreciate from Eq. (7.8), the Platinum constraints already come with large errors due to the small sample size and a large number of parameters, we decide to set Gaussian priors (instead of uniform priors) at 3σ on both $k_{L_{\rm X}}$ and $k_{L_{\rm peak}}$ to avoid non-physical results for these parameters. We also tested what happens if we consider uniform priors at 3σ. We have checked that the results for a_{ev}, b_{ev}, and $C_{o,ev}$ are not affected by this choice.

In Fig. 7.7, we show the corresponding posteriors of the evolutionary coefficients. At 68% C.L., we obtain $k_{L_{\rm X}} = 2.50^{+1.06}_{-1.05}$ and $k_{L_{\rm peak}} = 0.20^{+4.67}_{-4.66}$ when we employ priors from the Platinum sample, while we find $k_{L_{\rm X}} = 3.12 \pm 0.90$ and $k_{L_{\rm peak}} = 2.23 \pm 0.89$ from the Whole sample. As expected, the uncertainties for the latter case are smaller since the fundamental plane fitting analysis for the Whole sample has more constraining power (see Eq. (7.8)), being the data set larger. We here notice that from our analysis, similarly to the analysis performed by [159] the parameters of the evolution are compatible within 1σ for both $k_{L_{\rm X}}$, $k_{L_{\rm peak}}$ showing the reliability of this analysis as well. For what concerns the parameters of interest, we prefer to show their constraints in a whisker plot in Fig. 7.8, to compare the results throughout all the different cases described above (i.e., Cases 1 and 2, and considering no evolution), using flat priors at 5σ C.L.[5]. It is remarkable to notice, again, that different settings provide very stable results on the correlation parameters, even when redshift evolution corrections are accounted for. Additionally, despite very small differences, all the scenarios lead to a tight relation, especially when the k's vary freely. Indeed, in this case we find $\sigma_{int} = 0.20^{+0.03}_{-0.05}$ instead of $\sigma_{int} = 0.22^{+0.03}_{-0.05}$ (with mode values 0.18 instead of 0.20, respectively). If we consider that σ_{int} is a

[5]We have also tested the case with uniform priors at 3σ on $a_{ev}, b_{ev}, C_{o,ev}, \sigma_{int,ev}$. However, for a specific set of k's (Whole or Platinum), the posteriors from 3- or 5σ do not change. Therefore, we prefer to show only the comparison between the analyses for a specific prior range choice (in this case, 5σ).

measure of the scatter, which can depend on the spin period and magnetic field variability in each GRB, values so close to each other mean that the system has similar values of these parameters, with small variations.

7.3 Extended ladder with GRBs

Supported by the stability of the results achieved in the previous Sections, it becomes natural to ask how such results can be leveraged in cosmological applications. As already mentioned, the advantage of using probes such as GRBs lies in their ability to extend the ladder beyond SNIa and BAO redshifts. This is the reason why we now employ the calibration results obtained by making use of the GRB data at $z \lesssim 2$ to obtain luminosity distances from the remaining GRBs contained in the Platinum sample and cover the region up to $z = 5$[6]. We first check that the correlation coefficients between the calibration and nuisance parameters of the 20 GRBs involved in the calibration process are negligible and also that the posterior distributions of the nuisance parameters are highly in accordance with the corresponding prior distributions. Indeed, we find that the posterior and prior distributions are almost indistinguishable, with only a couple of exceptions (one nuisance parameter in two out of the 20 redshift points) in which we find noticeable changes, which remain in any case small ($\lesssim 1.9\sigma$). This allows us to sample the nuisance parameters of the GRBs at $z > 2$ together with the nuisance and calibration parameters of those GRBs at $z < 2$ to finally obtain the luminosity distances and build the extended distance ladder. In this way, we make sure to propagate the errors from the MCMC analysis to the final result. In particular, on top of these errors, we add the contribution of the intrinsic scatter to obtain the final uncertainties on the GRB luminosity distances. In the upper plot of Fig. 7.9, we present the extended distance ladder obtained with our *baseline* calibration without considering evolution effects and compare it with the one obtained when the latter are also taken into account. In particular, for the latter, we employ the results obtained when the evolutionary coefficients, $k_{L_{\rm X}}$ and $k_{L_{\rm peak}}$, are left free to vary according to the priors from the Whole sample since they lead to the tightest results and the smallest σ_{int} for the Dainotti relations (see Sec. 7.2). To quantify possible deviations from the GP+CCH distances, for each calibration result, we compute the bias between their mean and the mean of the GP+CCH reconstruction at each redshift, $\beta = \log D_L^{\rm GRB} - \log D_L^{\rm GP+CCH}$. In the calibrated GRB data points of $\log D_L(z)$ obtained without evolution effects, displayed in the upper plot of Fig. 7.9, one can already see a trend towards negative values of β in the region $z > 2$. The latter behavior was already found in previous works (see, e.g., [157]). To keep track of this trend in a more precise way, we compute a binned bias. More concretely, we opt to bin the redshift range, composed of 50 points, in 10 equi-populated redshift bins. In order to account for the existing correlations between the various data points in each bin, we compute the weighted mean and its uncertainty as follows:

[6]The remaining GRBs data can be found in Table A1 of [151]

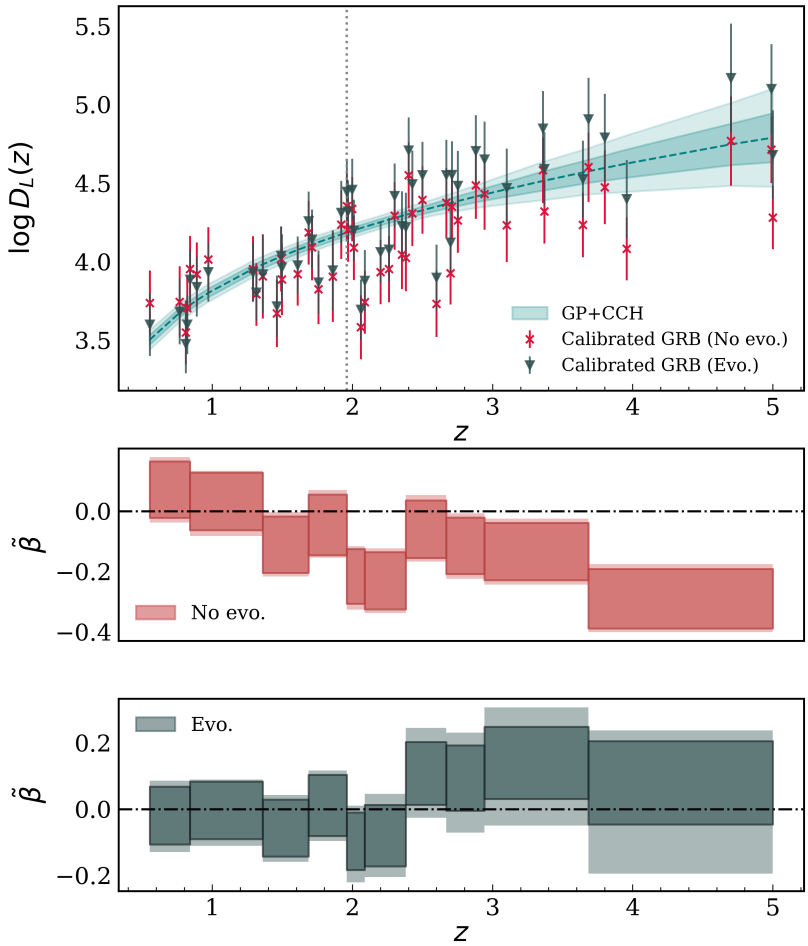

Figure 7.9. *Upper plot*: The extended distance ladder. The GP+CCH reconstruction of the logarithm of the luminosity distance as a function of the redshift is shown in light green. The calibrated GRB data obtained with and without evolution effects are presented in grey and light red, respectively. The dotted vertical line at $z = 2$ is used to mark the border between the data employed in the calibration process and those used only in the extension of the ladder. The error bars of the calibrated GRB distances stand at 1σ C.L., while for the GP result we show both the 1σ and 2σ bands. The luminosity distance is given in Mpc; *Middle plot*: Weighted mean of the bias between the GP+CCH reconstruction and the calibrated GRB data with its uncertainty, as given in Eq. (7.9), when the evolution effects are neglected. Lighter-coloured boxes are obtained when correlations are accounted for; *Bottom plot*: The same as in the middle plot, but considering the evolution effects.

$$\tilde{\beta}_k = \frac{\sum_{i,j=e_k}^{f_k} \beta_i \omega_{ij}}{\sum_{i,j=e_k}^{f_k} \omega_{ij}}, \qquad \tilde{\sigma}_k = \sqrt{\frac{1}{\sum_{i,j=e_k}^{f_k} \omega_{ij}}}, \tag{7.9}$$

with $\omega_{ij} = (C^{-1})_{ij}$ the elements of the inverse of the covariance matrix of the GRB luminosity distances, $e_k = 1+5(k-1)$, and $f_k = 5k$. This is an accurate computation since the distribution of the GRB luminosity distances is Gaussian in very good

approximation, as we have explicitly checked and in accordance with a recent work of [110]. We present our results in the middle and bottom panels of Fig. 7.9, neglecting and considering the evolution corrections, respectively. In each of these two plots, we also show the weighted bias obtained when we neglect the off-diagonal terms of C. By comparing the middle and bottom plots, one can see that accounting for redshift evolution corrections is very important to decrease the bias in the region $z > 2$. In fact, when no evolution effects are considered, there is a clear trend towards smaller luminosity distances, as already noted in the upper plot of Fig. 7.9. We show now that correcting for evolutionary effects enables us to cure this trend, and this is even more true when we consider the existing correlations between the various GRB luminosity distances. Indeed, it is a well-known result that the physical properties of astrophysical objects at high z are more affected by the Malmquist bias [507] due to the difficulty of observing faint events at larger distances. This proves that if one wants to exploit probes at higher z for cosmological purposes, it is of utmost importance to use correlations in which possible biases and effects of redshift evolution have been properly evaluated and corrected.

7.4 Final discussion

All the analyses presented in this Chapter share a common result: our method results in being stable under the choice of the priors on the parameters that characterize the fundamental plane relation of GRBs – a, b, C_o, σ_{int}. Even when using Gaussian priors at 1σ, the posteriors on the parameters are compatible within $\sim 1-2\sigma$ to the other cases with wider priors. The differences between all the cases analyzed are very small, although we achieve the tightest constraints for the 3D relation parameters when flat priors at 5σ are employed (see for clarity Fig. 7.3). In addition, we find that the contribution of the peak luminosity in the prompt emission to the 3D Dainotti relation is not particularly favoured from a Bayesian perspective, but cannot be excluded either. Our results only set an upper bound on b. More specifically, we find that $b \lesssim 0.2$ at 95% C.L.

The baseline calibration both for the 2D and 3D Dainotti relations leads to an intrinsic scatter of the order of ≈ 0.2 with a relative precision of $\sim 20\%$. Specifically, for the 3D relation we obtain $\sigma_{int} = 0.21^{+0.03}_{-0.05}$. If compared with standard analyses, such as the fundamental plane fitting result with the same number of GRBs (see Table 7.1), we obtain a decrease of $\sim 40\%$ in its central value, outlining the achievement of a tighter relation. In particular, we can also quantify the compatibility of the two aforementioned results by calculating the relative difference of $\sigma_{int,\mathrm{FP}}$ compared to σ_{int} normalized by the maximum of the two uncertainties which reads as: $(\sigma_{int,\mathrm{FP}} - \sigma_{int})/\delta$, with $\delta = \max(\delta_{\sigma_{int}}, \delta_{\sigma_{int,\mathrm{FP}}})$. We find it to be 1.99, showing that the calibration result is consistent within 2σ with the standard (model-dependent) analysis results. As a term of comparison, employing a different OHD data set and thus a different set of 23 GRBs, [455] calibrate the 3D Dainotti relation with the D'Agostini method [437] and obtain a very large scatter, $\sigma_{int} = 0.70 \pm 0.10$. In general, a lower dispersion is expected when GRBs are employed closer to the plane. One example can be found in [147], where the 10 GRBs closest to the plane are selected from the Platinum sample, leading to $\sigma_{int} = 0.05 \pm 0.05$ (assuming a

flat ΛCDM model). But what is the impact of the intrinsic scatter on the CCH calibration? The answer comes from the analysis done at the end of Sec. 7.1. There, we show that our results remain unchanged whether or not we include the uncertainties on the reconstruction of the luminosity distance in the likelihood. This result holds for both the 2D and 3D relations and has two main implications. First, it confirms even more the stability of all the results obtained throughout this work. It establishes the CCH as a reliable calibrator for pinpointing a specific GRB sub-set with low intrinsic scatter. This is remarkable if one considers that this result holds even when the redshift evolution corrections are accounted for, thus making the relation and the results themselves more robust if also compared with previous results in the literature. Indeed, we obtain a mode value for σ_{int} which stands between 0.18 and 0.20, the lowest being obtained when also the evolutionary coefficients are left free in the analysis. As a comparison, [435] find $\sigma_{int} = 0.22 \pm 0.10$, and most recently this value has been better constrained in [159], where they find $\sigma_{int} = 0.18 \pm 0.07$. Both results are obtained using the full Platinum sample and assuming a flat ΛCDM model. When we compare the uncertainty on this latter result including the correction for evolution, $\delta_{\sigma_{int}} = 0.07$, with our result, $\delta_{\sigma_{int}} = 0.04$, we obtain a decrease of 43%. This result makes this method competitive with standard approaches, especially for using GRBs for cosmological purposes in light of the circularity problem (see Sec. 2.1.1). Additionally, there is still a non-negligible dispersion on the GRB plane compared to other probes. As it stands, this dispersion is sufficiently large to prevent a better calibration regardless of the potential increase in the amount of CCH data at $z \lesssim 2$ through dedicated galaxy surveys in the future (see, e.g., [490]). Fig. 7.9 is exactly telling us that, although GRB data alone cannot achieve yet the same constraining power as other low-redshift probes (see the difference in the error bars with respect to GP+CCH at the lowest redshifts), their strength lies precisely in their capability of extending the ladder to higher redshifts. We remark here that this has motivated in the last two decades the effort to build several correlations that can be used in this context (see Sec. 2.1.1), provided that understanding of their physical meaning and reliability regardless of selection biases do hold. However, these two aspects have not yet been fully addressed in many of the correlations. These correlations have been similarly calibrated with low-z anchors, and their intrinsic scatter ranges from ~ 0.2 to 0.55. For instance, the Amati relation has been widely calibrated with SNIa using GP or simultaneous fitting analyses. The former approach was followed, for example, by [508] and [163], who found an intrinsic scatter between 0.46 and 0.52. The last authors further conducted simultaneous fitting with 31 OHD within the ΛCDM and wCDM models, yielding central values ranging from 0.39 to 0.46, depending on whether the A220 or A118 sample is used [150]. [164] calibrated the Amati relation using GP and 32 CCH, along with the A220. They determined the scatter to be $0.289^{+0.015}_{-0.014}$. To mention a few others, [173] used SNIa with GP in the A118 GRB sample at redshift less than 1.4, finding central values of 0.49 to 0.55, depending on the likelihood employed, whereas [162] obtained a dispersion of 0.54 with SNIa in conjunction with the A220 sample. [509] found a scatter around 0.36 employing a simultaneous fitting for the Yonetoku relation. In light of these mentioned results, it is evident that a common low dispersion is not still reached for relations based solely on the prompt emission phase. The result achieved in this work represents so far, and at

the best of our knowledge, one of the tightest correlations present in the literature. One possible explanation could be related to the fact that the plateau phase is less varied in its intrinsic properties with respect to the prompt emission. The scatter we find is robust to corrections for selection biases and redshift evolution, in contrast with other correlations, in which these effects still play a non-negligible role. If these corrections significantly affect the correlations, the correlations will no longer exist intrinsically in a reliable way. Also, the physical explanation of a relation meant to be used as a standard candle should be clear. For the correlations analyzed in this work, the most accredited theoretical scenario is the magnetar emission, and we actually found our results to support this model as the slope of the correlation is compatible with -1.

However, in the general scenario, the spread in the GRBs observed luminosities is still a non-negligible issue due to the not yet well-defined nature of their origin (core collapse of a massive star, merger of two neutron stars in a binary system or a neutron star-black hole system merger). Therefore, it becomes essential to investigate the reliability of these alternative probes and the relations that govern their intrinsic properties, possibly taking advantage also of the improvement both in data quality and quantity with upcoming surveys, e.g., SVOM [510] or THESEUS [511] missions. In this way, model-independent calibration methods could play a significant role in standardizing these probes effectively, thereby further extending the cosmic distance ladder and broadening our ability to probe the fundamental cosmological parameters.

In the next Chapter, we will see that this methodology can indeed be further extended to another sample of standardizable objects.

Chapter 8

QSOs calibration

Building on the calibration technique of GRBs presented in Chapter 7, we turn our focus to another set of standardizable candles: Quasars. Introduced in Sec. 2.1.1 and discussed in detail in Sec. 4.6, these objects provide a valuable byproduct of our model-independent methodology, as they extend even further current GRBs observations, being detected up to $z \sim 7$ [106]. A key advantage of QSOs is the size of their samples: the most recent compilation includes 2421 objects spanning $0.009 \leq z \leq 7.52$ (see Sec. 4.6), offering a far denser data set than currently available GRB catalogs. Therefore, we feel motivated to see how the Hubble diagram is shaped by these alternative probes.

We devote the next Section to briefly illustrating the steps involved in the QSOs calibration, whose approach largely relies on the methodology already outlined in Chapter 7. After presenting and discussing the results, we illustrate the extended distance ladder derived from them.

8.1 Calibrating the Risaliti-Lusso relation

As discussed in Sec. 4.6, QSOs obey a tight non-linear relation between the rest-frame UV luminosity at 2500Å, L_{UV}, and the X-ray luminosity at 2 keV, L_X, known as Risaliti-Lusso (RL) relation (cf. Eq. (4.22)) [179]. This relation is defined by three parameters: $\gamma, \beta, \delta_{int}$. The latter can be thought as the intrinsic scatter of the relation, analogously to GRBs (and SNIa). We can therefore treat these three quantities as free parameters in our Monte Carlo analysis. Analogously to what is done in the GRBs fundamental plane fitting analysis, one can employ the D'Agostini or Kelly method [437, 438] to sample the RL relation while accounting for errors in both x and y directions. For QSOs calibration, relying on a Gaussian distribution of the residuals[1], the log-likelihood to evaluate takes the form

[1]The Gaussianity assumption of the likelihood for the L20 sample has been recently studied in [111], following the analysis in [110, 512]. The authors showed that the normalized residuals of the full sample exhibit a preference for the logistic distribution. It will thus be interesting to re-evaluate this assumption within our calibration approach, as an extension of our studies.

$$\begin{aligned}\ln\mathcal{L} &= -\frac{1}{2}\left[\sum_{i=1}^{N}\ln\{2\pi(\sigma^2_{\rm obs,i}+\delta^2_{int})\}+\chi^2\right] = \\ &= -\frac{1}{2}\sum_{i=1}^{N}\ln\{2\pi(\sigma^2_{\rm obs,i}+\delta^2_{int})\}-\frac{1}{2}\sum_{i=1}^{N}\frac{[\log F_X^{\rm obs}(z_i)-\log F_X^{\rm th}(z_i,\gamma,\beta)]^2}{\sigma^2_{\rm obs,i}+\delta^2_{int}}\,,\end{aligned} \tag{8.1}$$

where, from Eqs. (4.23),

$$\log F_X = \gamma\log F_{UV} + (\gamma-1)\log(4\pi) + \beta + 2(\gamma-1)\log D_L\,, \tag{8.2}$$

and the total error budget is therefore

$$\sigma^2_{\rm obs} = \sigma^2_{\log F_X} + \gamma^2\sigma^2_{\log F_{UV}} + [2(\gamma-1)]^2\sigma^2_{\log D_L}\,. \tag{8.3}$$

As done for GRBs, we also account for correlations between the GP-reconstructed shapes of $\log D_L(z)$. In that case, the log-likelihood takes the form in Eq. (7.6), with $\Delta_i \equiv \log F_X^{\rm obs}(z_i) - \log F_X^{\rm th}$ and the elements of the total covariance matrix, $C_{\rm T}$, which read $C_{\rm T,ij} = [2(\gamma-1)]^2 C_{\rm obs,ij} + \delta_{ij}[\sigma^2_{\log F_X,i} + \gamma^2\sigma^2_{\log F_{UV,i}}] + \delta^2_{int}\delta_{ij}$, which follows from Eq. (8.3).

Supported by our previous results in Chapter 7, we calibrate the RL relation under the *baseline* set-up, i.e., adopting flat priors on the parameters of interest. For this purpose, we use the full sample of 2421 quasars provided by [106] (hereafter L20) as well as the sub-sample of 1253 objects constructed in [186] (hereafter D24). This choice is motivated by the fact that D24 sample presents a reduced intrinsic scatter (see Sec. 4.6), being therefore more suitable for cosmological applications.[2]

Last ingredient is the correction for redshift evolution, as discussed for GRBs. The redshift evolution of QSO luminosities has already been thoroughly examined, along with different possible approaches for correcting it in cosmological applications [513, 514, 109, 515]. For instance, in the latter work it has been shown that, despite the presence of redshift evolution and selection effects, such as the Malmquist bias, correcting for these effects preserves the intrinsic slope of the correlation. This confirms that the relation arises from the underlying physics of QSOs rather than observational biases, marking a step forward in establishing QSOs as cosmological tools.

After selecting the sub-sample of QSOs that match the CCH redshift range up to $z \lesssim 2$, we reconstruct the QSOs luminosity distances with GP and CCH and use them in Eq. (8.1) to sample γ, β and δ_{int}. The corresponding results are then used to extend the ladder up to $z = 7.54$, the last QSO in both samples.

In Table 8.1, we report the results at 1σ C.L. of the calibration of the RL relation with both L20 and D24 data sets. The corresponding MCMC triangle plots are shown in Fig. 8.1. In particular, we present the calibration both with and without (i) evolution correction and (ii) the CCH+GP correlations. For the evolution case,

[2]The D24 sample is obtained via a σ-clipping methodology applied in narrow redshift bins. This procedure minimizes the intrinsic dispersion of the $\log(F_X) - \log(F_{UV})$ relation by down-weighting or removing sources whose vertical distance from the best-fit relation exceeds a chosen threshold. Importantly, this method is independent of any assumed cosmological model. For details, see [186].

Table 8.1. Constraints at 68% C.L. on the parameters of interest of the RL relation, using D24 (first half), and L20 (second half) samples for all the cases under study: with or without corrections for redshift evolution effects (*Evo*) and *No Evo*, respectively) and accounting for the correlation from GP+CCH reconstruction of $\log D_L(z)$ in the likelihood (*corr.*).

	γ	β	δ_{int}	k_{UV}	k_X
			D24		
No evo	0.640 ± 0.006	7.04 ± 0.17	0.090 ± 0.002	-	-
No evo *corr.*	0.626 ± 0.007	7.48 ± 0.21	0.090 ± 0.002	-	-
Evo	0.602 ± 0.008	8.08 ± 0.23	0.087 ± 0.002	4.59 ± 0.20	3.07 ± 0.12
Evo *corr.*	0.601 ± 0.008	8.12 ± 0.22	0.088 ± 0.002	4.55 ± 0.20	3.11 ± 0.12
			L20		
No evo	0.647 ± 0.010	6.83 ± 0.30	0.235 ± 0.004	-	-
No evo *corr.*	0.637 ± 0.011	7.15 ± 0.33	0.235 ± 0.004	-	-
Evo	0.592 ± 0.013	8.35 ± 0.38	0.232 ± 0.004	4.51 ± 0.20	3.17 ± 0.13
Evo *corr.*	0.592 ± 0.013	8.36 ± 0.38	0.233 ± 0.004	4.51 ± 0.20	3.17 ± 0.13

the parameters that enter the corrected RL relation are k_{UV} and k_X, which – as in the case of GRBs – modify the luminosities as $g(z) = (1+z)^{k_L}$, where k_L is the correction as a function of redshift. This is the standard procedure based on the Efron & Petrosian method [436] applied in [186]. We follow the same procedure here, and assume Gaussian priors at 3σ on k_{UV} and k_X based on their value in [186]: $k_{UV} = 4.36 \pm 0.08$ and $k_X = 3.36 \pm 0.07$.[3]

From Table 8.1, one can see that the results are pretty stable across all the cases. The γ parameter is compatible with the typical value obtained in RL relation fitting analyses, ~ 0.6, and the same for $\beta \sim 8$, see e.g. [179, 106]. In particular, let us consider the most conservative case, i.e. accounting for correlation from GP+CCH.

Using L20 without correcting for evolution, our results $\gamma = 0.637 \pm 0.011$, $\beta = 7.15 \pm 0.33$ and $\delta_{int} = 0.235 \pm 0.004$ are compatible at $< 1\sigma$ with results in [516, 517, 518, 519]. Accounting for evolution, the constraints $\gamma = 0.592 \pm 0.013$, $\beta = 8.36 \pm 0.38$ and $\delta_{int} = 0.233 \pm 0.004$ are also compatible at $< 1\sigma$ with analyses that account for these effect such as [515, 519]. Regarding the sub-sample D24, our results for γ and β are compatible within 1σ with those obtained in [186], while we obtain a lower intrinsic scatter, $\delta_{int} = 0.088 \pm 0.002$, at 2.3σ from the result in [186]. This, in particular, represents the lowest intrinsic scatter we are able to find for the RL relation within our approach. Of course, the small value compared to the full sample of L20 is also a consequence of the reduced scatter with which the D24 sample is constructed. We find that the combination of the correlated case and redshift evolution correction provides the best fit to the data. For instance, considering the D24 sample and evaluating $\chi^2_{\rm min} = -2\ln\mathcal{L}_{\rm max}$ we obtain, without evolution, $\chi^2_{\rm min} = -1712$ (uncorrelated) and $\chi^2_{\rm min} = -1722$ (correlated). When including evolution, the values improve to $\chi^2_{\rm min} = -1756$ (uncorrelated) and $\chi^2_{\rm min} = -1758$

[3]We checked that enlarging the parameter space for the evolutionary coefficients with Gaussian priors at 5σ does not have an impact on the parameters of the relation. For instance, considering L20, we obtain: $\gamma = 0.592 \pm 0.013$, $\beta = 8.36 \pm 0.38$, $\delta_{int} = 0.232 \pm 0.004$. The results for the evolutionary coefficients, instead, read: $k_{UV} = 4.53 \pm 0.33$ and $k_X = 3.16 \pm 0.20$. All of them are compatible within 1σ with the results obtained considering Gaussian priors at 3σ, see Table 8.1.

(correlated). As anticipated, the latter case yields the lowest $\chi^2_{\rm min}$. Note that these values include the penalty (normalization) term of the likelihood, $\mathcal{N} = \prod_i \sqrt{2\pi\sigma^2_{\rm tot,i}}$, which can contribute a significant negative term when the variances are small. As a result, $-2\ln\mathcal{L}_{\rm max}$ can be negative even for small residuals and high likelihood. In all cases, a lower value of $\chi^2_{\rm min}$ corresponds to a higher likelihood and therefore a better fit (see also [518]). In view of these results, we can conclude that accounting for evolution is crucial to improve the quality of the calibration.

Built on this, we use the calibration results gathered in the correlated case and present the extended Hubble Diagram in Fig. 8.2, for both L20 and D24. This represents the final product of this calibration, grounded in the methodology developed in Chapter 7, and which therefore provides a complementary set of standardized luminosity distances. Together with the GRB Hubble diagram, it constitutes a valuable resource for future cosmological analyses, offering an extended view of the expansion history deep into the high-redshift regime.

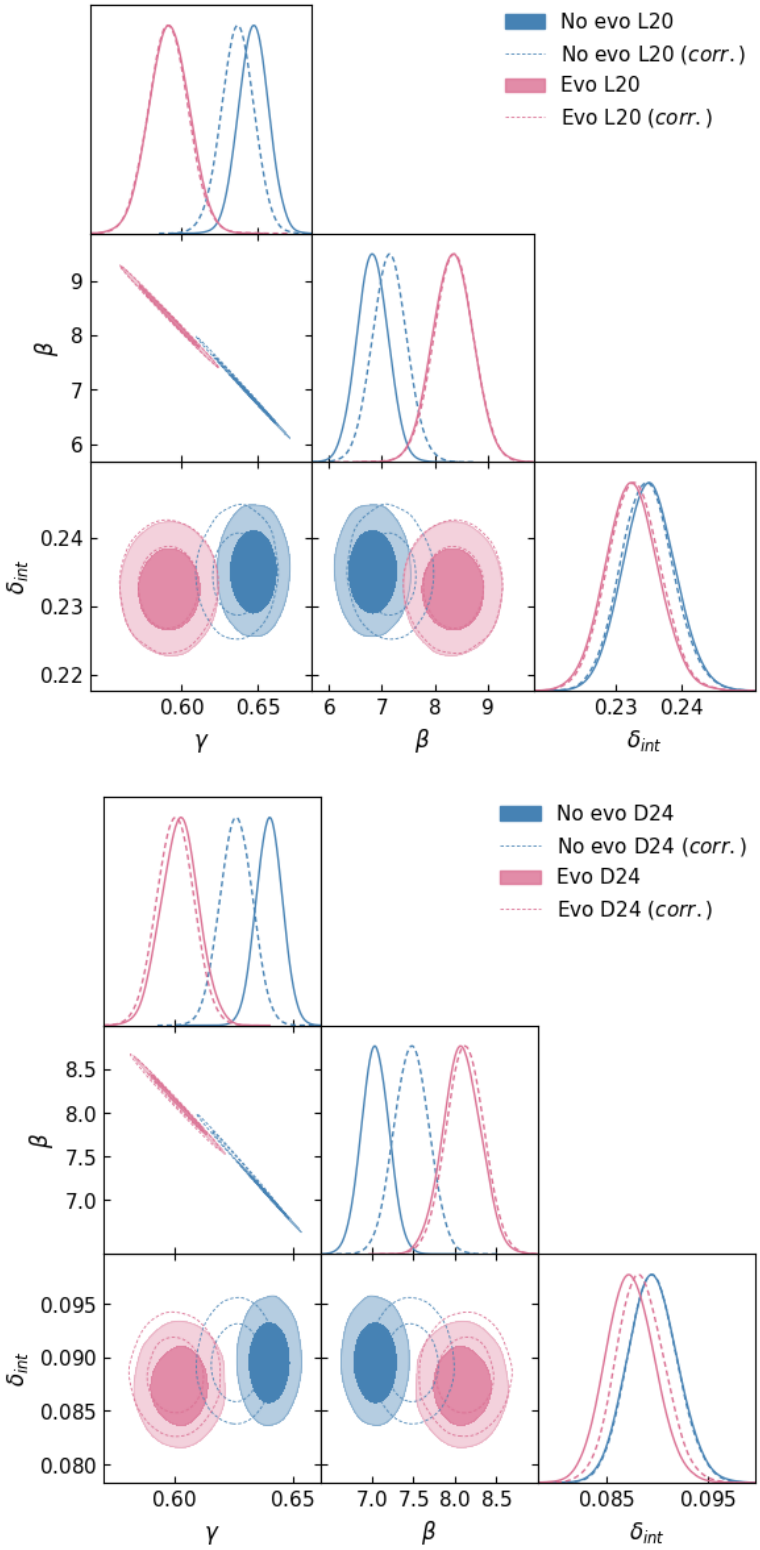

Figure 8.1. 1D posteriors and 2D contour plots at 68% and 95% C.L. obtained in the analysis of the LR relation using the baseline set-up and the L20 (upper plot) or D24 (lower plot) data sets. We show both the case in which the relation is corrected for redshift evolution effects (*Evo*) and the standard case (*No Evo*). We use dashed lines for the results obtained considering the correlation from GP+CCH reconstruction of $\log D_L(z)$ in the likelihood (*corr.* case). See main text for details.

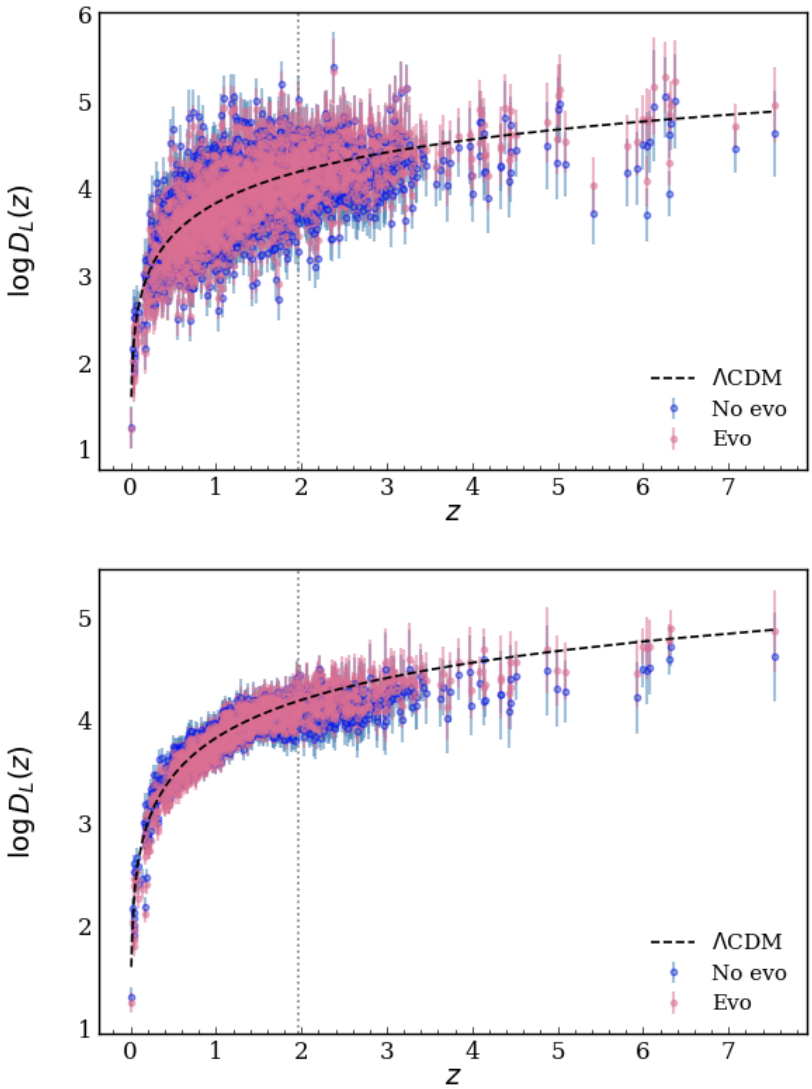

Figure 8.2. The extended distance ladder for QSOs from L20 (upper plot) and D24 (lower plot). The calibrated QSO data obtained with and without evolution effects are presented in light red and light blue, respectively. Both come from the MCMC analysis considering the correlated case, since it is the most conservative scenario. The dotted vertical line at $z \approx 2$ marks the border between the data employed in the calibration process and those used only in the extension of the ladder. The error bars of the calibrated GRB distances stand at 1σ C.L. In black, we plot the ΛCDM best-fit curve. The luminosity distance is given in Mpc.

Part V

On the consistency of BAO data and their impact on low-z solutions to the Hubble tension

Chapter 9

A late-time solution to the H_0 tension in view of BAO data

The content of this Chapter is based on our work published in [242].

In Sec. 3.1, we have seen that we can reframe the Hubble tension as a tension in the calibrators of the cosmic distance ladder, M and r_d. Indeed, Fig. 3.2 has shown us that uncalibrated SNIa and 3D BAO data force the calibrators of the direct and inverse distance ladders to lie in a quite narrow degeneracy band, which lacks of the overlap with the SH0ES constraint M^{R22} and the *Planck*/ΛCDM constraint r_d^{P18}. Indeed, if we believe in standard pre-recombination physics, i.e. if $r_d \sim 147$ Mpc, the absolute magnitude of SNIa must be $M \sim -19.4$ mag. This value is in clear tension with the SH0ES estimate in the second rung of the direct distance ladder (at $z \lesssim 0.02$), again at $\approx 5\sigma$. The discrepancy between the two cosmic ladders in the context of the standard model could be due to some issue with their calibrators [237, 238, 239, 241], either by unaccounted-for systematic errors or by new physics. However, let us consider the case in which the SH0ES determination of M, the *Planck* and SNIa data sets, are free from systematics. Then, the H_0 (or M) tension can be addressed with low-redshift solutions by considering the following possible scenarios.

- *Systematics in the anisotropic BAO data:* as already mentioned in Sec. 4.3, a fiducial cosmology is assumed in the 3D analysis to convert measured redshift and angles into comoving positions to build the 3D tracer map. Some model dependence introduced in the reconstruction of the BAO peak could in turn introduce some biases in the data. Transversal or angular BAO (2D BAO) data set, which is perhaps less subject to model dependencies [520, 420, 521], could open the window to solutions that keep a large value of $M \sim M^{R22}$ in a wider redshift range and introduce some new physics at $z \gtrsim 2$ to keep the location of the first peak of the CMB temperature power spectrum unaltered. In [240], it was already shown that there is a better agreement between SH0ES and the 2D BAO data, considering a constant M (see also [486]).

- *A sudden transition in M at some point of the second rung of the local distance*

ladder (at $z \lesssim 0.01$): this would lead to $M \sim -19.4$ mag in the Hubble flow and automatically reestablish the concordance between the SH0ES measurement and the value $H_0 \sim 67.5$ km/s/Mpc obtained from the fit of the ΛCDM to the 3D BAO and *Planck* data, essentially erasing the Hubble tension. Such a rapid transition could be due, for instance, to some difference of color correction between the SNIa in the calibration and cosmological samples, or to another unaccounted for refinement of the SNIa standardization procedure (the so-called Tripp calibration [522]) [523, 524, 228, 525], although the physical origin of these effects remains unknown. Alternatively, one can invoke some modified theory of gravity, as already discussed in Sec. 3.4, capable of an ultra-late-time change of the gravitational constant that could cause a rapid transition in M (see, e.g., [374, 370, 371, 372, 373]), as in Eq. (3.9), for instance. Nevertheless, it seems unlikely that such a redshift-dependent transition would leave the local Newton constant unchanged, as in the higher-redshift cosmological regime. Such a transition would be expected to modify the gravitational strength in the Friedmann equation, altering the ΛCDM background evolution and its ability to fit the CMB and anisotropic BAO data[1]. There is actually room for this transition to happen at higher redshifts, as we will discuss below.

- *A smoother transition in M together with an increase of $H(z)$ happening at $z \lesssim 0.2$:* if 3D BAO data are not affected by significant biases and if at the beginning of the third rung of the local distance ladder $M = M^{R22}$, we can ask ourselves how should we change the shape of $H(z)$ to explain the CMB and 3D BAO observations while keeping $H_0^{R22} \sim 73$ km/s/Mpc. We essentially need $H(z)$ to increase at small redshifts to reach the region of H_0 preferred by SH0ES but, at some redshift, the function has to go below the ΛCDM curve preferred by *Planck*. This is needed to compensate for the previous increase and leave the value of the angular diameter distance to the last scattering surface, $D_A(z_*)$, intact. These modifications must respect the good description of the 3D BAO data. Because 3D BAO calibrated with r_d^{P18} lead to angular diameter distances and values of $H(z)$ in good agreement with the standard model (see Fig. 9.1), the $H(z)$ reconstruction must enforce an evolution of M to bridge its low- and high-z estimates. Otherwise, the inverse distance ladder preserves the CMB–SH0ES tension at the level of M, even if H_0^{R22} is reproduced. This shows that, under standard pre-recombination physics and assuming no systematics, a varying M is unavoidable alongside any late-time new physics proposed to resolve the Hubble tension [526, 527].

Based on this last point, our aim in this Chapter is to study the background history required to solve the H_0 tension while not spoiling the good description of the CMB data. We consider standard pre-recombination physics, and pay special attention to the role played by the data on BAO employed to build the inverse

[1]Notice that $H_0^2 = 8\pi G\rho_c^0/3$. Hence, if we keep H_0 as in the *Planck*/ΛCDM model and consider a G different from the Newton constant, the critical energy density ρ_c^0 needs to be changed to fit the 3D BAO and CMB data properly. The only way of doing so by keeping $\Omega_m = \rho_m^0/\rho_c^0$ to the value preferred by the SNIa data is by changing, at least, the matter density ρ_m^0 as this would alter the amplitude and location of the CMB peaks.

distance ladder (see Sec. 2.2). In particular, the aim is to proceed in a model-independent way in constraining the shape of $H(z)$ at low redshifts using 3D BAO data calibrated with the measurement of r_d^{P18}, the SH0ES prior H_0^{R22}, and the CMB distance prior on $D_A(z_*)$ from *Planck*. The resulting $H(z)$ will be used to reconstruct the shape of $M(z)$, needed to avoid the inverse distance ladder bottleneck.

We will show that the shape preferred by the 2D BAO data set is quite different from the one preferred by the 3D BAO data. In the former case, the deviations from the ΛCDM appear also at much higher redshifts ($z \gtrsim 2$) and the transition is much smoother. In addition, we will study possible implications for the effective dark energy fluid and find that the data does not exclude a mild evolution of $M(z)$.

This Chapter is organized as follows.

- In Sec. 9.1, we propose the modification to the Hubble function at low-redshift and illustrate the methodology used in the reconstruction of $H(z)$ and $M(z)$.
- In Sec. 9.2, we describe two methods to test the fulfillment of the weak energy condition (WEC) by the effective dark energy fluid implied by these low-z solutions. We will do that with the aid of CCH data.
- In Sec. 9.3, we present the results of the methodology obtained using the anisotropic and angular BAO data sets, to illustrate which is their role in the late-time solutions to the H_0 tension. Implications for the effective dark energy fluid and the crossing of the phantom divide will be discussed as well.
- Results of the fulfillment of the WEC condition are detailed in Sec. 9.4.
- Final discussion and conclusion are presented in Sec. 9.5.

9.1 The modification to $H(z)$ at low-redshifts

Assuming a flat FLRW Universe, we propose a flexible parameterization of $H(z)$, which can reproduce phantom and quintessence behaviors, and also allows for the crossing of the phantom divide. The use of any dark energy or modified gravity model can be avoided, as well as the choice of how to split the energy budget of the dark sector at late times, while sticking to ΛCDM at higher redshifts. The proposed fitting expression reads

$$H(z) = \begin{cases} \bar{H}(z) + \delta H_1(z) & \text{if} \quad 0 < z \leq z_{\rm p} \\ \bar{H}(z) + \delta H_2(z) & \text{if} \quad z_p < z < z_{\rm max} \\ H_\Lambda(z) & \text{if} \quad z \geq z_{\rm max} \end{cases} \tag{9.1}$$

with

$$\bar{H}(z) \equiv \bar{H}_0 \sqrt{1 + \bar{\Omega}_m[(1+z)^3 - 1]}\,, \tag{9.2}$$

$$H_\Lambda(z) \equiv \tilde{H}_0 \sqrt{1 + \tilde{\Omega}_m[(1+z)^3 - 1] + \tilde{\Omega}_r[(1+z)^4 - 1]}\,, \tag{9.3}$$

and

$$\delta H_1(z) \equiv a + bz + cz^2 \quad ; \quad \delta H_2(z) \equiv d + ez + fz^2 \qquad . \tag{9.4}$$

The parameters $(\bar{\Omega}_m, \bar{H}_0) = (0.3153, 67.36)$ entering Eq. (9.2) are fixed to the best-fit values obtained in the TT,TE,EE+lowE+lensing ΛCDM analysis by *Planck* [11]. The quadratic polynomials $\delta H_1(z)$ and $\delta H_2(z)$ given in Eq. (9.4) parametrize deviations with respect to the mean Hubble function in the ΛCDM at $z < z_{\max}$. All the freedom of the model in this redshift range is transferred to the parameters $\{a, b, c, d, e, f\}$. For the part of $H(z)$ at $z \geq z_{\max}$ (see Eq. (9.3)) we use a Gaussian prior from *Planck* on $(\tilde{\Omega}_m, \tilde{H}_0)$ (taking into account their correlation, see Sec. 4.4), which allows us to make sure that at $z > z_{\max}$ the shape of $H(z)$ does not depart from the standard one, keeping also the physics at recombination untouched[2]. These parameters are left free in the fitting analyses. For more details on the CMB data employed, we refer the reader to Sec. 4.4.

We impose the following six constraints, which allow us to compute the parameters $\{a, b, c, d, e, f\}$ entering the functions $\delta H_1(z)$ and $\delta H_2(z)$,

$$\delta H_1(z = 0) = H_0 - \bar{H}_0 \equiv \delta H_0 \,, \tag{9.5}$$

$$\delta H_1(z_p) = \delta H_2(z_p) \equiv \delta H_p \,, \tag{9.6}$$

$$\left.\frac{\partial \delta H_1}{\partial z}\right|_{z=z_p} = \left.\frac{\partial \delta H_2}{\partial z}\right|_{z=z_p} = 0 \,, \tag{9.7}$$

$$\delta H_2(z_{\max}) = H(z_{\max}) - \bar{H}(z_{\max}) \equiv \delta H_{\max} \,, \tag{9.8}$$

with z_p the pivot redshift at which we have the extrema of δH_1 and δH_2. The two conditions in Eqs. (9.6) and (9.7) are obtained by demanding at z_p the continuity of $H(z)$ and its derivative, respectively, whereas the condition (9.8) enforces the continuity of the Hubble function at $z_{\max}$. All the conditions in (9.5)-(9.8) can be written in a very simple way as

$$\begin{pmatrix} \delta H_0 \\ \delta H_p \\ 0 \end{pmatrix} = \begin{pmatrix} 1 & 0 & 0 \\ 1 & z_p & z_p^2 \\ 0 & 1 & 2z_p \end{pmatrix} \begin{pmatrix} a \\ b \\ c \end{pmatrix} \tag{9.9}$$

and

$$\begin{pmatrix} \delta H_{\max} \\ \delta H_p \\ 0 \end{pmatrix} = \begin{pmatrix} 1 & z_{\max} & z_{\max}^2 \\ 1 & z_p & z_p^2 \\ 0 & 1 & 2z_p \end{pmatrix} \begin{pmatrix} d \\ e \\ f \end{pmatrix} \,, \tag{9.10}$$

so the constants $\{a, b, c, d, e, f\}$ needed to compute $H(z)$ can be obtained straightforwardly.

We consider the suite of parameters $\{\tilde{\Omega}_m, \tilde{H}_0, H_0, z_p, \delta H_p, z_{\max}\}$. The pair $\{\tilde{\Omega}_m, \tilde{H}_0\}$ and H_0 will be mainly controlled by the *Planck* and SH0ES priors, respectively. The triad $\{z_p, \delta H_p, z_{\max}\}$ is a priori more uncertain. However, we can already understand that if we set $z_{\max}$ to a value smaller than the smallest redshift in the BAO data set, $z_{\mathrm{BAO,min}}$, we will be unable to put strong constraints on the

[2]The uncertainties of $(\tilde{\Omega}_m, \tilde{H}_0)$ have an impact on the observables at $z > z_{\max}$, and also propagate to the uncertainties of the parameters entering the Hubble function at smaller redshifts. This is why it is important to consider them.

pair $\{z_p, \delta H_p\}$, since in this case there exists a full degeneracy between these two parameters, which is fixed by the CMB prior on $D_A(z_*)$. Thus, for $z_{\max} \leq z_{\mathrm{BAO,min}}$ we can only constrain the direction of the degeneracy line. We use uninformative flat priors for $\{z_p, \delta H_p\}$, much wider than the constraints we get from the fitting analyses.

We reconstruct the Hubble function in Eq. (9.1) by means of MCMC analysis, employing the M-H algorithm and ensuring convergence in all the runs with values of the Gelman-Rubin convergence statistic $R - 1 < 0.02$ for all the sampled parameters (see Sec. 5.2). We set $z_{\max}$ to different values in order to study its impact in our analyses, and sample the five parameters contained in the vector $\{\tilde{\Omega}_m, \tilde{H}_0, H_0, z_p, \delta H_p\}$. Using the resulting $H(z)$, it is also possible to reconstruct the following interesting quantities:

1. the shape of $M(z)$, since we want to assess whether the low-z solutions to the H_0 tension require the evolution of this quantity with the redshift. We use GP to generate samples of $m(z)$ from the Pantheon+ SNIa compilation, and combine them with our Markov chains of $H(z)$ to reconstruct $M(z)$. For the reconstruction of $m(z)$, we use the `GaPP` package, training the GP with Matérn 32 kernel and the optimization of its hyperparameters. This procedure has already been tested and employed in Chapter 6.

2. higher order cosmographical functions as the deceleration parameter q_0, which, making Eq. (2.7) explicit, reads

$$q(z) = -1 + \frac{(1+z)}{H(z)} \frac{dH}{dz} \,. \tag{9.11}$$

3. the typical shape of the density of a hypothetical effective dark energy fluid in these low-redshift solutions, provided that such a fluid is covariantly self-conserved. We define

$$H^2(z) \equiv \frac{8\pi G}{3} [\tilde{\rho}_m^0 (1+z)^3 + \rho_{\mathrm{de}}(z)] = \tilde{\Omega}_m \tilde{H}_0^2 (1+z)^3 + \frac{8\pi G}{3} \rho_{\mathrm{de}}(z) \,, \tag{9.12}$$

with $H(z)$ given by Eq. (9.1), and also use

$$H_\Lambda^2(z) = \frac{8\pi G}{3} [\tilde{\rho}_m^0 (1+z)^3 + \tilde{\rho}_\Lambda] = \tilde{\Omega}_m \tilde{H}_0^2 (1+z)^3 + \frac{8\pi G}{3} \tilde{\rho}_\Lambda \,, \tag{9.13}$$

where $H_\Lambda(z)$ takes the same form already assumed for $H(z)$ at $z > z_{\max}$ (cf. Eq. (9.3)) and $\tilde{\rho}_\Lambda$ is the energy density associated to the cosmological constant in the ΛCDM model. Using these two expressions we find the following relative difference between the effective dark energy density $\rho_{\mathrm{de}}(z)$ and $\tilde{\rho}_\Lambda$,

$$\Delta(z) \equiv \frac{\rho_{\mathrm{de}}(z) - \tilde{\rho}_\Lambda}{\tilde{\rho}_\Lambda} = \frac{H^2(z) - H_\Lambda^2(z)}{H_\Lambda^2(z) - \tilde{\Omega}_m \tilde{H}_0^2 (1+z)^3} \,. \tag{9.14}$$

To implement the methodology described so far, we make use of the following data sets:

- The SH0ES prior on the Hubble parameter, H_0^{R22} [94].
- The anisotropic (3D) BAO data listed in Table A.2, with the addition of the Ly-α forests eBOSS DR16 results at $z = 2.334$, given by $D_M/r_d = 37.5^{+1.2}_{-1.1}$ and $c/(Hr_d) = 8.99^{+0.20}_{-0.19}$ [528].
- The transversal (angular, 2D) BAO data listed in Table A.3 but without the DESY6 point at $z = 0.85$[3].
- The *Planck* 2018 CMB TT,TE,EE+lowE+lensing ΛCDM Gaussian priors on the quantities $\{D_A(z_*), r_d, \tilde{\Omega}_m, \tilde{H}_0\}$, including the corresponding covariance matrix. This information has been presented in Sec. 4.4.

  The use of this prior is justified by our assumption of standard pre-recombination physics. We generate samples of these parameters and the BAO data from multivariate Gaussian distributions and obtain a joint data vector which incorporates the BAO angular diameter distances, dilation scales, $H(z_i)$, together with $\{D_A(z_*), \tilde{\Omega}_m, \tilde{H}_0\}$, and their joint covariance matrix. The prior from SH0ES can be easily added, considering 0 correlation with the other parameters, since it is independent. The resulting vector of data and covariance matrix constitute our "Baseline_3D" or "Baseline_2D" data sets, depending on the BAO data set that we consider. They are 17- and 19-dimensional, respectively.
- The SNIa data from the Pantheon+ compilation [95], used only to reconstruct $M(z)$ with the help of the shapes of $H(z)$ obtained in the MCMC analysis.
- The data on CCH from Table A.1 and the corresponding covariance matrix. In Sec. 9.4, we employ CCH together with the SH0ES or *Planck* priors on the Hubble parameter to study the WEC.

The results of the three points above mentioned, obtained using either anisotropic or angular BAO data, are presented in Sec. 9.3.

9.2 The weak energy condition

The weak energy condition is fulfilled if the null energy condition

$$T_{\mu\nu}k^\mu k^\nu \geq 0 \tag{9.15}$$

is satisfied for any null vector ($k^\mu k_\mu = 0$) together with

$$T_{\mu\nu}u^\mu u^\nu \geq 0\,, \tag{9.16}$$

where $T_{\mu\nu}$ is the energy-momentum tensor (see Eq. (1.3) and u^μ is a time-like four-vector. In a FLRW Universe, for a perfect fluid with density ρ and pressure p, Eqs. (9.16) and (9.15) translate into the two conditions

$$\rho \geq 0 \qquad \text{and} \qquad \frac{d\rho}{dz} \geq 0\,, \tag{9.17}$$

[3]This measurement was not available yet.

which are satisfied by all the fluids considered in the ΛCDM model. This means that a violation of the WEC would automatically imply the existence of physics beyond the standard model[4]. Here, we test whether the effective dark energy driving cosmic acceleration satisfies the WEC, assuming it is covariantly self-conserved and that matter dilutes in the standard way as

$$\rho_m(z) = \rho_m^0 (1+z)^3 \,. \tag{9.18}$$

In this case, the Friedmann equation together with the second inequality of Eq. (9.17) lead to [529]

$$\Omega_m \leq \frac{E^2(z) - 1}{(1+z)^3 - 1} \,, \tag{9.19}$$

with $E(z)$ the normalized Hubble rate. We denote the right-hand side of this inequality as $\Omega_m^{\max}$. It is an upper bound that cannot be surpassed if the effective dark energy fluid is not phantom.

In [529], CCH are combined with a prior on H_0 to obtain an estimate of $\Omega_m^{\max}$ for each available CCH data point, by sampling Gaussian distributions of H_0 and the CCH data. Here, we improve the analysis by taking advantage of the larger sample of CCH measurements (33 data points instead of 9), also employing their corresponding covariance matrix. Moreover, we apply an advanced method to get a single representative value of $\Omega_m^{\max}$, duly accounting for the correlations and assessing the impact of non-Gaussian features in the multivariate distribution. This can be done by means of the so-called *Edgeworth expansion*. It allows us to compute an analytical approximation of the underlying (exact) distribution,

$$f(\vec{x}) = G(\vec{x}, \lambda)[1 + \frac{1}{6} k^{ijk} h_{ijk}(\vec{x}, \lambda) + \frac{1}{24} k^{ijkl} h_{ijkl}(\vec{x}, \lambda) + ...] \,, \tag{9.20}$$

see [530] and references therein. Here $x^i = d^i - \mu^i$, with $d^i = \Omega_m^{\max}(z_i)$ and $\vec{\mu}$ the mean vector, i.e. $\mu^i =< \Omega_m^{\max}(z_i) >$. $\lambda = C^{-1}$ is the inverse of the covariance matrix, with elements $C^{ij} =< x^i x^j >$. $G(\vec{x}, \lambda)$ is the multivariate Gaussian distribution built from that mean and covariance matrix, and $k^{ijk} =< x^i x^j x^k >$ and $k^{ijkl} =< x^i x^j x^k x^l > - C^{ij} C^{kl} - C^{ik} C^{jl} - C^{il} C^{jk}$ are the elements of the higher-order cumulant matrices, called skewness and kurtosis matrices, respectively. On the other hand,

$$h_{ij...}(\vec{x}, \lambda) = (-1)^r G^{-1}(\vec{x}, \lambda) \partial_{ij...} G(\vec{x}, \lambda) \,, \tag{9.21}$$

are the Hermite tensors of order r, with r the number of indices. The Hermite tensors of order 3 and 4 appearing in Eq. (9.20) read, respectively,

$$h_{ijk}(\vec{x}) = \lambda_{in} \lambda_{jt} \lambda_{kl} x^n x^t x^l - (\lambda_{ij} \lambda_{kt} + \lambda_{ik} \lambda_{jt} + \lambda_{jk} \lambda_{it}) x^t \,, \tag{9.22}$$

$$\begin{aligned} h_{lijk}(\vec{x}) =& \lambda_{ln} x^n h_{ijk}(\vec{x}) + \lambda_{ij} \lambda_{kl} + \lambda_{ik} \lambda_{jl} + \lambda_{jk} \lambda_{il} \\ & - (\lambda_{il} \lambda_{jt} \lambda_{kn} + \lambda_{in} \lambda_{jl} \lambda_{kt} + \lambda_{in} \lambda_{jt} \lambda_{kl}) x^n x^t \,. \end{aligned} \tag{9.23}$$

In this calculation we have made use of the fact that $\partial_i G = -G \lambda_{ij} x^j$ and of Einstein's summation convention. All these objects can be directly computed from the chain

[4]The cosmological constant Λ satisfies the weak energy condition, but not the strong one, which reads, instead, $\rho + p \geq 0$ and $\rho + 3p \geq 0$.

of $\Omega_m^{\max}(z_i)$, with i the index that runs over the CCH data points. Once we have Eq. (9.20), we can sample it treating it as a one-dimensional distribution for $\Omega_m^{\max}$ (instead of a multivariate distribution for the array $\{\Omega_m^{\max}(z_i)\}$). If the non-Gaussian features are negligible, then it reduces of course to a Gaussian with the following weighted mean and variance,

$$\bar{\Omega}_m^{\max} = \frac{\sum_{i,j=1}^{33} \mu^i \lambda_{ij}}{\sum_{i,j=1}^{33} \lambda_{ij}} \quad ; \quad \sigma^2 = \frac{1}{\sum_{i,j=1}^{33} \lambda_{ij}} \,. \tag{9.24}$$

Otherwise, Eq. (9.20) introduces some corrections in the computation of the central value and confidence intervals of $\Omega_m^{\max}$.

The WEC can also be tested by considering the following relation,

$$\frac{\rho_{\rm de}(z)}{\rho_{\rm de}^0} = \frac{E^2(z) - \Omega_m(1+z)^3}{1-\Omega_m} \,, \tag{9.25}$$

which is directly obtained from the Friedmann equation (cf. Eq. (1.19)). By sampling $H(z)$ from the CCH data and combining it with a prior on H_0 and ω_m to compute Ω_m, one can constrain Eq. (9.25) at the redshifts probed by the CCH. Negative values of this quantity hint at a violation of the first WEC of Eq. (9.17). Instead, $0 < \rho_{\rm de}(z)/\rho_{\rm de}^0 < 1$ means that the second condition is not fulfilled.

We will present the results of this analysis in Sec. 9.4.

9.3 Results: the impact of the BAO data

We begin this Section with Fig. 9.1, which can already give a prediction of what we should expect from the results of the analysis presented in Sec. 9.1. The figure tells us that 3D BAO data are in good agreement with fiducial cosmology[5], and this is why in order to accommodate the SH0ES measurement one has to modify the model at redshifts below ~ 0.1, which is the minimum BAO redshift in the 3D data set, cf. Table A.2. Conversely, there is an obvious tension between the best-fit *Planck*/ΛCDM cosmology and the 2D BAO data in the redshift range $0.4 \lesssim z \lesssim 0.7$, since all the blue points of the upper-left plot in that redshift range fall below the black curve. These 2D BAO angular diameter distances are smaller than preferred by the standard model. Consequently, $H(z)$ values are larger, thereby more in agreement with SH0ES [240]. To reestablish the concordance in the context of the distance ladder built with *Planck* and the 2D BAO data, we expect that we need to modify the shape of $H(z)$ at much higher redshifts too, $z \sim 1$.

Now, let us see what the actual results are.

[5]There are only mild tensions with the DES Y3 data point at $z = 0.835$ and the Ly-α forest data at $z = 2.334$ from eBOSS DR16, but they are much less significant than the Hubble tension.

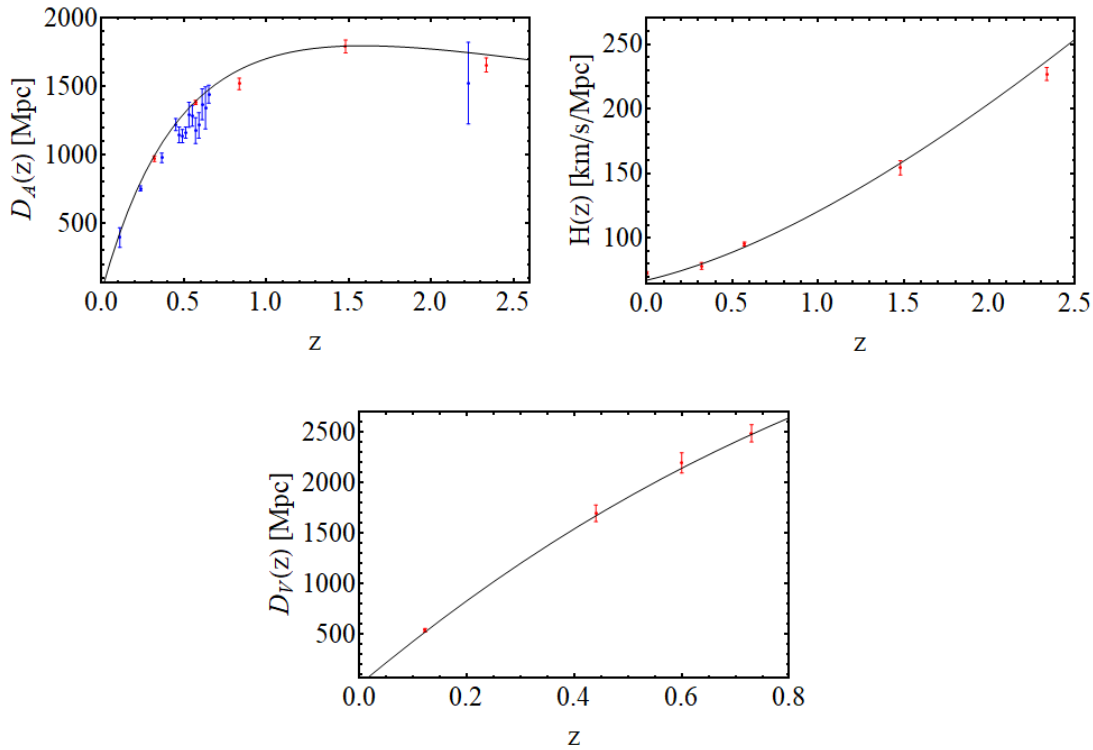

Figure 9.1. 3D and 2D BAO data, in red and blue, respectively, calibrated with the *Planck*/ΛCDM value of the sound horizon r_d^{P18}. We also plot (in black) the curves of the various observables computed with the best-fit *Planck*/ΛCDM cosmology.

Results from Baseline_3D

We present in the left two panels of Fig. 9.2 the reconstructed curves of $H(z)$, and the associated curves of $M(z)$, obtained from the fit to the Baseline_3D data set, following the method explained in Sec. 9.1. More concretely, we show only the 68% curves with the lowest χ^2. Triangle plots for the parameters entering the Baseline_3D (but also Baseline_2D) analysis are provided in Appendix C.

We have fixed $z_{\rm max} = 1$, although we have checked that values of $z_{\rm max} = 0.5, 2, 4$ do not introduce any significant change in the shape of the reconstructed function and the minimum values of the χ^2. Therefore, the results obtained with the Baseline_3D data set are stable and basically insensitive to the parameter $z_{\rm max}$. We find in all cases a phantom-like increase of $H(z)$ at $z \lesssim 0.2$ with respect to the best-fit *Planck*/ΛCDM model, and slightly smaller values of $H(z)$ at higher redshifts. This is consistent with the results reported in [526]. This upper bound is close to the minimum redshift of the 3D BAO data, as expected from Fig. 9.1. In contrast, there is no lower bound on the redshift at which the non-standard growth of $H(z)$ starts. This means that the Baseline_3D data set is not capable of arbitrating between an ultra-late-time transition at $z \lesssim 0.01$ and a late-time transition at $0.01 \lesssim z \lesssim 0.2$. We denote this (transition) redshift as z_t, and define it as the redshift at which $H(z_t) = 1.005 H_\Lambda(z_t)$, see its posterior distribution in the left plot of Fig. 9.3. The smaller is z_t the faster the increase of $H(z)$ and $M(z)$ in the transition, of course.

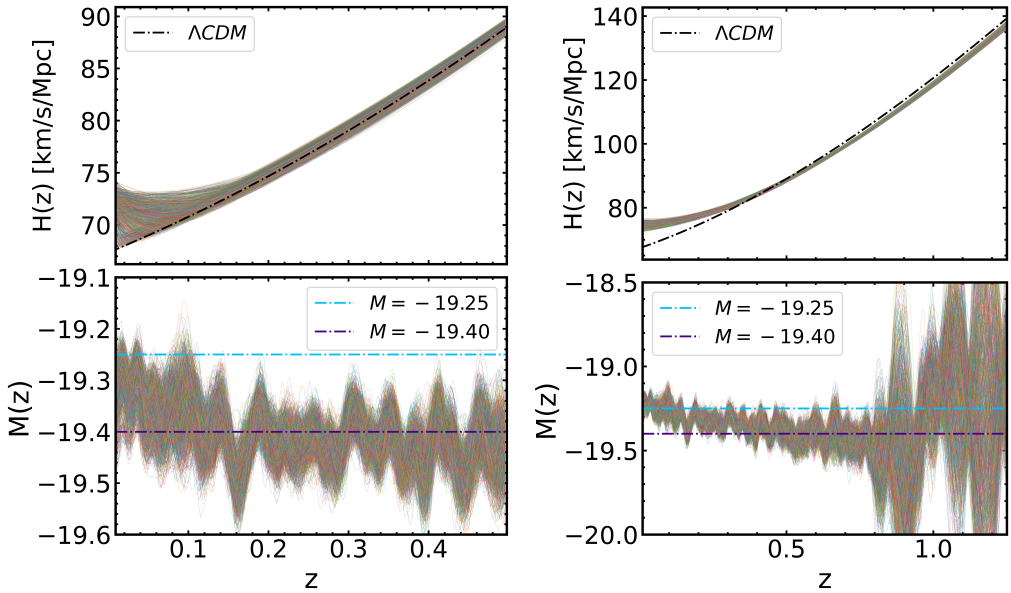

Figure 9.2. *Left panels:* 68% curves of $H(z)$ (upper plot) with the smallest χ^2 obtained with the Baseline_3D data set, using Eq. (9.1) and fixing $z_{\max} = 1$, and the corresponding shape of $M(z)$ (lower plot). We zoom in the region $z < 0.5$ to better appreciate the increase of $H(z)$ and $M(z)$ at small redshifts. At $z \gtrsim 0.2$ $H(z) \simeq H_\Lambda(z)$ (see Eq. 9.3) and $M(z)$ becomes compatible with the value obtained with the inverse distance ladder assuming the ΛCDM, $M \sim -19.4$ mag. *Right panels:* same, but for Baseline_2D and using $z_{\max} = 4$. The curves of $H(z)$ deviate from the *Planck*/ΛCDM prediction in a broader redshift range, with a transition from $H < H_{\Lambda\mathrm{CDM}}$ to $H > H_{\Lambda\mathrm{CDM}}$ happening now at $z_t \sim 0.5 - 0.8$. This is also reflected in the transition of $M(z)$ (lower plot), which also happens at much higher z than in the 3D BAO case analysis.

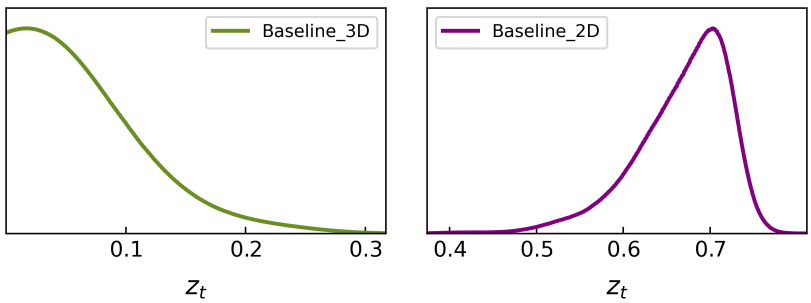

Figure 9.3. Posterior distributions of the transition redshift z_t obtained with the Baseline_3D (left) and Baseline_2D (right) data sets from the corresponding Monte Carlo analyses.

Although there is a clear trend towards the value of M measured by SH0ES at $z \sim 0$, M^{R22}, it is not easy to grasp the details of the transition for a fixed z_t due to the large number of curves contained in the plots of Fig. 9.2. This is why we choose to show in Fig. 9.4 only those curves with $0.09 < z_t < 0.15$, as an illustrative example.

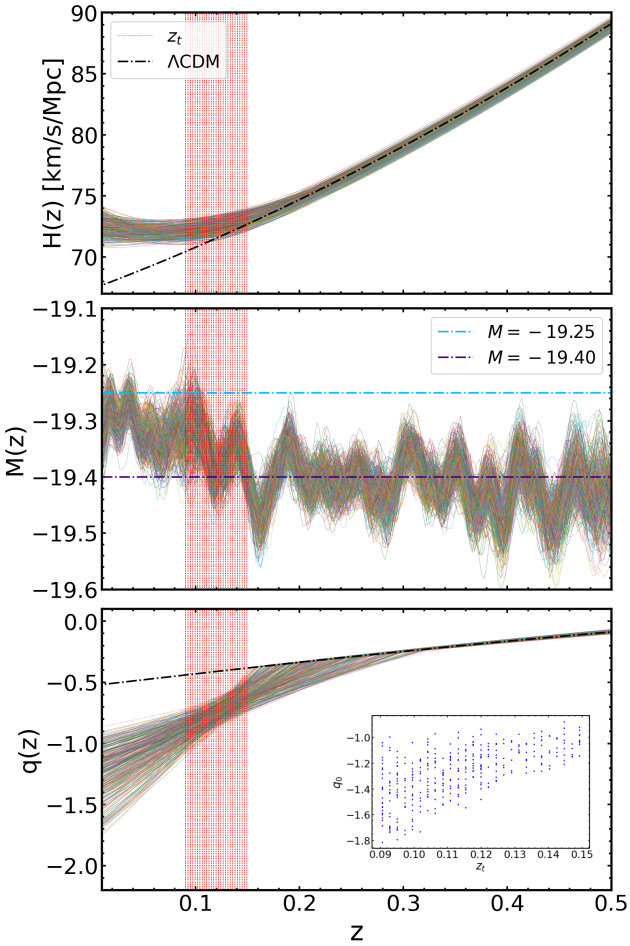

Figure 9.4. Same as in Fig. 9.2, but only for the curves with $0.09 < z_t < 0.15$. The vertical red band indicates the range of values of z_t covered. In the bottom plot, we present the corresponding shapes of the deceleration parameter $q(z)$, Eq. (9.11), and include an inner plot with the positive correlation between its value at $z = 0$, q_0, and z_t.

Also, we study an additional consequence of the fast increase of the Hubble function at those very low redshifts: a natural drop in the deceleration parameter, given by Eq. (9.11). Its shape is shown in the bottom plot of Fig. 9.4. The values of $q(z = 0) \equiv q_0$ are typically 2 or 3 times smaller than the one preferred by ΛCDM, $q_0 \approx -0.55$, and can be even larger for lower values of z_t[6]. We also observe a positive correlation between the transition redshift and q_0, as expected. We show this in the inner plot. The smaller the value of z_t, the more accelerated has to be the Universe to transition to H_0^{R22} and, hence, the more negative the value of q_0.

In Fig. 9.5 we show some shapes of $\Delta(z)$ (cf. Eq. (9.14)) obtained with $z_{\max} = 0.5$ and $z_{\max} = 1$. They have been selected from the group of 68% curves with lowest χ^2 in the MCMC, and their form can be considered to be quite representative of the behavior that is required to explain the data and alleviate the Hubble tension. By construction of Eq. (9.1), we always find a crossing of the phantom divide, of course.

[6]These small values of q_0 would be excluded if we considered a fixed M [481].

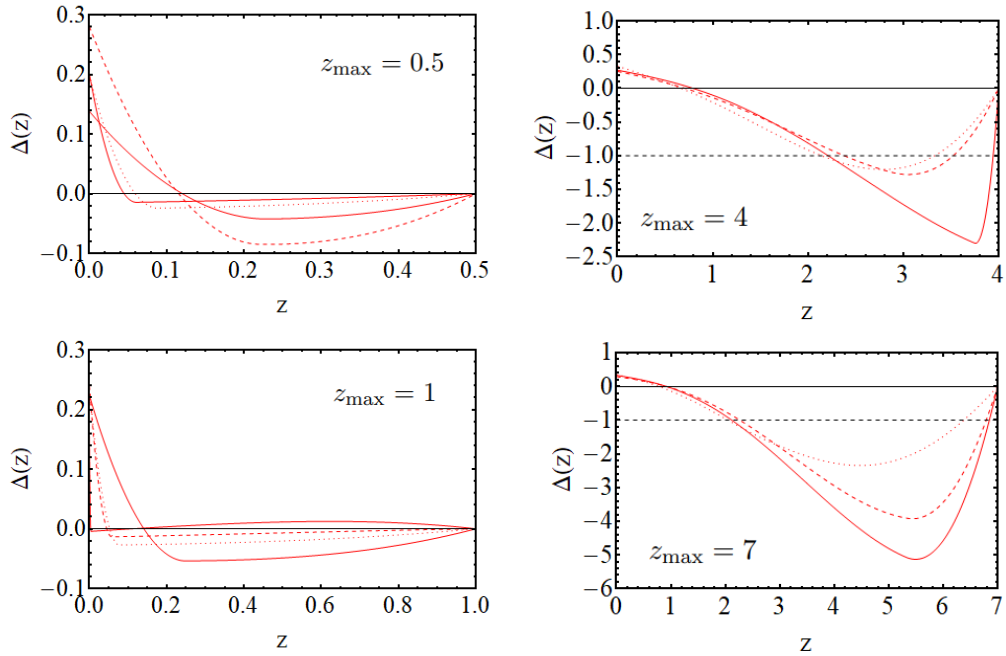

Figure 9.5. Curves of $\Delta(z)$ (Eq. (9.14)) selected from the group of 68% curves with lowest χ^2 in the MCMC and represent the typical behavior of $\Delta(z)$ required to solve the Hubble tension. *Left panels*: results from Baseline_3D data set with $z_{\max} = 0.5$ (upper plot) and $z_{\max} = 1$ (lower plot). The transition happens in both analyses at $z_t \lesssim 0.2$. *Right panels*: results from Baseline_2D data set with $z_{\max} = 4$ (upper plot) and $z_{\max} = 7$ (lower plot). The transition happens in both cases at $z_t \lesssim 1$, with the dark energy density becoming negative ($\Delta < -1$) at $z \sim 2$.

Nevertheless, we want to remark that the steepness of the quintessence evolution between z_p and $z_{\max}$ depends on both parameters. Larger values of z_p and smaller values of $z_{\max}$ favor a transition from quintessence to phantom, but the Baseline_3D data set cannot exclude a solution with an almost constant $\tilde{\rho}_{\rm de}$ before the transition for some combinations of these two parameters. What is always needed is a very fast phantom evolution in the last stages of the cosmic expansion, which is faster for smaller values of z_t. Our results resonate well with the conclusions of [526, 531, 532], and also with [533, 534]. In addition, if we decrease $z_{\max}$ we can find more negative values of Δ at its minimum.

We can also study the goodness of fit through a reduced χ^2 as

$$\chi^2_{\rm red} = \chi^2_{\rm min}/(N-n)\,, \tag{9.26}$$

with $N = 17$ the number of data points and $n = 5$ the number of fitting parameters (see Sec. 9.1). We obtain $\chi^2_{\rm red} \sim 1.3$, slightly above 1. This can be explained essentially by the $\sim 2\sigma$ tension between ΛCDM and the BAO data from DES and Lyα eBOSS DR16, and also by the fact that the effective number degrees of freedom can be significantly larger due to the existence of strong correlations between the parameters, see e.g. [535]. If we remove the aforesaid data points, we get $\chi^2_{\rm red} \lesssim 1$. In any case, the value $\chi^2_{\rm red} \sim 1.3$ corresponds to a p-value $= 0.21$ for $N - n = 12$

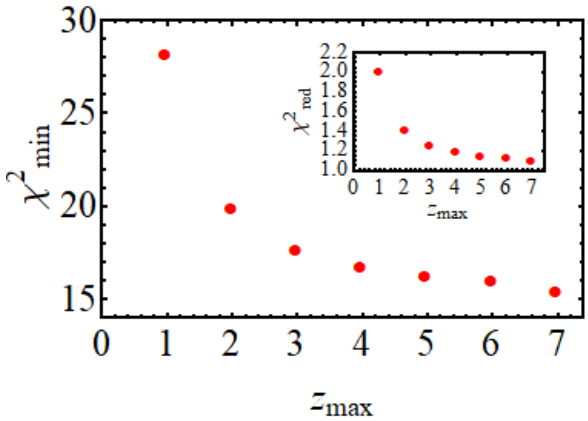

Figure 9.6. Minimum χ^2 values obtained in the fitting analyses with the Baseline_2D data set, as a function of $z_{\rm max}$. We also show the reduced χ^2 (Eq. (9.26)) in the inner plot. The minimum χ^2 reaches a plateau at $z_{\rm max} \sim 4$. This explains why the transition redshift remains stable for $z_{\rm max} \gtrsim 4$, with $0.5 \lesssim z_t \lesssim 0.8$. The value $\chi^2_{\rm red} \sim 1.1$ (p-value=0.38) in the plateau proves the appropriateness of the fitting function, Eq. (9.1).

degrees of freedom, hence we can conclude that our fitting function is performing well.

Finally, we have also checked that the inclusion of the CCH data does not alter our results in a significant way. We will explain why in Sec. 9.4.

Results from Baseline_2D

The reconstructions of $H(z)$ and $M(z)$ obtained with the Baseline_2D data set are presented in the right panels of Fig. 9.2. We set $z_{\rm max} = 4$. In Fig. 9.6 one can see what is the decrease of the χ^2 as a function of $z_{\rm max}$. The former remains stable for values of $z_{\rm max} \gtrsim 4$. Indeed, we find that in these cases the transition always happens at $0.5 \lesssim z_t \lesssim 0.8$ and, hence, at a much higher redshift than that required by 3D BAO, see again Fig. 9.3. The explanation is actually very simple, and we already had a hint for it by looking at Fig. 9.1: transversal BAO data calibrated with r_d^{P18} leads to smaller angular diameter distances than in ΛCDM (and larger values of $H(z)$) at $z \lesssim 0.7$. Thus, the shape of the Hubble function has to go below the standard one after these redshifts in order to compensate for these effects and respect the CMB preferred value of $D_A(z_*)$.

For sufficiently large values of $z_{\rm max}$ one can increase the compatibility with M^{R22} within a larger redshift range, up to $z \gtrsim 0.5$, and the deviation at higher redshifts cannot be considered to be statistically significant. The shapes of $H(z)$ and $M(z)$ leading to a potential solution to the Hubble tension are therefore quite different from those required by the 3D BAO data. In this case we do not find significant departures of the deceleration parameter from the ΛCDM value at $z \ll 1$. Again, our results remain stable under the inclusion of CCH data.

If interpreted in terms of an effective self-conserved dark energy fluid, the change of $H(z)$ with respect to the ΛCDM requires in this case negative values of the dark energy density at $z \gtrsim 2$. The matter energy density at these redshifts is very large, so we need also a large value of $|\tilde{\rho}_{\rm de}|$ to have a sizable effect on the Hubble function,

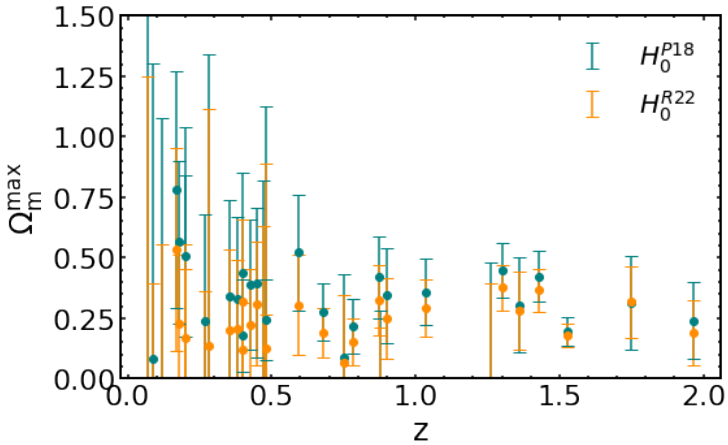

Figure 9.7. Upper bounds on the present value of Ω_m imposed by the WEC, see Eq. (9.19). Only the (physical) range of positive values of $\Omega_m^{\max}$ is shown. Since the distributions for $\Omega_m^{\max}$ at some redshifts are highly non-Gaussian, we indicate their corresponding peaks (with dots) and the confidence intervals at 68% C.L. We show the results when H_0 is sampled using the *Planck*/ΛCDM value H_0^{P18} (in blue) and the SH0ES measurement H_0^{R22} (in orange).

and $\tilde{\rho}_{\rm de}$ has to be negative in order the change to happen in the right direction. A couple of representative plots showing this characteristic behavior are presented in Fig. 9.5 (right panels). The crossing of the phantom divide is also allowed by the angular BAO data set.

Models with a negative dark energy density at these redshifts are available in the literature. Some examples are the sign-switching cosmological constant model of [536, 487], the self-conserved dark energy model of [537]. In addition, several studies have suggested the presence of unaccounted systematics in the standardization of SNIa [538, 539, 540]. Such effects could potentially account for the smooth evolution of $M(z)$ indicated by our analysis, particularly when the SH0ES prior and 2D BAO data are employed, rather than 3D BAO, in constructing the inverse distance ladder.

9.4 Results of the WEC violation

The results presented in Sec. 9.3 indicate that all low-z solutions to the Hubble tension involving new physics at $z \gtrsim 0.01$ necessarily require a violation of the WEC, irrespective of the BAO data set used to construct the inverse distance ladder. In both cases, the outcome is a phantom-like evolution of the effective dark energy component, though manifesting at different stages of cosmic expansion. Specifically, the Baseline_3D analysis places this transition at $z \lesssim 0.2$, whereas for Baseline_2D it occurs within $0.5 \lesssim z \lesssim 0.8$. In the latter case, the effective dark energy density even becomes negative at $z \gtrsim 2$.

We now apply the method of [529], as outlined in Sec. 9.2, to test whether the CCH data, which are independent of the Baseline data sets, necessitate a violation of the WEC given in Eq. (9.19), under the assumption of a self-conserved effective dark energy fluid. This condition is satisfied provided that the energy density does

not increase with cosmic expansion, i.e., if dark energy is not phantom. We examine how the outcome changes when adopting the SH0ES and *Planck* priors on H_0. In Fig. 9.7, we show the 33 constraints on $\Omega_m^{\max}$ obtained from the sampling of the CCH data listed in Table A.1. In this calculation we have duly accounted for the correlations between the CCH data points. From the values of $\Omega_m^{\max}$, we extract a single representative upper bound on the matter parameter Ω_m. From Eq. (9.24), using the SH0ES and *Planck* priors on H_0, we obtain, respectively,

$$\Omega_m^{\max} = 0.250 \pm 0.031 \qquad [\mathrm{CCH} + H_0^{R22}]\,, \tag{9.27}$$

$$\Omega_m^{\max} = 0.314 \pm 0.036 \qquad [\mathrm{CCH} + H_0^{P18}]\,. \tag{9.28}$$

To assess whether the WEC is violated, we examine whether current constraints on Ω_m fall above or below the upper bounds set by $\Omega_m^{\max}$, as determined from the CCH data set and the local H_0 values considered in the computation of $\Omega_m^{\max}$. As a natural starting point, we compare with the value of Ω_m inferred from CMB observations. If we consider standard physics before recombination, we can take the *Planck* constraint $\omega_m^{P18} = 0.1415 \pm 0.0009$ [11] and combine it with SH0ES and *Planck* priors on H_0, yielding

$$\Omega_m = 0.265 \pm 0.008 \qquad [\omega_m^{P18} + H_0^{R22}]\,, \tag{9.29}$$

$$\Omega_m = 0.315 \pm 0.007 \qquad [\omega_m^{P18} + H_0^{P18}]\,. \tag{9.30}$$

These two results represent the constraints on Ω_m preferred by CMB, depending on whether we rely on a small or large value of the Hubble constant. Although the central values of Ω_m lie slightly above the upper bounds $\Omega_m^{\max}$, there is no important evidence for the violation of the WEC according to the CCH+H_0^{R22} and CCH+H_0^{P18} data sets if we assume standard prerecombination physics, since the values (9.29) and (9.30) fall below the upper bounds (9.27) and (9.28), respectively, at 1σ C.L.

Some of the error bars in Fig. 9.7 are quite asymmetric, which means that the underlying multivariate distribution has some non-Gaussian features. Nevertheless, the deviation from Gaussianity in the case of the most precise values of $\Omega_m^{\max}$ is small, so we do not expect this to have a big effect on the final result. However, we duly quantify its impact making use of the Edgeworth expansion, Eq. (9.20). We find that our conclusions still hold true if we consider the non-Gaussian corrections, meaning that the impact of the non-Gaussian features in the distribution of $\Omega_m^{\max}$ is practically negligible, as expected. Indeed, we find $\Omega_m^{\max} = 0.240 \pm 0.030$ and $\Omega_m^{\max} = 0.308 \pm 0.036$ at 68% C.L. using the H_0^{R22} and H_0^{P18} priors, respectively. These results are fully compatible with those in Eqs. (9.27) and (9.28).

In the standard model, the WEC is automatically fulfilled due to the constancy of the dark energy density. Hence, we can explain the CCH data with the aforesaid values of H_0 and Ω_m without requiring phantom dark energy. This is the same conclusion reached applying the method of [529]. The CCH+H_0 data themselves do not exclude the violation of the WEC, but do not require its fulfilment either. At the moment, they cannot be used to strongly discriminate among possible solutions to the H_0 tension, and this is why the addition of CCH on top of Baseline_2D and

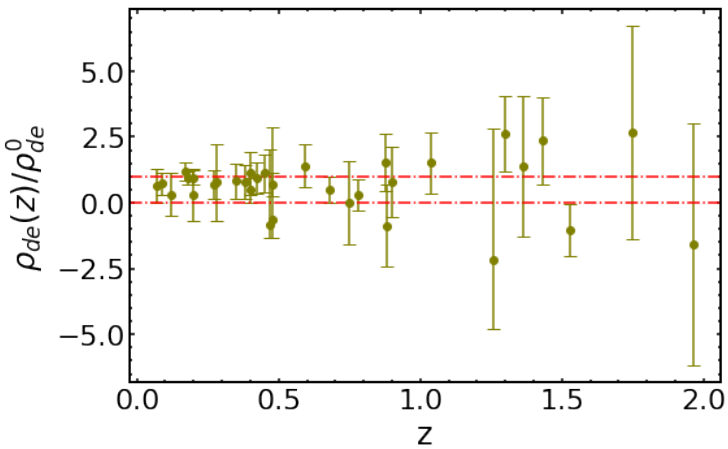

Figure 9.8. Constraints on the ratio $\rho_{\rm de}(z)/\rho^0_{\rm de}$ obtained by using Eq. (9.25) and sampling the CCH data together with the priors ω_m^{P18} and H_0^{R22}. We report the most probable values and 68% confidence intervals. The dashed red lines at 0 and 1 denote the lower bounds for which the two conditions of Eq. (9.17) are satisfied, i.e. the positivity of the effective dark energy density and the non-phantom nature of the dark energy, respectively.

Baseline_3D does not have a major impact on our results. This resonates with the results we obtained in Chapter 6, where it is shown that cosmic chronometers do not offer yet a very competitive calibration of the cosmic distance ladders. For instance, in Sec. 6.2, the reconstruction of $M(z)$ using CCH and SNIa is compatible with a constant, although it does not exclude an evolution in redshift.

Fig. (9.8) gives more support to our conclusions. We present there the constraints on the ratio $\rho_{\rm de}(z)/\rho^0_{\rm de}$ at 68% C.L. obtained by using Eq. (9.25) and sampling the CCH data together with the priors ω_m^{P18} and H_0^{R22}. Any of these measurements points to a clear violation of the WEC. We note, though, that the vast majority of the central points below $z = 1$ fall in the range $0 < \rho_{\rm de}(z)/\rho^0_{\rm de} < 1$, which could be an indication of the preference of the data for a phantom behavior of the effective dark energy fluid. Moreover, the central point at $z = 1.53$ is 1σ away from the positive region, and 2σ away from the border between the phantom and quintessence regions. This resonates very well with Fig. 9.7 because the point at $z = 1.5$ is the one that leads to the lowest upper bound on $\Omega_m^{\rm max}$, which is $\sim 2\sigma$ below the best-fit *Planck*/ΛCDM value, and hence in small tension with the standard model, as firstly noted in [529]. However, as already mentioned above, these hints of new physics are still mild.

9.5 Final discussion

In this Chapter, we illustrate the phenomenological approach we undertook to propose a solution to the H_0 discrepancy in the context of standard physics before recombination. We, in particular, have put the accent on the role played by two distinct BAO data sets, which are crucial in the construction of the cosmic inverse

distance ladder and which, before this work, in [240] have already been found to need further investigations. We have shown that anisotropic and angular BAO data require a phantom-like increase of the Hubble function and the absolute magnitude of SNIa at $0.01 \lesssim z \lesssim 0.2$, whereas the angular 2D BAO need this increase to happen much earlier in the cosmic expansion, at $z_t \sim 0.5 - 0.8$, and more smoothly. $M(z)$ is in this case still compatible with a constant, but an evolution is not excluded. Interestingly, if the new physics is attributed to an effective self-conserved dark energy component, the angular BAO data require the dark energy density to become negative during, at least, some period of the cosmic history at $z \gtrsim 2$. Hence, any low-z solution to the Hubble tension with conserved effective dark energy demands a violation of the WEC, and the possibility of a crossing of the phantom divide is not excluded. Coupled dark energy scenarios do not have to follow the conclusions that we have found assuming the conservation of dark energy, but have to give rise to forms of $H(z)$ and $M(z)$ compatible with our reconstructions. Another option to solve the Hubble tension is a local (ultra-late-time) change in M, in the second rung of the direct distance ladder, i.e. at $z \lesssim 0.01$, leaving intact the ΛCDM expansion history. Our results are in agreement with previous works that made use of anisotropic BAO data [526] and also support the conclusions of [531, 532]. Here, though, we make more definite statements than the latter, e.g. about the redshift ranges in which the phantom-like evolution should be active. We also perform for the first time in the literature an analysis on similar lines using 2D BAO.

On top of that, we have also shown that current CCH data cannot determine whether the WEC must be violated. They hint only very mildly to such a violation. Therefore, we can conclude that CCH, as standalone data, are not particularly helpful for constraining the form of the low-redshift solutions. This resonates well with the conclusion we get in Chapters 6 and 7, and also with findings in [241].

A detailed investigation of the nature of these solutions lies beyond the scope of the present work. Nevertheless, the possibility of late- or ultra-late–time resolutions to the Hubble tension remains open, and, interestingly, their concrete realization depends strongly on the choice of BAO data set.

Future background and BAO data as those from Euclid [279] are meant to be pivotal on the discussion. Of particular importance are the methods employed by the various collaborations to extract information from galaxy catalogs. In this regard, model-independent techniques are expected to play a key role in producing data sets that are as robust as possible, even at the expense of reduced precision [488, 489].

This point will become clearer in the next Chapter. By now, the reader can indeed appreciate that there is a nontrivial difference between the two types of BAO data. Ending this work with the same impression, we were motivated to further investigate the nature of this discrepancy, focusing solely on the data themselves, without embedding the discussion within a specific phenomenological framework.

Chapter 10

Tension between 2D and 3D BAO data sets

The content of this Chapter is based on our work published in [541].

The discrepancy between 2D and 3D BAO data pointed out in Chapter 9 and already introduced in Sec. 4.3 is worrisome, since many of the points contained in these data sets are obtained from the same parent catalogs of tracers and, therefore, we would expect them to be consistent. Since BAO measurements play a pivotal role in the building of the inverse distance ladder, this mismatch impacts the discourse on the Hubble tension and the study of theoretical solutions to the latter, as we extensively illustrated in Chapter 9.

So far, the discrepancy between 2D and 3D BAO has been pointed out only in the context of fitting analyses of cosmological models or parameterizations that, in practice, involve the choice of a concrete calibration of r_d. For instance, [487] have found that, in the context of a model with a sign-switching cosmological constant, it is possible to get rid of the H_0 and growth tensions when angular BAO is employed in the fitting analysis, instead of 3D BAO (see also [542]). Fitting results improve even more if dark energy is of quintessence type at late times, after the transition, something that can be realized in the model with phantom matter proposed by [276]. Analyses of interacting dark energy [486] carried out with 2D and 3D BAO data lead to completely inconsistent results too.

However, so far, there has been no accurate quantification of the statistical tension between these two BAO data sets. In the work presented in this Chapter, we provide a method to perform this quantification in a quite model-independent way, avoiding the use of any calibration and cosmological model in the process. We apply it to state-of-the-art BAO data, including the anisotropic measurements reported by DESI in their first year release[1], and compare these results with those obtained using the 3D BAO data from BOSS/eBOSS. Moreover, we also study the effect of a possible underestimation of the 3D BAO uncertainties on our results. This is motivated by the work by [428], which showed that, in the standard 3D analysis, the fitting of the two-point correlation function within fiducial cosmology leads to

[1]DESI DR2 was not released yet at the moment of this work.

an underestimation of the errors by a factor of two. Indeed, the aforementioned conflict between anisotropic and angular BAO data could either point to unknown systematic errors affecting one or both BAO data sets, or to an underestimation of their uncertainties (see Fig. 4.2).

To quantify the discrepancy between the BAO measurements, we take the fulfillment of the Etherington relation [75] – or cosmic distance duality relation (CDDR), see Eq. (1.81) and Sec. 1.3 – for granted. However, we also apply a calibrator-independent method to investigate the robustness of this assumption when analyzed not only with 3D BAO measurements, but also with 2D BAO. Since the CDDR holds in metric theories of gravity with photons conserved and propagating in null geodesics, this analysis is a test of fundamental physics, which covers, among other aspects, variations of the speed of light with the cosmic expansion (see e.g. [543, 544]) or possible interactions between the dark and electromagnetic sectors e.g. with axions or axion-like particles (see e.g. [545, 546]). Of course, these deviations could also hint at the existence of unknown systematic errors in the data.

Tests of the CDDR have been carried out using SNIa in combination with 3D BAO [547, 548, 549, 550, 76], CCH [551], strong lensing time delays [77] or data on compact radio quasars [552], and even with luminosity distances from high-redshift quasars and data from strong gravitational lenses [553]. See also [554, 80]. Most of these studies adopt specific functional forms for the possible deviation of the CDDR, such as linear or polynomial parameterizations. While this approach allows for stronger constraints, it necessarily introduces additional assumptions which reduce the generality of the method. In any of these works, a significant deviation from the CDDR has been found. In view of the discrepancy between the 2D and 3D BAO data sets, we deem it interesting and very timely to also study what happens if we employ angular BAO, instead of 3D BAO, to test the Etherington relation and see whether the tension between these two data sets also reflects into differences at the level of the CDDR. It is of utmost importance to check whether this relation holds, since it is taken for granted in our quantification of the tension between the 2D and 3D BAO. Thus, any significant departure from the CDDR would invalidate the results obtained in that analysis.

This Chapter is structured as follows:

- In Sec. 10.1, we describe the method and the data used to quantify the tension between the angular and anisotropic BAO measurements and show the corresponding results. In particular, we discuss how they change when we substitute the BOSS/eBOSS data with the recent DESI data, and also the impact of the SNIa sample employed in the analysis.

- In Sec. 10.2, we describe the calibrator-independent test of the Etherington relation, and again report the results against different BAO and SNIa compilations.

- Our conclusions follow in Sec. 10.3.

10.1 A model-independent estimator for the tension between anisotropic and angular BAO

We employ the angular and anisotropic BAO data listed in Tables A.3 and A.4, respectively. In the case of the 3D BAO, we use two alternative data sets: one contains the data from BOSS/eBOSS, whereas the other contains the data from DESI Y1. We refer to these two data sets as 3D_BOSS and 3D_DESI, respectively. The BOSS/eBOSS and DESI compressed data points have been obtained from catalogs with partially overlapping population and non-disjoint patches in the sky, so we opt not to combine them and proceed as explained above in order to avoid double-counting issues, since the correlations between these two sets of data are not known. In particular, we use the comoving sound horizon r_d as a cosmic standard ruler. As seen in Sec. 4.3, galaxy surveys have been able to measure the angle

$$\theta(z) = \frac{r_d}{D_M(z)} \tag{10.1}$$

at various redshifts. This is the angular information provided by the BAO signal, and it is the only type of data included in the 2D data set. The model- and calibrator-independent methods that we will employ to quantify the tension between the 3D and 2D BAO data sets and the test of the CDDR make only use of the angular component of the 3D BAO measurements. Thus, we exclude the radial components and the data points provided in terms of the dilation scale (see Eq. (4.13)).

Clearly, this quantification cannot be carried out through a direct (one-to-one) comparison of the data points contained in the two BAO data sets, since their redshifts are different. In order to do it in a model-independent and parametrization-independent way, we make use of SNIa and the method described below. We employ SNIa as standard candles, therefore we make use of the relation between their apparent magnitude and the distance luminosity as in Eq. (4.8). We make use of two different SNIa samples separately: the Pantheon+ compilation[2] and the DESY5 compilation. The number of high-quality SNIa in DESY5 is fivefold that of Pantheon+ for $z > 0.5$. This difference will be particularly relevant in our discussion since most of the BAO data points lie in that region.

Any deviation from the CDDR relation in Eq. (1.81) would imply that

$$\eta(z) \equiv \frac{D_L(z)}{(1+z)^2 D_A(z)} \neq 1\,. \tag{10.2}$$

From Eqs. (10.1) and (4.8), it is straightforward to write the luminosity and angular diameter distances in terms of the calibrators (M and r_d) and the measured quantities ($m(z)$ and $\theta(z)$). Plugging these expressions into Eq. (10.2) we obtain,

$$\eta(z) = \frac{10^{m(z)/5}\theta(z)}{(1+z)} \frac{10^{-5-M/5}\mathrm{Mpc}}{r_d}\,. \tag{10.3}$$

[2]We consider a subsample of 1624 data points as for the analysis in Sec. 6.2, since we do not include those SNIa lying in Cepheid host galaxies, although we have explicitly checked that the impact of these objects on our results is completely negligible.

If the Etherington relation is fulfilled (i.e., if $\eta(z) = 1$) and if we have measurements of $\theta(z)$ and $m(z)$ at the same redshift, we can compute the degeneracy direction in the calibrators' plane,

$$\bar{r}_d 10^{M/5} = \frac{10^{m(z)/5}\theta(z)}{10^5(1+z)}\,, \tag{10.4}$$

with $\bar{r}_d \equiv r_d/(1\,\mathrm{Mpc})$ the dimensionless sound horizon. This calculation is independent of the curvature of the Universe, which we do not need to specify. As we do not have SNIa and BAO data at the very same redshifts, we need to employ some interpolation method to obtain the constrained values of $m(z)$ at the BAO redshifts. One of these methods is the GP technique, which we have widely used in this thesis[3]. Using GP we generate $N = 10^4$ samples of SNIa apparent magnitudes at the BAO redshifts z_i. For each redshift z_i, we also draw N realizations of $\theta(z_i)$ from a Gaussian distribution that has as mean the measured value and as standard deviation the associated uncertainty. With this information we can obtain a distribution of N samples of the product $\bar{r}_d 10^{M/5}$ (Eq. 10.4) at the BAO redshifts. There exist non-null correlations, since we employ correlated SNIa data. On the other hand, we expect non-zero positive correlations between several data points in the 2D and 3D data samples, simply because they have been obtained from the same parent catalogs of tracers (cf. Tables A.4 and A.3). However, these correlation coefficients have not been quantified, so we cannot use them in our analysis. This fact will lead us to estimate, in practice, a conservative lower bound of the tension between the angular and anisotropic BAO data sets.

We can measure the same quantity $\bar{r}_d \times 10^{M/5}$ from the BAO data at different redshifts, which is very convenient since it allows us to establish a bridge between the various BAO data and use it to quantify the tension.

The next step is to estimate representative values of $\bar{r}_d 10^{M/5}$ for the 2D and 3D BAO data sets. To do so we need to obtain first their distribution out of the Markov chain. This will allow us to quantify the tension between the two data sets, by means of the tension between the corresponding values of $\bar{r}_d 10^{M/5}$. As a starting point, we employ the Edgeworth expansion in Eq. (9.20)[4] already used in Sec. 9.2, to compute an analytical approximation of the underlying (exact) distribution, $f(\vec{x})$, which is a multivariate function with the same dimensionality as the total number of BAO data points contained in the 3D and 2D data sets. In this case, the quantity $x^i = d^i - \mu^i$ in Eq. (9.20) are defined as $d^i = \bar{r}_d 10^{M/5}|_i$ and $\vec{\mu}$ the mean vector, i.e. $\mu^i = \langle \bar{r}_d 10^{M/5}|_i \rangle$. The subscript i labels the BAO data point, which can belong to the 2D or 3D BAO data sets. Once we build the distribution of Eq. (9.20), we can sample it treating it as a two-dimensional distribution for $\bar{r}_d 10^{M/5}$, with one dimension for the 2D BAO data set, and the other for the 3D BAO data set, i.e. $f(x_{\mathrm{2D}}, x_{\mathrm{3D}})$. When the non-Gaussian features are negligible, the resulting distribution reduces to a Gaussian with the following weighted mean vector $\tilde{\mu}$ and

[3]Here, we opt to follow the same approach already tested in Sec. 6.1, where it is shown that differences in the reconstructed shapes obtained with the marginalization and optimization procedures are smaller than 0.1σ in the case under study, thus not impacting significantly the final results.

[4]We have explicitly checked that in the case under study it is more than sufficient to keep only the first correction.

inverse covariance matrix $\tilde{\lambda}$,

$$\tilde{\mu}_I = \tilde{\lambda}_{IJ}^{-1} v_J \qquad ; \qquad \tilde{\lambda}_{IJ} = \sum_{i\in I}\sum_{j\in J} \lambda_{ij}\,, \tag{10.5}$$

with

$$v_I = \sum_{i\in I}\sum_{j=1}^{N} \lambda_{ij}\mu_j \tag{10.6}$$

and N the total number of BAO data points contained in the 2D and 3D data sets. Here we have indicated sums over all the elements contained in the data set I as $\sum_{i\in I}$, with I referring to the 2D or 3D BAO data sets. If we perform the analysis with 3D_BOSS and Pantheon+, $N = 20$; if, instead, we use 3D_DESI, $N = 21$. When we employ DESY5, our analysis is restricted to $z < 1.13$, since this is the maximum redshift of the SNIa sample. Hence, our BAO data set reduces to $N = 17$ if we employ 3D_BOSS and $N = 18$ if we employ 3D_DESI.

To quantify the tension between the anisotropic and angular BAO data we can just build the histogram of $\chi^2 = -2\ln f(x_{\rm 2D}, x_{\rm 3D})$ resulting from the sampling of the two-dimensional distribution obtained with the procedure described above, and then compute the p-value associated to the hypothesis of having only one single BAO data set (built out from the joint 2D and 3D BAO data sets). In point of fact, we can obtain the full distribution of p-values, which allows us to compute also the associated uncertainty. The smaller the p-value, the more the hypothesis is excluded, of course, indicating greater inconsistency between the two data sets. We repeat this exercise with both 3D_BOSS and 3D_DESI (one at a time) in combination with 2D BAO to determine if the level of tension between the angular and the anisotropic BAO data sets changes. In addition, we also test the impact of the SNIa sample by replacing Pantheon+ with DESY5.

In Fig. 10.1, we present the outcome of this analysis. In particular,

- in the left upper plot, we show the constraints on the product $\bar{r}_d \times 10^{M/5}$ defined in Eq. (10.4), obtained by making use of the individual BAO angles in combination with the SNIa apparent magnitudes of Pantheon+ or DESY5;
- in the lower plots, we present the overall constraints obtained from each BAO data set, see the horizontal bands at 68% C.L. and the results reported in Table 10.1;
- the contour plot on the top right complements the preceding information and helps to better assess visually the tension between the 2D and 3D BAO data sets.

The latter points to a $\sim 2\sigma$ C.L. tension when the anisotropic BOSS data are used, and grows up to the $\sim 2.5\sigma$ C.L. with DESI. This result is obtained employing SNIa from Pantheon+. If, instead, we perform the analysis using the DESY5 SNIa sample, the statistical significance of the tension reaches the $\sim 4.6\sigma$ level with both BOSS and DESI. As anticipated before, this increase is mainly driven by the high number of SNIa observed within the redshift range $0.5 \lesssim z \lesssim 0.9$ by DESY5, which is roughly five times the number of SNIa in the same range as reported by Pantheon+ [412].

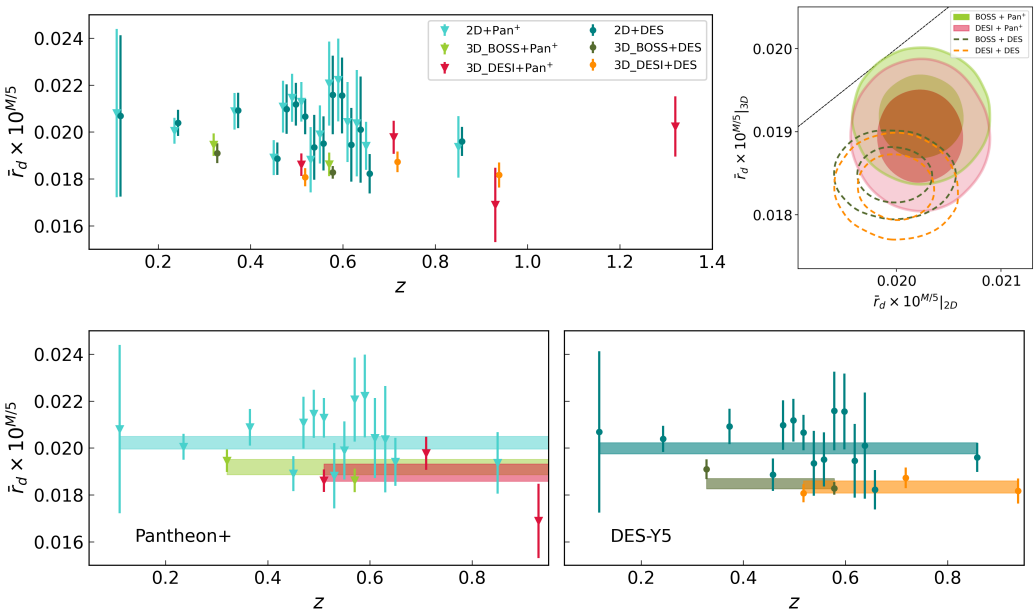

Figure 10.1. *Left upper plot:* Constraints at 68% C.L. on the product $\bar{r}_d \times 10^{M/5}$ obtained making use of the SNIa of Pantheon+ or DESY5 and the individual 3D and 2D BAO data points. We follow the method explained in Sec. 10.1. We plot the points obtained with DESY5 shifted by $\Delta z = 0.01$ to visually distinguish them from those obtained with Pantheon+. We only show the points at $z < 1.4$ because at higher redshifts error bars are large and exceed the displayed range of values. *Lower plots:* Same as the left upper plot, but with a zoom in the range $z \in [0.05, 0.95]$ using the Pantheon+ and DESY5 samples, respectively. The horizontal bands represent the 2D, 3D_BOSS and 3D_DESI BAO constraints at 68% C.L. *Right upper plot*: The corresponding contours at 68% and 95% C.L obtained using `GetDist` [467]. The dashed straight line in black represents the null hypothesis of consistency between the 3D and 2D BAO data sets, i.e., $\bar{r}_d \cdot 10^{M/5}|_{\rm 3D} = \bar{r}_d \cdot 10^{M/5}|_{\rm 2D}$.

Most of the BAO data used in this work lie precisely in that region (see, respectively, the left upper plot and the horizontal bands in the lower panels of Fig. 10.1)[5]

It is also important to note that the roughly circular shape of the contour lines in Fig. 10.1 responds to the fact that the correlations introduced by SNIa turn out to be very small and we have not considered correlations between the 2D and 3D BAO data sets. Indeed, a positive correlation between these two data sets would leave the individual uncertainties of $\bar{r}_d \times 10^{M/5}$ stable, but the shape of the contour lines would be more elongated in the direction of the straight line shown in the top right plot of Fig. 10.1. Therefore, the effective distance (measured in terms of $\Delta\chi^2$) between the best-fit point and the straight line would be larger and the tension

[5]We recall that the replacement of the SNIa from Pantheon+ with those from DESY5 also enhances the evidence for dynamical dark energy from 2.5σ to $\sim 4\sigma$ C.L. when these data sets are combined with DESI+CMB data [555, 201]. Although the discussion at hand is different from the one in this work, this is another manifestation of the significant statistical power of the DESY5 SNIa compilation. Given the impact that the SNIa data have in these analyses, as also seen in the analyses of Sec. 6.3.2, it seems increasingly important to track the effect of systematic errors in these samples.

Table 10.1. Constraints at 68% C.L. on the product $\bar{r}_d 10^{M/5}$ for the 2D and 3D BAO data sets obtained using the SNIa from Pantheon+ and DESY5, following the procedure explained in Sec. 10.1. They incorporate possible deviations from Gaussianity, encapsulated in Eq. (9.20), which are, in any case, derisory, as we have explicitly checked by comparing these results with those obtained with Eqs. (10.5)-(10.6). The level of tension between the 2D and 3D BAO data sets is quantified by the p-value, reported in the third and fifth columns of the table for the case of Pantheon+ and DESY5, respectively. In the second rows of 3D_BOSS and 3D_DESI, we present the results obtained by doubling the uncertainties associated with the 3D BAO measurements. These results are labeled with an asterisk.

BAO data set	$\bar{r}_d 10^{M/5}$	p-value	$\bar{r}_d 10^{M/5}$	p-value
	Pantheon+		DES Y5	
2D	$(20.23 \pm 0.27) \cdot 10^{-3}$	–	$(19.98 \pm 0.24) \cdot 10^{-3}$	-
3D_BOSS	$(19.19 \pm 0.33) \cdot 10^{-3}$	$0.048^{+0.008}_{-0.009}$	$(18.48 \pm 0.22) \cdot 10^{-3}$	$< 10^{-5}$
3D_BOSS*	$(19.10 \pm 0.48) \cdot 10^{-3}$	$0.116^{+0.016}_{-0.008}$	$(18.47 \pm 0.38) \cdot 10^{-3}$	$< 10^{-3}$
3D_DESI	$(18.95 \pm 0.37) \cdot 10^{-3}$	$0.018^{+0.011}_{-0.002}$	$(18.34 \pm 0.26) \cdot 10^{-5}$	$< 10^{-5}$
3D_DESI*	$(18.98 \pm 0.53) \cdot 10^{-3}$	$0.105^{+0.014}_{-0.008}$	$(18.29 \pm 0.43) \cdot 10^{-3}$	$< 10^{-3}$

between the 3D and 2D BAO data would increase. This is why we actually obtain a lower bound of the tension by neglecting the existing correlations between the anisotropic and angular BAO data.

The distribution of p-values associated with the hypothesis of having only one single BAO data set read $0.048^{+0.009}_{-0.008}$ and $0.018^{+0.011}_{-0.002}$ when employing the SNIa of Pantheon+ in combination with 3D_BOSS and 3D_DESI, respectively. When we use the SNIa of DESY5, instead, the p-values become smaller than 10^{-5}, see Table 10.1. These more quantitative results are fully aligned with those of Fig. 10.1 and highlight a significant tension between the two types of BAO data. This tension persists across different SNIa compilations but is particularly pronounced with the DESY5 data.

It is crucial to emphasize again that this significant tension is derived in a largely model-independent way, assuming only the validity of the CDDR relation. The addition of the radial component of the 3D BAO data, which has not been considered in our analysis because it is not feasible to incorporate it following a model- and calibrator-independent approach, increases the tension even more[6] . This explains why fitting analyses with angular and anisotropic BAO data yield completely different results, as shown, for example, in [486].

[6]Several recent works have pointed out that the DESI BAO data obtained from luminous red galaxies at $z = 0.51$ are possibly driving the signs of dynamical dark energy found by combining DESI with CMB, OHD and SNIa [555, 556, 557, 558]. It is therefore worthwhile to closely examine these data and their impact on our results. However, the $\sim 2\sigma$ offset of the DESI data at $z = 0.51$ from the Planck/ΛCDM model reported by [300] is only found in the radial measurement, $D_H(z)/r_d = c/H(z)r_d$, i.e., it is not present in the transversal BAO component (see their Figure 15 and also our Fig. 4.2). The latter is fully consistent with Planck/ΛCDM, as are the other 3D BAO data. Thus, we can conclude that this data point is not playing a major role in our analysis, apart from tightening the constraint on the product $\bar{r}_d \times 10^{M/5}$ extracted with 3D_DESI.

Finally, motivated by the work by [428], we have also studied to what extent the tension loosens if we increase the uncertainties of the 3D BAO measurements by a factor of two. The results are displayed in Table 10.1. The p-values are approximately 0.1 in this case when the 2D BAO is combined with both 3D BAO data sets using the SNIa of Pantheon+, resulting in a discrepancy of less than 2σ and, hence, in no significant statistical tension. When the SNIa of Pantheon+ are replaced with those of DESY5, the statistical tension remains, instead, at $\sim 3.5\sigma$ C.L. An underestimation of the 3D BAO uncertainties, as the one estimated by [428], could mitigate the tension between angular and anisotropic measurements, improving in this way their concordance. However, the tension persists at high confidence level in the light of the most complete SNIa sample, even when the uncertainties of the anisotropic BAO data are increased by a factor two.

10.2 Test of the Etherington relation

To validate the analysis presented in Sec. 10.1, we verify whether the CDDR relation holds within the data sets used in this work. To this purpose, we follow the calibrator-independent method employed by [552]. It is based on the quantity

$$\eta_{i,j} \equiv \frac{\eta(z_i)}{\eta(z_j)} = \frac{10^{m(z_i)/5}\theta(z_i)}{10^{m(z_j)/5}\theta(z_j)} \left(\frac{1+z_j}{1+z_i}\right) , \tag{10.7}$$

which is built from the ratio of Eq. (10.3) at two different redshifts. Avoiding the use of the calibrators of the distance ladders in this test is important not to propagate possible biases that might have been introduced in their measurement. This is relevant on account of the Hubble tension. Departures of $\eta_{i,j}$ from unity could hint at a violation of the CDDR.

In practice, we obtain the values of $\eta_{i,i+1}$ (Eq. 10.7) using the various BAO and SNIa data sets. For each of them, we compute the following function

$$\tilde{\eta}_I(z) = \sum_{i=1}^{N_I-1} \eta_{i,i+1}\Theta(z-z_i)\Theta(z_{i+1}-z) , \tag{10.8}$$

where $\Theta(\cdot)$ is the Heaviside step function. This expression accounts for all the independent $N_I - 1$ couples of z. The subscript I labels the BAO+SNIa data set employed in the calculation and N_I is the number of BAO data points contained in it. Eq. (10.8) allows us to present the results in a very visual way and maximizes the statistical content of our sample without unnecessary repetition. There are only $N_I - 1$ independent values of $\eta_{i,j}$ out of the $N_I(N_I - 1)$ non-zero values that can be computed using the N_I values of $\eta(z_i)$, with $i \in I$. Eq. (10.8) can be used to detect deviations from the CDDR. In each of the bins, the quantity $\eta_{i,j} \neq 1$ if $\eta(z_i) \neq \eta(z_j)$. This can only happen if $\eta(z_i) \neq 1$ or/and $\eta(z_j) \neq 1$. This obviously implies a violation of the CDDR. On the other hand, $\eta_{i,j} = 1$ if $\eta(z_i) = \eta(z_j)$. If the derivative of $\eta(z)$, $f(z) \equiv d\eta/dz$, is well-defined, we can always do

$$\eta(z) = \eta(z=0) + \int_0^z f(z')dz' . \tag{10.9}$$

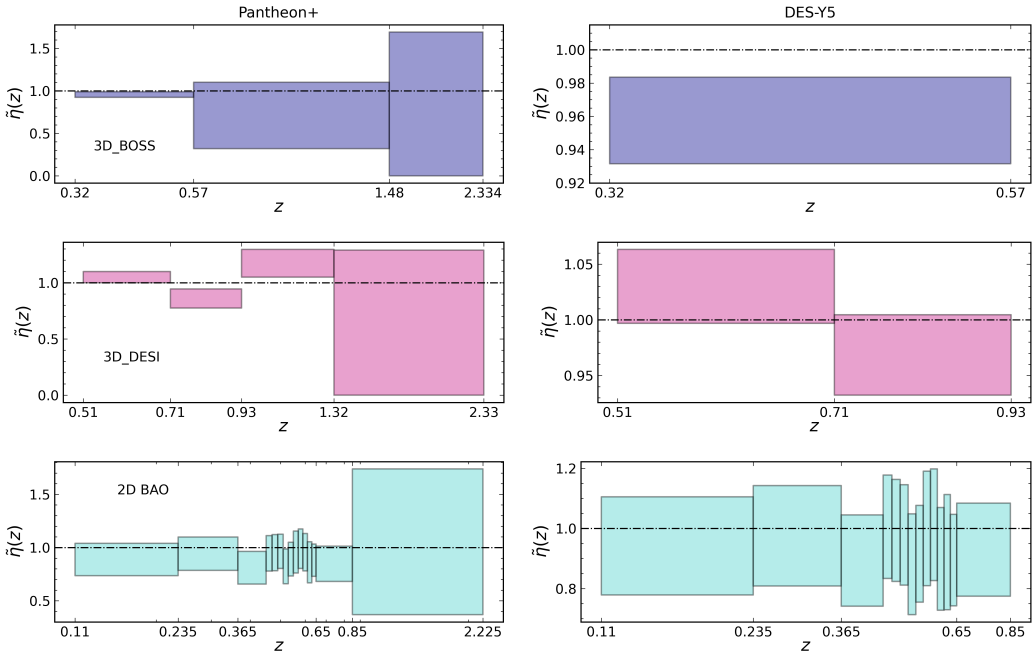

Figure 10.2. Constraints at 68% C.L. on $\tilde{\eta}(z)$, as defined in Eq. (10.8), obtained making use of the 3D and 2D BAO data sets in combination with the SNIa of the Pantheon+ and DESY5 compilations. The x-axes are in logarithmic scale for the sake of a better visualization. We write the z values of the various BAO data points employed in the construction of $\tilde{\eta}(z)$, except in the region of redshifts in the 2D BAO plot where the density of points is too high, see Table A.4.

Assuming that $z_j > z_i$, the condition $\eta(z_i) = \eta(z_j)$ is satisfied if $f(z) = 0\ \forall z \in [z_i, z_j]$. Hence, our diagnostic is sensitive to sources of violation of the DDR in the redshift interval between z_i and z_j. Thus, our estimator $\tilde{\eta}_I(z)$ is able to detect violations of the Etherington relation by construction. The only limitation of our method is the precision of the available data.

In Fig. 10.2, we present the resulting 68% C.L. constraints on Eq. (10.8), obtained with 2D, 3D_BOSS and 3D_DESI BAO, in combination with the SNIa from Pantheon+ or DESY5 compilations. We do not find any significant hint of a violation of the CDDR. This result supports the validity of the Etherington relation, which is used to quantify the tension between the two BAO data sets in Sec. 10.1, thereby supporting the conclusions of the latter as well. Regardless of the BAO and SNIa data sets employed in the analysis, the quantity $\tilde{\eta}(z)$ is compatible with 1 at approximately $1 - 2\sigma$ C.L. While this result is consistent with previous analyses using the anisotropic 3D_BOSS data set (see e.g., [76]), our study represents the first investigation in the literature to test the CDDR using both the 3D and 2D BAO data sets, and the SNIa compilation from DESY5. The tension between the anisotropic and angular BAO data sets discussed in Section 10.1 does not manifest as a deviation from the CDDR when considering the angular BAO data. To date, uncertainties on $\tilde{\eta}_I(z)$ are still large, especially at high redshift, where they can reach 100% due to large errors in SNIa data.

10.3 Final discussion

Motivated by the conclusions gathered in Chapter 9, here, we illustrate a novel method to quantify the existing tension between current angular and anisotropic data on BAO, which are extracted from the same parent catalog of tracers but using two independent techniques. These techniques, notably, have different degrees of model dependency. The method we propose to investigate such a discrepancy only relies on the fulfilment of the Etherington relation and is also independent of the calibrators of the direct and inverse distance ladders. Furthermore, by construction, it excludes the radial 3D BAO data. Our conclusions point to a tension at $\sim 2\sigma$ C.L. between the 2D BAO and the anisotropic data set constructed with BOSS/eBOSS data when using the SNIa from the Pantheon+ compilation. This tension increases to approximately $\sim 2.5\sigma$ C.L. when we employ the DESI DR1 instead of BOSS/eBOSS. The replacement of the Pantheon+ SNIa with those of DESY5 triggers a substantial increase of the tension, which now reaches the 4.6σ C.L. Notably, this can be considered a lower bound of the actual tension because we cannot account for the positive correlations between the 2D and 3D BAO data sets, as these correlations have not been reported in the literature. In addition, incorporating the radial 3D component in the context of model-dependent analyses is expected to exacerbate the tension.

The statistical significance of the aforesaid discrepancy would be softened if, for some reason, the BAO uncertainties had been underestimated. This is a plausible possibility according to [428], who found that the errors in standard anisotropic BAO analyses might be underestimated by a factor of two. To investigate this, we have repeated the analysis doubling the uncertainties of 3D_BOSS and 3D_DESI and find that, as expected, the tension decreases below the 2σ C.L. with Pantheon+ and remains at 3.5σ C.L. with DESY5. This tells us that the tension between angular and anisotropic BAO can be mitigated if the error bars in the compressed BAO data are not being properly estimated in current analyses. However, it is still pretty high according to the latest SNIa sample.

We have also deemed it interesting to check whether this mismatch can be translated into a deviation from the Etherington relation. This is also a consistency test, since we have assumed the validity of the latter in the first part of the methodology (see Eq. (10.3)). We have applied a calibrator- and model-independent approach previously used by [552], although this is the first time it is applied using BAO data, and also the first time that the robustness of the CDDR is studied using angular BAO and the SNIa of DESY5. Our constraints are quite loose: they allow for violations of $\sim 20\%$ below $z \sim 0.8 - 1$ at 68% C.L., and even greater at larger redshifts. When we combine 3D BAO and DESY5 SNIa, though, the maximum deviations are of about 10%. We do not find any compelling evidence for departures from the standard scenario neither in the anisotropic nor the 2D BAO data sets. The maximum incompatibility is found at $\sim 1\sigma$ C.L. in some redshift ranges for the 3D_DESI and 2D BAO data sets, which is not significant at all. Stronger constraints have been obtained in the literature, but they typically require the use of parametrizations of $\eta(z)$ and, hence, additional assumptions to those considered here (see, e.g., [76, 77, 78, 79, 80]).

In the era of precision cosmology and the existing tensions afflicting the standard

ΛCDM model, it is crucial to elucidate what is causing the discrepancies between the various BAO data sets. It will be important to reassess the level of tension between angular and anisotropic BAO once future data releases from DESI and future data from Euclid become available. Our hope is that these surveys will provide both 3D and 2D BAO data, extracted by the same collaborations. This would be extremely healthy and useful for the community in order to test both methods and pinpoint possible sources of biases. In this context, our model- and calibrator-independent methodology would be beneficial to cross-validate future measurements.

Part VI

LSS tensions: consequences of using σ_8 in cosmology

Chapter 11

The bias introduced by σ_8

The content of this Chapter is based on the work published in [278].

So far, the studies reviewed in this thesis underscore the importance of agnostic approaches for scrutinizing the complex puzzle posed by the discrepancy in the current expansion rate. Living in an era enriched by a multitude of surveys probing the cosmos from local to high redshifts, it seems inevitable that some data sets exhibit a degree of inconsistency, further complicating the urgent need for deeper investigations. Many pieces of this puzzle remain missing, and their correct placement within the broader picture requires careful handling. One such piece concerns the physical interpretation of large-scale structure measurements in terms of structure growth. As discussed in Sec. 3.2, using σ_8 to extract information from LSS and to assess a model's performance in addressing cosmological tensions can be problematic. In particular, quantifying the growth tension through σ_8 may introduce significant biases and entangle the growth and Hubble tensions in an intricate and uncontrolled manner – especially when σ_8 is inferred from galaxy clustering data.

The parameter σ_8 is commonly used to quantify the amplitude of matter fluctuations at linear cosmological scales. However, the dependence of R_8 on h complicates direct comparisons of σ_8 values obtained under different assumptions about H_0, since σ_8 in such cases characterizes the amount of structure at different physical scales. This issue arises both when comparing σ_8 values from fitting analyses of cosmological models with differing H_0 posteriors, and when contrasting constraints from galaxy clustering experiments that employ different priors on the Hubble parameter. It is therefore of utmost importance to remove this source of potential bias. As outlined in Sec. 3.2, a possible solution – which is actually very simple – consists of replacing σ_8 with another quantity that can be used to describe the amplitude of matter fluctuations at linear scales, but is independent of h. This parameter was introduced by Ariel G. Sánchez [264] and it is called σ_{12}, i.e. the amplitude of matter fluctuation evaluated at a fixed scale of 12 Mpc, which essentially removes the dependence on h.

We devote this Chapter to illustrate the biases introduced by the use of σ_8 through some clear examples (in this regard, see again Fig. 3.3), to motivate the community to adopt σ_{12} as a more robust alternative. We show that the bias found in models with large values of H_0 is more prominent. This artificially complicates

the search for a model that can efficiently resolve the Hubble tension without exacerbating the growth tension inferred from galaxy clustering measurements. We argue that the worsening of the growth tension in these models is much less pronounced than previously thought or may even be nonexistent.

We structure the Chapter as follows:

- In Sec. 11.1, we concretely study the impact of the bias in the light of current data. In particular,
  - in Sec. 11.1.1, we first provide an approximate formula for the σ_8 bias as a function of the Hubble parameter, which we derive semi-analytically. Then, we show how it affects the constraints extracted from current data on peculiar velocity and RSD. This Section will help the reader understand the extent to which σ_8 can obscure the physical interpretation of results in cosmological studies.
  - Sec. 11.1.2 is dedicated to analyzing the impact of the bias in the light of current CMB, BAO and SNIa data, and on different cosmological models, including ΛCDM, late-time dynamical dark energy, some extensions of the standard model with massive neutrinos and/or additional ultra-relativistic species, and early dark energy. All of them can leave a non-negligible imprint on the LSS and some of them can even help to bring the Hubble parameter closer to the SH0ES value. This is why we deem it important to analyze and quantify the σ_8-bias in these scenarios. After outlining the data and methodology used to constrain the various cosmological models, we discuss our results.
- In Sec. 11.2 we provide our final considerations.

11.1 The problem in light of current data

11.1.1 Some first examples

The behavior of $\sigma_8(z)$ can be derived and understood semi-analytically, by Taylor-expanding the Fourier transform of the window function $W_R(r)$ given in Eq. (3.5) around R_{12} and substituting the result into the $\sigma_8(z)$ formula in Eq. (3.4), thereby establishing a simple relation between $\sigma_8(z)$ and $\sigma_{12}(z)$. The Taylor expansion of Eq. (3.5) at leading order in the difference $\delta h = h - h_*$, where $h_* = 8/12 \simeq 0.667$, reads,

$$W^2(kR_8) = W^2(kR_{12}) + 2W(kR_{12}) \left[\frac{\partial W(kR_8)}{\partial R_8}\frac{\partial R_8}{\partial h}\right]_{h=h_*} \delta h + \mathcal{O}(\delta h^2)\,. \tag{11.1}$$

Plugging this expression into Eq. (3.4), and after some algebra, one can find

$$\sigma_8^2(z) = \sigma_{12}^2(z)[1 + 9\delta h] - 9\delta h I(z) + \mathcal{O}(\delta h^2)\,, \tag{11.2}$$

with

$$I(z) = \frac{1}{2\pi^2} \int dk\, k^2\, P(k,z)\, W(kR_{12}) \left[\frac{\sin(kR_{12})}{kR_{12}}\right] . \tag{11.3}$$

The integral $I(z)$ can be further expressed in terms of $\sigma_{12}^2(z)$ to simplify Eq. (11.2). Unfortunately, this cannot be done analytically. Nevertheless, for models like ΛCDM, where the time dependence of the density contrast at the scales of interest during the matter-dominated epoch and beyond can be expressed as

$$\delta(k,z) = D_+(z)\delta(k,0)\,, \tag{11.4}$$

one finds numerically that [1]

$$\frac{I(z)}{\sigma_{12}^2(z)} = A\,, \tag{11.5}$$

with $A \simeq 0.77(2)$[2]. The time-dependence carried by $D_+(z)$ cancels in the ratio. This result allows us to write the relation (11.2) in the following very compact form,

$$\sigma_8(z) \approx \sigma_{12}(z)[1 + 1.035\,\delta h] + \mathcal{O}(\delta h^2)\,. \tag{11.6}$$

This expression is central to understanding the results displayed in Fig. 3.3. In the matter-dominated era, $\sigma_{12}(z)$ is the same for all the ΛCDM models under study, so the bias can be estimated using the formula

$$\frac{[\sigma_8(z) - \sigma_{12}(z)]}{\sigma_{12}(z)} = 1.035\delta h\,, \tag{11.7}$$

which is independent of the redshift. As an example, for $h = 0.75$, the bias is of order $\sim 8 - 9\%$, which is indeed a number pretty close to the one shown in the rightmost plot of Fig. 3.3. Also visible is an unphysical shift which increases for larger values of $|\delta h|$, even if the initial conditions and all the relevant energy densities are the same at large redshifts. Moreover, formula (11.6) indicates that the shift in $\sigma_8(z)$ induced by $\delta h \neq 0$ persists at all redshifts. Although σ_{12} decreases at late times for larger values of h, this reduction is far smaller than the positive shift resulting from the change in the scale R_8. This leads to the counterintuitive behavior observed in the central plot, discussed above: for larger values of h (or equivalently, of Λ, with the other parameters held fixed), σ_8 suggests a greater amount of structure. This outcome is, of course, physically unreasonable and underscores the difficulties of deriving meaningful interpretations from $\sigma_8(z)$ analyses.

Now, let us examine the concrete consequences of the bias of σ_8 with some current data. In particular, we study the constraints extracted from current data on peculiar velocity and RSD. Peculiar velocities introduce spurious anisotropies in tracer maps which allow galaxy surveys to measure the quantity $f(z)\sigma_R(z)$, with $f(z) = d\ln\delta/d\ln a$ the growth rate. This measurement is performed under the

[1] Here, $D_+(z)$ represents the growing mode of the solution to the density contrast equation, with $D_+(0) = 1$ [559].

[2] Although A formally depends on the model and its parameters, we find that it is only weakly sensitive to the model details, as long as $P(k,z)$ has a reasonable shape. Its values consistently fall within $A \in (0.75, 0.79)$.

assumption of a ΛCDM fiducial model with fixed parameters, typically adopting a value of H_0 close to the *Planck*/ΛCDM best-fit. Galaxy surveys report constraints on the quantity $f(z)\sigma_8(z)$. However, for the fiducial h used in these analyses, we have $R_8 \approx R_{12}$[3], so these data can, to first approximation, be treated as measurements of $f(z)\sigma_{12}(z)$. In fact, this is likely a more accurate representation, since RSD measurements capture clustering information associated with a scale close to R_{12}. Therefore, one cannot interpret them as characterizing the amplitude of the power spectrum at scales that depend strongly on h. This approach is effectively what is done in practice when RSD and peculiar velocity data are interpreted as measurements of $f(z)\sigma_8(z)$ and used to constrain non-standard cosmological models with h values significantly different from the *Planck*/ΛCDM best-fit[4].

We can illustrate the impact of this bias using data from several galaxy surveys, collected, e.g., in Table I of [561], exploiting the parameterization of the growth rate first introduced in [562] and subsequently in [563],

$$f(a) = \Omega_m^\gamma(a)\,, \tag{11.8}$$

where γ is the so-called growth index, and is a constant. In the context of ΛCDM, $\gamma_\Lambda \simeq 0.55$ [563]. Using Eq. (11.8), we find that the late-time evolution of the matter density contrast takes the form,

$$D_+(a) = \exp\left[\int_1^a \frac{da'}{a'}\Omega_m^\gamma(a')\right]. \tag{11.9}$$

Hence, the RSD observable can be expressed as follows,

$$f(z)\sigma_R(z) = \Omega_m^\gamma(z)\sigma_R^0 D_+(z)\,. \tag{11.10}$$

where $\sigma_R^0 \equiv \sigma_R(z=0)$ and recalling that $z = a^{-1} - 1$. Assuming a background cosmology, RSD measurements provide constraints on γ and σ_R^0. The former governs the evolution of perturbations with cosmic expansion, while the latter determines the present-day amplitude of the power spectrum at the scale R.

The correspondence $\sigma_8 \simeq \sigma_{12}$ holds in the context of the fiducial models commonly used to process survey data. However, this is not generally true: σ_8 is a continuous collection of constraints at different scales $R_8(h)$, one for each possible value of h, which is unrealistic. In other words, different values of h lead to the same constraint on the amplitude of fluctuations, but linked to different scales. Therefore, using RSD data obtained under a fiducial model with $h \simeq h_* = 8/12$ to constrain models with significantly different values of h can lead to biased constraints on the amplitude of fluctuations if we mistakenly assume that the RSD measurements constrain σ_8^0 rather than σ_R^0 at $R \simeq R_{12}$.

We can further illustrate this with a concrete example, in which we extract constraints on γ and σ_{12}^0 from the RSD and peculiar velocity data assuming that the correct background cosmology is ΛCDM and, hence, that

[3]We recall that $\sigma_{12} \approx \sigma_8$ for $h = 0.667$.

[4]In principle, the bias is unrelated to the model dependence of the RSD measurements, which arises from the choice of a fiducial cosmology. The σ_8-bias can be eliminated (or at least mitigated) by replacing it with σ_{12}, although the issue of model dependence may persist. See Refs. [489, 560] for a possible way of solving the model-dependence problem in galaxy clustering studies.

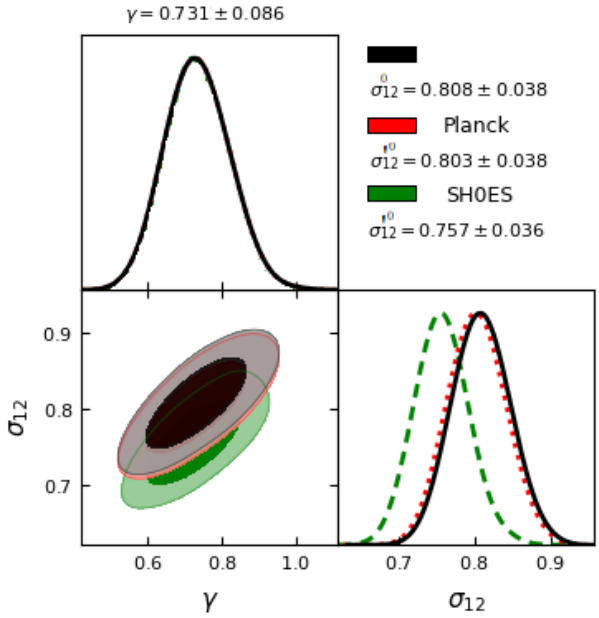

Figure 11.1. 1D and 2D posterior distributions of the growth index γ and the amplitudes σ_{12}^0 (in black) and $\sigma_{12}'^0$ (in red, green) obtained making use of RSD and peculiar velocity data. The constraint on $\sigma_{12}'^0$ derived with the *Planck* prior H_0^{P18} is shown in red. No significant bias is found for σ_{12}^0 in this case, since $h \approx h_*$. The constraint on $\sigma_{12}'^0$ obtained with the H_0^{R22} SH0ES prior is shown in green and exhibits a much larger bias, as expected. See main text for details.

$$\Omega_m(z) = \frac{\Omega_m^0 (1+z)^3}{1 + \Omega_m^0 \left[(1+z)^3 - 1\right]} \,. \tag{11.11}$$

We do so under two different assumptions: (i) we assume that the data is on the quantity $f(z)\sigma_{12}$, and (ii) we assume that the data is on $f(z)\sigma_8(z)$. In this case, we need to translate our measurement of σ_8^0 into a measurement of σ_{12}^0 making use of Eq. (11.6). We refer to the resulting value as $\sigma_{12}'^0$ to distinguish it from the one measured in (i), which we call simply σ_{12}^0. Since this translation will depend on h, we use a prior on this parameter. In particular, to study how the bias depends on the value of the Hubble parameter, we use both H_0^{P18} [11] and H_0^{R22} [94]. The H_0 prior only affects the constraint on $\sigma_{12}'^0$, being γ and σ_{12}^0 completely insensitive to it. We also employ the prior $\Omega_m^0 = 0.30 \pm 0.01$. The results obtained with the *Planck* and SH0ES priors are displayed in Fig. 11.1. To quantify the bias caused by interpreting the RSD measurements as measurements of $f(z)\sigma_8(z)$, we use the ratio $\Delta_\sigma \equiv (\sigma_{12}'^0 - \sigma_{12}^0)/\delta\sigma_{12}^0$, with $\delta\sigma_{12}^0$ the uncertainty of σ_{12}^0.

When the *Planck* prior is used the bias is quite small ($\Delta_\sigma = -0.13$), as expected, given that $h \approx h_*$. In contrast, when we force H_0 to be close to the SH0ES value, $\Delta_\sigma = -1.3$, indicating a substantial increase of the absolute value of the bias.

As noted in Fig. 3.3, the bias becomes more significant in models with larger values of H_0. If interpreted as measurements of $f(z)\sigma_8(z)$, the RSD and peculiar velocity measurements typically lead to smaller estimates of the rms mass

fluctuations at 12 Mpc, i.e., $\sigma_{12}'^0 < \sigma_{12}^0$, and this can incorrectly penalize models that favor larger values of H_0, making them to enter (artificially) in conflict with the LSS measurements. From this exercise, we obtain a growth index which is $\approx 2.1\sigma$ above the ΛCDM value, γ_Λ. This result is consistent with previously published results (see, e.g., [258]) and, of course, is just a reflection of the growth tension.

These preliminary considerations already highlight the critical importance of correcting the bias introduced by using σ_8, in order to reliably analyze model performance, compare experimental results from different galaxy surveys, and draw meaningful conclusions. Since the bias increases with larger values of $|\delta h|$, it is particularly pronounced for models that alleviate or resolve the H_0 tension, as these models predict higher values of H_0, close to 73 km/s/Mpc. This is highly concerning because analyses based on σ_8 often suggest that models which effectively relieve the Hubble tension tend to exacerbate the growth tension, complicating the search for a theoretical framework capable of simultaneously accommodating the data and mitigating the shortcomings of the standard model. This is what happens, for instance, with EDE models [235]. In Sec. 11.1.2, we will quantify the impact of all these effects on a heterogeneous selection of models by performing fits with current data and comparing the posterior constraints on $\sigma_8(z)$ and $\sigma_{12}(z)$.

As a final remark, we stress here that, as already anticipated in Sec. 3.2, the bias introduced by σ_8 does not affect weak lensing studies. Indeed, WL alone is not capable of constraining the Hubble parameter [265] because WL measurements are fundamentally angular; therefore, S_8 constraints are stable under changes in the h prior. Since, however, the physical scale varies with h, the constraints on the parameter $S_{12} = \sigma_{12}(\omega_m/0.14)^{0.4}$ [264], changes with the prior on h, see [266, 267]. The quantification of tensions in WL studies can be robustly performed using either S_8 or S_{12}, provided the analysis is carried out within a sufficiently broad parameter space – at minimum (Ω_m, S_8) or (Ω_m, S_{12}, h) [266]. However, the triad (Ω_m, S_{12}, h) may offer a clearer physical interpretation of the WL measurements [264, 266, 267].

11.1.2 σ_8 vs σ_{12} in model fitting analyses

Data & Methodology

In this Section, we further illustrate the implications of a misuse of σ_8 in cosmological fitting analyses. We do so by performing a full Monte Carlo analysis with state-of-the-art data from CMB, BAO and SNIa, in the context of five different cosmological models. This, of course, requires the estimation of the central values and uncertainties of $\sigma_{12}(z)$ and $\sigma_8(z)$. The MCMC analysis is performed using `Cobaya` [463] (see Sec. 5.2), whereas in order to compute the theoretical values of the various cosmological observables we solve the Einstein-Boltzmann set of coupled differential equations making use of modified versions of the code `CLASS` [564] that allow us to obtain as derived parameters the values of $\sigma_8(z)$ and $\sigma_{12}(z)$ at the redshifts of interest. Regarding the data sets, we utilise the following:

- the CMB temperature and polarization power spectra *plik*TTTEEE+lowl+lowE

(hereafter Planck) from the legacy Planck release as reference for CMB observations [11, 429].

- the full Pantheon+ compilation, and use the SH0ES [94] distance moduli of the host galaxies to calibrate the absolute magnitude of SNIa in the second rung of the distance ladder. Here, we refer to this dataset as PPS, for short. By combining it with Planck, we obtain larger values of H_0, allowing us to study the impact of the bias in frameworks designed to mitigate the Hubble tension. As per Eq. (11.6) and as previously explained, these scenarios result in larger values of the bias, making them an interesting case study.

- DESI BAO measurements from DR1 [555]. For completeness, we also validate our results using BAO measurements from BOSS DR12 [565] and eBOSS DR16 [566], collectively referred to as the BOSS dataset.

We obtain our main results using the two data combinations Planck+BOSS+PPS and Planck+DESI+PPS. This allows us to demonstrate that both the fitting results and the conclusions regarding the bias introduced by σ_8 are completely stable under the choice of BAO data employed in the analysis.

The cosmological models considered have been selected based on their impact on the LSS and their ability to increase H_0, which is relevant for our discussion and also affects the bias described in Eq. (11.6). We explore the following models:

1. Λ*CDM.* We treat ΛCDM as a benchmark model, so we also obtain fitting results for it. We consider the six ΛCDM parameters, which are described in Sec. 1.2 : $\{\omega_b, \omega_{cdm}, \theta_*, \tau, \log(10^{10}A_s), n_s\}$. For these parameters, we choose flat-prior distributions, varying them uniformly in the ranges listed in Table 11.1.

2. w_0w_a*CDM parameterization.* We adopt the CPL or w_0w_aCDM parameterization [354] described in Sec. 3.4, which introduces a linear dependence on the scale factor in the dark energy equation of state, $w(a)$ (see Eq. (3.8)). The evolution of the dark energy density $\rho_{\rm DE}$ is governed by

$$\rho_{\rm DE}(a) = \rho^0_{\rm DE}\exp\left(3\int_a^1 \frac{1+w(a')}{a'}da'\right) , \tag{11.12}$$

with $\rho^0_{\rm DE} \equiv \rho_{\rm DE}(a=1)$. This versatility in affecting structure formation makes the model particularly compelling to study. As described in Sec. 3.4, for a fixed present-day abundance of cosmic species, the growth of large-scale structures is more suppressed in the past if dark energy increases with redshift (quintessence, $w > -1$), whereas the opposite occurs for phantom dark energy ($w < -1$). The w_0w_aCDM parameterization can accommodate both behaviors, including crossing the phantom divide. This is especially interesting given recent observational hints favoring dynamical dark energy within the w_0w_aCDM framework at more than 2σ [555, 567, 300], a result that does not appear to rely solely on DESI data (see, e.g., [568, 277]). In our Monte Carlo analyses of the w_0w_aCDM model, the parameters w_0 and w_a are varied using the flat priors listed in Table 11.1.

Table 11.1. List of priors for the baseline parameters, as well as for the additional parameters in the alternative scenarios, described in Sec. 11.1.2.

Parameter	Prior
$\omega_{\rm b}$	$[0.005\,,\,0.1]$
$\omega_{\rm c} h^2$	$[0.001\,,\,0.99]$
$100\,\theta_*$	$[0.5\,,\,10]$
τ	$[0.01\,,\,0.8]$
$\log(10^{10} A_s)$	$[1.61\,,\,3.91]$
$n_{\rm s}$	$[0.8\,,\,1.2]$
$N_{\rm eff}$	$[0\,,\,5]$
$\sum m_\nu$ [eV]	$[0.06\,,\,0.6]$
w_0	$[-2\,,\,2]$
w_a	$[-4\,,\,2]$
$f_{\rm EDE}$	$[0.001, 0.5]$
$\log_{10} z_c$	$[3.0, 4.3]$
θ_i	$[0.1, 3.1]$

3. *Neutrino Sector.* By means of $N_{\rm eff}$ and $\sum m_\nu$ we parameterize the neutrino sector (see Sec. 3.4). In the context of ΛCDM, $N_{\rm eff} \simeq 3.043$ [340, 341, 342]. Variations of $N_{\rm eff}$ (see, e.g., [343, 344, 345]) modify the sound horizon at recombination, because it is directly proportional to the contribution of neutrinos to the total radiation energy density. Larger $N_{\rm eff}$ values decrease the horizon and, therefore, require higher values of H_0 and enhance the LSS tension when analyzed in terms of σ_8. We will show, though, that in terms of the more reliable parameter σ_{12}, the growth of LSS remains close to the one predicted in ΛCDM.

   The parameter $\sum m_\nu$ denotes the sum of neutrino masses. A normal mass hierarchy, corresponding to the minimal value $\sum m_\nu = 0.06$ eV, is assumed in the Planck ΛCDM baseline model (see Sec. 3.3). However, neutrino oscillation experiments only set this lower bound, so larger values remain viable. Increasing the neutrino mass tends to reduce H_0 and suppresses power on scales below the neutrino free-streaming length. For this reason, it is particularly interesting to study $\sum m_\nu$ in combination with $N_{\rm eff}$ and explore their interplay. We consider the following two extensions of ΛCDM for the neutrino sector: ΛCDM+$N_{\rm eff}$ and ΛCDM+$N_{\rm eff} + \Sigma m_\nu$. The flat-prior ranges for $N_{\rm eff}$ and $\sum m_\nu$ are reported in Table 11.1.

4. *Early Dark Energy.* EDE models posit a non-negligible dark energy contribution in the early Universe, which can be realized, for example, through inhomogeneous dark energy fluids or scalar fields (see Sec. 3.4). In our analysis, we adopt the implementation of [332], where a light scalar field is initially frozen far from the minimum of its potential and, due to Hubble friction, behaves effectively as a cosmological constant. At a critical redshift z_c before recombination, the Hubble rate drops below the field mass, triggering the field to roll down its potential and oscillate around the minimum. Its energy density

subsequently redshifts faster than radiation, ensuring that it becomes subdominant by the time of decoupling [270, 338]. The model is typically described by additional parameters such as the maximum fractional energy density at z_c, $f_{\rm EDE} \equiv \rho_{\rm EDE}(z_c)/\rho_{\rm tot}(z_c)$, and the initial field displacement θ_i. By increasing the early-Universe energy density, reducing the sound horizon, and raising the CMB-inferred value of H_0, this dynamics renders EDE a compelling candidate to alleviate the Hubble tension and a natural choice for our analysis. To solve the coupled system of Einstein–Boltzmann equations in the EDE scenario, we use the publicly available code `CLASS_EDE`[5] [569]. For the Monte Carlo analyses, we adopt the flat priors listed in Table 11.1 for $f_{\rm EDE}$, $\log_{10} z_c$, and θ_i.

Since we are dealing with multiple extensions of the standard model, we decided to perform a simple comparison with respect to ΛCDM. To achieve this, we utilize the AIC defined by Eq. (5.8), which allows us to penalize extra model parameters. We compare the AIC values of the non-standard models to that of ΛCDM by computing the difference $\Delta{\rm AIC} = {\rm AIC}_{\Lambda{\rm CDM}} - {\rm AIC}_i$, i.e., using the standard model as the benchmark. A positive difference of ΔAIC signals a preference for the non-standard model. More concretely, we quantify such a preference by means of the Jeffreys' scale [444]. See Chapter 5 for further details on this statistical method.

Results

The posterior distributions of H_0 and corresponding posteriors of R_8 obtained for the various models under study using the datasets Planck+BOSS+PPS and Planck+DESI+PPS are shown in Fig. 11.2. It is already known that late-time dynamical dark energy alone is completely unable to produce large enough values of H_0, even by taking into account the SH0ES data in the fitting analysis[6], and the w_0w_aCDM parameterization is no exception. On the other hand, as expected, regardless of the BAO dataset employed in the analysis (BOSS or DESI), we find values of H_0 that are much larger in those models that allow for some additional energy contribution before recombination compared to the ΛCDM. This additional energy induces a decrease of the sound horizon at the baryon-drag and decoupling epochs and forces the increase of $H(z)$ in the late Universe in order to properly explain the BAO data and the location of the first peak of the CMB temperature angular power spectrum, measured very precisely by the Planck collaboration [11]. This is the case of ΛCDM+$N_{\rm eff}$ (considering or not the variation of $\sum m_\nu$) and EDE, for which we obtain central values $H_0 \gtrsim 71.2$ km/s/Mpc and $H_0 \gtrsim 72$ km/s/Mpc, respectively. In Table 11.2, we provide for completeness the fitting results for all the model parameters, while the relative contour plots are reported in Appendix C, cf. Figs. C.3 - C.7. Finally, in Fig. 11.3 we display the values of $\sigma_8(z)$ and $\sigma_{12}(z)$ obtained at different redshift. The results warrant a few remarks. In the ΛCDM+$N_{\rm eff}$ model, an increase in H_0 is made possible by a rise in the number of ultra-relativistic species, which reaches $N_{\rm eff} = 3.5 - 3.6$. This value deviates from the standard one by approximately 4.2σ when the Planck+BOSS+PPS dataset is

[5] `https://github.com/mwt5345/class_ede`

[6] Anisotropic BAO data as those employed in this work, do not give room for purely cosmological late-time solutions to the Hubble tension, see Chapter 9.

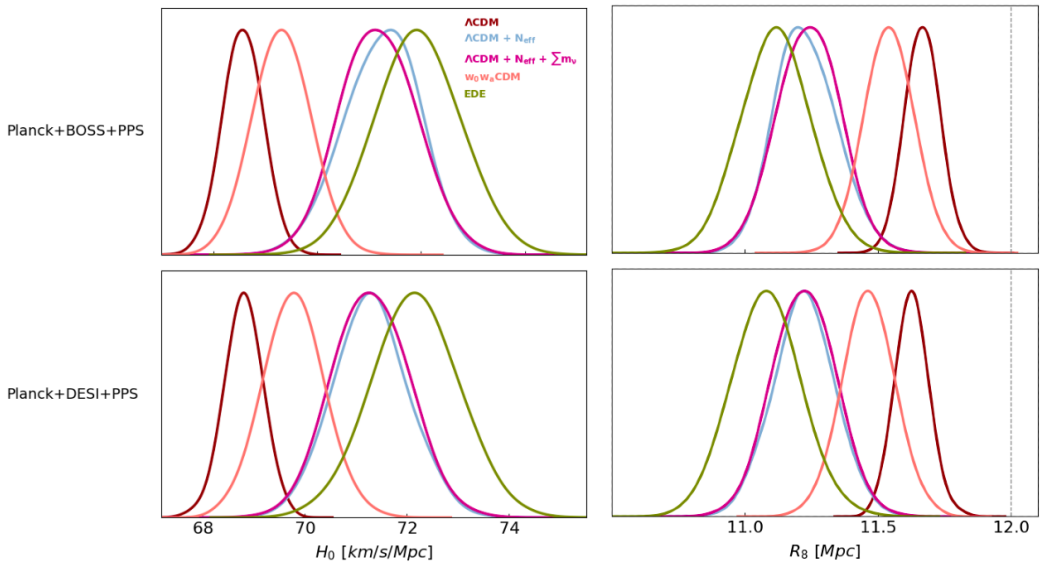

Figure 11.2. Posterior distributions of H_0 (left panels) and $R_8 = 8/h$ (right panels) obtained from Planck+BOSS+PPS (first row) and Planck+DESI+PPS (second row) for the five cosmological models listed in the legend. The vertical dashed line in the right-hand side plots indicates the reference scale of $R_{12} = 12$ Mpc.

used for the fitting analysis, and by about 3.7σ when Planck+DESI+PPS is used instead. In EDE, larger values of H_0 are possible thanks to an energy injection around redshift $z_c \sim 4200$, with a maximum EDE fraction $f_{\rm EDE} \sim 13\%$ (see Table 11.2). Our findings for w_0w_aCDM and EDE are aligned with those provided in [276] and [570], respectively. See also [332, 319].

Two key points can be revealed from the right-hand side plot of Fig. 11.2:

1. the differences in the values of R_8 obtained across the various models are significant, particularly between ΛCDM or w_0w_aCDM and the models that introduce new physics before the decoupling era;

2. in all cases, the values of R_8 are substantially smaller than R_{12}, even in ΛCDM and w_0w_aCDM, where h remains far below the SH0ES measurement but is still larger than h_*.

As a consequence, comparing the $\sigma_8(z)$ curves obtained from the Monte Carlo analyses across different models is largely uninformative, since they reflect the amplitude of fluctuations at distinct physical scales. Thus, σ_8 values alone cannot provide reliable conclusions about the relative clustering performance of the models. A more meaningful strategy is to compare σ_R at a fixed scale, such as R_{12}. Given the sizable difference between R_8 and R_{12}, this fairer comparison is expected to lead to significantly different conclusions.

This behavior is illustrated in Fig. 11.3, which displays the constraints on $\sigma_8(z)$ and $\sigma_{12}(z)$ for all models at seven redshifts between $z = 0$ and $z = 2.96$. Remarkably, the values of $\sigma_{12}(z)$ show no statistically significant differences across models, regardless of redshift: at any given z, they remain consistent within $< 1\sigma$. This demonstrates that the data constrain the shape of $\sigma_{12}(z)$ in a way that is

Table 11.2. Fitting results for the parameters of the various models described in Sec. 11.1.2 at 68% C.L., obtained from the analysis with the datasets Planck+BOSS+PPS (upper half) and Planck+DESI+PPS (lower half). Upper bounds are given at 95% C.L. The parameter $\omega_m = \Omega_m^0 h^2$ is the sum of the baryon and CDM reduced density parameters. In the last rows of both the subtables, we provide the minimum values of χ^2 as well as the differences of AIC values with respect to ΛCDM.

Planck+BOSS+PPS

Parameter	ΛCDM	w_0w_aCDM	ΛCDM + $N_{\rm eff}$	ΛCDM + $N_{\rm eff}$ + Σm_ν	EDE
ω_m	0.1407 ± 0.0008	0.1430 ± 0.0010	$0.1511^{+0.0028}_{-0.0021}$	0.1514 ± 0.0026	0.1570 ± 0.0035
H_0 [km/s/Mpc]	68.57 ± 0.39	69.32 ± 0.56	$71.28^{+0.78}_{-0.67}$	71.19 ± 0.75	$72.06^{+0.84}_{-0.83}$
$\log(10^{10}A_s)$	3.051 ± 0.016	$3.042^{+0.015}_{-0.014}$	$3.070^{+0.015}_{-0.017}$	3.074 ± 0.018	$3.073^{+0.016}_{-0.017}$
n_s	0.971 ± 0.004	0.965 ± 0.004	0.986 ± 0.005	0.987 ± 0.005	0.992 ± 0.006
σ_8	0.806 ± 0.007	0.832 ± 0.010	0.834 ± 0.009	0.828 ± 0.011	0.846 ± 0.011
σ_{12}	0.791 ± 0.009	0.810 ± 0.009	0.796 ± 0.009	$0.791^{+0.010}_{-0.009}$	0.800 ± 0.008
S_8	0.805 ± 0.012	0.829 ± 0.012	0.830 ± 0.013	0.826 ± 0.014	0.848 ± 0.015
$N_{\rm eff}$	-	-	$3.58^{+0.14}_{-0.11}$	3.60 ± 0.13	-
Σm_ν [eV]	-	-	-	< 0.15	-
w_0	-	$-0.859^{+0.050}_{-0.054}$	-	-	-
w_a	-	$-0.82^{+0.24}_{-0.21}$	-	-	-
$f_{\rm EDE}$	-	-	-	-	0.133 ± 0.024
$\log_{10}(z_c)$	-	-	-	-	$3.619^{+0.082}_{-0.133}$
θ_i	-	-	-	-	> 2.13
Ω_m^0	0.299 ± 0.005	0.298 ± 0.006	0.297 ± 0.005	0.299 ± 0.005	0.302 ± 0.005
r_d [Mpc]	147.53 ± 0.23	147.06 ± 0.25	$142.026^{+0.97}_{-1.36}$	$141.956^{+1.24}_{-1.25}$	$139.64^{+1.53}_{-1.51}$
M	-19.398 ± 0.019	-19.374 ± 0.022	-19.314 ± 0.026	-19.317 ± 0.028	-19.290 ± 0.030
$\chi^2_{\rm min}$	4279.90	4262.29	4261.42	4258.96	4246.83
ΔAIC	-	13.61	16.48	16.94	27.07

Planck+DESI+PPS

Parameter	ΛCDM	w_0w_aCDM	ΛCDM + $N_{\rm eff}$	ΛCDM + $N_{\rm eff}$ + Σm_ν	EDE
ω_m	0.1402 ± 0.0008	0.1429 ± 0.0010	0.1494 ± 0.0025	0.1499 ± 0.0027	0.1556 ± 0.0036
H_0 [km/s/Mpc]	68.80 ± 0.38	$69.78^{+0.59}_{-0.60}$	$71.30^{+0.73}_{-0.72}$	$71.30^{+0.76}_{-0.75}$	$72.27^{+0.87}_{-0.86}$
$\log(10^{10}A_s)$	$3.046^{+0.017}_{-0.018}$	3.043 ± 0.016	$3.069^{+0.017}_{-0.019}$	$3.070^{+0.016}_{-0.018}$	3.071 ± 0.017
n_s	0.972 ± 0.004	0.965 ± 0.004	0.986 ± 0.005	0.987 ± 0.005	0.993 ± 0.006
σ_8	$0.803^{+0.007}_{-0.008}$	$0.836^{+0.012}_{-0.011}$	0.830 ± 0.010	$0.824^{+0.012}_{-0.011}$	0.842 ± 0.011
σ_{12}	0.785 ± 0.008	0.810 ± 0.010	0.792 ± 0.009	$0.786^{+0.011}_{-0.009}$	0.795 ± 0.009
S_8	0.798 ± 0.011	0.827 ± 0.013	0.822 ± 0.013	0.816 ± 0.014	0.838 ± 0.015
$N_{\rm eff}$	-	-	3.53 ± 0.13	3.56 ± 0.14	-
Σm_ν [eV]	-	-	-	< 0.15	-
w_0	-	$-0.808^{+0.064}_{-0.071}$	-	-	-
w_a	-	$-1.10^{+0.34}_{-0.29}$	-	-	-
$f_{\rm EDE}$	-	-	-	-	0.129 ± 0.025
$\log_{10}(z_c)$	-	-	-	-	$3.622^{+0.083}_{-0.130}$
θ_i	-	-	-	-	> 2.43
Ω_m^0	0.296 ± 0.005	0.293 ± 0.005	0.294 ± 0.005	0.295 ± 0.005	0.298 ± 0.005
r_d [Mpc]	147.65 ± 0.22	$147.11^{+0.25}_{-0.26}$	$142.68^{+1.20}_{-1.19}$	$142.47^{+1.31}_{-1.30}$	$140.08^{+1.56}_{-1.58}$
M	$-19.390^{+0.018}_{-0.019}$	-19.360 ± 0.023	$-19.314^{+0.027}_{-0.026}$	-19.314 ± 0.027	-19.283 ± 0.030
$\chi^2_{\rm min}$	4268.11	4250.18	4256.69	4255.69	4235.97
ΔAIC	-	13.93	9.42	8.42	26.14

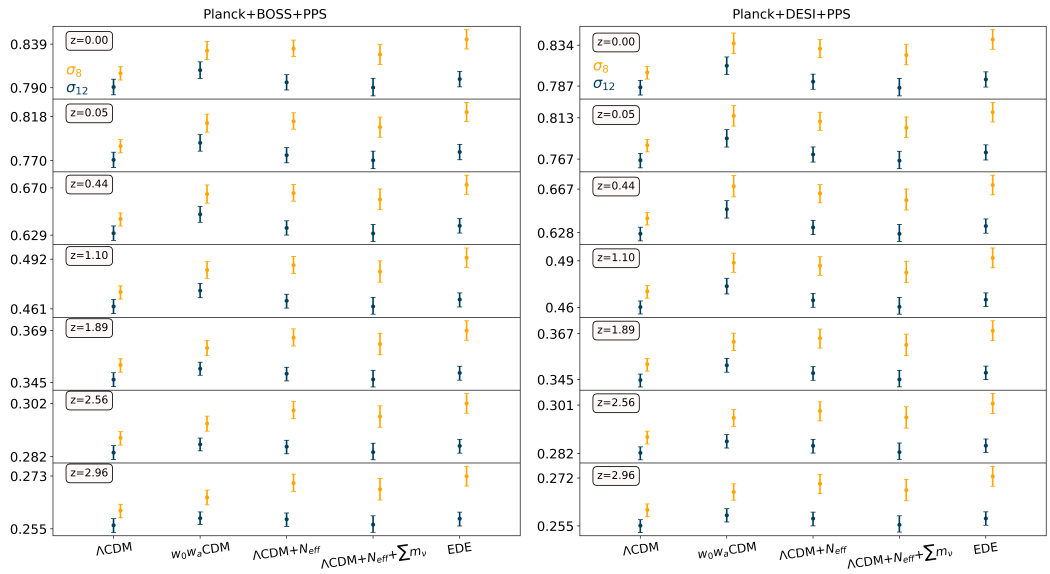

Figure 11.3. Constraints at 68% C.L. on σ_{12} (in green) and σ_8 (in orange) at different redshifts in the range $z \in [0, 2.96]$, obtained from the analysis of Sec. 11.1.2 for each of the five cosmological models studied in this work. We show the results obtained by exploiting the full combination of data, i.e. Planck+BOSS+PPS (left panel) and Planck+DESI+PPS (right panel). Notice that the σ_8 error bars are slightly shifted on the x-axis in order to better distinguish them from the σ_{12} results. This allows us to clearly visualize the relative shift (on the y-axis) between the two parameters for each model, which is present regardless of the redshift at which they are evaluated (see Eq (11.6)).

almost independent of the diverse underlying physics of the models considered. By contrast, $\sigma_8(z)$ exhibits substantial deviations from the stable behavior of $\sigma_{12}(z)$, with the largest discrepancies arising in models that prefer higher values of H_0. Let us consider, for instance, the constraints on these two functions for EDE (see Table 11.2) obtained under Planck+DESI+PPS[7] and let us consider in particular the result at $z = 0$. We find $\sigma_{12} = 0.795 \pm 0.009$, which is fully compatible with the ΛCDM constraint, $\sigma_{12,\Lambda} = 0.785 \pm 0.008$. However, $\sigma_8 = 0.842 \pm 0.011$ is 3.3σ higher than σ_{12} in EDE and 2.9σ higher than $\sigma_{8,\Lambda} = 0.803^{+0.007}_{-0.008}$. Hence, comparing the values of σ_8 obtained in ΛCDM and EDE, as is commonly done in the literature, would lead to the conclusion that EDE produces significantly greater clustering in the Universe than the standard model. This, in turn, would suggest that EDE is only capable of resolving the Hubble tension at the expense of worsening substantially the growth tension. This conclusion is clearly biased, and is caused by the incorrect use of σ_8. The values of σ_{12} and $\sigma_{12,\Lambda}$ indicate that the increase in the amplitude of fluctuations at linear scales in EDE is only mild and does not lead to a significant worsening of the growth tension. A similar discussion applies to the other models. The contour plots obtained for EDE, shown in Fig. C.7, reinforce our arguments. One can check that the correlation between $f_{\rm EDE}$ and σ_{12} is derisory, whereas for σ_8 the correlation

[7]The constraints obtained with Planck+BOSS+PPS and Planck+DESI+PPS are very similar, so we restrict the discussion to the latter, without loss of generality.

is positive and non-negligible. Therefore, the parameter responsible for the increase of H_0, i.e., $f_{\rm EDE}$, does not lead to a significant increase in σ_{12} because the model can adjust other parameters to compensate for its effects at the perturbation level. Similar compensations are also encountered in the other models. For instance, in Fig. C.5 we observe only a positive correlation between σ_8 and the parameter that helps to decrease the size of the sound horizon at recombination in ΛCDM+$N_{\rm eff}$ and ΛCDM+$N_{\rm eff}$+$\sum m_\nu$, $N_{\rm eff}$. This correlation is again absent in the $\sigma_{12} - N_{\rm eff}$ plane.

When expressed in terms of the parameter S_8, as measured by weak lensing surveys, the growth tension remains small in all models under study according to the latest KiDS release [255], which reports $S_8 = 0.815^{+0.016}_{-0.021}$. In fact, the tension essentially disappears, since the differences between the posterior values of S_8 and the KiDS result always stay below the 1σ level, with the sole exception of EDE with Planck+DES+PPS, where the discrepancy increases to a still mild 1.4σ CL. The same conclusion holds when the tension is assessed in the (Ω_m, S_8) plane: for all models, the constraints on Ω_m peak near 0.3 (cf. Table 11.2), fully consistent with KiDS [255].

Regarding the results for the sum of neutrino masses in ΛCDM+$N_{\rm eff}$+$\sum m_\nu$, we find an upper bound $\sum m_\nu < 0.15$ eV at 95% C.L. using Planck+BOSS+PPS and Planck+DESI+PPS. This constraint is somewhat weaker than other results in the literature that combine CMB and BAO data with $N_{\rm eff}$ fixed to its standard value (see, e.g., [11, 571, 555]). The reason is that larger neutrino masses suppress small-scale power, driving the amplitude of fluctuations closer to that of ΛCDM. Crucially, this conclusion becomes evident only when examining σ_{12}. In both ΛCDM and ΛCDM+$N_{\rm eff}$+$\sum m_\nu$, we find central values of σ_{12} in the range 0.785–0.791. By contrast, the values of σ_8 derived from Planck+BOSS+PPS and Planck+DESI+PPS are 1.7σ and 1.5σ larger, respectively, in ΛCDM+$N_{\rm eff}$+$\sum m_\nu$ than in ΛCDM. Once again, the underlying physics is best understood by considering σ_{12} rather than σ_8.

We now turn to the question of what error in χ^2 would be introduced by incorporating RSD and peculiar velocity data, treating the latter either as measurements of $f(z)\sigma_8(z)$ or of $f(z)\sigma_{12}(z)$. These data span the redshift range $z \in (0.01, 1.50)$. To obtain a rough estimate, we perform a simple exercise: we take the best-fit values for the different models (e.g., those derived from Planck+DESI+PPS) and compute the following two χ^2 statistics:

$$\chi^2_{f\sigma_8} = \sum_{i=1}^{15} \left(\frac{f(z_i)\sigma_8(z_i) - f(z_i)\sigma_8(z_i)|_{\rm obs}}{\sigma_i} \right)^2 , \tag{11.13}$$

and

$$\chi^2_{f\sigma_{12}} = \sum_{i=1}^{15} \left(\frac{f(z_i)\sigma_{12}(z_i) - f(z_i)\sigma_{12}(z_i)|_{\rm obs}}{\sigma_i} \right)^2 . \tag{11.14}$$

Here, $f(z_i)\sigma_{12}(z_i)|_{\rm obs}$ are the same observational values of $f(z_i)\sigma_8(z_i)|_{\rm obs}$, but treated as data points on $f(z_i)\sigma_{12}(z_i)$ (see discussion in Sec. 11.1.1). The aim is to show that by incorrectly treating the data as data on $f(z)\sigma_8(z)$, the models with larger values of H_0 are unfairly penalized, since the clustering in these models is overestimated

when it is evaluated in terms of the σ_8 parameter. The theoretical quantity of interest can be computed as follows,

$$f(z)\sigma_R(z) = -(1+z)\frac{d\sigma_R}{dz}\,, \tag{11.15}$$

and the derivative on the right-hand side can be calculated numerically with `CLASS`, by simply evaluating $d\sigma_R/dz \simeq (\sigma_R(z+\delta z) - \sigma_R(z))/\delta z$. Here, δz is just a small variation in redshift, which we take to be equal to 10^{-3}.

For the ΛCDM model, we obtain $\chi^2_{f\sigma_8} \approx 35$, whereas $\chi^2_{f\sigma_{12}} \approx 10$. Models favoring a Hubble parameter around $\sim 71-72$ km/s/Mpc exhibit an even clearer manifestation of this issue. For instance, in the ΛCDM+$N_{\rm eff}$+$\sum m_\nu$ scenario, we find $\chi^2_{f\sigma_8} \approx 78$ and $\chi^2_{f\sigma_{12}} \approx 11$. The disparity becomes even more striking in the EDE scenario, where $\chi^2_{f\sigma_8}$ rises dramatically to ≈ 118, while $\chi^2_{f\sigma_{12}}$ remains relatively small at ≈ 13. This demonstrates that all best-fit models can accommodate the data well when interpreted as measurements of $f(z)\sigma_{12}(z)$, whereas they are strongly, and artificially, penalized if the data are treated as $f(z)\sigma_8(z)$.

As a final result, by means of the AIC in (5.8) and simply comparing the χ^2 values, we find a very substantial improvement in the description of the cosmological data employed in this study in all the non-standard cosmologies, compared to ΛCDM. Using Planck+BOSS+PPS we find values ΔAIC > 10 for all models, which allows us to conclude that there exists very strong Bayesian evidence supporting the non-standard models against the ΛCDM. For w_0w_aCDM with the BOSS combination, ΔAIC $= 13.61$ and it remains stable when the BAO data are taken from DESI; for ΛCDM+$N_{\rm eff}$ and ΛCDM+$N_{\rm eff}+\sum m_\nu$, ΔAIC $\sim 16-17$ using BOSS and such value is lowered to ΔAIC ~ 9 when we use the Planck+DESI+PPS combination; however, it is still above the *strong evidence* threshold. As for the EDE model, we obtain the highest ΔAIC value for both data combinations, indicating very strong evidence in favor of a non-zero fraction of energy injected before recombination (ΔAIC ~ 27 for BOSS and ΔAIC ~ 26 for DESI). Consequently, EDE is strongly preferred over the other models due to its effectiveness in alleviating the Hubble tension, based on the data analyzed in this study. Although, to the best of our knowledge, not all of these model–data combinations have been previously investigated, our results are consistent with earlier analyses based on CMB, BAO, and SNIa observations (see e.g., [277, 570]).

However, rather than focusing on these pieces of evidence – which are, of course, a subject of considerable debate in the literature – our aim here is to stress that any theoretical resolution of the Hubble tension requires high H_0 values, which inevitably introduces significant biases when LSS analyses are performed using σ_8.

11.2 Final discussion

Clear examples made in this Chapter have underscored the need to abandon the use of σ_8 in galaxy clustering analyses and in the comparison of the clustering properties of cosmological models. Our arguments build upon the work of A.G. Sánchez [264] and consolidate insights previously presented in a scattered form across the literature [270, 271, 272, 235, 273, 266, 274, 267, 275, 276, 572, 277]. Nevertheless, the necessity

of transitioning from σ_8 to σ_{12} has apparently gone unnoticed by the majority of the community.

In this work, we aimed to further motivate this transition with some novel and very illustrative examples that bring to light the impact of the bias. After obtaining an approximate analytical formula of the difference $\sigma_8 - \sigma_{12}$ as a function of h, Eq. (11.6), we illustrated how the bias impacts our interpretation of the RSD and peculiar velocity measurements of $f(z)\sigma_R(z)$. As a last exercise, we have performed a detailed full Monte Carlo analysis considering five alternative cosmological models, namely, the ΛCDM, the w_0w_aCDM parameterization of dynamical dark energy, an extension of the standard model considering a larger amount of ultra-relativistic species with or without a non-minimal sum of the neutrino masses, and early dark energy. This selection of models includes scenarios with both late-time and early-time new physics, exhibiting varying abilities to alleviate the Hubble tension. We have constrained them using state-of-the-art CMB data from *Planck*, BAO data from BOSS and DESI, and SNIa data from the Pantheon+SH0ES. Our study demonstrates that the shapes of $\sigma_{12}(z)$ obtained across the five models are stable and compatible with each other within 1σ C.L., while the shapes of $\sigma_8(z)$ suffer from spurious very large positive shifts, more evident in the models that alleviate the H_0 tension. These shifts do not point to a real enhancement of clustering power, but are mainly induced by the shift in the scale R_8, which makes σ_8 characterize the amplitude of fluctuations at completely different physical scales. In terms of σ_{12}, we do not observe any statistically significant increase of the amplitude of fluctuations at linear scales in models that are able to soften or even erase the Hubble tension, like EDE. This is in contrast to σ_8, which points exactly in the opposite direction. Correcting for the bias by replacing σ_8 with σ_{12} enables a more reliable interpretation of fitting results and a better assessment of model performance in LSS growth. Consequently, previous objections to EDE and other early-time new physics models should be revisited, as they do not significantly increase structure relative to ΛCDM at linear scales. Our results also emphasize the importance of evaluating models' ability to simultaneously assess the Hubble and growth tension in the H_0–σ_{12} plane when considering RSD data, while weak lensing analyses can still be safely performed in terms of S_8 [266, 267].

Removing the bias introduced by σ_8 in current cosmological analyses is already urgent, and future data from ongoing surveys like Euclid and DESI will make the issue even more pressing (see leftmost plot of Fig. 3.3). We therefore advocate adopting σ_{12} as a standard metric to ensure robust and unbiased analyses, particularly in the conflictive scenarios considered here.

Conclusions and Prospects

The cosmic puzzle still has many missing pieces. Despite the remarkable success of the standard cosmological model, numerous open questions remain unresolved (see Chapter 3), and their persistence over the past decade has placed cosmology at a critical crossroads. The work presented in this thesis seeks to contribute to the community's efforts to illuminate these issues. By applying advanced statistical techniques, non-parametric reconstructions, and a rigorous treatment of data consistency, we aimed to extract as much model-independent information as possible from state-of-the-art observations (see Chapters 4 and 5). This strategy provides fresh insights into the fundamental tensions challenging the ΛCDM model and offers a complementary perspective on the expansion history of the Universe, while probing the physics underlying cosmic acceleration. Ultimately, the methodologies developed in this thesis set the stage for harnessing the power of next-generation surveys to address the Hubble tension and other anomalies, bringing us closer to a deeper and more unified understanding of the Universe's evolution.

The following points summarize both the challenges we tackled and the main conclusions derived from our investigations (see Chapters 6-11).

- The role that the calibrators of the local and inverse distance ladder – the SNIa absolute magnitude, M, and the sound horizon at the baryon-drag epoch, r_d – have in measuring cosmic distances across our Universe is crucial. They can be considered as two of the main players of the "H_0 Olympics". Potential unknown systematics or hidden model dependencies may bias our understanding of fundamental cosmological properties and impact the discourse on the Hubble tension in a dangerous way. In this context, we believe there is an urgent need to measure these quantities following a methodology as model-independent as possible. On the other hand, having also an accurate and agnostic determination of the spatial curvature, Ω_k, through CMB-independent data offers a crucial insight into the early Universe. To this end, the contribution of low-redshift data gathered by current surveys and telescopes is becoming increasingly valuable.

- Leveraging data from BAO, SNIa, and CCH, we have therefore tested some fundamental cosmological assumptions, including the constancy of the absolute magnitude of SNIa and the homogeneity of the Universe at large scales. We have found no hint of a violation of both at $z \lesssim 2$ using Pantheon+ SNIa and 3D BAO. This has legitimated us to independently estimate the curvature of the Universe and calibrate both the direct and inverse distance ladders under the validity of the Cosmological Principle, the metric description of gravity

and standard physics in the vicinity of stellar objects. The methodology we proposed relies on Gaussian Processes (GPs), a Machine Learning tool which enables data-driven reconstructions of functions of interest. With CCH and the latest available data sets on SNIa and 3D BAO – DESY5 and DESI DR2, respectively – we have obtained: $\Omega_k = -0.143 \pm 0.085$, $M = -19.324^{+0.092}_{-0.095}$ and $r_d = (144.00^{+5.38}_{-4.88})$ Mpc. This led to $H_0 = (68.83^{+3.03}_{-3.07})$ km/s/Mpc, a value closer to the CMB-inferred value. Remarkably, substituting M with the SH0ES value (M^{R22}), we have found $H_0 = (70.84 \pm 1.16)$ km/s/Mpc, which reduces the tension with CMB estimates below 3σ. This may have implications for the discussion about possible systematics in low-z SNIa that could bias the local estimate of the Hubble parameter.

- As current uncertainties limit the precision of our constraints and prevent us from arbitrating the Hubble tension, we have studied the constraining power of our methodology with future SNIa, CCH, and BAO observations from surveys such as Vera C. Rubin Observatory - LSST, Euclid, and DESI. This is the first time that an analysis of this kind has been carried out in the literature. Our forecast analysis indicated that, in an optimistic scenario, upcoming data will improve agnostic constraints on the ladder calibrators - M by $\sim$54%, r_d by $\sim$66% - which enable us to constrain the Hubble parameter, H_0, at a 2% level. Precision on Ω_k will increase by $\sim 50\%$. The relative precision on the sound horizon, $\sigma_{r_d}/r_d \sim 1.2\%$, will instead be valuable for assessing early-time solutions to the Hubble tension, as those which require new physics prior to recombination that would reduce the value of r_d. Our analysis, though not yet as precise as model-dependent analyses, outlines which improvements in future data — whether in quality, quantity, or redshift coverage — are likely to have the greatest impact on tightening the constraints on these cosmological parameters. Therefore, it paves the way for model-independent constraints expected in the coming decade. This could be the case of the Roman Space Telescope, which is expected to considerably extend the detection of SNIa up to $z \sim 3$. This broader redshift coverage will allow for a more robust anchoring of the Hubble diagram and improved sensitivity to cosmic curvature, enabling tighter tests of the distance ladder and potential deviations from ΛCDM.

- The use of CCH as calibrators of the distance ladders can be naturally extended to higher-redshift probes such as GRBs and QSOs, providing the opportunity to explore previously uncharted regions of cosmic history. Building on this, we have performed a model-independent calibration of GRBs and QSOs to construct unbiased luminosity distances up to $z \sim 5$ and $z \sim 7$, respectively. This approach extends the cosmic distance ladder beyond the reach of current SNIa and BAO samples ($z \sim 2.5$), offering a critical handle on intermediate- to high-redshift cosmology. At the same time, it allows us to assess the potential contribution of high-redshift probes to the H_0 debate, and to evaluate the current limitations of these observables. Indeed, the use of GRBs (or QSOs) correlations is still a challenge due to the spread in their intrinsic properties, stemming largely from the still not fully understood nature of their physical origins. Our methodology successfully calibrated one particular

GRB correlation – the 3D Dainotti relation [138] – achieving one of the lowest intrinsic scatter observed to date, $\sigma_{int} = 0.20^{+0.03}_{-0.05}$. This result is obtained after correcting the relation for possible redshift evolution of the physical parameters forming the GRBs plane. We have ensured the robustness of our approach against different prior choices and the modeling of CCH uncertainties and covariance. Furthermore, we have obtained constraints on the parameters of the relation compatible with the physics of the relation itself, thus supporting its theoretical interpretation. The same conclusions hold for QSOs. Calibrating the Risaliti-Lusso relation [179], we have found $\delta_{int} = 0.088 \pm 0.002$ when GP correlations and redshift evolution are considered. In the current quest to minimize uncertainties in high-z probes and thereby sharpen constraints on cosmological parameters, we have introduced a methodology able to model-independently pinpoint samples that can be used as robust sets of standardizable candles, offering a promising avenue for extending the cosmic distance ladder.

- We have then turned again our focus to the current discrepancy between the calibrators of the distance ladder, which is just a reframe of the Hubble tension. We have investigated how, from a phenomenological perspective, the shape of the Hubble function and SNIa absolute magnitude at low redshifts should be modified in order to reestablish the agreement between the local value of H_0, while keeping the good description of the CMB and BAO data at the last scattering surface. In this *late-time solution* to the Hubble tension, we have put particular emphasis on the role played by two different BAO data: anisotropic and angular measurements. Remarkably, we have found that they lead to very different results. Anisotropic BAO data favor an ultra-late-time (phantom-like) enhancement of $H(z)$ at $z \lesssim 2$, which must be accompanied by a transition in $M(z)$ in the same redshift range. This agrees with previous findings in the literature. Instead, when employing angular BAO data (claimed to be less subject to model dependencies), we have found that the increase of $H(z)$ starts at much higher redshifts, typically in the range $z \sim 0.5 - 0.8$. In this case, M is compatible with the SH0ES value. A slight transition, though, is not rejected by the data. Notably, this also requires the effective dark energy density to become negative at $z \gtrsim 2$. Despite leaving an imprint on completely different redshift ranges and having a different impact on the perturbed observables, both scenarios require a violation of the weak energy condition and allow for the effective crossing of the phantom divide.

- The above point has motivated us to develop a novel calibrator- and model-independent diagnostic to test the consistency of different BAO distance measurements. This diagnostic only depends on the validity of the Etherington relation and makes use of SNIa as redshift interpolator. By comparing 2D and 3D BAO datasets, we have revealed for the first time an unexpectedly high level of mismatch between them. This discrepancy is worrisome, since many of the points contained in these data sets are obtained from the same parent catalogs of tracers and, therefore, we would expect them to be consistent. We have found anisotropic and angular BAO to be in tension at a level of $\sim 2.5\sigma$

with Pantheon+ SNIa, and $\sim 4.6\sigma$ using SNIa from DESY5. This is a lower bound of the actual discrepancy, since we cannot account for the positive correlations between the two data sets that have not been reported in the literature. Moreover, we have validated our findings by assessing the validity of the Etherington relation across the probed redshift range. We have found that the relation is fulfilled by both 2D and 3D BAO, under either Pantheon+ and DESY5 samples. The maximum incompatibility is found to exist at $\sim 1\sigma$ C.L. in some redshift ranges for 3D BAO from DESI DR1 and 2D BAO data sets, which is not significant at all. Stronger constraints have been obtained in the literature, but they typically require the use of additional assumptions beyond those considered by us.

- The BAO discrepancy may highlight hidden systematics in the data or possible underestimation of the uncertainties. Indeed, [428] suggest that standard anisotropic BAO analyses could underestimate errors by up to a factor of two. Motivated by this, we have repeated our analysis under this scenario and found that, although the tension is somewhat alleviated, it remains significant when using the latest SNIa sample, reaching 3.5σ C.L. with DES Y5. Our study thus emphasizes the importance of independent verification and consistent methodologies in future galaxy surveys, ideally allowing BAO measurements to be extracted by a single team to ensure internal consistency.

- Building on the work by [264], we have advocated for the adoption of alternative LSS parameterizations that reduce biases in evaluating the growth of structure, providing also a more robust framework for testing potential solutions to the Hubble tension. This requires replacing σ_8 with a new parameter σ_R associated with a scale R that is unaffected by h, such as σ_{12}. We aimed to further motivate this transition with some novel and illustrative examples that highlight the impact of the bias. We have illustrated how it affects our interpretation of the RSD and peculiar velocity measurements of $f(z)\sigma_R(z)$, and have performed a detailed Monte Carlo analysis across five alternative cosmological models – such as the w_0w_aCDM parameterization and early dark energy – which encompass scenarios featuring both late-time and early-time new physics, with varying ability to alleviate the Hubble tension. We have constrained them using state-of-the-art CMB data from *Planck*, BAO data from BOSS and DESI, and SNIa data from Pantheon+SH0ES. Our study has demonstrated that $\sigma_8(z)$ suffers from spurious large positive shifts that do not point to a real enhancement of clustering power, but are instead mainly induced by the shift in the scale R_8, causing σ_8 to characterize the amplitude of fluctuations at completely different physical scales. When expressed in terms of σ_{12}, no statistically significant increase in the amplitude of linear-scale fluctuations is observed for models proposed to alleviate the Hubble tension. Indeed, by employing σ_{12}, we have demonstrated that these solutions exacerbate the growth tension far less than previously thought, allowing for a more physically meaningful interpretation of their impact on structure formation.

The points discussed above represent our effort to shed light on some of the most pressing challenges in modern cosmology while seeking to address them. In summary,

we have assessed the robustness of the cosmic distance ladder, examined the reliability of high-redshift indicators, clarified the interpretation of different BAO data, and advocated for more reliable large-scale structure parameterizations, providing new insights into the cosmological tensions. Through the development of model-independent techniques and data-driven reconstructions, we have demonstrated how current and future data can be exploited to test fundamental assumptions of the standard cosmological model while reducing biases induced by specific parameterizations. Together, these studies highlight both the robustness and limitations of ΛCDM and existing probes, while laying the groundwork for future surveys to provide sharper insights and more reliable conclusions about the physics driving current tensions.

Our effort has culminated in the present thesis, which I hope the reader has found both engaging and insightful.

Much remains to be said, and many discoveries still await us in the near future. The story of Cosmology still has to be completed, and I see many commas rather than a full stop. Yet, this is precisely the beauty of our pursuit, isn't it?

Rome, November 2025

Bibliography

[1] A. Einstein. "Die Grundlage der allgemeinen Relativitätstheorie". In: *Annalen der Physik* 354.7 (1916), pp. 769–822. DOI: https://doi.org/10.1002/andp.19163540702. eprint: https://onlinelibrary.wiley.com/doi/pdf/10.1002/andp.19163540702. URL: https://onlinelibrary.wiley.com/doi/abs/10.1002/andp.19163540702.

[2] Edwin Hubble. "A relation between distance and radial velocity among extra-galactic nebulae". In: *Proc. Nat. Acad. Sci.* 15 (1929), pp. 168–173. DOI: 10.1073/pnas.15.3.168.

[3] G. Lemaître. "Un Univers homogène de masse constante et de rayon croissant rendant compte de la vitesse radiale des nébuleuses extra-galactiques". In: *Annales de la Société Scientifique de Bruxelles* 47 (Jan. 1927).

[4] A. Friedmann. "Über die Krümmung des Raumes". In: *Zeitschrift fur Physik* 10 (Jan. 1922), pp. 377–386. DOI: 10.1007/BF01332580.

[5] A. Friedmann. "Über die Möglichkeit einer Welt mit konstanter negativer Krümmung des Raumes". In: *Zeitschrift fur Physik* 21.1 (Dec. 1924), pp. 326–332. DOI: 10.1007/BF01328280.

[6] Particle Data Group, P A Zyla, and Barnett et al. "Review of Particle Physics". In: *Progress of Theoretical and Experimental Physics* 2020.8 (Aug. 2020). 083C01. ISSN: 2050-3911. DOI: 10.1093/ptep/ptaa104. eprint: https://academic.oup.com/ptep/article-pdf/2020/8/083C01/34673722/ptaa104.pdf. URL: https://doi.org/10.1093/ptep/ptaa104.

[7] R. H. Dicke et al. "Cosmic Black-Body Radiation." In: *apj* 142 (July 1965), pp. 414–419. DOI: 10.1086/148306.

[8] A. A. Penzias and R. W. Wilson. "A Measurement of Excess Antenna Temperature at 4080 Mc/s." In: *ApJ* 142 (1965), pp. 419–421. DOI: 10.1086/148307.

[9] J. C. Mather et al. "Measurement of the Cosmic Microwave Background Spectrum by the COBE FIRAS Instrument". In: *ApJ* 420 (Jan. 1994), p. 439. DOI: 10.1086/173574.

[10] C. L. Bennett et al. "Nine-year Wilkinson Microwave Anisotropy Probe (WMAP) Observations: final maps and results". In: *The Astrophysical Journal Supplement Series* 208.2 (Sept. 2013), p. 20. DOI: 10.1088/0067-0049/208/2/20. URL: https://doi.org/10.1088%2F0067-0049%2F208%2F2%2F20.

[11] N. Aghanim et al. "Planck 2018 results. VI. Cosmological parameters". In: *Astron. Astrophys.* 641 (2020). [Erratum: Astron.Astrophys. 652, C4 (2021)], A6. DOI: 10.1051/0004-6361/201833910. arXiv: 1807.06209 [astro-ph.CO].

[12] Simone Aiola et al. "The Atacama Cosmology Telescope: DR4 maps and cosmological parameters". In: *JCAP* 2020.12, 047 (Dec. 2020), p. 047. DOI: 10.1088/1475-7516/2020/12/047. arXiv: 2007.07288 [astro-ph.CO].

[13] Adam G. Riess et al. "Observational evidence from supernovae for an accelerating universe and a cosmological constant". In: *Astron. J.* 116 (1998), pp. 1009–1038. DOI: 10.1086/300499. arXiv: astro-ph/9805201.

[14] S. Perlmutter et al. "Measurements of Ω and Λ from 42 high redshift supernovae". In: *Astrophys. J.* 517 (1999), pp. 565–586. DOI: 10.1086/307221. arXiv: astro-ph/9812133.

[15] Alan H. Guth. "Inflationary universe: A possible solution to the horizon and flatness problems". In: *Phys. Rev. D* 23 (2 1981), pp. 347–356. DOI: 10.1103/PhysRevD.23.347. URL: https://link.aps.org/doi/10.1103/PhysRevD.23.347.

[16] Alexei A. Starobinsky. "Dynamics of Phase Transition in the New Inflationary Universe Scenario and Generation of Perturbations". In: *Phys. Lett. B* 117 (1982), pp. 175–178. DOI: 10.1016/0370-2693(82)90541-X.

[17] A. D. Linde. "A new inflationary universe scenario: A possible solution of the horizon, flatness, homogeneity, isotropy and primordial monopole problems". In: *Physics Letters B* 108.6 (Feb. 1982), pp. 389–393. DOI: 10.1016/0370-2693(82)91219-9.

[18] P. D. B. Collins, Alan D. Martin, and E. J. Squires. *Particle physics and Cosmology.* 1989.

[19] Albert Einstein. "The Foundation of the General Theory of Relativity". In: *Annalen Phys.* 49.7 (1916). Ed. by Jong-Ping Hsu and D. Fine, pp. 769–822. DOI: 10.1002/andp.19163540702.

[20] W. de Sitter. "Einstein's theory of gravitation and its astronomical consequences, First Paper". In: *Mon. Not. Roy. Astron. Soc.* 76 (1916), pp. 699–728. DOI: 10.1093/mnras/76.9.699.

[21] Alan A. Coley and David L. Wiltshire. "What is general relativity?" In: *physscr* 92.5, 053001 (May 2017), p. 053001. DOI: 10.1088/1402-4896/aa6857. arXiv: 1612.09309 [gr-qc].

[22] Dominik J. Schwarz. "Thoughts on the Cosmological Principle". In: *Fundamental Interactions.* WORLD SCIENTIFIC, 2009, pp. 267–276. DOI: 10.1142/9789814277839_0015. URL: https://doi.org/10.1142%2F9789814277839_0015.

[23] Pavan Kumar Aluri et al. "Is the observable Universe consistent with the cosmological principle?" In: *Class. Quant. Grav.* 40.9 (2023), p. 094001. DOI: 10.1088/1361-6382/acbefc. arXiv: 2207.05765 [astro-ph.CO].

[24] N. Vittorio. *Cosmology.* CRC Press, 2017.

[25] S. Navas et al. "Review of particle physics". In: *Phys. Rev. D* 110.3 (2024), p. 030001. DOI: 10.1103/PhysRevD.110.030001.

[26] T. Padmanabhan. "Cosmological constant: The Weight of the vacuum". In: *Phys. Rept.* 380 (2003), pp. 235–320. DOI: 10.1016/S0370-1573(03)00120-0. arXiv: hep-th/0212290.

[27] P. J. E. Peebles and Bharat Ratra. "The Cosmological Constant and Dark Energy". In: *Rev. Mod. Phys.* 75 (2003). Ed. by Jong-Ping Hsu and D. Fine, pp. 559–606. DOI: 10.1103/RevModPhys.75.559. arXiv: astro-ph/0207347.

[28] Will Handley. "Curvature tension: evidence for a closed universe". In: *Phys. Rev. D* 103.4 (2021), p. L041301. DOI: 10.1103/PhysRevD.103.L041301. arXiv: 1908.09139 [astro-ph.CO].

[29] Eleonora Di Valentino, Alessandro Melchiorri, and Joseph Silk. "Planck evidence for a closed Universe and a possible crisis for cosmology". In: *Nature Astron.* 4.2 (2019), pp. 196–203. DOI: 10.1038/s41550-019-0906-9. arXiv: 1911.02087 [astro-ph.CO].

[30] George Efstathiou and Steven Gratton. "The evidence for a spatially flat Universe". In: *Mon. Not. Roy. Astron. Soc.* 496.1 (2020), pp. L91–L95. DOI: 10.1093/mnrasl/slaa093. arXiv: 2002.06892 [astro-ph.CO].

[31] Sunny Vagnozzi et al. "The galaxy power spectrum take on spatial curvature and cosmic concordance". In: *Phys. Dark Univ.* 33 (2021), p. 100851. DOI: 10.1016/j.dark.2021.100851. arXiv: 2010.02230 [astro-ph.CO].

[32] Sunny Vagnozzi, Abraham Loeb, and Michele Moresco. "Eppur è piatto? The Cosmic Chronometers Take on Spatial Curvature and Cosmic Concordance". In: *Astrophys. J.* 908.1 (2021), p. 84. DOI: 10.3847/1538-4357/abd4df. arXiv: 2011.11645 [astro-ph.CO].

[33] Javier de Cruz Pérez, Chan-Gyung Park, and Bharat Ratra. "Updated observational constraints on spatially flat and nonflat ΛCDM and XCDM cosmological models". In: *Phys. Rev. D* 110.2 (2024), p. 023506. DOI: 10.1103/PhysRevD.110.023506. arXiv: 2404.19194 [astro-ph.CO].

[34] Simone Aiola et al. "The Atacama Cosmology Telescope: DR4 Maps and Cosmological Parameters". In: *JCAP* 12 (2020), p. 047. DOI: 10.1088/1475-7516/2020/12/047. arXiv: 2007.07288 [astro-ph.CO].

[35] M. Tristram et al. "Cosmological parameters derived from the final Planck data release (PR4)". In: *Astron. Astrophys.* 682 (2024), A37. DOI: 10.1051/0004-6361/202348015. arXiv: 2309.10034 [astro-ph.CO].

[36] Jacobo Asorey and Javier de Cruz Pérez. "Revisiting ΛCDM extensions in light of re-analyzed CMB data". In: (June 2025). arXiv: 2506.13537 [astro-ph.CO].

[37] Eleonora Di Valentino et al. "Snowmass2021 - Letter of interest cosmology intertwined IV: The age of the universe and its curvature". In: *Astropart. Phys.* 131 (2021), p. 102607. DOI: 10.1016/j.astropartphys.2021.102607. arXiv: 2008.11286 [astro-ph.CO].

[38] P. J. E. Peebles. "Tests of cosmological models constrained by inflation". In: *apj* 284 (Sept. 1984), pp. 439–444. DOI: 10.1086/162425.

[39] G. Efstathiou, W. J. Sutherland, and S. J. Maddox. "The cosmological constant and cold dark matter". In: *Nature* 348 (1990), pp. 705–707. DOI: 10.1038/348705a0.

[40] Luca Amendola and Shinji Tsujikawa. *Dark Energy: Theory and Observations*. Cambridge University Press, 2015. ISBN: 978-1-107-45398-2.

[41] Albert Einstein. "Zum Kosmologischen Problem der allgemeinen Relativitätstheorie". In: *Verlag der Königlich-Preussischen Akademie der Wissenschaften* (1931).

[42] Steven Weinberg. "The Cosmological Constant Problem". In: *Rev. Mod. Phys.* 61 (1989). Ed. by Jong-Ping Hsu and D. Fine, pp. 1–23. DOI: 10.1103/RevModPhys.61.1.

[43] Jerome Martin. "Everything You Always Wanted To Know About The Cosmological Constant Problem (But Were Afraid To Ask)". In: *Comptes Rendus Physique* 13 (2012), pp. 566–665. DOI: 10.1016/j.crhy.2012.04.008. arXiv: 1205.3365 [astro-ph.CO].

[44] Joan Sola Peracaula. "The cosmological constant problem and running vacuum in the expanding universe". In: *Phil. Trans. Roy. Soc. Lond. A* 380 (2022), p. 20210182. DOI: 10.1098/rsta.2021.0182. arXiv: 2203.13757 [gr-qc].

[45] Mario Hamuy et al. "A Hubble diagram of distant type IA supernovae". In: *Astron. J.* 109 (1995), pp. 1–13. DOI: 10.1086/117251.

[46] Saul Perlmutter. "Supernovae, Dark Energy, and the Accelerating Universe". In: *Phys. Today* 56.4 (2003), pp. 53–60. DOI: 10.1063/1.1580050.

[47] Matts Roos. "Dark Matter: The evidence from astronomy, astrophysics and cosmology". In: *arXiv e-prints*, arXiv:1001.0316 (Jan. 2010), arXiv:1001.0316. arXiv: 1001.0316 [astro-ph.CO].

[48] A. V. Zasov et al. "Dark matter in galaxies". In: *Physics Uspekhi* 60.1 (Apr. 2017), p. 3. DOI: 10.3367/UFNe.2016.03.037751. arXiv: 1710.10630 [astro-ph.GA].

[49] Katherine Freese. "Status of dark matter in the universe". In: *International Journal of Modern Physics D* 26.6, 1730012-223 (Jan. 2017), pp. 1730012–223. DOI: 10.1142/S0218271817300129. arXiv: 1701.01840 [astro-ph.CO].

[50] C. P. Burgess. "The Cosmological Constant Problem: Why it's hard to get Dark Energy from Micro-physics". In: *arXiv e-prints*, arXiv:1309.4133 (Sept. 2013), arXiv:1309.4133. arXiv: 1309.4133 [hep-th].

[51] Alan H. Guth. "Inflationary universe: A possible solution to the horizon and flatness problems". In: *PRD* 23.2 (Jan. 1981), pp. 347–356. DOI: 10.1103/PhysRevD.23.347.

[52] A. A. Starobinsky. "A new type of isotropic cosmological models without singularity". In: *Physics Letters B* 91.1 (Mar. 1980), pp. 99–102. DOI: 10.1016/0370-2693(80)90670-X.

[53] S.W. Hawking. "The development of irregularities in a single bubble inflationary universe". In: *Physics Letters B* 115.4 (1982), pp. 295–297. ISSN: 0370-2693. DOI: https://doi.org/10.1016/0370-2693(82)90373-2. URL: https://www.sciencedirect.com/science/article/pii/0370269382903732.

[54] Alan H. Guth and So-Young Pi. "Fluctuations in the New Inflationary Universe". In: *Phys. Rev. Lett.* 49 (15 1982), pp. 1110–1113. DOI: 10.1103/PhysRevLett.49.1110. URL: https://link.aps.org/doi/10.1103/PhysRevLett.49.1110.

[55] J. Martin. "The Theory of Inflation". In: *arXiv e-prints* (July 2018). arXiv: 1807.11075.

[56] Viatcheslav F. Mukhanov. "Gravitational Instability of the Universe Filled with a Scalar Field". In: *JETP Lett.* 41 (1985), pp. 493–496.

[57] Misao Sasaki. "Large Scale Quantum Fluctuations in the Inflationary Universe". In: *Prog. Theor. Phys.* 76 (1986), p. 1036. DOI: 10.1143/PTP.76.1036.

[58] Patrick Peter. "Cosmological Perturbation Theory". In: *arXiv e-prints*, arXiv:1303.2509 (2013). arXiv: 1303.2509 [astro-ph.CO].

[59] G. F. Smoot et al. "Structure in the COBE Differential Microwave Radiometer First-Year Maps". In: *ApJL* 396 (Sept. 1992), p. L1. DOI: 10.1086/186504.

[60] Robert H. Brandenberger. "Lectures on the Theory of Cosmological Perturbations". In: *The early universe and observational cosmology, edited by N. Breton, J.L. Cervantes-Cota, and M. Salgado, Lecture Notes in Physics, vol. 646, 2004., p.127-167.* Ed. by Nora Bretón, Jorge Luis Cervantes-Cota, and Marcelo Salgad. Vol. 646. 2004, pp. 127–167. DOI: 10.1007/978-3-540-40918-2_5.

[61] R. H. Dicke et al. "Cosmic Black-Body Radiation." In: *ApJ* 142 (1965), pp. 414–419. DOI: 10.1086/148306.

[62] D. J. Fixsen and J. C. Mather. "The Spectral Results of the Far-Infrared Absolute Spectrophotometer Instrument on COBE". In: *ApJ* 581.2 (2002), pp. 817–822. DOI: 10.1086/344402.

[63] B. J. T. Jones and R. F. G. Wyse. "The ionisation of the primeval plasma at the time of recombination". In: *A&A* 149.1 (1985), pp. 144–150.

[64] C. J. MacTavish et al. "Cosmological Parameters from the 2003 Flight of BOOMERANG". In: *ApJ* 647 (Aug. 2006), pp. 799–812. DOI: 10.1086/505558. eprint: astro-ph/0507503.

[65] E. Komatsu et al. "Seven-year Wilkinson Microwave Anisotropy Probe (WMAP) Observations: Cosmological Interpretation". In: *ApJs* 192.2, 18 (2011), p. 18. DOI: 10.1088/0067-0049/192/2/18. arXiv: 1001.4538 [astro-ph.CO].

[66] Planck Collaboration et al. "Planck 2018 results. V. CMB power spectra and likelihoods". In: *A&A* 641, A5 (Sept. 2020), A5. DOI: 10.1051/0004-6361/201936386. arXiv: 1907.12875 [astro-ph.CO].

[67] W. L. K. Wu et al. "Initial Performance of Bicep3: A Degree Angular Scale 95 GHz Band Polarimeter". In: *Journal of Low Temperature Physics* 184 (Aug. 2016), pp. 765–771. DOI: 10.1007/s10909-015-1403-x. arXiv: 1601.00125 [astro-ph.IM].

[68] Brian G. Keating et al. "BICEP: a large angular scale CMB polarimeter". In: *Polarimetry in Astronomy*. Ed. by Silvano Fineschi. Vol. 4843. Society of Photo-Optical Instrumentation Engineers (SPIE) Conference Series. Feb. 2003, pp. 284–295. DOI: 10.1117/12.459274.

[69] D. Hanson et al. "Detection of B-mode Polarization in the Cosmic Microwave Background with Data from the South Pole Telescope". In: *Phys. Rev. Lett.* 111.14 (2013), p. 141301. DOI: 10.1103/PhysRevLett.111.141301. arXiv: 1307.5830 [astro-ph.CO].

[70] R. K. Sachs and A. M. Wolfe. "Perturbations of a Cosmological Model and Angular Variations of the Microwave Background". In: *ApJ* 147 (Jan. 1967), p. 73. DOI: 10.1086/148982.

[71] Joseph Silk. "Cosmic Black-Body Radiation and Galaxy Formation". In: *ApJ* 151 (1968), p. 459. DOI: 10.1086/149449.

[72] Planck Collaboration et al. "Planck 2018 results. I. Overview and the cosmological legacy of Planck". In: *A&A* 641, A1 (Sept. 2020), A1. DOI: 10.1051/0004-6361/201833880. arXiv: 1807.06205 [astro-ph.CO].

[73] R. A. Sunyaev and Ya. B. Zeldovich. "Small-Scale Fluctuations of Relic Radiation". In: *Apss* 7.1 (Apr. 1970), pp. 3–19. DOI: 10.1007/BF00653471.

[74] Steven Weinberg. *Gravitation and Cosmology: Principles and Applications of the General Theory of Relativity*. New York: John Wiley and Sons, 1972. ISBN: 978-0-471-92567-5, 978-0-471-92567-5.

[75] I.M.H. Etherington. "On the definition of distance in general relativity". In: *Philos. Mag.* 15 (1933), p. 761. DOI: 10.1080/14786443309462220.

[76] Fabrizio Renzi, Natalie B. Hogg, and William Giarè. "The resilience of the Etherington–Hubble relation". In: *Mon. Not. Roy. Astron. Soc.* 513.3 (2022), pp. 4004–4014. DOI: 10.1093/mnras/stac1030. arXiv: 2112.05701 [astro-ph.CO].

[77] Jing-Zhao Qi et al. "Testing the cosmic distance duality relation using strong gravitational lensing time delays and Type Ia supernovae". In: (July 2024). arXiv: 2407.07336 [astro-ph.CO].

[78] Li Tang, Hai-Nan Lin, and Ying Wu. "Cosmic distance duality relation in light of time-delayed strong gravitational lensing". In: *Chin. Phys. C* 49.1 (2025), p. 015104. DOI: 10.1088/1674-1137/ad83a8. arXiv: 2410.08595 [astro-ph.CO].

[79] Felicitas Keil et al. "Probing the Distance Duality Relation with Machine Learning and Recent Data". In: *arXiv preprint 2504.01750* (Apr. 2025). arXiv: 2504.01750 [astro-ph.CO].

[80] Elsa M. Teixeira et al. "Implications of distance duality violation for the H_0 tension and evolving dark energy". In: (Apr. 2025). arXiv: 2504.10464 [astro-ph.CO].

[81] J. O. Dickey et al. "Lunar Laser Ranging: A Continuing Legacy of the Apollo Program". In: *Science* 265 (1994), pp. 482–490. DOI: 10.1126/science.265.5171.482.

[82] Gaia Collaboration et al. "The Gaia mission". In: *aap* 595, A1 (Nov. 2016), A1. DOI: 10.1051/0004-6361/201629272. arXiv: 1609.04153 [astro-ph.IM].

[83] Henrietta S. Leavitt and Edward C. Pickering. "Periods of 25 Variable Stars in the Small Magellanic Cloud". In: *Harvard Obs. Circ.* 173 (1912), pp. 1–3.

[84] A.S. Eddington. "The Mathematical Theory of Relativity". In: *Cambridge Univ. Press, Cambridge* (1924).

[85] Antonella Vallenari et al. "Gaia data release 3-summary of the content and survey properties". In: *Astronomy & Astrophysics* 674 (2023), A1.

[86] Grzegorz Pietrzyński et al. "A distance to the Large Magellanic Cloud that is precise to one per cent". In: *Nature* 567.7747 (2019), pp. 200–203.

[87] M. J. Reid, D. W. Pesce, and A. G. Riess. "An Improved Distance to NGC 4258 and its Implications for the Hubble Constant". In: *Astrophys. J. Lett.* 886.2 (2019), p. L27. DOI: 10.3847/2041-8213/ab552d. arXiv: 1908.05625 [astro-ph.GA].

[88] Wendy L. Freedman and Barry F. Madore. "Progress in direct measurements of the Hubble constant". In: *JCAP* 11 (2023), p. 050. DOI: 10.1088/1475-7516/2023/11/050. arXiv: 2309.05618 [astro-ph.CO].

[89] Wendy L. Freedman et al. "Status Report on the Chicago-Carnegie Hubble Program (CCHP): Measurement of the Hubble Constant Using the Hubble and James Webb Space Telescopes". In: *Astrophys. J.* 985.2 (2025), p. 203. DOI: 10.3847/1538-4357/adce78. arXiv: 2408.06153 [astro-ph.CO].

[90] Caroline D. Huang et al. "The Mira Distance to M101 and a 4% Measurement of H_0". In: *Astrophys. J.* 963.2 (2024), p. 83. DOI: 10.3847/1538-4357/ad1ff8. arXiv: 2312.08423 [astro-ph.CO].

[91] Siyang Li et al. "Reconnaissance with JWST of the J-region Asymptotic Giant Branch in Distance Ladder Galaxies: From Irregular Luminosity Functions to Approximation of the Hubble Constant". In: *Astrophys. J.* 966.1 (2024), p. 20. DOI: 10.3847/1538-4357/ad2f2b. arXiv: 2401.04777 [astro-ph.CO].

[92] Abigail J. Lee et al. "The Chicago–Carnegie Hubble Program: The JWST J-region Asymptotic Giant Branch Extragalactic Distance Scale". In: *Astrophys. J.* 985.2 (2025), p. 182. DOI: 10.3847/1538-4357/adc8a1. arXiv: 2408.03474 [astro-ph.GA].

[93] Adam G. Riess et al. "A 2.4% Determination of the Local Value of the Hubble Constant". In: *Astrophys. J.* 826.1 (2016), p. 56. DOI: 10.3847/0004-637X/826/1/56. arXiv: 1604.01424 [astro-ph.CO].

[94] Adam G. Riess et al. "A Comprehensive Measurement of the Local Value of the Hubble Constant with 1 km/s/Mpc Uncertainty from the Hubble Space Telescope and the SH0ES Team". In: *Astrophys. J. Lett.* 934.1 (2022), p. L7. DOI: 10.3847/2041-8213/ac5c5b. arXiv: 2112.04510 [astro-ph.CO].

[95] Dan Scolnic et al. "The Pantheon+ Analysis: The Full Data Set and Light-curve Release". In: *Astrophys. J.* 938.2 (2022), p. 113. DOI: 10.3847/1538-4357/ac8b7a. arXiv: 2112.03863 [astro-ph.CO].

[96] John P. Blakeslee et al. "The Hubble Constant from Infrared Surface Brightness Fluctuation Distances". In: *Astrophys. J.* 911.1 (2021), p. 65. DOI: 10.3847/1538-4357/abe86a. arXiv: 2101.02221 [astro-ph.CO].

[97] T. de Jaeger et al. "A 5∼per cent measurement of the Hubble–Lemaître constant from Type II supernovae". In: *Mon. Not. Roy. Astron. Soc.* 514.3 (2022), pp. 4620–4628. DOI: 10.1093/mnras/stac1661. arXiv: 2203.08974 [astro-ph.CO].

[98] Ehsan Kourkchi et al. "Cosmicflows-4: the baryonic Tully–Fisher relation providing ∼10000 distances". In: *Monthly Notices of the Royal Astronomical Society* 511.4 (Feb. 2022), 6160–6178. ISSN: 1365-2966. DOI: 10.1093/mnras/stac303. URL: http://dx.doi.org/10.1093/mnras/stac303.

[99] Ivo Labbe et al. "A population of red candidate massive galaxies ~600 Myr after the Big Bang". In: *Nature* 616.7956 (2023), pp. 266–269. DOI: 10.1038/s41586-023-05786-2. arXiv: 2207.12446 [astro-ph.GA].

[100] Guido Risaliti and Elisabeta Lusso. "Cosmological constraints from the Hubble diagram of quasars at high redshifts". In: *Nature Astron.* 3.3 (2019), pp. 272–277. DOI: 10.1038/s41550-018-0657-z. arXiv: 1811.02590 [astro-ph.CO].

[101] E. Lusso et al. "Tension with the flat ΛCDM model from a high-redshift Hubble diagram of supernovae, quasars, and gamma-ray bursts". In: *Astron. Astrophys.* 628 (2019), p. L4. DOI: 10.1051/0004-6361/201936223. arXiv: 1907.07692 [astro-ph.CO].

[102] Giada Bargiacchi et al. "Cosmography by orthogonalized logarithmic polynomials". In: *Astron. Astrophys.* 649 (2021), A65. DOI: 10.1051/0004-6361/202140386. arXiv: 2101.08278 [astro-ph.CO].

[103] Matilde Signorini et al. "Building the high-redshift Hubble Diagram with quasars". In: *Memorie della Societa Astronomica Italiana.* Vol. 94. Sept. 2023, p. 259. DOI: 10.36116/MEMSAIT_94N2.2023.259. arXiv: 2401.07909 [astro-ph.CO].

[104] Guido Risaliti and Elisabeta Lusso. "A Hubble Diagram for Quasars". In: *Astrophys. J.* 815 (2015), p. 33. DOI: 10.1088/0004-637X/815/1/33. arXiv: 1505.07118 [astro-ph.CO].

[105] G. Risaliti and E. Lusso. "Cosmology with AGN: can we use quasars as standard candles?" In: *Astron. Nachr.* 338.2/3 (2017), pp. 329–333. DOI: 10.1002/asna.201713351. arXiv: 1612.02838 [astro-ph.CO].

[106] E. Lusso et al. "Quasars as standard candles III. Validation of a new sample for cosmological studies". In: *Astron. Astrophys.* 642 (2020), A150. DOI: 10.1051/0004-6361/202038899. arXiv: 2008.08586 [astro-ph.GA].

[107] Maria Giovanna Dainotti et al. "Quasar Standardization: Overcoming Selection Biases and Redshift Evolution". In: *Astrophys. J.* 931.2 (2022), p. 106. DOI: 10.3847/1538-4357/ac6593. arXiv: 2203.12914 [astro-ph.HE].

[108] Eoin Ó. Colgáin et al. "Revealing intrinsic flat ΛCDM biases with standardizable candles". In: *Phys. Rev. D* 106.4 (2022), p. L041301. DOI: 10.1103/PhysRevD.106.L041301. arXiv: 2203.10558 [astro-ph.CO].

[109] Aleksander Łukasz Lenart et al. "A Bias-free Cosmological Analysis with Quasars Alleviating H_0 Tension". In: *Astrophys. J. Suppl.* 264.2 (2023), p. 46. DOI: 10.3847/1538-4365/aca404. arXiv: 2211.10785 [astro-ph.CO].

[110] Maria Giovanna Dainotti et al. "Reducing the Uncertainty on the Hubble Constant up to 35% with an Improved Statistical Analysis: Different Best-fit Likelihoods for Type Ia Supernovae, Baryon Acoustic Oscillations, Quasars, and Gamma-Ray Bursts". In: *Astrophys. J.* 951.1 (2023), p. 63. DOI: 10.3847/1538-4357/acd63f. arXiv: 2305.10030 [astro-ph.CO].

[111] G. Bargiacchi et al. "Gamma-ray bursts, quasars, baryonic acoustic oscillations, and supernovae Ia: new statistical insights and cosmological constraints". In: *Mon. Not. Roy. Astron. Soc.* 521.3 (2023), pp. 3909–3924. DOI: 10.1093/mnras/stad763. arXiv: 2303.07076 [astro-ph.CO].

[112] Eduardo Banados et al. "An 800-million-solar-mass black hole in a significantly neutral Universe at redshift 7.5". In: *Nature* 553.7689 (2018), pp. 473–476. DOI: 10.1038/nature25180. arXiv: 1712.01860 [astro-ph.GA].

[113] A. Cucchiara et al. "Constraining GRB Emission Physics with Extensive Early-Time, Multiband Follow-up". In: *Astrophys. J.* 743 (2011), p. 154. DOI: 10.1088/0004-637X/743/2/154. arXiv: 1107.3352 [astro-ph.HE].

[114] Donald Q. Lamb. "Gamma-ray bursts as a probe of cosmology". In: *AIP Conf. Proc.* 662.1 (2003). Ed. by G. R. Ricker and R. K. Vanderspek, pp. 433–437. DOI: 10.1063/1.1579395. arXiv: astro-ph/0210434.

[115] L. Amati et al. "Intrinsic spectra and energetics of BeppoSAX gamma-ray bursts with known redshifts". In: *Astron. Astrophys.* 390 (2002), p. 81. DOI: 10.1051/0004-6361:20020722. arXiv: astro-ph/0205230.

[116] Lorenzo Amati et al. "Measuring the cosmological parameters with the E_p-E_{iso} correlation of gamma-ray bursts". In: *MNRAS* 391.2 (Dec. 2008), pp. 577–584. DOI: 10.1111/j.1365-2966.2008.13943.x. arXiv: 0805.0377 [astro-ph].

[117] D. Yonetoku et al. "Gamma-ray burst formation rates inferred from the spectral peak energy-peak luminosity relation". In: *Astrophys. J.* 609 (2004), p. 935. DOI: 10.1086/421285. arXiv: astro-ph/0309217.

[118] J. P. Norris, G. F. Marani, and J. T. Bonnell. "Connection between energy dependent lags and Lorentz factor in gamma-ray bursts". In: *Astrophys. J.* 534 (2000), pp. 248–257. DOI: 10.1086/308725. arXiv: astro-ph/9903233.

[119] En-Wei Liang et al. "Constraining GRB Initial Lorentz Factor with the Afterglow Onset Feature and Discovery of a Tight Γ_0-E_{iso} Correlation". In: *Astrophys. J.* 725 (2010), pp. 2209–2224. DOI: 10.1088/0004-637X/725/2/2209. arXiv: 0912.4800 [astro-ph.HE].

[120] G. Ghirlanda et al. "Gamma Ray Bursts in the comoving frame". In: *Mon. Not. Roy. Astron. Soc.* 420 (2012), p. 483. DOI: 10.1111/j.1365-2966.2011.20053.x. arXiv: 1107.4096 [astro-ph.HE].

[121] Andrew C. Collazzi et al. "A Significant Problem with Using the Amati Relation for Cosmological Purposes". In: *ApJ* 747.1, 39 (Mar. 2012), p. 39. DOI: 10.1088/0004-637X/747/1/39. arXiv: 1112.4347 [astro-ph.HE].

[122] V. Heussaff, J-L. Atteia, and Y. Zolnierowski. "The E_{peak}-E_{iso} relation revisited with Fermi GRBs: Resolving a long-standing debate?" In: *Astron. Astrophys.* 557 (2013), A100. DOI: 10.1051/0004-6361/201321528. arXiv: 1306.1757 [astro-ph.HE].

[123] Vahé Petrosian, Ellie Kitanidis, and Daniel Kocevski. "Cosmological Evolution of Long Gamma-ray Bursts and the Star Formation Rate". In: *Astrophys. J.* 806.1 (2015), p. 44. DOI: 10.1088/0004-637X/806/1/44. arXiv: 1504.01414 [astro-ph.HE].

[124] Maria G. Dainotti and L. Amati. "Gamma-ray burst prompt correlations: selection and instrumental effects". In: *Publ. Astron. Soc. Pac.* 130.987 (2018), p. 051001. DOI: 10.1088/1538-3873/aaa8d7. arXiv: 1704.00844 [astro-ph.HE].

[125] M. G. Dainotti, R. Del Vecchio, and M. Tarnopolski. "Gamma-Ray Burst Prompt Correlations". In: *Advances in Astronomy* 2018, 4969503 (Jan. 2018), p. 4969503. DOI: 10.1155/2018/4969503.

[126] Tyler Parsotan and Hirotaka Ito. "GRB Prompt Emission: Observed Correlations and Their Interpretations". In: *Universe* 8.6, 310 (May 2022), p. 310. DOI: 10.3390/universe8060310. arXiv: 2204.09729 [astro-ph.HE].

[127] M. G. Dainotti, V. F. Cardone, and S. Capozziello. "A time - luminosity correlation for Gamma Ray Bursts in the X - rays". In: *Mon. Not. Roy. Astron. Soc.* 391 (2008), p. 79. DOI: 10.1111/j.1745-3933.2008.00560.x. arXiv: 0809.1389 [astro-ph].

[128] M. G. Dainotti et al. "Discovery of a tight correlation for gamma ray burst afterglows with 'canonical' light curves". In: *Astrophys. J. Lett.* 722 (2010), p. L215. DOI: 10.1088/2041-8205/722/2/L215. arXiv: 1009.1663 [astro-ph.HE].

[129] Maria Giovanna Dainotti et al. "Study of possible systematics in the L_X^* - T_a^* correlation of Gamma Ray Bursts". In: *Astrophys. J.* 730 (2011), p. 135. DOI: 10.1088/0004-637X/730/2/135. arXiv: 1101.1676 [astro-ph.HE].

[130] M. G. Dainotti et al. "Slope evolution of GRB correlations and cosmology". In: *Monthly Notices of the Royal Astronomical Society* 436.1 (Sept. 2013), pp. 82–88. ISSN: 0035-8711. DOI: 10.1093/mnras/stt1516. URL: https://doi.org/10.1093/mnras/stt1516.

[131] Maria G. Dainotti et al. "A study of gamma ray bursts with afterglow plateau phases associated with supernovae". In: *Astron. Astrophys.* 600 (2017), A98. DOI: 10.1051/0004-6361/201628384. arXiv: 1612.02917 [astro-ph.HE].

[132] M. G. Dainotti et al. "The Optical Luminosity–Time Correlation for More than 100 Gamma-Ray Burst Afterglows". In: *Astrophys. J. Lett.* 905.2 (2020), p. L26. DOI: 10.3847/2041-8213/abcda9. arXiv: 2011.14493 [astro-ph.HE].

[133] Maria Giovanna Dainotti et al. "The Optical Two- and Three-dimensional Fundamental Plane Correlations for Nearly 180 Gamma-Ray Burst Afterglows with Swift/UVOT, RATIR, and the Subaru Telescope". In: *Astrophys. J. Supp.* 261.2 (2022), p. 25. DOI: 10.3847/1538-4365/ac7c64. arXiv: 2203.12908 [astro-ph.HE].

[134] Eleonora Di Valentino et al. "The CosmoVerse White Paper: Addressing observational tensions in cosmology with systematics and fundamental physics". In: *Phys. Dark Univ.* 49 (2025), p. 101965. DOI: 10.1016/j.dark.2025.101965. arXiv: 2504.01669 [astro-ph.CO].

[135] V. F. Cardone, S. Capozziello, and M. G. Dainotti. "An updated Gamma Ray Bursts Hubble diagram". In: *Mon. Not. Roy. Astron. Soc.* 400.2 (2009), pp. 775–790. DOI: 10.1111/j.1365-2966.2009.15456.x. arXiv: 0901.3194 [astro-ph.CO].

[136] V. F. Cardone et al. "Constraining cosmological parameters by gamma-ray burst X-ray afterglow light curves". In: *mnras* 408 (Oct. 2010), pp. 1181–1186. DOI: 10.1111/j.1365-2966.2010.17197.x. arXiv: 1005.0122 [astro-ph.CO].

[137] M. G. Dainotti et al. "Determination of the Intrinsic Luminosity Time Correlation in the X-Ray Afterglows of Gamma-Ray Bursts". In: *apj* 774, 157 (Sept. 2013), p. 157. DOI: 10.1088/0004-637X/774/2/157. arXiv: 1307.7297 [astro-ph.HE].

[138] M. G. Dainotti et al. "A fundamental plane for gamma-ray bursts with X-ray plateaus". In: *The Astrophysical Journal* 825.2 (2016), p. L20. DOI: 10.3847/2041-8205/825/2/l20. URL: https://doi.org/10.3847%2F2041-8205%2F825%2F2%2Fl20.

[139] M. G. Dainotti et al. "A Study of the Gamma-Ray Burst Fundamental Plane". In: *The Astrophysical Journal* 848.2 (2017), p. 88. DOI: 10.3847/1538-4357/aa8a6b. URL: https://doi.org/10.3847%2F1538-4357%2Faa8a6b.

[140] A. Rowlinson et al. "Constraining properties of GRB magnetar central engines using the observed plateau luminosity and duration correlation". In: *mnras* 443.2 (Sept. 2014), pp. 1779–1787. DOI: 10.1093/mnras/stu1277. arXiv: 1407.1053 [astro-ph.HE].

[141] Maria Grazia Bernardini. "Gamma-ray bursts and magnetars: Observational signatures and predictions". In: *Journal of High Energy Astrophysics* 7 (2015), pp. 64–72.

[142] Nanda Rea et al. "Constraining the GRB-magnetar model by means of the Galactic pulsar population". In: *Astrophys. J.* 813.2 (2015), p. 92. DOI: 10.1088/0004-637X/813/2/92. arXiv: 1510.01430 [astro-ph.HE].

[143] Giulia Stratta et al. "On the magnetar origin of the GRBs presenting X-ray afterglow plateaus". In: *Astrophys. J.* 869.2 (2018), p. 155. DOI: 10.3847/1538-4357/aadd8f. arXiv: 1804.08652 [astro-ph.HE].

[144] Simone Dall'Osso et al. "Magnetar Central Engines in Gamma-Ray Bursts Follow the Universal Relation of Accreting Magnetic Stars". In: *Astrophys. J. Lett.* 949.2 (2023), p. L32. DOI: 10.3847/2041-8213/acccec. arXiv: 2305.00029 [astro-ph.HE].

[145] Z. Lucas Uhm and Andrei M. Beloborodov. "On the Mechanism of Gamma-Ray Burst Afterglows". In: *The Astrophysical Journal* 665.2 (Aug. 2007), L93–L96. ISSN: 1538-4357. DOI: 10.1086/519837. URL: http://dx.doi.org/10.1086/519837.

[146] R. Hascoet, F. Daigne, and R. Mochkovitch. "The prompt–early afterglow connection in gamma-ray bursts: implications for the early afterglow physics". In: *Mon. Not. Roy. Astron. Soc.* 442.1 (2014), pp. 20–27. DOI: 10.1093/mnras/stu750. arXiv: 1401.0751 [astro-ph.HE].

[147] M G Dainotti et al. "Optical and X-ray GRB Fundamental Planes as cosmological distance indicators". In: *Monthly Notices of the Royal Astronomical Society* 514.2 (June 2022), pp. 1828–1856. ISSN: 0035-8711. DOI: 10.1093/mnras/stac1141. URL: https://doi.org/10.1093/mnras/stac1141.

[148] Lorenzo Amati et al. "Addressing the circularity problem in the $E_{\rm p} - E_{\rm iso}$ correlation of gamma-ray bursts". In: *Mon. Not. Roy. Astron. Soc.* 486.1 (2019), pp. L46–L51. DOI: 10.1093/mnrasl/slz056. arXiv: 1811.08934 [astro-ph.HE].

[149] Narayan Khadka and Bharat Ratra. "Constraints on cosmological parameters from gamma-ray burst peak photon energy and bolometric fluence measurements and other data". In: *Monthly Notices of the Royal Astronomical Society* 499.1 (Sept. 2020), pp. 391–403. ISSN: 0035-8711. DOI: 10.1093/mnras/staa2779. URL: https://doi.org/10.1093/mnras/staa2779.

[150] Narayan Khadka et al. "Do gamma-ray burst measurements provide a useful test of cosmological models?" In: *JCAP* 09 (2021), p. 042. DOI: 10.1088/1475-7516/2021/09/042. arXiv: 2105.12692 [astro-ph.CO].

[151] Shulei Cao, Maria Dainotti, and Bharat Ratra. "Gamma-ray burst data strongly favor the three-parameter fundamental plane (Dainotti) correlation relation over the two-parameter one". In: *Monthly Notices of the Royal Astronomical Society* 516.1 (2022), pp. 1386–1405. ISSN: 0035-8711, 1365-2966. DOI: 10.1093/mnras/stac2170. URL: http://arxiv.org/abs/2204.08710 (visited on 07/07/2023).

[152] G. Ghisellini et al. "Cosmology with Gamma-Ray Bursts". In: *Il Nuovo Cimento C* 28.405 (2005), 639–646. ISSN: 03905551, 03905551. DOI: 10.1393/ncc/i2005-10119-0. URL: https://doi.org/10.1393/ncc/i2005-10119-0.

[153] Giancarlo Ghirlanda, G Ghisellini, and C Firmani. "Gamma-ray bursts as standard candles to constrain the cosmological parameters". In: *New Journal of Physics* 8.7 (2006), p. 123.

[154] FY Wang, ZG Dai, and EW Liang. "Gamma-ray burst cosmology". In: *New Astronomy Reviews* 67 (2015), pp. 1–17.

[155] Giancarlo Ghirlanda et al. "Gamma-ray bursts: new rulers to measure the universe". In: *The Astrophysical Journal* 613.1 (2004), p. L13.

[156] Hong Li et al. "Overcoming the circular problem for gamma-ray bursts in cosmological global-fitting analysis". In: *The Astrophysical Journal* 680.1 (2008), p. 92.

[157] Sergey Postnikov et al. "Nonparametric Study of the Evolution of the Cosmological Equation of State with SNeIa, BAO, and High-redshift GRBs". In: *Astrophys. J.* 783 (2014), p. 126. DOI: 10.1088/0004-637X/783/2/126. arXiv: 1401.2939 [astro-ph.CO].

[158] Shulei Cao, Maria Dainotti, and Bharat Ratra. "Standardizing Platinum Dainotti-correlated gamma-ray bursts, and using them with standardized Amati-correlated gamma-ray bursts to constrain cosmological model parameters". In: *Mon. Not. Roy. Astron. Soc.* 512.1 (2022), pp. 439–454. DOI: 10.1093/mnras/stac517. arXiv: 2201.05245 [astro-ph.CO].

[159] M. G. Dainotti et al. "The Gamma-ray Bursts fundamental plane correlation as a cosmological tool". In: *Mon. Not. Roy. Astron. Soc.* (Sept. 2022). DOI: 10.1093/mnras/stac2752. arXiv: 2209.08675 [astro-ph.HE].

[160] Nan Liang et al. "A cosmology-independent calibration of gamma-ray burst luminosity relations and the Hubble diagram". In: *The Astrophysical Journal* 685.1 (2008), p. 354.

[161] Orlando Luongo and Marco Muccino. "Kinematic constraints beyond $z \simeq 0$ using calibrated GRB correlations". In: *Astron. Astrophys.* 641 (2020), A174. DOI: 10.1051/0004-6361/202038264. arXiv: 2010.05218 [astro-ph.CO].

[162] Yuhao Mu, Baorong Chang, and Lixin Xu. "Cosmography via Gaussian process with gamma ray bursts". In: *JCAP* 09 (2023), p. 041. DOI: 10.1088/1475-7516/2023/09/041. arXiv: 2302.02559 [astro-ph.CO].

[163] Nan Liang et al. "Calibrating Gamma-Ray Bursts by Using a Gaussian Process with Type Ia Supernovae". In: *ApJ* 941.1 (2022), p. 84. ISSN: 0004-637X, 1538-4357. DOI: 10.3847/1538-4357/aca08a. URL: https://iopscience.iop.org/article/10.3847/1538-4357/aca08a (visited on 07/07/2023).

[164] Darshan Kumar et al. "Gamma Rays Bursts: A Viable Cosmological Probe?" In: *J. Cosmol. Astropart. Phys.* 2023.7 (2023), p. 021. ISSN: 1475-7516. DOI: 10.1088/1475-7516/2023/07/021. arXiv: 2212.05731[astro-ph]. URL: http://arxiv.org/abs/2212.05731 (visited on 07/18/2023).

[165] Maria Dainotti and Roberta Del Vecchio. "Gamma Ray Burst afterglow and prompt-afterglow relations: an overview". In: *New Astron. Rev.* 77 (2017), pp. 23–61. DOI: 10.1016/j.newar.2017.04.001. arXiv: 1703.06876 [astro-ph.HE].

[166] Leandros Perivolaropoulos and Foteini Skara. "On the homogeneity of SnIa absolute magnitude in the Pantheon+ sample". In: *Mon. Not. Roy. Astron. Soc.* 520.4 (2023), pp. 5110–5125. DOI: 10.1093/mnras/stad451. arXiv: 2301.01024 [astro-ph.CO].

[167] George Efstathiou. "Evolving dark energy or supernovae systematics?" In: *Mon. Not. Roy. Astron. Soc.* 538.2 (2025), pp. 875–882. DOI: 10.1093/mnras/staf301. arXiv: 2408.07175 [astro-ph.CO].

[168] Alessio Notari, Michele Redi, and Andrea Tesi. "BAO vs. SN evidence for evolving dark energy". In: *JCAP* 04 (2025), p. 048. DOI: 10.1088/1475-7516/2025/04/048. arXiv: 2411.11685 [astro-ph.CO].

[169] M. Vincenzi et al. "Comparing the DES-SN5YR and Pantheon+ SN cosmology analyses: Investigation based on "Evolving Dark Energy or Supernovae systematics?"" In: *arXiv preprint 2501.06664* (Jan. 2025). arXiv: 2501.06664 [astro-ph.CO].

[170] Lu Huang, Rong-Gen Cai, and Shao-Jiang Wang. "The DESI DR1/DR2 evidence for dynamical dark energy is biased by low-redshift supernovae". In: (Feb. 2025). arXiv: 2502.04212 [astro-ph.CO].

[171] Yu-Yang Wang and FY Wang. "Calibration of Gamma-Ray Burst Luminosity Correlations Using Gravitational Waves as Standard Sirens". In: *The Astrophysical Journal* 873.1 (2019), p. 39.

[172] Gowri Govindaraj and Shantanu Desai. "Low redshift calibration of the Amati relation using galaxy clusters". In: *Journal of Cosmology and Astroparticle Physics* 2022.10 (2022), p. 069.

[173] Zihao Li, Bin Zhang, and Nan Liang. "Testing Dark Energy Models with Gamma-Ray Bursts Calibrated from the Observational $H(z)$ Data through a Gaussian Process". In: *Monthly Notices of the Royal Astronomical Society* 521.3 (2023), pp. 4406–4413. ISSN: 0035-8711, 1365-2966. DOI: 10.1093/mnras/stad838. arXiv: 2212.14291[astro-ph]. URL: http://arxiv.org/abs/2212.14291 (visited on 07/04/2023).

[174] Ariadna Montiel, J I Cabrera, and Juan Carlos Hidalgo. "Improving sampling and calibration of gamma-ray bursts as distance indicators". In: *Monthly Notices of the Royal Astronomical Society* 501.3 (Dec. 2020), pp. 3515–3526. ISSN: 0035-8711. DOI: 10.1093/mnras/staa3926. URL: https://doi.org/10.1093/mnras/staa3926.

[175] Orlando Luongo and Marco Muccino. "Model-independent calibrations of gamma-ray bursts using machine learning". In: *Mon. Not. Roy. Astron. Soc.* 503.3 (2021), pp. 4581–4600. DOI: 10.1093/mnras/stab795. arXiv: 2011.13590 [astro-ph.CO].

[176] Orlando Luongo and Marco Muccino. "Intermediate redshift calibration of Gamma-ray Bursts and cosmic constraints in non-flat cosmology". In: *Monthly Notices of the Royal Astronomical Society* 518.2 (2022), pp. 2247–2255. ISSN: 0035-8711, 1365-2966. DOI: 10.1093/mnras/stac2925. URL: http://arxiv.org/abs/2207.00440 (visited on 07/18/2023).

[177] Roland Svensson and Andrzej A. Zdziarski. "Black Hole Accretion Disks with Coronae". In: *Apj* 436 (Dec. 1994), p. 599. DOI: 10.1086/174934.

[178] Y. Avni and H. Tananbaum. "On the cosmological evolution of the X-ray emission from quasars". In: *apjl* 262 (Nov. 1982), pp. L17–L21. DOI: 10.1086/183903.

[179] E Lusso and G Risaliti. "The tight relation between X-ray and ultraviolet luminosity of quasars". In: *The Astrophysical Journal* 819.2 (2016), p. 154.

[180] Narayan Khadka and Bharat Ratra. "Quasar X-ray and UV flux, baryon acoustic oscillation, and Hubble parameter measurement constraints on cosmological model parameters". In: *mnras* 492.3 (Mar. 2020), pp. 4456–4468. DOI: 10.1093/mnras/staa101. arXiv: 1909.01400 [astro-ph.CO].

[181] Michal Zajaček et al. "Effect of Extinction on Quasar Luminosity Distances Determined from UV and X-Ray Flux Measurements". In: *Astrophys. J.* 961.2 (2024), p. 229. DOI: 10.3847/1538-4357/ad11dc. arXiv: 2305.08179 [astro-ph.GA].

[182] A. Sacchi et al. "Quasars as high-redshift standard candles". In: *Astron. Astrophys.* 663 (2022), p. L7. DOI: 10.1051/0004-6361/202243411. arXiv: 2206.13528 [astro-ph.CO].

[183] Hamid Shabani et al. "Cosmology of f(Q) gravity in non-flat Universe". In: *Eur. Phys. J. C* 84.3 (2024), p. 285. DOI: 10.1140/epjc/s10052-024-12582-3. arXiv: 2306.13324 [gr-qc].

[184] G. Bargiacchi, M. G. Dainotti, and S. Capozziello. "Tensions with the flat ΛCDM model from high-redshift cosmography". In: *Mon. Not. Roy. Astron. Soc.* 525.2 (2023), pp. 3104–3116. DOI: 10.1093/mnras/stad2326. arXiv: 2307.15359 [astro-ph.CO].

[185] Maria Giovanna Dainotti et al. "Quasars: Standard Candles up to z = 7.5 with the Precision of Supernovae Ia". In: *Astrophys. J.* 950.1 (2023), p. 45. DOI: 10.3847/1538-4357/accea0. arXiv: 2305.19668 [astro-ph.CO].

[186] Maria Giovanna Dainotti et al. "A new binning method to choose a standard set of Quasars". In: *Phys. Dark Univ.* 44 (2024), p. 101428. DOI: 10.1016/j.dark.2024.101428. arXiv: 2401.12847 [astro-ph.HE].

[187] Maria Giovanna Dainotti et al. "The Scavenger Hunt for Quasar Samples to Be Used as Cosmological Tools". In: *Galaxies* 12.1 (2024), p. 4. DOI: 10.3390/galaxies12010004. arXiv: 2401.11998 [astro-ph.CO].

[188] Mario Hamuy. "Observed and physical properties of core-collapse supernovae". In: *Astrophys. J.* 582 (2003), pp. 905–914. DOI: 10.1086/344689. arXiv: astro-ph/0209174.

[189] John Tonry and Donald P. Schneider. "A New Technique for Measuring Extragalactic Distances". In: *AJ* 96 (Sept. 1988), p. 807. DOI: 10.1086/114847.

[190] Nandita Khetan et al. "A new measurement of the Hubble constant using Type Ia supernovae calibrated with surface brightness fluctuations". In: *Astron. Astrophys.* 647 (2021), A72. DOI: 10.1051/0004-6361/202039196. arXiv: 2008.07754 [astro-ph.CO].

[191] Ricardo Chávez et al. "Mapping the Hubble flow from z∼0 to z∼7.5 with HII Galaxies". In: *Mon. Not. Roy. Astron. Soc.* 538.2 (2025), pp. 1264–1271. DOI: 10.1093/mnras/staf386. arXiv: 2404.16261 [astro-ph.CO].

[192] Dillon Brout et al. "The Pantheon+ Analysis: Cosmological Constraints". In: *Astrophys. J.* 938.2 (2022), p. 110. DOI: 10.3847/1538-4357/ac8e04. arXiv: 2202.04077 [astro-ph.CO].

[193] Edvard Mortsell et al. "The Hubble Tension Revisited: Additional Local Distance Ladder Uncertainties". In: *Astrophys. J.* 935.1 (2022), p. 58. DOI: 10.3847/1538-4357/ac7c19. arXiv: 2106.09400 [astro-ph.CO].

[194] Harry Desmond, Bhuvnesh Jain, and Jeremy Sakstein. "Local resolution of the Hubble tension: The impact of screened fifth forces on the cosmic distance ladder". In: *Phys. Rev. D* 100.4 (2019), p. 043537. DOI: 10.1103/PhysRevD.100.043537. arXiv: 1907.03778 [astro-ph.CO].

[195] Harry Desmond and Jeremy Sakstein. "Screened fifth forces lower the TRGB-calibrated Hubble constant too". In: *Phys. Rev. D* 102.2 (2020), p. 023007. DOI: 10.1103/PhysRevD.102.023007. arXiv: 2003.12876 [astro-ph.CO].

[196] Marcus Högås and Edvard Mörtsell. "Hubble tension and fifth forces". In: *Phys. Rev. D* 108.12 (2023), p. 124050. DOI: 10.1103/PhysRevD.108.124050. arXiv: 2309.01744 [astro-ph.CO].

[197] Radosław Wojtak and Jens Hjorth. "Consistent extinction model for type Ia supernovae in Cepheid-based calibration galaxies and its impact on H_0". In: (Mar. 2024). arXiv: 2403.10388 [astro-ph.CO].

[198] Adam G. Riess et al. "JWST Validates HST Distance Measurements: Selection of Supernova Subsample Explains Differences in JWST Estimates of Local H $_0$". In: *Astrophys. J.* 977.1 (2024), p. 120. DOI: 10.3847/1538-4357/ad8c21. arXiv: 2408.11770 [astro-ph.CO].

[199] Shaun Cole et al. "The 2dF Galaxy Redshift Survey: Power-spectrum analysis of the final dataset and cosmological implications". In: *Mon. Not. Roy. Astron. Soc.* 362 (2005), pp. 505–534. DOI: 10.1111/j.1365-2966.2005.09318.x. arXiv: astro-ph/0501174.

[200] Daniel J. Eisenstein et al. "Detection of the Baryon Acoustic Peak in the Large-Scale Correlation Function of SDSS Luminous Red Galaxies". In: *Astrophys. J.* 633 (2005), pp. 560–574. DOI: 10.1086/466512. arXiv: astro-ph/0501171.

[201] M. Abdul Karim et al. "DESI DR2 Results II: Measurements of Baryon Acoustic Oscillations and Cosmological Constraints". In: *arXiv preprint 2503.14738* (Mar. 2025). arXiv: 2503.14738 [astro-ph.CO].

[202] Kyle S. Dawson et al. "The Baryon Oscillation Spectroscopic Survey of SDSS-III". In: *AJ* 145.1, 10 (Jan. 2013), p. 10. DOI: 10.1088/0004-6256/145/1/10. arXiv: 1208.0022 [astro-ph.CO].

[203] Shadab Alam et al. "The clustering of galaxies in the completed SDSS-III Baryon Oscillation Spectroscopic Survey: cosmological analysis of the DR12 galaxy sample". In: *Mon. Not. Roy. Astron. Soc.* 470.3 (2017), pp. 2617–2652. DOI: 10.1093/mnras/stx721. arXiv: 1607.03155 [astro-ph.CO].

[204] Blake D. Sherwin and Martin White. "The Impact of Wrong Assumptions in BAO Reconstruction". In: *JCAP* 02 (2019), p. 027. DOI: 10.1088/1475-7516/2019/02/027. arXiv: 1808.04384 [astro-ph.CO].

[205] Paul Carter et al. "The impact of the fiducial cosmology assumption on BAO distance scale measurements". In: *Mon. Not. Roy. Astron. Soc.* 494.2 (2020), pp. 2076–2089. DOI: 10.1093/mnras/staa761. arXiv: 1906.03035 [astro-ph.CO].

[206] José Luis Bernal et al. "Robustness of baryon acoustic oscillation constraints for early-Universe modifications of ΛCDM cosmology". In: *Phys. Rev. D* 102.12 (2020), p. 123515. DOI: 10.1103/PhysRevD.102.123515. arXiv: 2004.07263 [astro-ph.CO].

[207] Samuel Brieden, Héctor Gil-Marín, and Licia Verde. "ShapeFit: extracting the power spectrum shape information in galaxy surveys beyond BAO and RSD". In: *JCAP* 12.12 (2021), p. 054. DOI: 10.1088/1475-7516/2021/12/054. arXiv: 2106.07641 [astro-ph.CO].

[208] Samuel Brieden, Héctor Gil-Marín, and Licia Verde. "Model-independent versus model-dependent interpretation of the SDSS-III BOSS power spectrum: Bridging the divide". In: *Phys. Rev. D* 104.12 (2021), p. L121301. DOI: 10.1103/PhysRevD.104.L121301. arXiv: 2106.11931 [astro-ph.CO].

[209] T. M. C. Abbott et al. "Dark Energy Survey Year 1 Results: A Precise H0 Estimate from DES Y1, BAO, and D/H Data". In: *Mon. Not. Roy. Astron. Soc.* 480.3 (2018), pp. 3879–3888. DOI: 10.1093/mnras/sty1939. arXiv: 1711.00403 [astro-ph.CO].

[210] A. J. Cuesta et al. "The cosmic inverse distance ladder: baryon acoustic oscillations and type-Ia supernovae". In: *Highlights of Spanish Astrophysics VIII.* May 2015, pp. 172–176.

[211] Éric Aubourg et al. "Cosmological implications of baryon acoustic oscillation measurements". In: *Physical Review D* 92.12 (2015). DOI: 10.1103/physrevd.92.123516. URL: https://doi.org/10.1103%2Fphysrevd.92.123516.

[212] G. E. Addison et al. "Elucidating ΛCDM: Impact of Baryon Acoustic Oscillation Measurements on the Hubble Constant Discrepancy". In: *Astrophys. J.* 853.2 (2018), p. 119. DOI: 10.3847/1538-4357/aaa1ed. arXiv: 1707.06547 [astro-ph.CO].

[213] Stephen M. Feeney et al. "Prospects for resolving the Hubble constant tension with standard sirens". In: *Phys. Rev. Lett.* 122.6 (2019), p. 061105. DOI: 10.1103/PhysRevLett.122.061105. arXiv: 1802.03404 [astro-ph.CO].

[214] E Macaulay et al. "First cosmological results using Type Ia supernovae from the Dark Energy Survey: measurement of the Hubble constant". In: *Monthly Notices of the Royal Astronomical Society* 486.2 (2019), pp. 2184–2196. DOI: 10.1093/mnras/stz978. URL: https://doi.org/10.1093%2Fmnras%2Fstz978.

[215] David Camarena and Valerio Marra. "A new method to build the (inverse) distance ladder". In: *Monthly Notices of the Royal Astronomical Society* 495.3 (2020), pp. 2630–2644. DOI: 10.1093/mnras/staa770. URL: https://doi.org/10.1093%2Fmnras%2Fstaa770.

[216] Pablo Lemos et al. "Model independent $H(z)$ reconstruction using the cosmic inverse distance ladder". In: *Mon. Not. Roy. Astron. Soc.* 483.4 (2019), pp. 4803–4810. DOI: 10.1093/mnras/sty3082. arXiv: 1806.06781 [astro-ph.CO].

[217] R. Camilleri et al. "The Dark Energy Survey Supernova Program: An updated measurement of the Hubble constant using the Inverse Distance Ladder". In: (June 2024). arXiv: 2406.05049 [astro-ph.CO].

[218] Radosław Wojtak and Adriano Agnello. "The Hubble–Lemaître constant and sound horizon from low-redshift probes". In: *Mon. Not. Roy. Astron. Soc.* 486.4 (2019), pp. 5046–5051. DOI: 10.1093/mnras/stz1163. arXiv: 1908.02401 [astro-ph.CO].

[219] S. Taubenberger et al. "The Hubble constant determined through an inverse distance ladder including quasar time delays and Type Ia supernovae". In: *A&A* 628, L7 (Aug. 2019), p. L7. DOI: 10.1051/0004-6361/201935980. arXiv: 1905.12496 [astro-ph.CO].

[220] Leandros Perivolaropoulos and Foteini Skara. "Challenges for ΛCDM: An update". In: *New Astron. Rev.* 95 (2022), p. 101659. DOI: 10.1016/j.newar.2022.101659. arXiv: 2105.05208 [astro-ph.CO].

[221] Edwin Hubble. "A Relation between Distance and Radial Velocity among Extra-Galactic Nebulae". In: *Proceedings of the National Academy of Science* 15.3 (Mar. 1929), pp. 168–173. DOI: 10.1073/pnas.15.3.168.

[222] Elcio Abdalla et al. "Cosmology intertwined: A review of the particle physics, astrophysics, and cosmology associated with the cosmological tensions and anomalies". In: *JHEAp* 34 (2022), pp. 49–211. DOI: 10.1016/j.jheap.2022.04.002. arXiv: 2203.06142 [astro-ph.CO].

[223] Nils Schöneberg et al. "The H0 Olympics: A fair ranking of proposed models". In: *Phys. Rept.* 984 (2022), pp. 1–55. DOI: 10.1016/j.physrep.2022.07.001. arXiv: 2107.10291 [astro-ph.CO].

[224] Eleonora Di Valentino et al. "In the realm of the Hubble tension—a review of solutions". In: *Class. Quant. Grav.* 38.15 (2021), p. 153001. DOI: 10.1088/1361-6382/ac086d. arXiv: 2103.01183 [astro-ph.CO].

[225] G. Efstathiou. "A Lockdown Perspective on the Hubble Tension (with comments from the SH0ES team)". In: (July 2020). arXiv: 2007.10716 [astro-ph.CO].

[226] Leandros Perivolaropoulos. "Hubble tension or distance ladder crisis?" In: *Phys. Rev. D* 110.12 (2024), p. 123518. DOI: 10.1103/PhysRevD.110.123518. arXiv: 2408.11031 [astro-ph.CO].

[227] Wendy L. Freedman. "Measurements of the Hubble Constant: Tensions in Perspective*". In: *The Astrophysical Journal* 919.1 (Sept. 2021), p. 16. ISSN: 1538-4357. DOI: 10.3847/1538-4357/ac0e95. URL: http://dx.doi.org/10.3847/1538-4357/ac0e95.

[228] Leandros Perivolaropoulos and Foteini Skara. "A Reanalysis of the Latest SH0ES Data for H_0: Effects of New Degrees of Freedom on the Hubble Tension". In: *Universe* 8.10 (2022), p. 502. DOI: 10.3390/universe8100502. arXiv: 2208.11169 [astro-ph.CO].

[229] Christa Gall et al. "The Hubble Constant from Blue Type Ia Supernovae". In: (Nov. 2024). arXiv: 2411.05642 [astro-ph.CO].

[230] Mohit K. Sharma, Leandros Perivolaropoulos, and M. Sami. "Multi-Parameter Transitions in Cosmological Calibrators: A Resolution to the Hubble Tension from SH0ES Data Analysis". In: (Apr. 2025). arXiv: 2504.19807 [astro-ph.CO].

[231] L. Verde, T. Treu, and A. G. Riess. "Tensions between the Early and the Late Universe". In: *Nature Astron.* 3 (July 2019), p. 891. DOI: 10.1038/s41550-019-0902-0. arXiv: 1907.10625 [astro-ph.CO].

[232] Thibaut Louis et al. "The Atacama Cosmology Telescope: DR6 Power Spectra, Likelihoods and ΛCDM Parameters". In: (Mar. 2025). arXiv: 2503.14452 [astro-ph.CO].

[233] Éric Aubourg et al. "Cosmological implications of baryon acoustic oscillation measurements". In: *Phys. Rev. D* 92.12 (2015), p. 123516. DOI: 10.1103/PhysRevD.92.123516. arXiv: 1411.1074 [astro-ph.CO].

[234] Antonio J. Cuesta et al. "Calibrating the cosmic distance scale ladder: the role of the sound horizon scale and the local expansion rate as distance anchors". In: *Mon. Not. Roy. Astron. Soc.* 448.4 (2015), pp. 3463–3471. DOI: 10.1093/mnras/stv261. arXiv: 1411.1094 [astro-ph.CO].

[235] Adrià Gómez-Valent. "Fast test to assess the impact of marginalization in Monte Carlo analyses and its application to cosmology". In: *Phys. Rev. D* 106.6 (2022), p. 063506. DOI: 10.1103/PhysRevD.106.063506. arXiv: 2203.16285 [astro-ph.CO].

[236] B. P. Abbott et al. "A gravitational-wave standard siren measurement of the Hubble constant". In: *Nature* 551.7678 (2017), pp. 85–88. DOI: 10.1038/nature24471. URL: https://doi.org/10.1038%2Fnature24471.

[237] Jose Luis Bernal, Licia Verde, and Adam G. Riess. "The trouble with H_0". In: *JCAP* 10 (2016), p. 019. DOI: 10.1088/1475-7516/2016/10/019. arXiv: 1607.05617 [astro-ph.CO].

[238] Kevin Aylor et al. "Sounds Discordant: Classical Distance Ladder & ΛCDM -based Determinations of the Cosmological Sound Horizon". In: *Astrophys. J.* 874.1 (2019), p. 4. DOI: 10.3847/1538-4357/ab0898. arXiv: 1811.00537 [astro-ph.CO].

[239] David Camarena and Valerio Marra. "Local determination of the Hubble constant and the deceleration parameter". In: *Phys. Rev. Res.* 2.1 (2020), p. 013028. DOI: 10.1103/PhysRevResearch.2.013028. arXiv: 1906.11814 [astro-ph.CO].

[240] David Camarena and Valerio Marra. "A new method to build the (inverse) distance ladder". In: *Mon. Not. Roy. Astron. Soc.* 495.3 (2020), pp. 2630–2644. DOI: 10.1093/mnras/staa770. arXiv: 1910.14125 [astro-ph.CO].

[241] Adrià Gómez-Valent. "Measuring the sound horizon and absolute magnitude of SNIa by maximizing the consistency between low-redshift data sets". In: *Phys. Rev. D* 105.4 (2022), p. 043528. DOI: 10.1103/PhysRevD.105.043528. arXiv: 2111.15450 [astro-ph.CO].

[242] Adrià Gómez-Valent et al. "Late-time phenomenology required to solve the H0 tension in view of the cosmic ladders and the anisotropic and angular BAO datasets". In: *Phys. Rev. D* 109.2 (2024), p. 023525. DOI: 10.1103/PhysRevD.109.023525. arXiv: 2309.07795 [astro-ph.CO].

[243] Weikang Lin and Mustapha Ishak. "Cosmological discordances: A new measure, marginalization effects, and application to geometry versus growth current data sets". In: *Phys. Rev. D* 96.2 (2017), p. 023532. DOI: 10.1103/PhysRevD.96.023532. arXiv: 1705.05303 [astro-ph.CO].

[244] Catherine Heymans et al. "KiDS-1000 Cosmology: Multi-probe weak gravitational lensing and spectroscopic galaxy clustering constraints". In: *Astron. Astrophys.* 646 (2021), A140. DOI: 10.1051/0004-6361/202039063. arXiv: 2007.15632 [astro-ph.CO].

[245] T. M. C. Abbott et al. "Dark Energy Survey Year 3 results: Cosmological constraints from galaxy clustering and weak lensing". In: *Phys. Rev. D* 105.2 (2022), p. 023520. DOI: 10.1103/PhysRevD.105.023520. arXiv: 2105.13549 [astro-ph.CO].

[246] A. G. Adame et al. "DESI 2024 VII: cosmological constraints from the full-shape modeling of clustering measurements". In: *JCAP* 07 (2025), p. 028. DOI: 10.1088/1475-7516/2025/07/028. arXiv: 2411.12022 [astro-ph.CO].

[247] Eleonora Di Valentino et al. "Cosmology Intertwined III: $f\sigma_8$ and S_8". In: *Astropart. Phys.* 131 (2021), p. 102604. DOI: 10.1016/j.astropartphys.2021.102604. arXiv: 2008.11285 [astro-ph.CO].

[248] Erminia Calabrese et al. "The Atacama Cosmology Telescope: DR6 Constraints on Extended Cosmological Models". In: (Mar. 2025). arXiv: 2503.14454 [astro-ph.CO].

[249] Edward Macaulay, Ingunn Kathrine Wehus, and Hans Kristian Eriksen. "Lower Growth Rate from Recent Redshift Space Distortion Measurements than Expected from Planck". In: *Phys. Rev. Lett.* 111.16 (2013), p. 161301. DOI: 10.1103/PhysRevLett.111.161301. arXiv: 1303.6583 [astro-ph.CO].

[250] Shahab Joudaki et al. "KiDS-450 + 2dFLenS: Cosmological parameter constraints from weak gravitational lensing tomography and overlapping redshift-space galaxy clustering". In: *Mon. Not. Roy. Astron. Soc.* 474.4 (2018), pp. 4894–4924. DOI: 10.1093/mnras/stx2820. arXiv: 1707.06627 [astro-ph.CO].

[251] Adrià Gómez-Valent and Joan Solà. "Relaxing the σ_8-tension through running vacuum in the Universe". In: *EPL* 120.3 (2017), p. 39001. DOI: 10.1209/0295-5075/120/39001. arXiv: 1711.00692 [astro-ph.CO].

[252] David Benisty. "Quantifying the S_8 tension with the Redshift Space Distortion data set". In: *Phys. Dark Univ.* 31 (2021), p. 100766. DOI: 10.1016/j.dark.2020.100766. arXiv: 2005.03751 [astro-ph.CO].

[253] Angus H. Wright et al. "KiDS+VIKING-450: Improved cosmological parameter constraints from redshift calibration with self-organising maps". In: *Astron. Astrophys.* 640 (2020), p. L14. DOI: 10.1051/0004-6361/202038389. arXiv: 2005.04207 [astro-ph.CO].

[254] Rafael C. Nunes and Sunny Vagnozzi. "Arbitrating the S8 discrepancy with growth rate measurements from redshift-space distortions". In: *Mon. Not. Roy. Astron. Soc.* 505.4 (2021), pp. 5427–5437. DOI: 10.1093/mnras/stab1613. arXiv: 2106.01208 [astro-ph.CO].

[255] Angus H. Wright et al. "KiDS-Legacy: Cosmological constraints from cosmic shear with the complete Kilo-Degree Survey". In: (Mar. 2025). arXiv: 2503.19441 [astro-ph.CO].

[256] Savvas Nesseris, George Pantazis, and Leandros Perivolaropoulos. "Tension and constraints on modified gravity parametrizations of $G_{\rm eff}(z)$ from growth rate and Planck data". In: *Phys. Rev. D* 96.2 (2017), p. 023542. DOI: 10.1103/PhysRevD.96.023542. arXiv: 1703.10538 [astro-ph.CO].

[257] Adrià Gómez-Valent and Joan Solà Peracaula. "Density perturbations for running vacuum: a successful approach to structure formation and to the σ_8-tension". In: *Mon. Not. Roy. Astron. Soc.* 478.1 (2018), pp. 126–145. DOI: 10.1093/mnras/sty1028. arXiv: 1801.08501 [astro-ph.CO].

[258] Nhat-Minh Nguyen, Dragan Huterer, and Yuewei Wen. "Evidence for Suppression of Structure Growth in the Concordance Cosmological Model". In: *Phys. Rev. Lett.* 131.11 (2023), p. 111001. DOI: 10.1103/PhysRevLett.131.111001. arXiv: 2302.01331 [astro-ph.CO].

[259] Shahnawaz A. Adil et al. "S8 increases with effective redshift in ΛCDM cosmology". In: *Mon. Not. Roy. Astron. Soc.* 528.1 (2023), pp. L20–L26. DOI: 10.1093/mnrasl/slad165. arXiv: 2303.06928 [astro-ph.CO].

[260] Özgür Akarsu et al. "Further support for S_8 increasing with effective redshift". In: (Oct. 2024). arXiv: 2410.23134 [astro-ph.CO].

[261] E. Artis et al. "The SRG/eROSITA All-Sky Survey : Constraints on the structure growth from cluster number counts". In: *Astron. Astrophys.* 696 (2025), A5. DOI: 10.1051/0004-6361/202452584. arXiv: 2410.09499 [astro-ph.CO].

[262] Joan Solà, Adrià Gómez-Valent, and Javier de Cruz Pérez. "The H_0 tension in light of vacuum dynamics in the Universe". In: *Phys. Lett. B* 774 (2017), pp. 317–324. DOI: 10.1016/j.physletb.2017.09.073. arXiv: 1705.06723 [astro-ph.CO].

[263] Edward W. Kolb. *The Early Universe*. Vol. 69. Taylor and Francis, May 2019. ISBN: 978-0-429-49286-0, 978-0-201-62674-2. DOI: 10.1201/9780429492860.

[264] Ariel G. Sánchez. "Arguments against using h^{-1}Mpc units in observational cosmology". In: *Phys. Rev. D* 102.12 (2020), p. 123511. DOI: 10.1103/PhysRevD.102.123511. arXiv: 2002.07829 [astro-ph.CO].

[265] Alex Hall. "Cosmology from weak lensing alone and implications for the Hubble tension". In: *Mon. Not. Roy. Astron. Soc.* 505.4 (2021), pp. 4935–4955. DOI: 10.1093/mnras/stab1563. arXiv: 2104.12880 [astro-ph.CO].

[266] Lucas F. Secco et al. "Role of the Hubble scale in the weak lensing versus CMB tension". In: *Phys. Rev. D* 107.8 (2023), p. 083532. DOI: 10.1103/PhysRevD.107.083532. arXiv: 2209.12997 [astro-ph.CO].

[267] Carlos García-García et al. "Cosmic shear with small scales: DES-Y3, KiDS-1000 and HSC-DR1". In: *JCAP* 08 (2024), p. 024. DOI: 10.1088/1475-7516/2024/08/024. arXiv: 2403.13794 [astro-ph.CO].

[268] Jiamin Hou et al. "The Completed SDSS-IV extended Baryon Oscillation Spectroscopic Survey: BAO and RSD measurements from anisotropic clustering analysis of the Quasar Sample in configuration space between redshift 0.8 and 2.2". In: *Mon. Not. Roy. Astron. Soc.* 500.1 (2020), pp. 1201–1221. DOI: 10.1093/mnras/staa3234. arXiv: 2007.08998 [astro-ph.CO].

[269] A. G. Adame et al. "Validation of the Scientific Program for the Dark Energy Spectroscopic Instrument". In: *Astron. J.* 167.2 (2024), p. 62. DOI: 10.3847/1538-3881/ad0b08. arXiv: 2306.06307 [astro-ph.CO].

[270] Adrià Gómez-Valent et al. "Early dark energy in the pre- and postrecombination epochs". In: *Phys. Rev. D* 104.8 (2021), p. 083536. DOI: 10.1103/PhysRevD.104.083536. arXiv: 2107.11065 [astro-ph.CO].

[271] Agne Semenaite et al. "Cosmological implications of the full shape of anisotropic clustering measurements in BOSS and eBOSS". In: *Mon. Not. Roy. Astron. Soc.* 512.4 (2022), pp. 5657–5670. DOI: 10.1093/mnras/stac829. arXiv: 2111.03156 [astro-ph.CO].

[272] Ariel G. Sánchez et al. "Evolution mapping: a new approach to describe matter clustering in the non-linear regime". In: *Mon. Not. Roy. Astron. Soc.* 514.4 (2022), pp. 5673–5685. DOI: 10.1093/mnras/stac1656. arXiv: 2108.12710 [astro-ph.CO].

[273] Adrià Gómez-Valent et al. "Coupled and uncoupled early dark energy, massive neutrinos, and the cosmological tensions". In: *Phys. Rev. D* 106.10 (2022), p. 103522. DOI: 10.1103/PhysRevD.106.103522. arXiv: 2207.14487 [astro-ph.CO].

[274] Agne Semenaite et al. "Beyond – ΛCDM constraints from the full shape clustering measurements from BOSS and eBOSS". In: *Mon. Not. Roy. Astron. Soc.* 521.4 (2023), pp. 5013–5025. DOI: 10.1093/mnras/stad849. arXiv: 2210.07304 [astro-ph.CO].

[275] Adrià Gómez-Valent, Nick E. Mavromatos, and Joan Solà Peracaula. "Stringy running vacuum model and current tensions in cosmology". In: *Class. Quant. Grav.* 41.1 (2024), p. 015026. DOI: 10.1088/1361-6382/ad0fb8. arXiv: 2305.15774 [gr-qc].

[276] Adri Gómez-Valent and Joan Solà Peracaula. "Phantom Matter: A Challenging Solution to the Cosmological Tensions". In: *Astrophys. J.* 975.1 (2024), p. 64. DOI: 10.3847/1538-4357/ad7a62. arXiv: 2404.18845 [astro-ph.CO].

[277] Adria Gómez-Valent and Joan Solà Peracaula. "Composite dark energy and the cosmological tensions". In: *Phys. Lett. B* 864 (2025), p. 139391. DOI: 10.1016/j.physletb.2025.139391. arXiv: 2412.15124 [astro-ph.CO].

[278] Matteo Forconi, Arianna Favale, and Adrià Gómez-Valent. "Illustrating the consequences of a misuse of $\sigma 8$ in cosmology". In: *Phys. Rev. D* 112.2 (2025), p. 023517. DOI: 10.1103/rpf5-ldks. arXiv: 2501.11571 [astro-ph.CO].

[279] R. Laureijs et al. "Euclid Definition Study Report". In: *arXiv:1110.3193* (Oct. 2011). arXiv: 1110.3193 [astro-ph.CO].

[280] Luca Amendola et al. "Cosmology and fundamental physics with the Euclid satellite". In: *Living Rev. Rel.* 16 (2013), p. 6. DOI: 10.12942/lrr-2013-6. arXiv: 1206.1225 [astro-ph.CO].

[281] Dominik J. Schwarz et al. "CMB Anomalies after Planck". In: *Class. Quant. Grav.* 33.18 (2016), p. 184001. DOI: 10.1088/0264-9381/33/18/184001. arXiv: 1510.07929 [astro-ph.CO].

[282] Eiichiro Komatsu. "New physics from the polarized light of the cosmic microwave background". In: *Nature Rev. Phys.* 4.7 (2022), pp. 452–469. DOI: 10.1038/s42254-022-00452-4. arXiv: 2202.13919 [astro-ph.CO].

[283] Giacomo Galloni et al. "Unraveling the CMB lack-of-correlation anomaly with the cosmological gravitational wave background". In: *JCAP* 10 (2023), p. 013. DOI: 10.1088/1475-7516/2023/10/013. arXiv: 2305.18184 [astro-ph.CO].

[284] Amirhossein Samandar et al. "Cosmic topology. Part IIIa. Microwave background parity violation without parity-violating microphysics". In: *JCAP* 11 (2024), p. 020. DOI: 10.1088/1475-7516/2024/11/020. arXiv: 2407.09400 [astro-ph.CO].

[285] Nathan J. Secrest et al. "A Test of the Cosmological Principle with Quasars". In: *Astrophys. J. Lett.* 908.2 (2021), p. L51. DOI: 10.3847/2041-8213/abdd40. arXiv: 2009.14826 [astro-ph.CO].

[286] Yehuda Hoffman et al. "The Dipole Repeller". In: (Feb. 2017). DOI: 10.1038/s41550-016-0036. arXiv: 1702.02483 [astro-ph.CO].

[287] Maria Lopes et al. "Bulk Flow Motion Detection in the Local Universe with Pantheon+ Type Ia Supernovae". In: *Astrophys. J.* 967.1 (2024), p. 47. DOI: 10.3847/1538-4357/ad3735. arXiv: 2405.11077 [astro-ph.CO].

[288] Erik Rosenberg, Steven Gratton, and George Efstathiou. "CMB power spectra and cosmological parameters from Planck PR4 with CamSpec". In: *Mon. Not. Roy. Astron. Soc.* 517.3 (2022), pp. 4620–4636. DOI: 10.1093/mnras/stac2744. arXiv: 2205.10869 [astro-ph.CO].

[289] Brian D. Fields et al. "Big-Bang Nucleosynthesis after Planck". In: *JCAP* 03 (2020). [Erratum: JCAP 11, E02 (2020)], p. 010. DOI: 10.1088/1475-7516/2020/03/010. arXiv: 1912.01132 [astro-ph.CO].

[290] Brian D. Fields. "The primordial lithium problem". In: *Ann. Rev. Nucl. Part. Sci.* 61 (2011), pp. 47–68. DOI: 10.1146/annurev-nucl-102010-130445. arXiv: 1203.3551 [astro-ph.CO].

[291] Julien Lesgourgues and Sergio Pastor. "Massive neutrinos and cosmology". In: *Phys. Rept.* 429 (2006), pp. 307–379. DOI: 10.1016/j.physrep.2006.04.001. arXiv: astro-ph/0603494.

[292] R. Allison et al. "Towards a cosmological neutrino mass detection". In: *PRD* 92.12, 123535 (Dec. 2015), p. 123535. DOI: 10.1103/PhysRevD.92.123535. arXiv: 1509.07471 [astro-ph.CO].

[293] Elena Giusarma et al. "Improvement of cosmological neutrino mass bounds". In: *PRD* 94.8, 083522 (Oct. 2016), p. 083522. DOI: 10.1103/PhysRevD.94.083522. arXiv: 1605.04320 [astro-ph.CO].

[294] Aoife Boyle and Eiichiro Komatsu. "Deconstructing the neutrino mass constraint from galaxy redshift surveys". In: *JCAP* 2018.3, 035 (Mar. 2018), p. 035. DOI: 10.1088/1475-7516/2018/03/035. arXiv: 1712.01857 [astro-ph.CO].

[295] Massimiliano Lattanzi and Martina Gerbino. "Status of neutrino properties and future prospects - Cosmological and astrophysical constraints". In: *arXiv e-prints*, arXiv:1712.07109 (Dec. 2017), arXiv:1712.07109. arXiv: 1712.07109 [astro-ph.CO].

[296] Toni Bertólez-Martínez et al. "Origin of cosmological neutrino mass bounds: background versus perturbations". In: *JCAP* 06 (2025), p. 058. DOI: 10.1088/1475-7516/2025/06/058. arXiv: 2411.14524 [astro-ph.CO].

[297] Michael S. Turner. "Early-Universe Thermal Production of Not-So-Invisible Axions". In: *Phys. Rev. Lett.* 59 (21 1987), pp. 2489–2492. DOI: 10.1103/PhysRevLett.59.2489. URL: https://link.aps.org/doi/10.1103/PhysRevLett.59.2489.

[298] Alexey Boyarsky, Oleg Ruchayskiy, and Mikhail Shaposhnikov. "The Role of Sterile Neutrinos in Cosmology and Astrophysics". In: *Annual Review of Nuclear and Particle Science* 59.1 (Nov. 2009), pp. 191–214. DOI: 10.1146/annurev.nucl.010909.083654. arXiv: 0901.0011 [hep-ph].

[299] M. Kawasaki, K. Kohri, and Naoshi Sugiyama. "Cosmological Constraints on Late-time Entropy Production". In: *PRL* 82.21 (May 1999), pp. 4168–4171. DOI: 10.1103/PhysRevLett.82.4168. arXiv: astro-ph/9811437 [astro-ph].

[300] A. G. Adame et al. "DESI 2024 III: baryon acoustic oscillations from galaxies and quasars". In: *JCAP* 04 (2025), p. 012. DOI: 10.1088/1475-7516/2025/04/012. arXiv: 2404.03000 [astro-ph.CO].

[301] Wayne Hu. "Crossing the phantom divide: Dark energy internal degrees of freedom". In: *Phys. Rev. D* 71 (2005), p. 047301. DOI: 10.1103/PhysRevD.71.047301. arXiv: astro-ph/0410680.

[302] Alexander Vikman. "Can dark energy evolve to the phantom?" In: *Phys. Rev. D* 71 (2005), p. 023515. DOI: 10.1103/PhysRevD.71.023515. arXiv: astro-ph/0407107.

[303] Gen Ye et al. "Hints of Nonminimally Coupled Gravity in DESI 2024 Baryon Acoustic Oscillation Measurements". In: *Phys. Rev. Lett.* 134.18 (2025), p. 181002. DOI: 10.1103/PhysRevLett.134.181002. arXiv: 2407.15832 [astro-ph.CO].

[304] Anton Chudaykin and Martin Kunz. "Modified gravity interpretation of the evolving dark energy in light of DESI data". In: *Phys. Rev. D* 110.12 (2024), p. 123524. DOI: 10.1103/PhysRevD.110.123524. arXiv: 2407.02558 [astro-ph.CO].

[305] Sergei D. Odintsov, Diego Sáez-Chillón Gómez, and German S. Sharov. "Modified gravity/dynamical dark energy vs ΛCDM: is the game over?" In: *Eur. Phys. J. C* 85.3 (2025), p. 298. DOI: 10.1140/epjc/s10052-025-14013-3. arXiv: 2412.09409 [gr-qc].

[306] Amlan Chakraborty et al. "DESI results: Hint towards coupled dark matter and dark energy". In: (Mar. 2025). arXiv: 2503.10806 [astro-ph.CO].

[307] Ivo Labbé et al. "A population of red candidate massive galaxies ~600 Myr after the Big Bang". In: *Nature* 616.7956 (2023). arXiv:2207.12446., pp. 266–269. DOI: 10.1038/s41586-023-05786-2. arXiv: 2207.12446 [astro-ph.GA].

[308] N. Menci et al. "Constraints on Dynamical Dark Energy Models from the Abundance of Massive Galaxies at High Redshifts". In: *Astrophys. J.* 900.2 (2020), p. 108. DOI: 10.3847/1538-4357/aba9d2. arXiv: 2007.12453 [astro-ph.CO].

[309] Matteo Forconi et al. "A double take on early and interacting dark energy from JWST". In: *JCAP* 05 (2024), p. 097. DOI: 10.1088/1475-7516/2024/05/097. arXiv: 2312.11074 [astro-ph.CO].

[310] Nicola Menci, Anjan Ananda Sen, and Marco Castellano. "The Excess of JWST Bright Galaxies: A Possible Origin in the Ground State of Dynamical Dark Energy in the Light of DESI 2024 Data". In: *Astrophys. J.* 976.2 (2024), p. 227. DOI: 10.3847/1538-4357/ad8d5b. arXiv: 2410.22940 [astro-ph.CO].

[311] C. Wetterich. "Cosmology and the fate of dilatation symmetry". In: *Nuclear Physics B* 302.4 (1988), pp. 668–696. DOI: 10.1016/0550-3213(88)90193-9. URL: https://doi.org/10.1016%2F0550-3213%2888%2990193-9.

[312] Bharat Ratra and P. J. E. Peebles. "Cosmological consequences of a rolling homogeneous scalar field". In: *Phys. Rev. D* 37 (12 1988), pp. 3406–3427. DOI: 10.1103/PhysRevD.37.3406. URL: https://link.aps.org/doi/10.1103/PhysRevD.37.3406.

[313] P. J. E. Peebles and Bharat Ratra. "Cosmology with a Time-Variable Cosmological "Constant"". In: *ApJL* 325 (Feb. 1988), p. L17. DOI: 10.1086/185100.

[314] Ivaylo Zlatev, Li-Min Wang, and Paul J. Steinhardt. "Quintessence, cosmic coincidence, and the cosmological constant". In: *Phys. Rev. Lett.* 82 (1999), pp. 896–899. DOI: 10.1103/PhysRevLett.82.896. arXiv: astro-ph/9807002.

[315] Joan Solà, Adrià Gómez-Valent, and Javier de Cruz Pérez. "Hints of dynamical vacuum energy in the expanding Universe". In: *Astrophys. J. Lett.* 811 (2015), p. L14. DOI: 10.1088/2041-8205/811/1/L14. arXiv: 1506.05793 [gr-qc].

[316] Joan Solà, Adrià Gómez-Valent, and Javier de Cruz Pérez. "First evidence of running cosmic vacuum: challenging the concordance model". In: *Astrophys. J.* 836.1 (2017), p. 43. DOI: 10.3847/1538-4357/836/1/43. arXiv: 1602.02103 [astro-ph.CO].

[317] Joan Solà Peracaula, Javier de Cruz Pérez, and Adria Gomez-Valent. "Possible signals of vacuum dynamics in the Universe". In: *Mon. Not. Roy. Astron. Soc.* 478.4 (2018), pp. 4357–4373. DOI: 10.1093/mnras/sty1253. arXiv: 1703.08218 [astro-ph.CO].

[318] Joan Solà Peracaula et al. "Brans–Dicke Gravity with a Cosmological Constant Smoothes Out ΛCDM Tensions". In: *Astrophys. J. Lett.* 886.1 (2019), p. L6. DOI: 10.3847/2041-8213/ab53e9. arXiv: 1909.02554 [astro-ph.CO].

[319] Guillermo Ballesteros, Alessio Notari, and Fabrizio Rompineve. "The H_0 tension: ΔG_N vs. $\Delta N_{\rm eff}$". In: *JCAP* 11 (2020), p. 024. DOI: 10.1088/1475-7516/2020/11/024. arXiv: 2004.05049 [astro-ph.CO].

[320] Joan Solà Peracaula et al. "Brans–Dicke cosmology with a Λ-term: a possible solution to ΛCDM tensions". In: *Class. Quant. Grav.* 37.24 (2020), p. 245003. DOI: 10.1088/1361-6382/abbc43. arXiv: 2006.04273 [astro-ph.CO].

[321] Matteo Braglia et al. "Larger value for H_0 by an evolving gravitational constant". In: *Phys. Rev. D* 102.2 (2020), p. 023529. DOI: 10.1103/PhysRevD.102.023529. arXiv: 2004.11161 [astro-ph.CO].

[322] Matteo Braglia et al. "Early modified gravity in light of the H_0 tension and LSS data". In: *Phys. Rev. D* 103.4 (2021), p. 043528. DOI: 10.1103/PhysRevD.103.043528. arXiv: 2011.12934 [astro-ph.CO].

[323] Giampaolo Benevento et al. "An Exploration of an Early Gravity Transition in Light of Cosmological Tensions". In: *Astrophys. J.* 935.2 (2022), p. 156. DOI: 10.3847/1538-4357/ac80fd. arXiv: 2202.09356 [astro-ph.CO].

[324] Joan Solà Peracaula et al. "Running Vacuum in the Universe: Phenomenological Status in Light of the Latest Observations, and Its Impact on the σ_8 and H_0 Tensions". In: *Universe* 9.6 (2023), p. 262. DOI: 10.3390/universe9060262. arXiv: 2304.11157 [astro-ph.CO].

[325] Joshua A. Kable et al. "Cosmological Tensions and the Transitional Planck Mass Model". In: *Astrophys. J.* 959.2 (2023), p. 143. DOI: 10.3847/1538-4357/acfed0. arXiv: 2307.12174 [astro-ph.CO].

[326] Miaoxin Liu et al. "Can Non-standard Recombination Resolve the Hubble Tension?" In: *Sci. China Phys. Mech. Astron.* 63.9 (2020), p. 290405. DOI: 10.1007/s11433-019-1509-5. arXiv: 1912.00190 [astro-ph.CO].

[327] Luke Hart and Jens Chluba. "Updated fundamental constant constraints from Planck 2018 data and possible relations to the Hubble tension". In: *Mon. Not. Roy. Astron. Soc.* 493.3 (2020), pp. 3255–3263. DOI: 10.1093/mnras/staa412. arXiv: 1912.03986 [astro-ph.CO].

[328] Toyokazu Sekiguchi and Tomo Takahashi. "Early recombination as a solution to the H_0 tension". In: *Phys. Rev. D* 103.8 (2021), p. 083507. DOI: 10.1103/PhysRevD.103.083507. arXiv: 2007.03381 [astro-ph.CO].

[329] Nanoom Lee et al. "What It Takes to Solve the Hubble Tension through Modifications of Cosmological Recombination". In: *Phys. Rev. Lett.* 130.16 (2023), p. 161003. DOI: 10.1103/PhysRevLett.130.161003. arXiv: 2212.04494 [astro-ph.CO].

[330] Dhiraj Kumar Hazra, Akhil Antony, and Arman Shafieloo. "One spectrum to cure them all: signature from early Universe solves major anomalies and tensions in cosmology". In: *JCAP* 08.08 (2022), p. 063. DOI: 10.1088/1475-7516/2022/08/063. arXiv: 2201.12000 [astro-ph.CO].

[331] Tanvi Karwal and Marc Kamionkowski. "Dark energy at early times, the Hubble parameter, and the string axiverse". In: *Phys. Rev. D* 94.10 (2016), p. 103523. DOI: 10.1103/PhysRevD.94.103523. arXiv: 1608.01309 [astro-ph.CO].

[332] Vivian Poulin et al. "Early Dark Energy Can Resolve The Hubble Tension". In: *Phys. Rev. Lett.* 122.22 (2019), p. 221301. DOI: 10.1103/PhysRevLett.122.221301. arXiv: 1811.04083 [astro-ph.CO].

[333] Prateek Agrawal et al. "Rock 'n' Roll Solutions to the Hubble Tension". In: *arXiv:1904.01016* (Apr. 2019). arXiv: 1904.01016 [astro-ph.CO].

[334] Meng-Xiang Lin et al. "Acoustic Dark Energy: Potential Conversion of the Hubble Tension". In: *Phys. Rev. D* 100.6 (2019), p. 063542. DOI: 10.1103/PhysRevD.100.063542. arXiv: 1905.12618 [astro-ph.CO].

[335] Florian Niedermann and Martin S. Sloth. "New early dark energy". In: *Phys. Rev. D* 103.4 (2021), p. L041303. DOI: 10.1103/PhysRevD.103.L041303. arXiv: 1910.10739 [astro-ph.CO].

[336] Florian Niedermann and Martin S. Sloth. "Hot new early dark energy". In: *Phys. Rev. D* 105.6 (2022), p. 063509. DOI: 10.1103/PhysRevD.105.063509. arXiv: 2112.00770 [hep-ph].

[337] Juan S. Cruz, Florian Niedermann, and Martin S. Sloth. "Cold New Early Dark Energy pulls the trigger on the H $_0$ and S $_8$ tensions: a simultaneous solution to both tensions without new ingredients". In: *JCAP* 11 (2023), p. 033. DOI: 10.1088/1475-7516/2023/11/033. arXiv: 2305.08895 [astro-ph.CO].

[338] Sunny Vagnozzi. "Consistency tests of ΛCDM from the early integrated Sachs-Wolfe effect: Implications for early-time new physics and the Hubble tension". In: *Phys. Rev. D* 104.6 (2021), p. 063524. DOI: 10.1103/PhysRevD.104.063524. arXiv: 2105.10425 [astro-ph.CO].

[339] Xuejian Shen et al. "Early galaxies and early dark energy: a unified solution to the hubble tension and puzzles of massive bright galaxies revealed by JWST". In: *Mon. Not. Roy. Astron. Soc.* 533.4 (2024), pp. 3923–3936. DOI: 10.1093/mnras/stae1932. arXiv: 2406.15548 [astro-ph.GA].

[340] Gianpiero Mangano et al. "Relic neutrino decoupling including flavor oscillations". In: *Nucl. Phys. B* 729 (2005), pp. 221–234. DOI: 10.1016/j.nuclphysb.2005.09.041. arXiv: hep-ph/0506164.

[341] Pablo F. de Salas and Sergio Pastor. "Relic neutrino decoupling with flavour oscillations revisited". In: *JCAP* 07 (2016), p. 051. DOI: 10.1088/1475-7516/2016/07/051. arXiv: 1606.06986 [hep-ph].

[342] Jack J. Bennett et al. "Towards a precision calculation of $N_{\rm eff}$ in the Standard Model II: Neutrino decoupling in the presence of flavour oscillations and finite-temperature QED". In: *JCAP* 04 (2021), p. 073. DOI: 10.1088/1475-7516/2021/04/073. arXiv: 2012.02726 [hep-ph].

[343] Michele Maggiore. "Gravitational wave experiments and early universe cosmology". In: *Phys. Rept.* 331 (2000), pp. 283–367. DOI: 10.1016/S0370-1573(99)00102-7. arXiv: gr-qc/9909001.

[344] P. F. de Salas et al. "Bounds on very low reheating scenarios after Planck". In: *Phys. Rev. D* 92.12 (2015), p. 123534. DOI: 10.1103/PhysRevD.92.123534. arXiv: 1511.00672 [astro-ph.CO].

[345] William Giarè et al. "Towards a reliable calculation of relic radiation from primordial gravitational waves". In: *Mon. Not. Roy. Astron. Soc.* 520 (2023), p. 2. DOI: 10.1093/mnras/stad258. arXiv: 2210.14159 [astro-ph.CO].

[346] Miguel Barroso Varela and Orfeu Bertolami. "Hubble tension in a nonminimally coupled curvature-matter gravity model". In: *JCAP* 06 (2024), p. 025. DOI: 10.1088/1475-7516/2024/06/025. arXiv: 2403.11683 [gr-qc].

[347] Lloyd Knox and Marius Millea. "Hubble constant hunter's guide". In: *Phys. Rev. D* 101.4 (2020), p. 043533. DOI: 10.1103/PhysRevD.101.043533. arXiv: 1908.03663 [astro-ph.CO].

[348] William Giarè et al. "Is the Harrison-Zeldovich spectrum coming back? ACT preference for $n_s \sim 1$ and its discordance with Planck". In: *Mon. Not. Roy. Astron. Soc.* 521.2 (2023), pp. 2911–2918. DOI: 10.1093/mnras/stad724. arXiv: 2210.09018 [astro-ph.CO].

[349] Rodrigo Calderón et al. "On the consistency of ΛCDM with CMB measurements in light of the latest Planck, ACT and SPT data". In: *JCAP* 08 (2023), p. 059. DOI: 10.1088/1475-7516/2023/08/059. arXiv: 2302.14300 [astro-ph.CO].

[350] William Giarè. "CMB Anomalies and the Hubble Tension". In: (May 2023). arXiv: 2305.16919 [astro-ph.CO].

[351] Eleonora Di Valentino et al. "In the realm of the Hubble tension—a review of solutions". In: *Classical and Quantum Gravity* 38.15 (2021), p. 153001. DOI: 10.1088/1361-6382/ac086d. URL: https://doi.org/10.1088%2F1361-6382%2Fac086d.

[352] R.R Caldwell. "A phantom menace? Cosmological consequences of a dark energy component with super-negative equation of state". In: *Physics Letters B* 545.1-2 (2002), pp. 23–29. DOI: 10.1016/s0370-2693(02)02589-3. URL: https://doi.org/10.1016%2Fs0370-2693%2802%2902589-3.

[353] Eleonora Di Valentino, Alessandro Melchiorri, and Joseph Silk. "Reconciling Planck with the local value of H 0 in extended parameter space". In: *Physics Letters B* 761 (2016), pp. 242–246. DOI: 10.1016/j.physletb.2016.08.043. URL: https://doi.org/10.1016%2Fj.physletb.2016.08.043.

[354] Michel Chevallier and David Polarski. "Accelerating Universe with scaling dark matter". In: *International Journal of Modern Physics D* 10.02 (2001), pp. 213–223. DOI: 10.1142/s0218271801000822. URL: https://doi.org/10.1142%2Fs0218271801000822.

[355] Ujjaini Alam et al. "Is there supernova evidence for dark energy metamorphosis ?" In: *Mon. Not. Roy. Astron. Soc.* 354 (2004), p. 275. DOI: 10.1111/j.1365-2966.2004.08189.x. arXiv: astro-ph/0311364.

[356] Ujjaini Alam, Varun Sahni, and A. A. Starobinsky. "The Case for dynamical dark energy revisited". In: *JCAP* 06 (2004), p. 008. DOI: 10.1088/1475-7516/2004/06/008. arXiv: astro-ph/0403687.

[357] Varun Sahni, Arman Shafieloo, and Alexei A. Starobinsky. "Model independent evidence for dark energy evolution from Baryon Acoustic Oscillations". In: *Astrophys. J. Lett.* 793.2 (2014), p. L40. DOI: 10.1088/2041-8205/793/2/L40. arXiv: 1406.2209 [astro-ph.CO].

[358] Valentina Salvatelli et al. "Indications of a late-time interaction in the dark sector". In: *Phys. Rev. Lett.* 113.18 (2014), p. 181301. DOI: 10.1103/PhysRevLett.113.181301. arXiv: 1406.7297 [astro-ph.CO].

[359] Joan Solà Peracaula, Javier de Cruz Pérez, and Adrià Gómez-Valent. "Dynamical dark energy vs. Λ = const in light of observations". In: *EPL* 121.3 (2018), p. 39001. DOI: 10.1209/0295-5075/121/39001. arXiv: 1606.00450 [gr-qc].

[360] Gong-Bo Zhao et al. "Dynamical dark energy in light of the latest observations". In: *Nature Astron.* 1.9 (2017), pp. 627–632. DOI: 10.1038/s41550-017-0216-z. arXiv: 1701.08165 [astro-ph.CO].

[361] Joan Solà Peracaula, Adrià Gómez-Valent, and Javier de Cruz Pérez. "Signs of Dynamical Dark Energy in Current Observations". In: *Phys. Dark Univ.* 25 (2019), p. 100311. DOI: 10.1016/j.dark.2019.100311. arXiv: 1811.03505 [astro-ph.CO].

[362] K. Lodha et al. "Extended Dark Energy analysis using DESI DR2 BAO measurements". In: (Mar. 2025). arXiv: 2503.14743 [astro-ph.CO].

[363] Alex González-Fuentes and Adrià Gómez-Valent. "Reconstruction of dark energy and late-time cosmic expansion using the Weighted Function Regression method". In: (June 2025). arXiv: 2506.11758 [astro-ph.CO].

[364] Emre Özülker, Eleonora Di Valentino, and William Giarè. "Dark Energy Crosses the Line: Quantifying and Testing the Evidence for Phantom Crossing". In: (June 2025). arXiv: 2506.19053 [astro-ph.CO].

[365] Ye-Huang Pang, Xue Zhang, and Qing-Guo Huang. "The impact of the Hubble tension on the evidence for dynamical dark energy". In: *Sci. China Phys. Mech. Astron.* 68.8 (2025), p. 280410. DOI: 10.1007/s11433-025-2713-8. arXiv: 2503.21600 [astro-ph.CO].

[366] Eleonora Di Valentino, Alessandro Melchiorri, and Olga Mena. "Can interacting dark energy solve the H_0 tension?" In: *Physical Review D* 96.4 (2017). DOI: 10.1103/physrevd.96.043503. URL: https://doi.org/10.1103%2Fphysrevd.96.043503.

[367] Joan Solà Peracaula et al. "Brans Dicke Gravity with a Cosmological Constant Smoothes Out ΛCDM Tensions". In: *The Astrophysical Journal* 886.1 (2019), p. L6. DOI: 10.3847/2041-8213/ab53e9. URL: https://doi.org/10.3847%2F2041-8213%2Fab53e9.

[368] Levon Pogosian et al. "Imprints of cosmological tensions in reconstructed gravity". In: *Nature Astron.* 6.12 (2022), pp. 1484–1490. DOI: 10.1038/s41550-022-01808-7. arXiv: 2107.12992 [astro-ph.CO].

[369] Alexei A. Starobinsky. "A New Type of Isotropic Cosmological Models Without Singularity". In: *Phys. Lett. B* 91 (1980). Ed. by I. M. Khalatnikov and V. P. Mineev, pp. 99–102. DOI: 10.1016/0370-2693(80)90670-X.

[370] Valerio Marra and Leandros Perivolaropoulos. "Rapid transition of G_{eff} at $z_t \simeq 0.01$ as a possible solution of the Hubble and growth tensions". In: *Phys. Rev. D* 104.2 (2021), p. L021303. DOI: 10.1103/PhysRevD.104.L021303. arXiv: 2102.06012 [astro-ph.CO].

[371] George Alestas, Ioannis Antoniou, and Leandros Perivolaropoulos. "Hints for a Gravitational Transition in Tully–Fisher Data". In: *Universe* 7.10 (2021), p. 366. DOI: 10.3390/universe7100366. arXiv: 2104.14481 [astro-ph.CO].

[372] Leandros Perivolaropoulos. "Is the Hubble Crisis Connected with the Extinction of Dinosaurs?" In: *Universe* 8.5 (2022), p. 263. DOI: 10.3390/universe8050263. arXiv: 2201.08997 [astro-ph.EP].

[373] Ruchika et al. "A gravitational constant transition within cepheids as supernovae calibrators can solve the Hubble tension". In: *JCAP* 06 (2024), p. 056. DOI: 10.1088/1475-7516/2024/06/056. arXiv: 2306.05450 [astro-ph.CO].

[374] Luca Amendola, Pier Stefano Corasaniti, and Franco Occhionero. "Time variability of the gravitational constant and type Ia supernovae". In: (July 1999). arXiv: astro-ph/9907222.

[375] Bill S. Wright and Baojiu Li. "Type Ia supernovae, standardizable candles, and gravity". In: *Phys. Rev. D* 97.8 (2018), p. 083505. DOI: 10.1103/PhysRevD.97.083505. arXiv: 1710.07018 [astro-ph.CO].

[376] Luca Amendola, Stefano Corasaniti, and Franco Occhionero. *Time variability of the gravitational constant and Type Ia supernovae.* 1999. DOI: 10.48550/ARXIV.ASTRO-PH/9907222. URL: https://arxiv.org/abs/astro-ph/9907222.

[377] E. Gaztanaga et al. "Bounds on the possible evolution of the gravitational constant from cosmological type Ia supernovae". In: *Phys. Rev. D* 65 (2002), p. 023506. DOI: 10.1103/PhysRevD.65.023506. arXiv: astro-ph/0109299.

[378] Leandros Perivolaropoulos and Ruchika. "Hubble Tension and the G-step Model: Re-examination of Recent Constraints on Modified Local Physics". In: (Aug. 2025). arXiv: 2508.04395 [astro-ph.CO].

[379] Habib Abedi et al. "Effective gravitational coupling in modified teleparallel theories". In: *Physical Review D* 97.8 (2018). DOI: 10.1103/physrevd.97.084008. URL: https://doi.org/10.1103%2Fphysrevd.97.084008.

[380] Valeria Pettorino. "Testing modified gravity with Planck: the case of coupled dark energy". In: *Phys. Rev. D* 88 (2013), p. 063519. DOI: 10.1103/PhysRevD.88.063519. arXiv: 1305.7457 [astro-ph.CO].

[381] Adrià Gómez-Valent, Valeria Pettorino, and Luca Amendola. "Update on coupled dark energy and the H_0 tension". In: *Phys. Rev. D* 101.12 (2020), p. 123513. DOI: 10.1103/PhysRevD.101.123513. arXiv: 2004.00610 [astro-ph.CO].

[382] Prateek Agrawal, Georges Obied, and Cumrun Vafa. "H_0 tension, swampland conjectures, and the epoch of fading dark matter". In: *Phys. Rev. D* 103.4 (2021), p. 043523. DOI: 10.1103/PhysRevD.103.043523. arXiv: 1906.08261 [astro-ph.CO].

[383] Maria Archidiacono et al. "Unveiling dark fifth forces with linear cosmology". In: *JCAP* 10 (2022), p. 074. DOI: 10.1088/1475-7516/2022/10/074. arXiv: 2204.08484 [astro-ph.CO].

[384] Lisa W. K. Goh et al. "Constraining constant and tomographic coupled dark energy with low-redshift and high-redshift probes". In: *Phys. Rev. D* 107.8 (2023), p. 083503. DOI: 10.1103/PhysRevD.107.083503. arXiv: 2211.13588 [astro-ph.CO].

[385] Karsten Jedamzik and Levon Pogosian. "Relieving the Hubble tension with primordial magnetic fields". In: *Phys. Rev. Lett.* 125.18 (2020), p. 181302. DOI: 10.1103/PhysRevLett.125.181302. arXiv: 2004.09487 [astro-ph.CO].

[386] Joan Solà Peracaula et al. "Running vacuum against the H_0 and σ_8 tensions". In: *EPL* 134.1 (2021), p. 19001. DOI: 10.1209/0295-5075/134/19001. arXiv: 2102.12758 [astro-ph.CO].

[387] Raul Jimenez and Abraham Loeb. "Constraining cosmological parameters based on relative galaxy ages". In: *Astrophys. J.* 573 (2002), pp. 37–42. DOI: 10.1086/340549. arXiv: astro-ph/0106145.

[388] Allan Sandage. "The Change of Redshift and Apparent Luminosity of Galaxies due to the Deceleration of Selected Expanding Universes." In: *ApJ* 136 (Sept. 1962), p. 319. DOI: 10.1086/147385.

[389] Abraham Loeb. "Direct Measurement of Cosmological Parameters from the Cosmic Deceleration of Extragalactic Objects". In: *Astrophys. J. Lett.* 499 (1998), pp. L111–L114. DOI: 10.1086/311375. arXiv: astro-ph/9802122.

[390] J. Liske et al. "Cosmic dynamics in the era of Extremely Large Telescopes". In: *Mon. Not. Roy. Astron. Soc.* 386 (2008), pp. 1192–1218. DOI: 10.1111/j.1365-2966.2008.13090.x. arXiv: 0802.1532 [astro-ph].

[391] Krzysztof Bolejko, Chengyi Wang, and Geraint F. Lewis. "Direct detection of the cosmic expansion: the redshift drift and the flux drift". In: (July 2019). arXiv: 1907.04495 [astro-ph.CO].

[392] Michele Moresco et al. "Setting the Stage for Cosmic Chronometers. II. Impact of Stellar Population Synthesis Models Systematics and Full Covariance Matrix". In: *Astrophys. J.* 898.1 (2020), p. 82. DOI: 10.3847/1538-4357/ab9eb0. arXiv: 2003.07362 [astro-ph.GA].

[393] Raul Jimenez and Abraham Loeb. "Constraining Cosmological Parameters Based on Relative Galaxy Ages". In: *The Astrophysical Journal* 573.1 (2002), pp. 37–42. DOI: 10.1086/340549. URL: https://doi.org/10.1086%2F340549.

[394] Alan Heavens, Raul Jimenez, and Licia Verde. "Standard rulers, candles, and clocks from the low-redshift Universe". In: *Phys. Rev. Lett.* 113.24 (2014), p. 241302. DOI: 10.1103/PhysRevLett.113.241302. arXiv: 1409.6217 [astro-ph.CO].

[395] Licia Verde et al. "The length of the low-redshift standard ruler". In: *Mon. Not. Roy. Astron. Soc.* 467.1 (2017), pp. 731–736. DOI: 10.1093/mnras/stx116. arXiv: 1607.05297 [astro-ph.CO].

[396] Hai Yu, Bharat Ratra, and Fa-Yin Wang. "Hubble Parameter and Baryon Acoustic Oscillation Measurement Constraints on the Hubble Constant, the Deviation from the Spatially Flat ΛCDM Model, the Deceleration–Acceleration Transition Redshift, and Spatial Curvature". In: *Astrophys. J.* 856.1 (2018), p. 3. DOI: 10.3847/1538-4357/aab0a2. arXiv: 1711.03437 [astro-ph.CO].

[397] Adrià Gómez-Valent and Luca Amendola. "H_0 from cosmic chronometers and Type Ia supernovae, with Gaussian Processes and the novel Weighted Polynomial Regression method". In: *JCAP* 04 (2018), p. 051. DOI: 10.1088/1475-7516/2018/04/051. arXiv: 1802.01505 [astro-ph.CO].

[398] Balakrishna S. Haridasu et al. "An improved model-independent assessment of the late-time cosmic expansion". In: *JCAP* 10 (2018), p. 015. DOI: 10.1088/1475-7516/2018/10/015. arXiv: 1805.03595 [astro-ph.CO].

[399] Bikash R. Dinda. "Minimal model-dependent constraints on cosmological nuisance parameters and cosmic curvature from combinations of cosmological data". In: *Int. J. Mod. Phys. D* 32.11 (2023), p. 2350079. DOI: 10.1142/S0218271823500797. arXiv: 2209.14639 [astro-ph.CO].

[400] Purba Mukherjee et al. "A possible late-time transition of M_B inferred via neural networks". In: *JCAP* 09 (2024), p. 060. DOI: 10.1088/1475-7516/2024/09/060. arXiv: 2402.10502 [astro-ph.CO].

[401] Michele Moresco. "Addressing the Hubble tension with cosmic chronometers". In: (July 2023). arXiv: 2307.09501 [astro-ph.CO].

[402] Michele Moresco et al. "Setting the Stage for Cosmic Chronometers. I. Assessing the Impact of Young Stellar Populations on Hubble Parameter Measurements". In: *The Astrophysical Journal* 868.2 (2018), p. 84. DOI: 10.3847/1538-4357/aae829. URL: https://doi.org/10.3847%2F1538-4357%2Faae829.

[403] Michele Moresco et al. *Unveiling the Universe with Emerging Cosmological Probes*. 2022. DOI: 10.48550/ARXIV.2201.07241. URL: https://arxiv.org/abs/2201.07241.

[404] Michele Moresco. "Measuring the expansion history of the Universe with cosmic chronometers". In: *arXiv preprint 2412.01994* (Dec. 2024). arXiv: 2412.01994 [astro-ph.CO].

[405] Michele Moresco et al. "Unveiling the Universe with emerging cosmological probes". In: *Living Rev. Rel.* 25.1 (2022), p. 6. DOI: 10.1007/s41114-022-00040-z. arXiv: 2201.07241 [astro-ph.CO].

[406] Rene Laureijs et al. "Euclid definition study report". In: *arXiv preprint arXiv:1110.3193* (2011).

[407] Vincenzo Mainieri et al. "The Wide-field Spectroscopic Telescope (WST) Science White Paper". In: *arXiv preprint 2403.05398* (Mar. 2024). arXiv: 2403.05398 [astro-ph.IM].

[408] Yun Wang et al. "ATLAS Probe: Breakthrough Science of Galaxy Evolution, Cosmology, Milky Way, and the Solar System". In: *arXiv preprint 1909.00070* (Aug. 2019). arXiv: 1909.00070 [astro-ph.IM].

[409] M. M. Phillips. "The Absolute Magnitudes of Type IA Supernovae". In: *ApJL* 413 (Aug. 1993), p. L105. DOI: 10.1086/186970.

[410] M. M. Phillips et al. "The Reddening-Free Decline Rate Versus Luminosity Relationship for Type Ia Supernovae". In: *The Astronomical Journal* 118.4 (1999), pp. 1766–1776. DOI: 10.1086/301032. URL: https://doi.org/10.1086%2F301032.

[411] Anthony Carr et al. "The Pantheon+ analysis: Improving the redshifts and peculiar velocities of Type Ia supernovae used in cosmological analyses". In: *Publ. Astron. Soc. Austral.* 39 (2022), e046. DOI: 10.1017/pasa.2022.41. arXiv: 2112.01471 [astro-ph.CO].

[412] T. M. C. Abbott et al. "The Dark Energy Survey: Cosmology Results with ∼1500 New High-redshift Type Ia Supernovae Using the Full 5 yr Data Set". In: *Astrophys. J. Lett.* 973.1 (2024), p. L14. DOI: 10.3847/2041-8213/ad6f9f. arXiv: 2401.02929 [astro-ph.CO].

[413] Paul A. Abell et al. "LSST Science Book, Version 2.0". In: *arXiv:0912.0201* (Dec. 2009). arXiv: 0912.0201 [astro-ph.IM].

[414] D. Spergel et al. "Wide-Field InfrarRed Survey Telescope-Astrophysics Focused Telescope Assets WFIRST-AFTA 2015 Report". In: *arXiv e-prints*, arXiv:1503.03757 (Mar. 2015), arXiv:1503.03757. DOI: 10.48550/arXiv.1503.03757. arXiv: 1503.03757 [astro-ph.IM].

[415] LSST Science Collaboration et al. "LSST Science Book, Version 2.0". In: *arXiv e-prints*, arXiv:0912.0201 (Dec. 2009), arXiv:0912.0201. DOI: 10.48550/arXiv.0912.0201. arXiv: 0912.0201 [astro-ph.IM].

[416] B. O. Sánchez et al. "SNIa Cosmology Analysis Results from Simulated LSST Images: From Difference Imaging to Constraints on Dark Energy". In: *Astrophys. J.* 934.2 (2022), p. 96. DOI: 10.3847/1538-4357/ac7a37. arXiv: 2111.06858 [astro-ph.CO].

[417] Alexandra Abate et al. "Large Synoptic Survey Telescope: Dark Energy Science Collaboration". In: *arXiv preprint 1211.0310* (Nov. 2012). arXiv: 1211.0310 [astro-ph.CO].

[418] C. Alcock and B. Paczynski. "An evolution free test for non-zero cosmological constant". In: *Nature* 281 (1979), pp. 358–359. DOI: 10.1038/281358a0.

[419] Nikhil Padmanabhan and Martin J. White. "Constraining Anisotropic Baryon Oscillations". In: *Phys. Rev. D* 77 (2008), p. 123540. DOI: 10.1103/PhysRevD.77.123540. arXiv: 0804.0799 [astro-ph].

[420] E. de Carvalho et al. "BAO angular scale at zeff = 0.11 with the SDSS blue galaxies". In: *Astron. Astrophys.* 649 (2021), A20. DOI: 10.1051/0004-6361/202039936. arXiv: 2103.14121 [astro-ph.CO].

[421] Jailson S. Alcaniz et al. "Measuring baryon acoustic oscillations with angular two-point correlation function". In: *Fundam. Theor. Phys.* 187 (2017), pp. 11–19. DOI: 10.1007/978-3-319-51700-1_2. arXiv: 1611.08458 [astro-ph.CO].

[422] E. de Carvalho et al. "Angular Baryon Acoustic Oscillation measure at $z = 2.225$ from the SDSS quasar survey". In: *JCAP* 04 (2018), p. 064. DOI: 10.1088/1475-7516/2018/04/064. arXiv: 1709.00113 [astro-ph.CO].

[423] Asta Heinesen, Chris Blake, and David L. Wiltshire. "Quantifying the accuracy of the Alcock-Paczynski scaling of baryon acoustic oscillation measurements". In: *JCAP* 01 (2020), p. 038. DOI: 10.1088/1475-7516/2020/01/038. arXiv: 1908.11508 [astro-ph.CO].

[424] Jiaming Pan et al. "Compressed baryon acoustic oscillation analysis is robust to modified-gravity models". In: *JCAP* 06 (2024), p. 051. DOI: 10.1088/1475-7516/2024/06/051. arXiv: 2312.05177 [astro-ph.CO].

[425] Santiago Sanz-Wuhl et al. "BAO cosmology in non-spatially flat background geometry from BOSS+eBOSS and lessons for future surveys". In: *JCAP* 05 (2024), p. 116. DOI: 10.1088/1475-7516/2024/05/116. arXiv: 2402.03427 [astro-ph.CO].

[426] Shi-Fan Chen et al. "Baryon Acoustic Oscillation Theory and Modelling Systematics for the DESI 2024 results". In: (Feb. 2024). arXiv: 2402.14070 [astro-ph.CO].

[427] Stefano Anselmi, Glenn D. Starkman, and Alessandro Renzi. "Cosmological forecasts for future galaxy surveys with the linear point standard ruler: Toward consistent BAO analyses far from a fiducial cosmology". In: *Phys. Rev. D* 107.12 (2023), p. 123506. DOI: 10.1103/PhysRevD.107.123506. arXiv: 2205.09098 [astro-ph.CO].

[428] Stefano Anselmi et al. "Cosmic distance inference from purely geometric BAO methods: Linear Point standard ruler and Correlation Function Model Fitting". In: *Phys. Rev. D* 99.12 (2019), p. 123515. DOI: 10.1103/PhysRevD.99.123515. arXiv: 1811.12312 [astro-ph.CO].

[429] N. Aghanim et al. "Planck 2018 results. V. CMB power spectra and likelihoods". In: *Astron. Astrophys.* 641 (2020), A5. DOI: 10.1051/0004-6361/201936386. arXiv: 1907.12875 [astro-ph.CO].

[430] D. J. Fixsen. "The temperature of the Cosmic Microwave Background". In: *The Astrophysical Journal* 707.2 (Nov. 2009), 916–920. ISSN: 1538-4357. DOI: 10.1088/0004-637x/707/2/916. URL: http://dx.doi.org/10.1088/0004-637X/707/2/916.

[431] Maria Giovanna Dainotti et al. "The X-ray fundamental plane of the Platinum Sample, the Kilonovae and the SNe Ib/c associated with GRBs". In: *Astrophys. J.* 904.2 (2020), p. 97. DOI: 10.3847/1538-4357/abbe8a. arXiv: 2010.02092 [astro-ph.HE].

[432] Simone Dall'Osso et al. "GRB Afterglows with Energy Injection from a spinning down NS". In: *arXiv preprint arXiv:1004.2788* (2010).

[433] Maria Giovanna Dainotti et al. "Selection Effects in Gamma-ray Burst Correlations: Consequences on the Ratio Between Gamma-ray Burst and Star Formation Rates". In: *Astrophys. J.* 800.1 (2015), p. 31. DOI: 10.1088/0004-637X/800/1/31. arXiv: 1412.3969 [astro-ph.HE].

[434] M. G. Dainotti et al. "Luminosity–time and luminosity–luminosity correlations for GRB prompt and afterglow plateau emissions". In: *Mon. Not. Roy. Astron. Soc.* 451.4 (2015), pp. 3898–3908. DOI: 10.1093/mnras/stv1229. arXiv: 1506.00702 [astro-ph.HE].

[435] Maria Giovanna Dainotti, Giuseppe Sarracino, and Salvatore Capozziello. "Gamma-ray bursts, supernovae Ia, and baryon acoustic oscillations: A binned cosmological analysis". In: *Publ. Astron. Soc. Jap.* 74.5 (2022), pp. 1095–1113–1113. DOI: 10.1093/pasj/psac057. arXiv: 2206.07479 [astro-ph.CO].

[436] Bradley Efron and Vahe Petrosian. "A simple test of independence for truncated data with applications to redshift surveys". In: *Astrophys. J.* 399 (1992), p. 345. DOI: 10.1086/171931.

[437] G. D'Agostini. "Fits, and especially linear fits, with errors on both axes, extra variance of the data points and other complications". In: *arXiv e-prints*, physics/0511182 (Nov. 2005), physics/0511182. DOI: 10.48550/arXiv.physics/0511182. arXiv: physics/0511182 [physics.data-an].

[438] Brandon C. Kelly. "Some Aspects of Measurement Error in Linear Regression of Astronomical Data". In: *Astrophys. J.* 665 (2007), pp. 1489–1506. DOI: 10.1086/519947. arXiv: 0705.2774 [astro-ph].

[439] P. A. Evans et al. "Methods and results of an automatic analysis of a complete sample ofSwift-XRT observations of GRBs". In: *Monthly Notices of the Royal Astronomical Society* 397.3 (Aug. 2009), 1177–1201. ISSN: 1365-2966. DOI: 10.1111/j.1365-2966.2009.14913.x. URL: http://dx.doi.org/10.1111/j.1365-2966.2009.14913.x.

[440] P. A. Evans et al. "The Swift Burst Analyser I: BAT and XRT spectral and flux evolution of Gamma Ray Bursts". In: *Astron. Astrophys.* 519 (2010), A102. DOI: 10.1051/0004-6361/201014819. arXiv: 1004.3208 [astro-ph.IM].

[441] E. Lusso and G. Risaliti. "Quasars as standard candles I: The physical relation between disc and coronal emission". In: *Astron. Astrophys.* 602 (2017), A79. DOI: 10.1051/0004-6361/201630079. arXiv: 1703.05299 [astro-ph.HE].

[442] Gideon Schwarz. "Estimating the Dimension of a Model". In: *Annals of Statistics* 6.2 (July 1978), pp. 461–464.

[443] Hirotugu Akaike. "A new look at the statistical model identification". In: *IEEE Trans. Autom. Control* 19 (1974), pp. 716–723. DOI: 10.1109/TAC.1974.1100705.

[444] Harold Jeffreys. *The Theory of Probability.* Oxford Classic Texts in the Physical Sciences. 1939. ISBN: 978-0-19-850368-2, 978-0-19-853193-7.

[445] Vinicius C. Busti, Chris Clarkson, and Marina Seikel. "Evidence for a Lower Value for H_0 from Cosmic Chronometers Data?" In: *Mon. Not. Roy. Astron. Soc.* 441 (2014), p. 11. DOI: 10.1093/mnrasl/slu035. arXiv: 1402.5429 [astro-ph.CO].

[446] Yingjie Yang et al. "Potentialities of Hubble parameter and expansion rate function data to alleviate Hubble tension". In: *Mon. Not. Roy. Astron. Soc.* 519.4 (2023), pp. 4938–4950. DOI: 10.1093/mnras/stac3617. arXiv: 2204.01020 [astro-ph.CO].

[447] Fabrizio Renzi and Alessandra Silvestri. "Hubble speed from first principles". In: *Phys. Rev. D* 107.2 (2023), p. 023520. DOI: 10.1103/PhysRevD.107.023520. arXiv: 2011.10559 [astro-ph.CO].

[448] Marina Seikel, Chris Clarkson, and Mathew Smith. "Reconstruction of dark energy and expansion dynamics using Gaussian processes". In: *JCAP* 06 (2012), p. 036. DOI: 10.1088/1475-7516/2012/06/036. arXiv: 1204.2832 [astro-ph.CO].

[449] Rong-Gen Cai, Zong-Kuan Guo, and Tao Yang. "Null test of the cosmic curvature using $H(z)$ and supernovae data". In: *Phys. Rev. D* 93.4 (2016), p. 043517. DOI: 10.1103/PhysRevD.93.043517. arXiv: 1509.06283 [astro-ph.CO].

[450] H. Yu and F.Y. Wang. "New model-independent method to test the curvature of the universe". In: *Astrophys. J.* 828.2 (2016), p. 85. DOI: 10.3847/0004-637X/828/2/85. arXiv: 1605.02483 [astro-ph.CO].

[451] Yingjie Yang and Yungui Gong. "Measurement on the cosmic curvature using the Gaussian process method". In: *Mon. Not. Roy. Astron. Soc.* 504.2 (2021), pp. 3092–3097. DOI: 10.1093/mnras/stab1085. arXiv: 2007.05714 [astro-ph.CO].

[452] Nan Liang et al. "Calibrating Gamma-Ray Bursts by Using a Gaussian Process with Type Ia Supernovae". In: *Astrophys. J.* 941.1 (2022), p. 84. DOI: 10.3847/1538-4357/aca08a. arXiv: 2211.02473 [astro-ph.CO].

[453] J P Hu, F Y Wang, and Z G Dai. "Measuring cosmological parameters with a luminosity–time correlation of gamma-ray bursts". In: *Monthly Notices of the Royal Astronomical Society* 507.1 (July 2021), pp. 730–742. ISSN: 0035-8711. DOI: 10.1093/mnras/stab2180. URL: https://doi.org/10.1093/mnras/stab2180.

[454] F. Y. Wang et al. "Standardized Long Gamma-Ray Bursts as a Cosmic Distance Indicator". In: *The Astrophysical Journal* 924.2 (2022), p. 97. DOI: 10.3847/1538-4357/ac3755. URL: https://doi.org/10.3847%2F1538-4357%2Fac3755.

[455] Xiao Tian et al. "Radio Plateaus in Gamma-Ray Burst Afterglows and Their Application in Cosmology". In: *Astrophys. J.* 958.1 (2023), p. 74. DOI: 10.3847/1538-4357/acfed8. arXiv: 2310.00596 [astro-ph.HE].

[456] Carl Edward Rasmussen and Christopher K. I. Williams. *Gaussian Processes for Machine Learning*. MIT Press, 2006.

[457] Seung-gyu Hwang et al. "How to use GP: effects of the mean function and hyperparameter selection on Gaussian process regression". In: *JCAP* 02 (2023), p. 014. DOI: 10.1088/1475-7516/2023/02/014. arXiv: 2206.15081 [astro-ph.CO].

[458] Ruchika, Purba Mukherjee, and Arianna Favale. "Revisiting Gaussian Process Reconstruction for Cosmological Inference: The Generalised GP (Gen GP) Framework". In: (Oct. 2025). arXiv: 2510.03742 [astro-ph.CO].

[459] Daniel Foreman-Mackey et al. "emcee: The MCMC Hammer". In: *Publications of the Astronomical Society of the Pacific* 125.925 (2013), pp. 306–312. DOI: 10.1086/670067. URL: https://doi.org/10.1086%2F670067.

[460] Jonathan Goodman and Jonathan Weare. "Ensemble samplers with affine invariance". In: *Communications in Applied Mathematics and Computational Science* 5.1 (Jan. 2010), pp. 65–80. DOI: 10.2140/camcos.2010.5.65.

[461] W. K. Hastings. "Monte Carlo Sampling Methods Using Markov Chains and Their Applications". In: *Biometrika* 57.1 (1970), pp. 97–109. ISSN: 00063444. URL: http://www.jstor.org/stable/2334940 (visited on 10/06/2022).

[462] Jonathan Goodman and Jonathan Weare. "Ensemble samplers with affine invariance". In: *Communications in Applied Mathematics and Computational Science* 5.1 (Jan. 2010), pp. 65–80. DOI: 10.2140/camcos.2010.5.65.

[463] Jesus Torrado and Antony Lewis. "Cobaya: Code for Bayesian Analysis of hierarchical physical models". In: *JCAP* 05 (2021), p. 057. DOI: 10.1088/1475-7516/2021/05/057. arXiv: 2005.05290 [astro-ph.IM].

[464] Antony Lewis and Sarah Bridle. "Cosmological parameters from CMB and other data: A Monte Carlo approach". In: *Phys. Rev. D* 66 (2002), p. 103511. DOI: 10.1103/PhysRevD.66.103511. arXiv: astro-ph/0205436.

[465] Antony Lewis. "Efficient sampling of fast and slow cosmological parameters". In: *Phys. Rev. D* 87.10 (2013), p. 103529. DOI: 10.1103/PhysRevD.87.103529. arXiv: 1304.4473 [astro-ph.CO].

[466] Andrew Gelman and Donald B. Rubin. "Inference from Iterative Simulation Using Multiple Sequences". In: *Statist. Sci.* 7 (1992), pp. 457–472. DOI: 10.1214/ss/1177011136.

[467] Antony Lewis. "GetDist: a Python package for analysing Monte Carlo samples". In: (Oct. 2019). arXiv: 1910.13970 [astro-ph.IM].

[468] Arianna Favale, Adrià Gómez-Valent, and Marina Migliaccio. "Cosmic chronometers to calibrate the ladders and measure the curvature of the Universe. A model-independent study". In: *Mon. Not. Roy. Astron. Soc.* 523.3 (2023), pp. 3406–3422. DOI: 10.1093/mnras/stad1621. arXiv: 2301.09591 [astro-ph.CO].

[469] Arianna Favale, Adrià Gómez-Valent, and Marina Migliaccio. "Revisiting model-independent constraints on spatial curvature and cosmic ladders calibration: updated and forecast analyses". In: (Nov. 2025). arXiv: 2511.19332 [astro-ph.CO].

[470] Will Sutherland. "On measuring the absolute scale of baryon acoustic oscillations". In: *Mon. Not. Roy. Astron. Soc.* 426 (2012), p. 1280. DOI: 10.1111/j.1365-2966.2012.21666.x. arXiv: 1205.0715 [astro-ph.CO].

[471] Suhail Dhawan, Justin Alsing, and Sunny Vagnozzi. "Non-parametric spatial curvature inference using late-Universe cosmological probes". In: *Mon. Not. Roy. Astron. Soc.* 506.1 (2021), pp. L1–L5. DOI: 10.1093/mnrasl/slab058. arXiv: 2104.02485 [astro-ph.CO].

[472] Kaituo Zhang et al. "Joint Constraints on the Hubble Constant, Spatial Curvature, and Sound Horizon from the Late-time Universe with Cosmography". In: *Astrophys. J.* 957.1 (2023), p. 5. DOI: 10.3847/1538-4357/acee6e. arXiv: 2310.16512 [astro-ph.CO].

[473] Jing-Zhao Qi et al. "Model-independent measurement of cosmic curvature with the latest H(z) and SNe Ia data: A comprehensive investigation". In: *Phys. Rev. D* 108.6 (2023), p. 063522. DOI: 10.1103/PhysRevD.108.063522. arXiv: 2302.08889 [astro-ph.CO].

[474] Jun-Qian Jiang et al. "Nonparametric late-time expansion history reconstruction and implications for the Hubble tension in light of recent DESI and type Ia supernovae data". In: *Phys. Rev. D* 110.12 (2024), p. 123519. DOI: 10.1103/PhysRevD.110.123519. arXiv: 2408.02365 [astro-ph.CO].

[475] Chris Clarkson, Bruce Bassett, and Teresa Hui-Ching Lu. "A general test of the Copernican Principle". In: *Phys. Rev. Lett.* 101 (2008), p. 011301. DOI: 10.1103/PhysRevLett.101.011301. arXiv: 0712.3457 [astro-ph].

[476] Yuting Liu et al. "Model-independent constraints on cosmic curvature: implication from updated Hubble diagram of high-redshift standard candles". In: *Astrophys. J.* 901.2 (2020), p. 129. DOI: 10.3847/1538-4357/abb0e4. arXiv: 2008.08378 [astro-ph.CO].

[477] David Benisty et al. "On the robustness of the constancy of the Supernova absolute magnitude: Non-parametric reconstruction & Bayesian approaches". In: *Phys. Dark Univ.* 39 (2023), p. 101160. DOI: 10.1016/j.dark.2022.101160. arXiv: 2202.04677 [astro-ph.CO].

[478] E. Tomasetti et al. "A new measurement of the expansion history of the Universe at z = 1.26 with cosmic chronometers in VANDELS". In: *Astron. Astrophys.* 679 (2023), A96. DOI: 10.1051/0004-6361/202346992. arXiv: 2305.16387 [astro-ph.CO].

[479] D. M. Scolnic et al. "The Complete Light-curve Sample of Spectroscopically Confirmed SNe Ia from Pan-STARRS1 and Cosmological Constraints from the Combined Pantheon Sample". In: *Astrophys. J.* 859.2 (2018), p. 101. DOI: 10.3847/1538-4357/aab9bb. arXiv: 1710.00845 [astro-ph.CO].

[480] Nicola Borghi, Michele Moresco, and Andrea Cimatti. "Toward a Better Understanding of Cosmic Chronometers: A New Measurement of H(z) at z $\sim$ 0.7". In: *Astrophys. J. Lett.* 928.1 (2022), p. L4. DOI: 10.3847/2041-8213/ac3fb2. arXiv: 2110.04304 [astro-ph.CO].

[481] Adrià Gómez-Valent. "Quantifying the evidence for the current speed-up of the Universe with low and intermediate-redshift data. A more model-independent approach". In: *JCAP* 05 (2019), p. 026. DOI: 10.1088/1475-7516/2019/05/026. arXiv: 1810.02278 [astro-ph.CO].

[482] M. P. Hobson, S. L. Bridle, and O. Lahav. "Combining cosmological datasets: hyperparameters and bayesian evidence". In: *Mon. Not. Roy. Astron. Soc.* 335 (2002), p. 377. DOI: 10.1046/j.1365-8711.2002.05614.x. arXiv: astro-ph/0203259.

[483] Louis Perenon et al. "Multi-tasking the growth of cosmological structures". In: *Phys. Dark Univ.* 34 (2021), p. 100898. DOI: 10.1016/j.dark.2021.100898. arXiv: 2105.01613 [astro-ph.CO].

[484] Louis Perenon et al. "Measuring dark energy with expansion and growth". In: *Phys. Dark Univ.* 37 (2022), p. 101119. DOI: 10.1016/j.dark.2022.101119. arXiv: 2206.12375 [astro-ph.CO].

[485] E. Camphuis et al. "SPT-3G D1: CMB temperature and polarization power spectra and cosmology from 2019 and 2020 observations of the SPT-3G Main field". In: *arXiv:2506.20707* (June 2025). arXiv: 2506.20707 [astro-ph.CO].

[486] Armando Bernui et al. "Exploring the H0 tension and the evidence for dark sector interactions from 2D BAO measurements". In: *Phys. Rev. D* 107.10 (2023), p. 103531. DOI: 10.1103/PhysRevD.107.103531. arXiv: 2301.06097 [astro-ph.CO].

[487] Özür Akarsu et al. "Λ_sCDM model: A promising scenario for alleviation of cosmological tensions". In: (July 2023). arXiv: 2307.10899 [astro-ph.CO].

[488] Luca Amendola and Miguel Quartin. "Measuring the Hubble function with standard candle clustering". In: *Mon. Not. Roy. Astron. Soc.* 504.3 (2021), pp. 3884–3889. DOI: 10.1093/mnras/stab887. arXiv: 1912.10255 [astro-ph.CO].

[489] Luca Amendola, Massimo Pietroni, and Miguel Quartin. "Fisher matrix for the one-loop galaxy power spectrum: measuring expansion and growth rates without assuming a cosmological model". In: *JCAP* 11 (2022), p. 023. DOI: 10.1088/1475-7516/2022/11/023. arXiv: 2205.00569 [astro-ph.CO].

[490] Michele Moresco et al. "Unveiling the Universe with emerging cosmological probes". In: *Living Rev. Rel.* 25.1 (2022), p. 6. DOI: 10.1007/s41114-022-00040-z. arXiv: 2201.07241 [astro-ph.CO].

[491] Alex G. Kim et al. "Effects of systematic uncertainties on the supernova determination of cosmologial parameters". In: *Mon. Not. Roy. Astron. Soc.* 347 (2004), pp. 909–920. DOI: 10.1111/j.1365-2966.2004.07260.x. arXiv: astro-ph/0304509.

[492] Isabela Matos et al. "A model-independent tripartite test of cosmic distance relations". In: *JCAP* 08 (2024), p. 007. DOI: 10.1088/1475-7516/2024/08/007. arXiv: 2311.17176 [astro-ph.CO].

[493] Yang Hu and Suhail Dhawan. "Constrain spatial curvature and dark energy with strong lenses and complementary probes: a forecast for next-generation surveys". In: *Mon. Not. Roy. Astron. Soc.* 535.4 (2024), pp. 3211–3217. DOI: 10.1093/mnras/stae2525. arXiv: 2411.05082 [astro-ph.CO].

[494] Luca Amendola, Marco Marinucci, and Miguel Quartin. "Cosmological Spatial Curvature with the Alcock-Paczyński Effect". In: *Phys. Rev. Lett.* 134.10 (2025), p. 101004. DOI: 10.1103/PhysRevLett.134.101004. arXiv: 2404.13124 [astro-ph.CO].

[495] Benjamin L'Huillier et al. "Litmus tests of the flat ΛCDM model and model-independent measurement of $H_0 r_d$ with LSST and DESI". In: *JCAP* 05 (2025), p. 030. DOI: 10.1088/1475-7516/2025/05/030. arXiv: 2407.07847 [astro-ph.CO].

[496] William Giarè et al. "A model-independent test of pre-recombination New Physics: Machine Learning based estimate of the Sound Horizon from Gravitational Wave Standard Sirens and the Baryon Acoustic Oscillation Angular Scale". In: (June 2024). arXiv: 2406.07493 [astro-ph.CO].

[497] Enis Belgacem et al. "Testing modified gravity at cosmological distances with LISA standard sirens". In: *JCAP* 07 (2019), p. 024. DOI: 10.1088/1475-7516/2019/07/024. arXiv: 1906.01593 [astro-ph.CO].

[498] Thomas Collett, Francesco Montanari, and Syksy Rasanen. "Model-Independent Determination of H_0 and Ω_{K0} from Strong Lensing and Type Ia Supernovae". In: *Phys. Rev. Lett.* 123.23 (2019), p. 231101. DOI: 10.1103/PhysRevLett.123.231101. arXiv: 1905.09781 [astro-ph.CO].

[499] Arianna Favale et al. "Towards a new model-independent calibration of Gamma-Ray Bursts". In: *JHEAp* 44 (2024), pp. 323–339. DOI: 10.1016/j.jheap.2024.10.010. arXiv: 2402.13115 [astro-ph.CO].

[500] An Kolmogorov. "Sulla determinazione empirica di una legge di distribuzione". In: *Giorn Dell'inst Ital Degli Att* 4 (1933), pp. 89–91.

[501] Nikolai V. Smirnov. "Estimate of deviation between empirical distribution functions in two independent samples." In: *Bulletin Moscow University* 2 (1939), pp. 3–16.

[502] T. W. Anderson and D. A. Darling. "Asymptotic theory of certain "goodness-of-fit" criteria based on stochastic processes". In: *Annals of Mathematical Statistics* 23 (1952), pp. 193–212.

[503] Maria Giovanna Dainotti, Michał Ostrowski, and Richard Willingale. "Towards a standard gamma-ray burst: tight correlations between the prompt and the afterglow plateau phase emission". In: *Monthly Notices of the Royal Astronomical Society* 418.4 (2011), pp. 2202–2206.

[504] Z. G. Dai and T. Lu. "Gamma-ray burst afterglows and evolution of postburst fireballs with energy injection from strongly magnetic millisecond pulsars". In: *Astron. Astrophys.* 333 (1998), p. L87. arXiv: astro-ph/9810402.

[505] Bing Zhang and Peter Meszaros. "Gamma-ray burst afterglow with continuous energy injection: Signature of a highly magnetized millisecond pulsar". In: *Astrophys. J. Lett.* 552 (2001), pp. L35–L38. DOI: 10.1086/320255. arXiv: astro-ph/0011133.

[506] F. Y. Wang et al. "Standardized Long Gamma-Ray Bursts as a Cosmic Distance Indicator". In: *Astrophys. J.* 924.2 (2022), p. 97. DOI: 10.3847/1538-4357/ac3755. arXiv: 2106.14155 [astro-ph.HE].

[507] K. G. Malmquist. "On some relations in stellar statistics". In: *Meddelanden fran Lunds Astronomiska Observatorium Serie I* 100 (Mar. 1922), pp. 1–52.

[508] Yang Liu et al. "Gamma-Ray Burst Constraints on Cosmological Models from the Improved Amati Correlation". In: *ApJ* 935.1 (2022), p. 7. ISSN: 0004-637X, 1538-4357. DOI: 10.3847/1538-4357/ac7de5. URL: https://iopscience.iop.org/article/10.3847/1538-4357/ac7de5 (visited on 07/07/2023).

[509] Anna Chiara Alfano et al. "Cosmological transition epoch from gamma-ray burst correlations". In: *JHEAp* 42 (2024), pp. 178–196. DOI: 10.1016/j.jheap.2024.05.002. arXiv: 2402.18967 [astro-ph.CO].

[510] J-L. Atteia, B. Cordier, and J. Wei. "The SVOM mission". In: *Int. J. Mod. Phys. D* 31.05 (2022), p. 2230008. DOI: 10.1142/S0218271822300087. arXiv: 2203.10962 [astro-ph.IM].

[511] L. Amati et al. "The THESEUS space mission: science goals, requirements and mission concept". In: *Exper. Astron.* 52.3 (2021), pp. 183–218. DOI: 10.1007/s10686-021-09807-8. arXiv: 2104.09531 [astro-ph.IM].

[512] M. G. Dainotti et al. "On the statistical assumption on the distance moduli of Supernovae Ia and its impact on the determination of cosmological parameters". In: *Journal of High Energy Astrophysics* 41 (Mar. 2024), pp. 30–41. DOI: 10.1016/j.jheap.2024.01.001.

[513] J. Singal et al. "On the Radio and Optical Luminosity Evolution of Quasars". In: *apj* 743.2, 104 (Dec. 2011), p. 104. DOI: 10.1088/0004-637X/743/2/104. arXiv: 1101.2930 [astro-ph.CO].

[514] J. Singal et al. "The Radio and Optical Luminosity Evolution of Quasars. II. The SDSS Sample". In: *apj* 764.1, 43 (Feb. 2013), p. 43. DOI: 10.1088/0004-637X/764/1/43. arXiv: 1207.3396 [astro-ph.CO].

[515] Maria Giovanna Dainotti et al. "Quasar Standardization: Overcoming Selection Biases and Redshift Evolution". In: *The Astrophysical Journal* 931.2 (2022), p. 106.

[516] Xiaolei Li et al. "Hubble diagram at higher redshifts: model independent calibration of quasars". In: *Mon. Not. Roy. Astron. Soc.* 507.1 (2021), pp. 919–926. DOI: 10.1093/mnras/stab2154. arXiv: 2103.16032 [astro-ph.CO].

[517] Xiaogang Zheng et al. "Multiple measurements of quasars acting as standard probes: model independent calibration and exploring the Dark Energy Equation of States". In: *Sci. China Phys. Mech. Astron.* 64.5 (2021), p. 259511. DOI: 10.1007/s11433-020-1664-9. arXiv: 2103.07139 [astro-ph.CO].

[518] Xiaolei Li, Ryan E. Keeley, and Arman Shafieloo. "Redshift Evolution of the X-Ray and Ultraviolet Luminosity Relation of Quasars: Calibrated Results from SNe Ia". In: *Astrophys. J.* 983.2 (2025), p. 141. DOI: 10.3847/1538-4357/adc2fe. arXiv: 2408.15547 [astro-ph.CO].

[519] Haixiang Zhang et al. "Constraints on cosmological models from quasars calibrated with type Ia supernova by a Gaussian process". In: *Mon. Not. Roy. Astron. Soc.* 530.4 (2024), pp. 4493–4500. DOI: 10.1093/mnras/stae1120. arXiv: 2404.15913 [astro-ph.CO].

[520] E. Sánchez et al. "Tracing The Sound Horizon Scale With Photometric Redshift Surveys". In: *Mon. Not. Roy. Astron. Soc.* 411 (2011), pp. 277–288. DOI: 10.1111/j.1365-2966.2010.17679.x. arXiv: 1006.3226 [astro-ph.CO].

[521] Rafael C. Nunes et al. "Cosmological parameter analyses using transversal BAO data". In: *Mon. Not. Roy. Astron. Soc.* 497.2 (2020), pp. 2133–2141. DOI: 10.1093/mnras/staa2036. arXiv: 2002.09293 [astro-ph.CO].

[522] Robert Tripp. "A two-parameter luminosity correction for Type IA supernovae". In: *aap* 331 (Mar. 1998), pp. 815–820.

[523] Leandros Perivolaropoulos and Foteini Skara. "Hubble tension or a transition of the Cepheid SnIa calibrator parameters?" In: *Phys. Rev. D* 104.12 (2021), p. 123511. DOI: 10.1103/PhysRevD.104.123511. arXiv: 2109.04406 [astro-ph.CO].

[524] Radosław Wojtak and Jens Hjorth. "Intrinsic tension in the supernova sector of the local Hubble constant measurement and its implications". In: *Mon. Not. Roy. Astron. Soc.* 515.2 (2022), pp. 2790–2799. DOI: 10.1093/mnras/stac1878. arXiv: 2206.08160 [astro-ph.CO].

[525] Radosław Wojtak, Jens Hjorth, and Jacob Osman Hjortlund. "Two-population Bayesian hierarchical model of Type Ia supernovae". In: *Mon. Not. Roy. Astron. Soc.* 525.4 (2023), pp. 5187–5203. DOI: 10.1093/mnras/stad2590. arXiv: 2302.01906 [astro-ph.SR].

[526] George Alestas, Lavrentios Kazantzidis, and Leandros Perivolaropoulos. "$w-M$ phantom transition at z_t <0.1 as a resolution of the Hubble tension". In: *Phys. Rev. D* 103.8 (2021), p. 083517. DOI: 10.1103/PhysRevD.103.083517. arXiv: 2012.13932 [astro-ph.CO].

[527] George Alestas et al. "Late-transition versus smooth $H(z)$-deformation models for the resolution of the Hubble crisis". In: *Phys. Rev. D* 105.6 (2022), p. 063538. DOI: 10.1103/PhysRevD.105.063538. arXiv: 2110.04336 [astro-ph.CO].

[528] Helion du Mas des Bourboux et al. "The Completed SDSS-IV Extended Baryon Oscillation Spectroscopic Survey: Baryon Acoustic Oscillations with Lyα Forests". In: *Astrophys. J.* 901.2 (2020), p. 153. DOI: 10.3847/1538-4357/abb085. arXiv: 2007.08995 [astro-ph.CO].

[529] A. A. Sen and Robert J. Scherrer. "The Weak Energy Condition and the Expansion History of the Universe". In: *Phys. Lett. B* 659 (2008), pp. 457–461. DOI: 10.1016/j.physletb.2007.11.070. arXiv: astro-ph/0703416.

[530] Luca Amendola. "Non-gaussian chi-squared method with the multivariate edgeworth expansion". In: *Astrophys. Lett. Commun.* 33 (1996), p. 63. arXiv: astro-ph/9810198.

[531] Lavinia Heisenberg, Hector Villarrubia-Rojo, and Jann Zosso. "Can late-time extensions solve the H0 and σ8 tensions?" In: *Phys. Rev. D* 106.4 (2022), p. 043503. DOI: 10.1103/PhysRevD.106.043503. arXiv: 2202.01202 [astro-ph.CO].

[532] Lavinia Heisenberg, Hector Villarrubia-Rojo, and Jann Zosso. "Simultaneously solving the H0 and σ8 tensions with late dark energy". In: *Phys. Dark Univ.* 39 (2023), p. 101163. DOI: 10.1016/j.dark.2022.101163. arXiv: 2201.11623 [astro-ph.CO].

[533] Eleonora Di Valentino, Ankan Mukherjee, and Anjan A. Sen. "Dark Energy with Phantom Crossing and the H_0 Tension". In: *Entropy* 23.4 (2021), p. 404. DOI: 10.3390/e23040404. arXiv: 2005.12587 [astro-ph.CO].

[534] Shahnawaz A. Adil et al. "Omnipotent dark energy: A phenomenological answer to the Hubble tension". In: (June 2023). arXiv: 2306.08046 [astro-ph.CO].

[535] Rene Andrae, Tim Schulze-Hartung, and Peter Melchior. "Dos and don'ts of reduced chi-squared". In: (Dec. 2010). arXiv: 1012.3754 [astro-ph.IM].

[536] Özgür Akarsu et al. "Graduated dark energy: Observational hints of a spontaneous sign switch in the cosmological constant". In: *Phys. Rev. D* 101.6 (2020), p. 063528. DOI: 10.1103/PhysRevD.101.063528. arXiv: 1912.08751 [astro-ph.CO].

[537] Adrià Gómez-Valent, Elahe Karimkhani, and Joan Solà. "Background history and cosmic perturbations for a general system of self-conserved dynamical dark energy and matter". In: *JCAP* 12 (2015), p. 048. DOI: 10.1088/1475-7516/2015/12/048. arXiv: 1509.03298 [gr-qc].

[538] Yijung Kang et al. "Early-type Host Galaxies of Type Ia Supernovae. II. Evidence for Luminosity Evolution in Supernova Cosmology". In: *Astrophys. J.* 889.1 (2020), p. 8. DOI: 10.3847/1538-4357/ab5afc. arXiv: 1912.04903 [astro-ph.GA].

[539] N. Nicolas et al. "Redshift evolution of the underlying type Ia supernova stretch distribution". In: *Astron. Astrophys.* 649 (2021), A74. DOI: 10.1051/0004-6361/202038447. arXiv: 2005.09441 [astro-ph.CO].

[540] Young-Wook Lee et al. "Evidence for strong progenitor age dependence of type Ia supernova luminosity standardization process". In: *Mon. Not. Roy. Astron. Soc.* 517.2 (2022), pp. 2697–2708. DOI: 10.1093/mnras/stac2840. arXiv: 2107.06288 [astro-ph.GA].

[541] Arianna Favale, Adrià Gómez-Valent, and Marina Migliaccio. "Quantification of 2D vs 3D BAO tension using SNIa as a redshift interpolator and test of the Etherington relation". In: *Phys. Lett. B* 858 (2024), p. 139027. DOI: 10.1016/j.physletb.2024.139027. arXiv: 2405.12142 [astro-ph.CO].

[542] Luis A. Anchordoqui et al. "From infinite to infinitesimal: Using the Universe as a dataset to probe Casimir corrections to the vacuum energy from fields inhabiting the dark dimension". In: (Apr. 2024). arXiv: 2404.17334 [astro-ph.CO].

[543] Seokcheon Lee. "The minimally extended Varying Speed of Light (meVSL)". In: *JCAP* 08 (2021), p. 054. DOI: 10.1088/1475-7516/2021/08/054. arXiv: 2011.09274 [astro-ph.CO].

[544] Rajendra P. Gupta. "JWST early Universe observations and ΛCDM cosmology". In: *Mon. Not. Roy. Astron. Soc.* 524.3 (2023), pp. 3385–3395. DOI: 10.1093/mnras/stad2032. arXiv: 2309.13100 [astro-ph.CO].

[545] Joerg Jaeckel and Andreas Ringwald. "The Low-Energy Frontier of Particle Physics". In: *Ann. Rev. Nucl. Part. Sci.* 60 (2010), pp. 405–437. DOI: 10.1146/annurev.nucl.012809.104433. arXiv: 1002.0329 [hep-ph].

[546] G. Carosi et al. "Probing the axion-photon coupling: phenomenological and experimental perspectives. A snowmass white paper". In: *Snowmass 2013: Snowmass on the Mississippi*. Sept. 2013. arXiv: 1309.7035 [hep-ph].

[547] Surhud More, Jo Bovy, and David W. Hogg. "Cosmic transparency: A test with the baryon acoustic feature and type Ia supernovae". In: *Astrophys. J.* 696 (2009), pp. 1727–1732. DOI: 10.1088/0004-637X/696/2/1727. arXiv: 0810.5553 [astro-ph].

[548] Remya Nair, Sanjay Jhingan, and Deepak Jain. "Cosmic distance duality and cosmic transparency". In: *JCAP* 12 (2012), p. 028. DOI: 10.1088/1475-7516/2012/12/028. arXiv: 1210.2642 [astro-ph.CO].

[549] Cong Ma and Pier-Stefano Corasaniti. "Statistical Test of Distance–Duality Relation with Type Ia Supernovae and Baryon Acoustic Oscillations". In: *Astrophys. J.* 861.2 (2018), p. 124. DOI: 10.3847/1538-4357/aac88f. arXiv: 1604.04631 [astro-ph.CO].

[550] M. Martinelli et al. "Euclid: Forecast constraints on the cosmic distance duality relation with complementary external probes". In: *Astron. Astrophys.* 644 (2020), A80. DOI: 10.1051/0004-6361/202039078. arXiv: 2007.16153 [astro-ph.CO].

[551] Anastasios Avgoustidis et al. "Constraints on cosmic opacity and beyond the standard model physics from cosmological distance measurements". In: *JCAP* 10 (2010), p. 024. DOI: 10.1088/1475-7516/2010/10/024. arXiv: 1004.2053 [astro-ph.CO].

[552] Liu Tonghua et al. "What are recent observations telling us in light of improved tests of distance duality relation?" In: *Phys. Lett. B* 838 (2023), p. 137687. DOI: 10.1016/j.physletb.2023.137687. arXiv: 2301.02997 [astro-ph.CO].

[553] Jin Qin, Fulvio Melia, and Tong-Jie Zhang. "Test of the cosmic distance duality relation for arbitrary spatial curvature". In: *Mon. Not. Roy. Astron. Soc.* 502.3 (2021), pp. 3500–3509. DOI: 10.1093/mnras/stab124. arXiv: 2101.05574 [astro-ph.CO].

[554] Jing-Zhao Qi et al. "Testing the Etherington distance duality relation at higher redshifts: Combined radio quasar and gravitational wave data". In: *Phys. Rev. D* 99.6 (2019), p. 063507. DOI: 10.1103/PhysRevD.99.063507. arXiv: 1902.01988 [astro-ph.CO].

[555] A. G. Adame et al. "DESI 2024 VI: cosmological constraints from the measurements of baryon acoustic oscillations". In: *JCAP* 02 (2025), p. 021. DOI: 10.1088/1475-7516/2025/02/021. arXiv: 2404.03002 [astro-ph.CO].

[556] Eoin Ó. Colgáin et al. "Does DESI 2024 Confirm ΛCDM?" In: (Apr. 2024). arXiv: 2404.08633 [astro-ph.CO].

[557] Youri Carloni, Orlando Luongo, and Marco Muccino. "Does dark energy really revive using DESI 2024 data?" In: (Apr. 2024). arXiv: 2404.12068 [astro-ph.CO].

[558] Deng Wang. "The Self-Consistency of DESI Analysis and Comment on "Does DESI 2024 Confirm ΛCDM?"" In: (Apr. 2024). arXiv: 2404.13833 [astro-ph.CO].

[559] Andrew R. Liddle and D. H. Lyth. *Cosmological inflation and large scale structure*. 2000. ISBN: 978-0-521-57598-0, 978-0-521-82849-9. DOI: 10.1017/CBO9781139175180.

[560] Adrian P. Schirra, Miguel Quartin, and Luca Amendola. "A model-independent measurement of the expansion and growth rates from BOSS using the FreePower method". In: (June 2024). arXiv: 2406.15347 [astro-ph.CO].

[561] Yo Toda, Adrià Gómez-Valent, and Kazuya Koyama. "Efficient compression of redshift-space distortion data for late-time modified gravity models". In: *JCAP* 12 (2024), p. 033. DOI: 10.1088/1475-7516/2024/12/033. arXiv: 2408.16388 [astro-ph.CO].

[562] Luca Amendola and Claudia Quercellini. "Skewness as a test of the equivalence principle". In: *Phys. Rev. Lett.* 92 (2004), p. 181102. DOI: 10.1103/PhysRevLett.92.181102. arXiv: astro-ph/0403019.

[563] Eric V. Linder. "Cosmic growth history and expansion history". In: *Phys. Rev. D* 72 (2005), p. 043529. DOI: 10.1103/PhysRevD.72.043529. arXiv: astro-ph/0507263.

[564] Julien Lesgourgues. "The Cosmic Linear Anisotropy Solving System (CLASS) I: Overview". In: (Apr. 2011). arXiv:1104.2932. arXiv: 1104.2932 [astro-ph.IM].

[565] Shadab Alam et al. "The clustering of galaxies in the completed SDSS-III Baryon Oscillation Spectroscopic Survey: cosmological analysis of the DR12 galaxy sample". In: *Mon. Not. Roy. Astron. Soc.* 470.3 (2017), pp. 2617–2652. DOI: 10.1093/mnras/stx721. arXiv: 1607.03155 [astro-ph.CO].

[566] Shadab Alam et al. "Completed SDSS-IV extended Baryon Oscillation Spectroscopic Survey: Cosmological implications from two decades of spectroscopic surveys at the Apache Point Observatory". In: *Phys. Rev. D* 103.8 (2021), p. 083533. DOI: 10.1103/PhysRevD.103.083533. arXiv: 2007.08991 [astro-ph.CO].

[567] A. G. Adame et al. "DESI 2024 IV: Baryon Acoustic Oscillations from the Lyman Alpha Forest". In: (Apr. 2024). arXiv: 2404.03001 [astro-ph.CO].

[568] Chan-Gyung Park, Javier de Cruz Pérez, and Bharat Ratra. "Using non-DESI data to confirm and strengthen the DESI 2024 spatially flat w0waCDM cosmological parametrization result". In: *Phys. Rev. D* 110.12 (2024), p. 123533. DOI: 10.1103/PhysRevD.110.123533. arXiv: 2405.00502 [astro-ph.CO].

[569] J. Colin Hill et al. "Early dark energy does not restore cosmological concordance". In: *Phys. Rev. D* 102.4 (2020), p. 043507. DOI: 10.1103/PhysRevD.102.043507. arXiv: 2003.07355 [astro-ph.CO].

[570] Rafaela Gsponer et al. "Cosmological constraints on early dark energy from the full shape analysis of eBOSS DR16". In: *Mon. Not. Roy. Astron. Soc.* 530.3 (2024), pp. 3075–3099. DOI: 10.1093/mnras/stae992. arXiv: 2312.01977 [astro-ph.CO].

[571] Laura Herold and Marc Kamionkowski. "Revisiting the impact of neutrino mass hierarchies on neutrino mass constraints in light of recent DESI data". In: *Phys. Rev. D* 111.8 (2025), p. 083518. DOI: 10.1103/PhysRevD.111.083518. arXiv: 2412.03546 [astro-ph.CO].

[572] Matteo Esposito et al. "Evolution mapping – II. Describing statistics of the non-linear cosmic velocity field". In: *Mon. Not. Roy. Astron. Soc.* 534.4 (2024), pp. 3906–3915. DOI: 10.1093/mnras/stae2351. arXiv: 2406.08539 [astro-ph.CO].

[573] M. Moresco et al. "Improved constraints on the expansion rate of the Universe up to z~1.1 from the spectroscopic evolution of cosmic chronometers". In: *JCAP* 08 (2012), p. 006. DOI: 10.1088/1475-7516/2012/08/006. arXiv: 1201.3609 [astro-ph.CO].

[574] Michele Moresco et al. "A 6% measurement of the Hubble parameter at $z \sim 0.45$: direct evidence of the epoch of cosmic re-acceleration". In: *JCAP* 05 (2016), p. 014. DOI: 10.1088/1475-7516/2016/05/014. arXiv: 1601.01701 [astro-ph.CO].

[575] G. Bruzual and Stephane Charlot. "Stellar population synthesis at the resolution of 2003". In: *Mon. Not. Roy. Astron. Soc.* 344 (2003), p. 1000. DOI: 10.1046/j.1365-8711.2003.06897.x. arXiv: astro-ph/0309134.

[576] Claudia Maraston and Gustav Stromback. "Stellar population models at high spectral resolution". In: *Mon. Not. Roy. Astron. Soc.* 418 (2011), p. 2785. DOI: 10.1111/j.1365-2966.2011.19738.x. arXiv: 1109.0543 [astro-ph.CO].

[577] Cong Zhang et al. "Four new observational $H(z)$ data from luminous red galaxies in the Sloan Digital Sky Survey data release seven". In: *Res. Astron. Astrophys.* 14.10 (2014), pp. 1221–1233. DOI: 10.1088/1674-4527/14/10/002. arXiv: 1207.4541 [astro-ph.CO].

[578] Daniel Stern et al. "Cosmic Chronometers: Constraining the Equation of State of Dark Energy. I: H(z) Measurements". In: *JCAP* 02 (2010), p. 008. DOI: 10.1088/1475-7516/2010/02/008. arXiv: 0907.3149 [astro-ph.CO].

[579] Raul Jimenez et al. "Constraints on the equation of state of dark energy and the Hubble constant from stellar ages and the CMB". In: *Astrophys. J.* 593 (2003), pp. 622–629. DOI: 10.1086/376595. arXiv: astro-ph/0302560.

[580] Joan Simon, Licia Verde, and Raul Jimenez. "Constraints on the redshift dependence of the dark energy potential". In: *Phys. Rev. D* 71 (2005), p. 123001. DOI: 10.1103/PhysRevD.71.123001. arXiv: astro-ph/0412269.

[581] Michele Moresco. "Raising the bar: new constraints on the Hubble parameter with cosmic chronometers at z $\sim$ 2". In: *Mon. Not. Roy. Astron. Soc.* 450.1 (2015), pp. L16–L20. DOI: 10.1093/mnrasl/slv037. arXiv: 1503.01116 [astro-ph.CO].

[582] A.L. Ratsimbazafy et al. "Age-dating Luminous Red Galaxies observed with the Southern African Large Telescope". In: *Mon. Not. Roy. Astron. Soc.* 467.3 (2017), pp. 3239–3254. DOI: 10.1093/mnras/stx301. arXiv: 1702.00418 [astro-ph.CO].

[583] Paul Carter et al. "Low redshift baryon acoustic oscillation measurement from the reconstructed 6-degree field galaxy survey". In: *Monthly Notices of the Royal Astronomical Society* 481.2 (2018), pp. 2371–2383. DOI: 10.1093/mnras/sty2405. URL: https://doi.org/10.1093%2Fmnras%2Fsty2405.

[584] Eyal A. Kazin et al. "The WiggleZ Dark Energy Survey: improved distance measurements to z∼1 with reconstruction of the baryonic acoustic feature". In: *Monthly Notices of the Royal Astronomical Society* 441.4 (2014), pp. 3524–3542. DOI: 10.1093/mnras/stu778. URL: https://doi.org/10.1093/mnras/stu778.

[585] Héctor Gil-Marín et al. "The clustering of galaxies in the SDSS-III Baryon Oscillation Spectroscopic Survey: RSD measurement from the power spectrum and bispectrum of the DR12 BOSS galaxies". In: *Monthly Notices of the Royal Astronomical Society* 465.2 (2016), pp. 1757–1788. DOI: 10.1093/mnras/stw2679. URL: https://doi.org/10.1093%2Fmnras%2Fstw2679.

[586] P.B. Abbott et al. "Dark Energy Survey Year 3 results: A 2.7% measurement of baryon acoustic oscillation distance scale at redshift 0.835". In: *Physical Review D* 105.4 (2022). DOI: 10.1103/physrevd.105.043512. URL: https://doi.org/10.1103%2Fphysrevd.105.043512.

[587] Richard Neveux et al. "The completed SDSS-IV extended Baryon Oscillation Spectroscopic Survey: BAO and RSD measurements from the anisotropic power spectrum of the quasar sample between redshift 0.8 and 2.2". In: *Monthly Notices of the Royal Astronomical Society* 499.1 (2020), pp. 210–229. DOI: 10.1093/mnras/staa2780. URL: https://doi.org/10.1093%2Fmnras%2Fstaa2780.

[588] Jiamin Hou et al. "The completed SDSS-IV extended Baryon Oscillation Spectroscopic Survey: BAO and RSD measurements from anisotropic clustering analysis of the quasar sample in configuration space between redshift 0.8 and 2.2". In: *Monthly Notices of the Royal Astronomical Society* 500.1 (2020), pp. 1201–1221. DOI: 10.1093/mnras/staa3234. URL: https://doi.org/10.1093/mnras/staa3234.

[589] Jiamin Hou et al. "The Completed SDSS-IV extended Baryon Oscillation Spectroscopic Survey: BAO and RSD measurements from anisotropic clustering analysis of the Quasar Sample in configuration space between redshift 0.8 and 2.2". In: *Mon. Not. Roy. Astron. Soc.* 500.1 (2020), pp. 1201–1221. DOI: 10.1093/mnras/staa3234. arXiv: 2007.08998 [astro-ph.CO].

[590] T. M. C. Abbott et al. "Dark Energy Survey: A 2.1% measurement of the angular Baryonic Acoustic Oscillation scale at redshift $z_{\rm eff}$=0.85 from the final dataset". In: (Feb. 2024). arXiv: 2402.10696 [astro-ph.CO].

[591] G. C. Carvalho et al. "Baryon Acoustic Oscillations from the SDSS DR10 galaxies angular correlation function". In: *Phys. Rev. D* 93.2 (2016), p. 023530. DOI: 10.1103/PhysRevD.93.023530. arXiv: 1507.08972 [astro-ph.CO].

[592] G. C. Carvalho et al. "The transverse baryonic acoustic scale from the SDSS DR11 galaxies". In: *Astropart. Phys.* 119 (2020), p. 102432. DOI: 10.1016/j.astropartphys.2020.102432. arXiv: 1709.00271 [astro-ph.CO].

[593] Amy Lien et al. "The Third Swift Burst Alert Telescope Gamma-Ray Burst Catalog". In: *Astrophys. J.* 829.1 (2016), p. 7. DOI: 10.3847/0004-637X/829/1/7. arXiv: 1606.01956 [astro-ph.HE].

Appendices

Appendix A

Data sets

In this Appendix, we list some of the relevant data sets employed in this thesis. For a comprehensive discussion of these observables, the reader is referred to Chapter 4.

Table A.1. In this table, we present the CCH data points used in this thesis, with the corresponding references. All the uncertainties are evaluated at 68% C.L. and, in the case of Refs. [573, 574], the central values of $H(z)$ are computed by performing the arithmetic mean of the measurements obtained with the BC03 [575] and MaStro [576] SPS models. In all the analyses presented in this thesis, we also incorporate the existing correlations between different measurements through the covariance matrix from [392].

z	$H(z)$ [Km/s/Mpc]	Ref.	z	$H(z)$ [Km/s/Mpc]	Ref.
0.07	69.0 ± 19.6	[577]	0.48	97.0 ± 62.0	[578]
0.09	69.0 ± 12.0	[579]	0.5929	107.0 ± 15.5	[573]
0.12	68.6 ± 26.2	[577]	0.6797	95.0 ± 10.5	[573]
0.17	83.0 ± 8.0	[580]	0.75	98.8 ± 33.6	[480]
0.1791	78.0 ± 6.2	[573]	0.7812	96.5 ± 12.5	[573]
0.1993	78.0 ± 6.9	[573]	0.8754	124.5 ± 17.4	[573]
0.2	72.9 ± 29.6	[577]	0.88	90.0 ± 40.0	[578]
0.27	77.0 ± 14.0	[580]	0.9	117.0 ± 23.0	[580]
0.28	88.8 ± 36.6	[577]	1.037	133.5 ± 17.6	[573]
0.3519	85.5 ± 15.7	[573]	1.26	135.0 ± 65.0	[478]
0.3802	86.2 ± 14.6	[574]	1.3	168.0 ± 17.0	[580]
0.4	95.0 ± 17.0	[580]	1.363	160.0 ± 33.6	[581]
0.4004	79.9 ± 11.4	[574]	1.43	177.0 ± 18.0	[580]
0.4247	90.4 ± 12.8	[574]	1.53	140.0 ± 14.0	[580]
0.4497	96.3 ± 14.4	[574]	1.75	202.0 ± 40.0	[580]
0.47	89.0 ± 49.6	[582]	1.965	186.5 ± 50.4	[581]
0.4783	83.8 ± 10.2	[574]			

Table A.2. List with the 11 BAO data points used in the analysis of Chapters 6 and 9. The fiducial values of the comoving sound horizon appearing in the third column are $r_d^{fid} = 147.5$ Mpc for [583] and $r_d^{fid} = 148.6$ Mpc for [584]. We have duly taken into account the existing correlations between the data points of WiggleZ, BOSS DR12 and eBOSS DR16.

Survey	z	Observable	Measurement	Ref.
6dFGS+SDSS MGS	0.122	$D_V(r_d^{fid}/r_d)$	539 ± 17 [Mpc]	[583]
WiggleZ	0.44	$D_V(r_d^{fid}/r_d)$	1716.4 ± 83.1 [Mpc]	[584]
	0.60	$D_V(r_d^{fid}/r_d)$	2220.8 ± 100.6 [Mpc]	
	0.73	$D_V(r_d^{fid}/r_d)$	2516.1 ± 86.1 [Mpc]	
BOSS DR12	0.32	$r_d H/(10^3 km/s)$	11.549 ± 0.385	[585]
		D_A/r_d	6.5986 ± 0.1337	
	0.57	$r_d H/(10^3 km/s)$	14.021 ± 0.225	
		D_A/r_d	9.389 ± 0.103	
DES Y3	0.835	D_M/r_d	18.92 ± 0.51	[586]
eBOSS DR16	1.48	D_M/r_d	30.21 ± 0.79	[587]
		$c/r_d H$	13.23 ± 0.47	[588]

Table A.3. List with the anisotropic BAO data points used in Chapter 10. See the quoted references for details. We use two alternative 3D BAO data sets, one containing the BOSS/eBOSS data points and another one with the DESI Y1 data.

Survey	z	D_A/r_d	Ref.
BOSS DR12	0.32	6.5986 ± 0.1337	[585]
	0.57	9.389 ± 0.103	
eBOSS DR16Q	1.48	12.18 ± 0.32	[589]
Lyα-F eBOSS DR16	2.334	$11.25^{+0.36}_{-0.33}$	[528]
LRG1 DESI Y1	0.51	9.02 ± 0.17	[300]
LRG2 DESI Y1	0.71	9.85 ± 0.19	[300]
LRG3+ELG1 DESI Y1	0.93	11.25 ± 0.16	[300]
ELG2 DESI Y1	1.32	11.98 ± 0.30	[300]
Lyα-F DESI Y1	2.33	11.92 ± 0.29	[567]

Table A.4. List with the 16 2D BAO data points used in Sec. 6.3.2 and in Chapters 9 and 10. Here, $\theta_{\rm BAO}(z)\,[{\rm rad}] = r_d/[(1+z)D_A(z)]$. The 2D BAO data point of DES Y6 has been computed using the values of $\alpha = (D_A/r_d)/(D_A/r_d)|_{\rm Planck}$ extracted with the angular correlation function (ACF) and the angular power spectrum (APS) methods, which read $\alpha_{\rm ACF} = 0.952 \pm 0.023$ and $\alpha_{\rm APS} = 0.962 \pm 0.022$, respectively, with a Pearson correlation coefficient $\rho = 0.863$ [590]. We have considered the full covariance matrix in the weighted average computation of the central value and the uncertainty. See the quoted references for further details.

Survey	z	θ_{BAO} [deg]	Ref.
SSDS DR12	0.11	19.8 ± 3.26	[420]
SDSS DR7	0.235	9.06 ± 0.23	[421]
	0.365	6.33 ± 0.22	
SDSS DR10	0.45	4.77 ± 0.17	[591]
	0.47	5.02 ± 0.25	
	0.49	4.99 ± 0.21	
	0.51	4.81 ± 0.17	
	0.53	4.29 ± 0.30	
	0.55	4.25 ± 0.25	
SDSS DR11	0.57	4.59 ± 0.36	[592]
	0.59	4.39 ± 0.33	
	0.61	3.85 ± 0.31	
	0.63	3.90 ± 0.43	
	0.65	3.55 ± 0.16	
DES Y6	0.85	2.932 ± 0.068	[590]
BOSS DR12Q	2.225	1.77 ± 0.31	[422]

Table A.5. Sub-sample of the 20 GRBs from the Platinum data set [431] used in the calibration of the 3D and 2D Dainotti relations (see Chapter 7). T_X^* has units of s, while the fluxes $F_{\rm peak}$ and $F_{\rm X}$ are given in $erg\ cm^{-2}\ s^{-1}$. The K-corrections are dimensionless. All the quantities are given with the associated 1σ error. These GRBs are provided by the *third Swift GRB Catalog* [593], except for the 091018 and 131105A GRBs, which are from the *Swift BAT burst analyser* [440]. We refer the reader to Table A1 of [151] for the remaining GRBs of the Platinum sample.

ID	z	$\log T_X^*$	$F_{\rm peak}$	$K_{\rm prompt}$	$\log F_X$	$K_{\rm plateau}$
070521	0.553	3.361 ± 0.048	$(8.71 \pm 1.20)e-08$	0.662 ± 0.053	-10.012 ± 0.049	0.991 ± 0.175
080430	0.767	3.970 ± 0.038	$(1.82 \pm 0.08)e-07$	0.868 ± 0.036	-11.172 ± 0.028	3.459 ± 2.059
151027A	0.810	3.741 ± 0.017	$(5.82 \pm 0.29)e-07$	0.637 ± 0.031	-9.935 ± 0.022	0.956 ± 0.021
070508	0.820	2.765 ± 0.012	$(2.24 \pm 0.03)e-06$	0.570 ± 0.032	-9.161 ± 0.011	0.868 ± 0.012
060814	0.840	3.959 ± 0.035	$(6.06 \pm 0.15)e-07$	0.653 ± 0.016	-10.911 ± 0.035	0.982 ± 0.036
140506A	0.889	3.031 ± 0.069	$(8.67 \pm 0.46)e-07$	0.664 ± 0.105	-9.904 ± 0.055	0.938 ± 0.136
091018	0.971	2.602 ± 0.034	$(5.91 \pm 0.12)e-07$	1.140 ± 0.030	-9.627 ± 0.024	0.941 ± 0.041
131030A	1.290	2.486 ± 0.028	$(2.65 \pm 0.05)e-06$	0.416 ± 0.041	-9.294 ± 0.025	0.775 ± 0.017
061121	1.314	3.423 ± 0.017	$(1.96 \pm 0.02)e-06$	0.451 ± 0.008	-10.030 ± 0.013	0.958 ± 0.037
150910A	1.360	3.481 ± 0.029	$(8.28 \pm 2.18)e-08$	0.632 ± 0.309	-9.971 ± 0.704	0.750 ± 0.037
110213A	1.460	3.450 ± 0.024	$(7.15 \pm 1.88)e-08$	2.100 ± 0.903	-9.897 ± 0.036	1.187 ± 0.295
060418	1.490	2.723 ± 0.057	$(4.99 \pm 0.16)e-07$	0.633 ± 0.031	-9.793 ± 0.049	0.982 ± 0.122
070306	1.496	4.472 ± 0.028	$(2.01 \pm 0.09)e-07$	0.639 ± 0.408	-11.274 ± 0.034	0.857 ± 0.040
090418A	1.608	3.112 ± 0.031	$(1.58 \pm 0.17)e-07$	0.508 ± 0.082	-10.047 ± 0.029	0.981 ± 0.083
131105A	1.686	3.520 ± 0.048	$(2.68 \pm 0.02)e-07$	0.582 ± 0.064	-10.911 ± 0.033	0.942 ± 0.093
091020	1.710	2.520 ± 0.045	$(3.64 \pm 0.17)e-07$	0.443 ± 0.033	-9.713 ± 0.034	0.901 ± 0.067
150314A	1.758	2.052 ± 0.016	$(3.81 \pm 0.06)e-06$	0.297 ± 0.033	-8.610 ± 0.015	0.760 ± 0.015
190106A	1.860	3.735 ± 0.031	$(3.36 \pm 0.13)e-07$	0.614 ± 0.073	-10.432 ± 0.029	2.675 ± 2.089
060708	1.920	3.040 ± 0.063	$(6.89 \pm 0.80)e-08$	0.467 ± 0.563	-10.869 ± 0.061	1.682 ± 0.803
160121A	1.960	3.353 ± 0.120	$(7.79 \pm 0.82)e-08$	0.822 ± 0.136	-11.173 ± 0.069	1.022 ± 0.161

Appendix B

Fit of the posteriors for forecast analysis in Chapter 6

As mentioned in Sec. 6.3.3, in the context of the forecast analysis, it may happen to have only a limited number of N realizations of $H(z)$ that can be computed to obtain Eq. 6.8, as a consequence of long runtime requirements. This yields the corresponding distributions for M, Ω_k and r_d to have some degree of noise. We smooth it out by fitting a skew-normal probability density function (PDF) to the one-dimensional posterior probability for each parameter. The choice of this particular function lies in the typical shape of the posteriors observed in both the analysis with current data in Secs. 6.3.1-6.3.2 (see, e.g., Fig. 6.10). The skewed-normal function accounts for small deviations from the Gaussian distribution, i.e. for skewness $\neq 0$. The PDF of this distribution takes the form:

$$f(x;\alpha,\nu,\delta) = \frac{2}{\delta}\cdot\phi\Big(\frac{x-\nu}{\delta}\Big)\cdot\Phi\Big(\alpha\cdot\frac{x-\nu}{\delta}\Big)\,, \tag{B.1}$$

where $\phi(x)$ is the standard normal PDF and $\Phi(x)$ its cumulative density function. The distribution is characterised by the triad (α,ν,δ), which are related, respectively, to the shape (skewness), location and scale parameters. When $\alpha = 0$, one recovers the normal distribution. We obtain $-1.7 < \alpha < 1.9$ for all the cases under study, positive or negative depending on whether we have a left- or right-skewed density function. As expected, these values of α point to only a mild deviation from the Gaussian distribution, with the effect being more pronounced in the posteriors of M and Ω_k, which also show some degree of mutual correlation (see again Fig. 6.10). Indeed, considering the CCH+BAO analysis, we always find $\alpha < 1.2$, whereas for the 3D joint analyses $\alpha < 1$. We report one example of this fit in Fig. B.1.

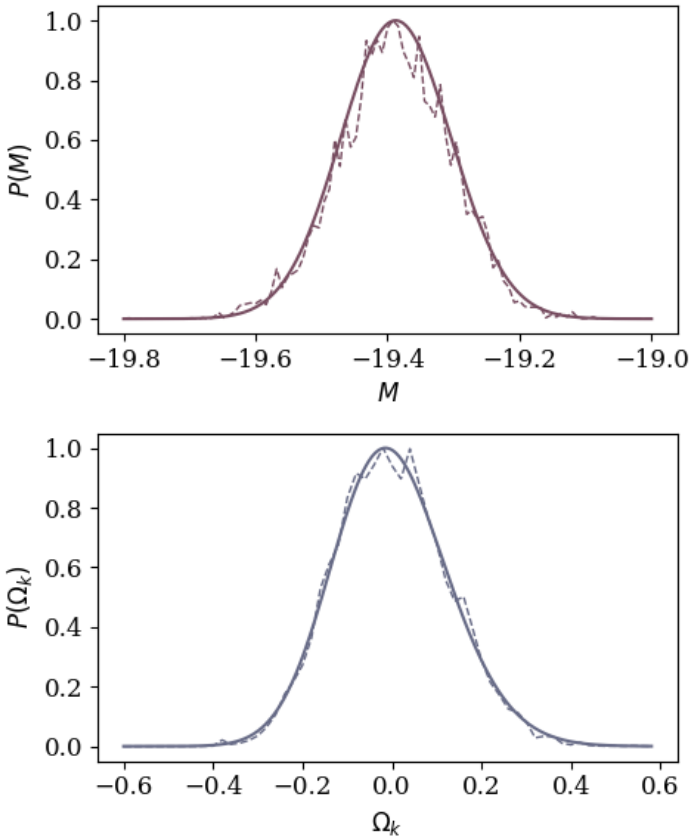

Figure B.1. Example of the application of the skewed-normal fit (solid lines) on the noisy posteriors (dashed lines) for M and Ω_k from the 2D joint analysis with $\mathrm{LSST_{opt}}$ + $\mathrm{CCH^*_{pes}}$. In this case, we obtain $\alpha_M = -1.09$ and $\alpha_{\Omega_k} = 1.16$.

Appendix C

Triangle plots for analysis in Chapter 9

We devote this Section to show the one-dimensional posterior distributions and two-dimensional contour plots of the fitting parameters $\{\tilde{\Omega}_m, \tilde{H}_0, H_0, z_p, \delta H_p\}$ and the transition redshift z_t obtained from the analyses of the Baseline_3D and Baseline_2D data sets in Figs. C.1 and C.2, respectively, presented in Chapter 9. For completeness, in Table C.1 we provide all the mean values and 68% C.L. uncertainties. As discussed in the main text, the constraints on $\tilde{\Omega}_m$ and $\tilde{H}_0$ are driven by the *Planck*/ΛCDM prior, while the constraint on H_0 is essentially fixed by the SH0ES prior. Conversely, the results for δH_p and z_p (and z_t) depend on the data set under study, and we find in both cases, as expected, a strong positive correlation between z_t and z_p and an anti-correlation between z_p and δH_p.

Table C.1. Mean values and 68% C.L. errors for the main and derived parameters obtained from the analyses with Baseline_3D and Baseline_2D. The upper bounds, instead, are given at 95% C.L. In the last two rows we report the best-fit χ^2 and the corresponding p-values. The number of degrees of freedom is 12 and 14 in the Baseline_3D and Baseline_2D analyses, respectively.

Parameter	Baseline_3D	Baseline_2D
$\tilde{\Omega}_m$	$0.305^{+0.004}_{-0.005}$	$0.313^{+0.008}_{-0.007}$
$\tilde{H}_0$ [km/s/Mpc]	$68.11^{+0.34}_{-0.29}$	$67.51^{+0.55}_{-0.49}$
H_0 [km/s/Mpc]	72.90 ± 1.10	$73.97^{+0.76}_{-0.69}$
δH_p [km/s/Mpc]	$0.08^{+0.58}_{-0.40}$	$-8.90^{+2.20}_{-2.60}$
z_p	< 0.41	$3.07^{+0.87}_{-0.44}$
z_t	< 0.17	$0.66^{+0.07}_{-0.04}$
$\chi^2_{\rm min}$	16.14	16.69
p-value	0.21	0.38

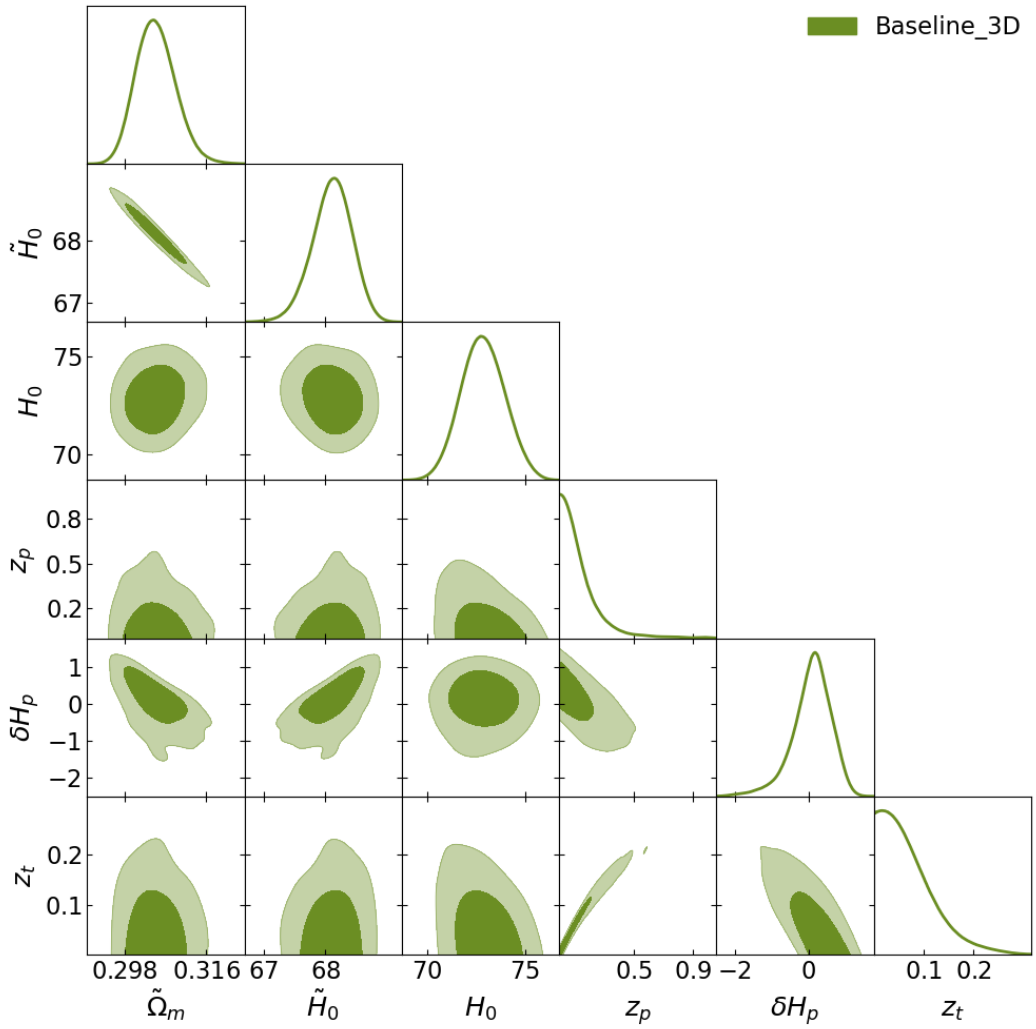

Figure C.1. Triangle plot with the constraints obtained for the various fitting parameters entering the Baseline_3D analysis and the derived parameter z_t, setting $z_{\max} = 1$. The triad $\{\tilde{H}_0, H_0, \delta H_p\}$ is given in units of km/s/Mpc. Contours contain 68% and 95% of the probability.

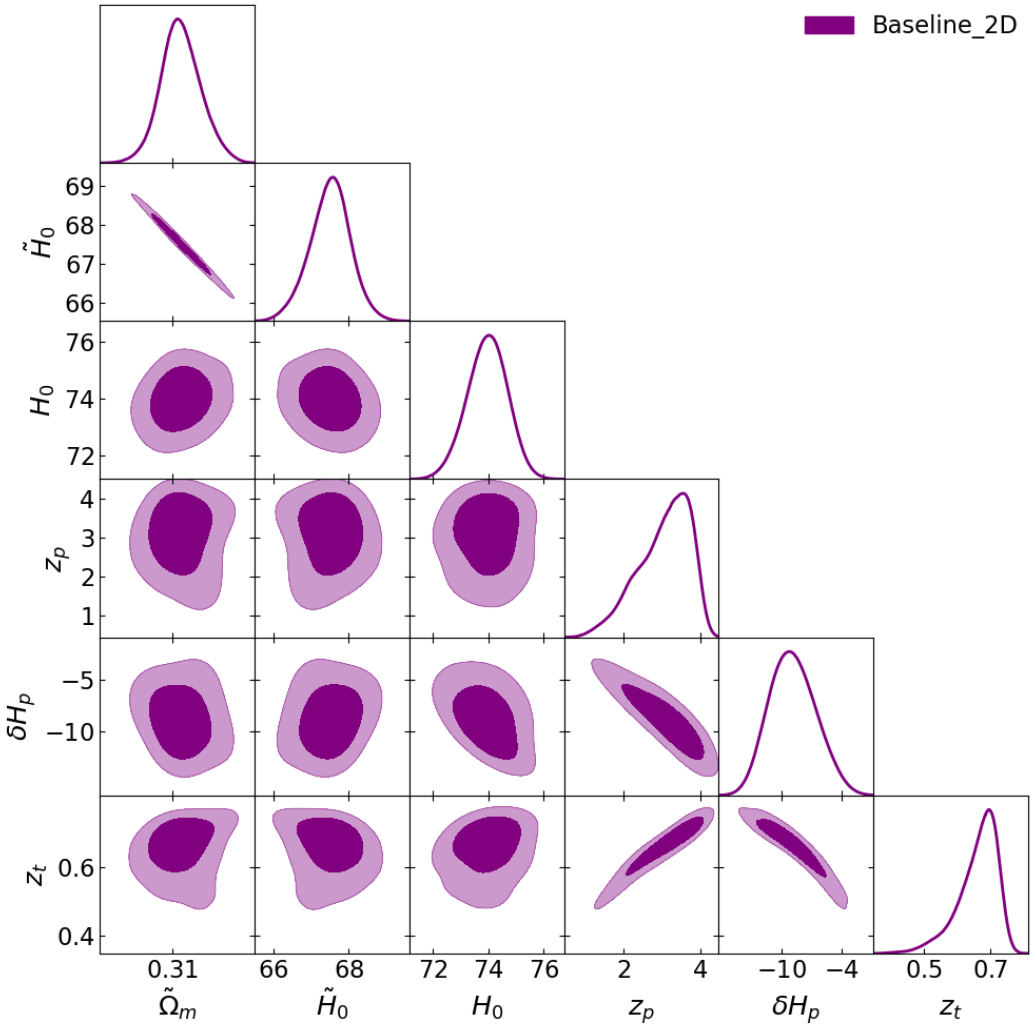

Figure C.2. Same as in Fig. C.1, but for the Baseline_2D analysis, with $z_{\max} = 4$.

Triangle plots for analysis in Chapter 11

In this Section, we present the one-dimensional posterior distributions and two-dimensional contour plots of all the fitting parameters in the five different cosmological models listed in Sec. 11.1.2. This complements the analysis presented in Chapter 11.

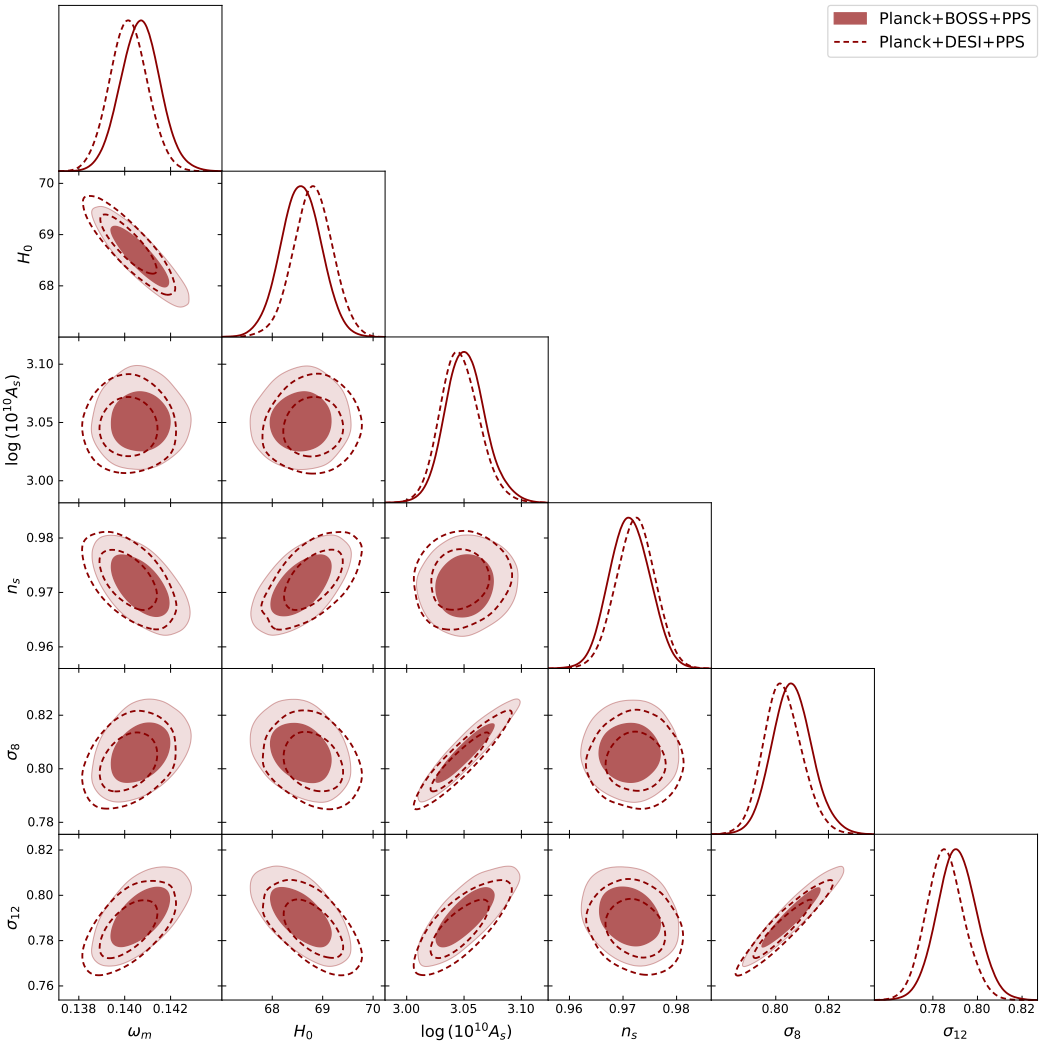

Figure C.3. Triangle plot for ΛCDM obtained from the fitting analysis with Planck+BOSS+PPS (solid contours) and Planck+DESI+PPS (dashed contours). The parameter $\omega_m = \Omega_m^0 h^2$ is the sum of the baryon and CDM reduced density parameters, ω_b and ω_{cdm} respectively. The results for σ_8 and σ_{12} are those computed at $z = 0$.

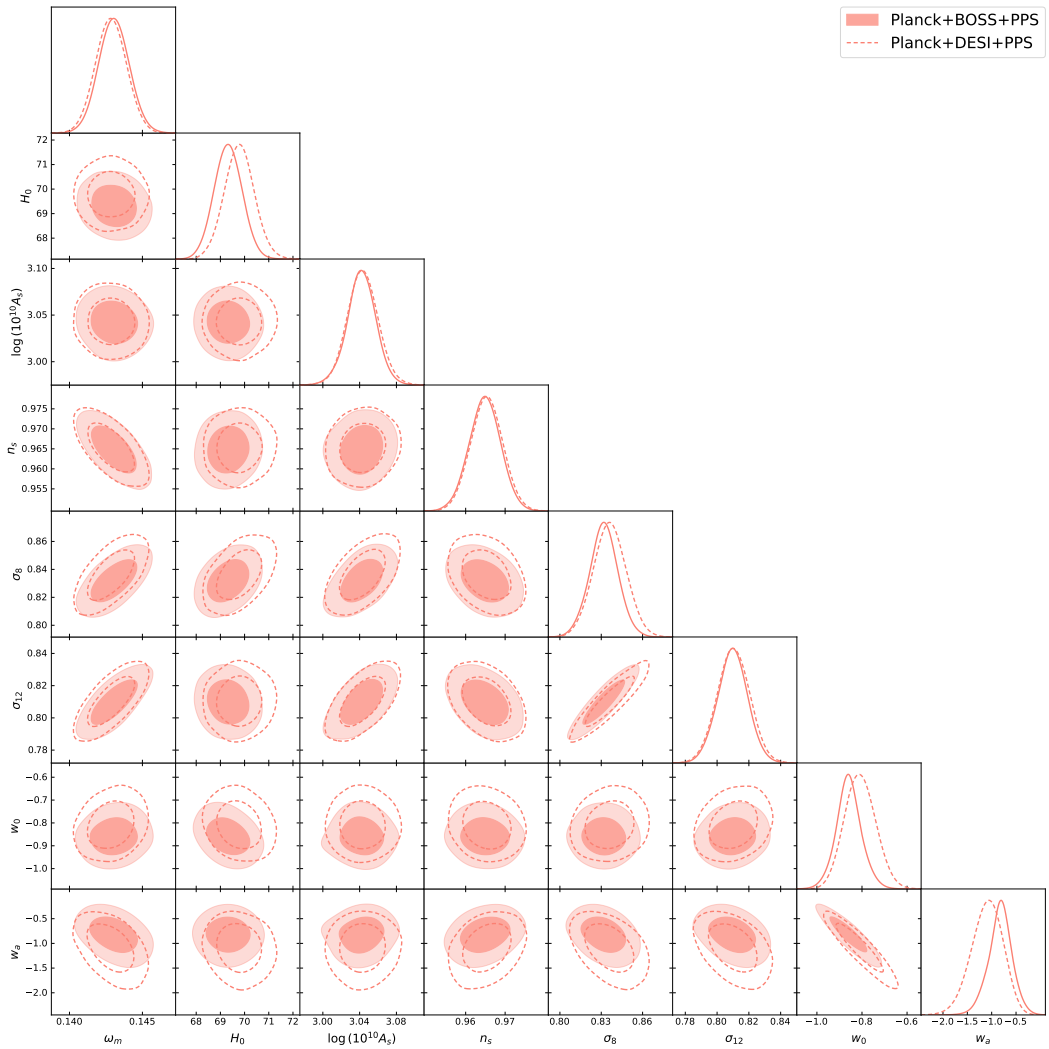

Figure C.4. Same as in Fig. C.3 but for w_0w_aCDM.

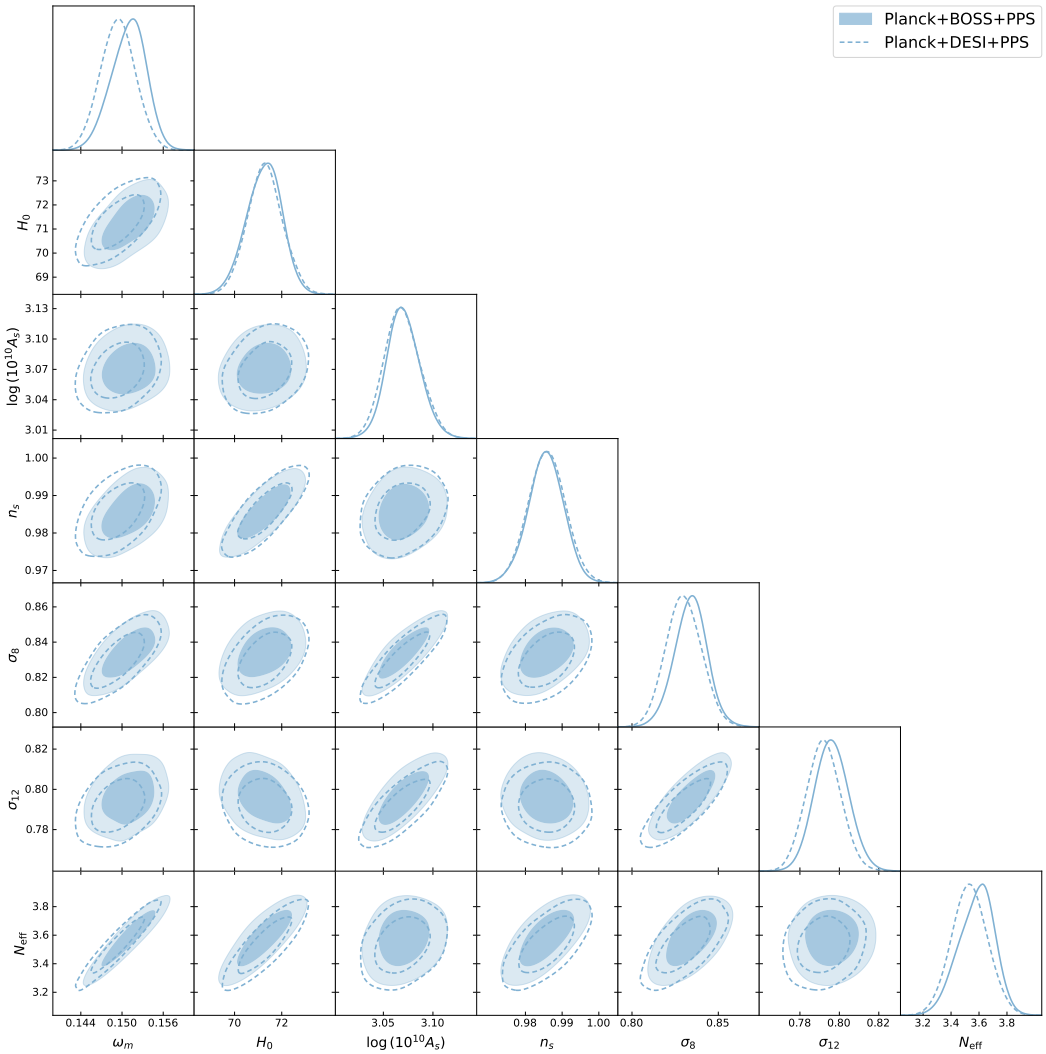

Figure C.5. ame as in Fig. C.3 but for ΛCDM+$N_{\rm eff}$.

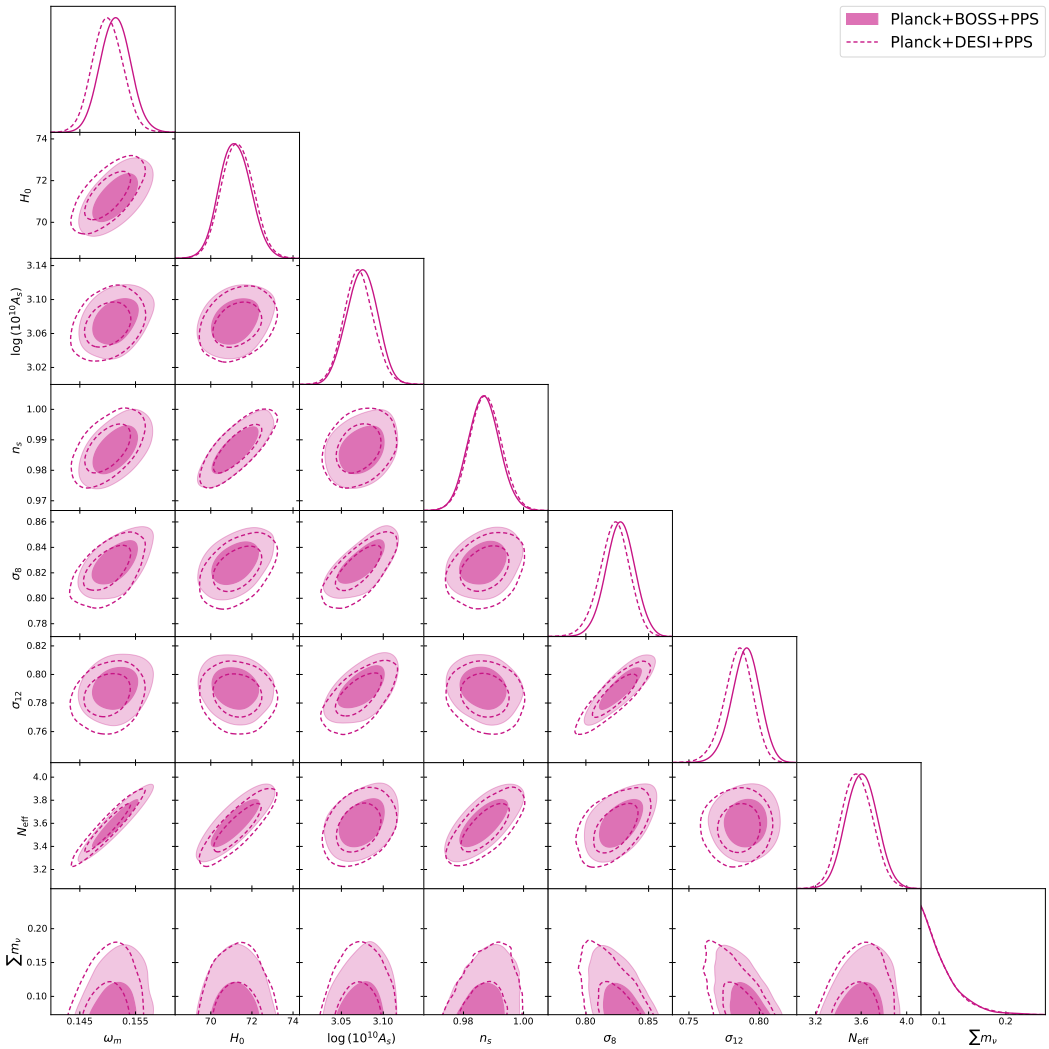

Figure C.6. ame as in Fig. C.3 but for ΛCDM+$N_{\rm eff} + \Sigma m_\nu$.

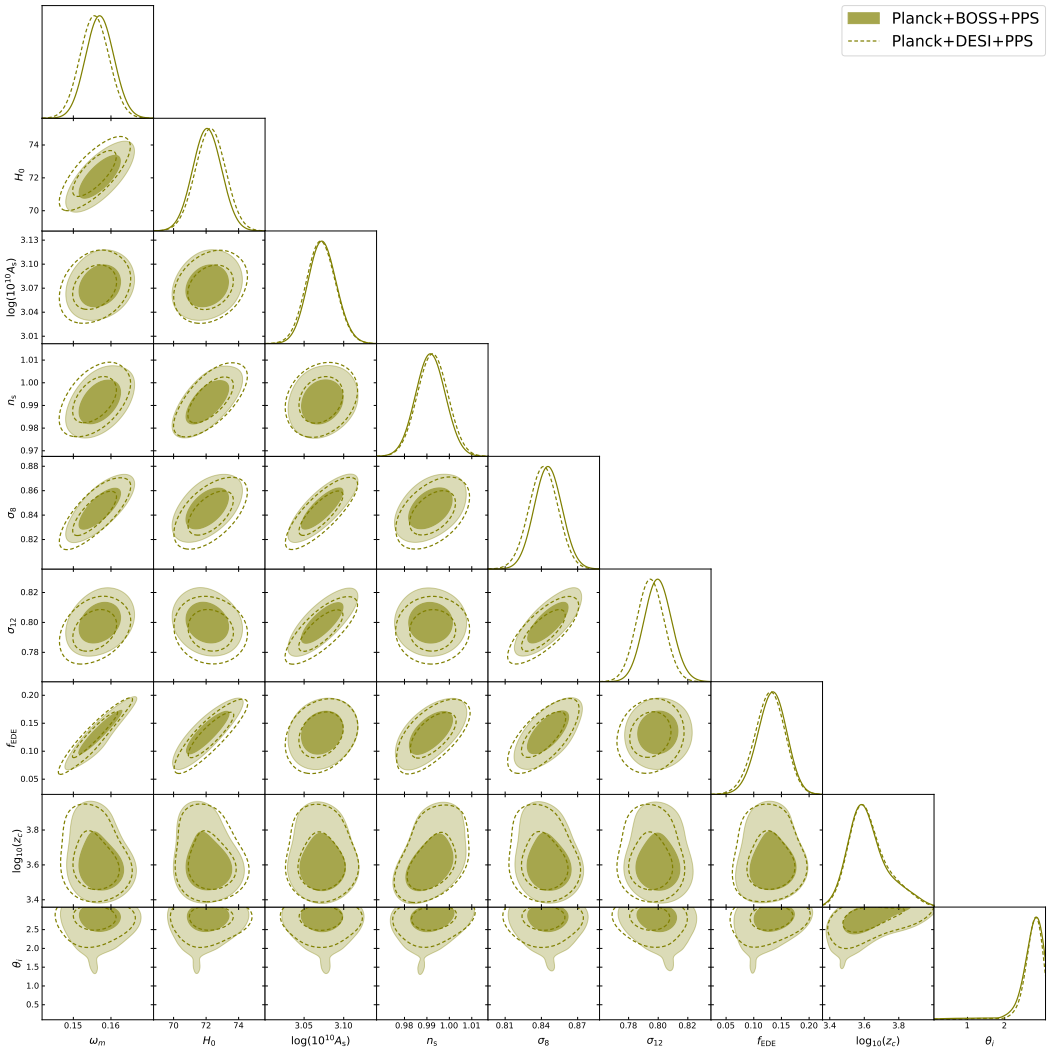

Figure C.7. Same as in Fig. C.3 but for EDE.

List of Figures

1.1 Homogeneous and isotropic two-dimensional surfaces 11
1.2 SNIa observations that led to the discovery of an accelerating Universe 15
1.3 The cosmic history 17
1.4 CMB black-body spectrum 23
1.5 CMB intensity anisotropies observed by Planck 24
1.6 Planck 2018 TT angular power spectrum 29

2.1 The Hubble law (1929) 35
2.2 A visual representation of the local distance ladder 36
2.3 Three-rungs local distance ladder by the SH0ES collaboration 38
2.4 Example of BAO signal in power spectrum and correlation function 44

3.1 Review of H_0 measurements 50
3.2 Calibrators degeneracy band 51
3.3 An example to understand the bias introduced by σ_8 55
3.4 Alternative theories to ΛCDM 59

4.1 CCH data 67
4.2 2D and 3D BAO measurements of $\theta(z)$ 73
4.3 GRBs fundamental plane for the Platinum sample 78

6.1 Histograms of the $\tilde{\chi}^2_\mu$ for the GP reconstruction of $H(z)$ with different kernels 100
6.2 GP reconstruction of $H(z)$ and $m(z)$ 101
6.3 Testing $M(z)$ 103
6.4 Testing $\Omega_k(z)$ 105
6.5 Testing internal consistency of the 3D BAO data 106
6.6 Dependence of $\bar{M}$ and $\bar{r}_d$ on the prior value of Ω_k 106
6.7 Results on (M, Ω_k, r_d) with baseline data sets 109
6.8 Results on (M, Ω_k, r_d) including SNIa employed by SH0ES 112
6.9 Summary and comparison of the results on (M, Ω_k, r_d) with baseline data sets 113
6.10 Results on (M, Ω_k, r_d) with updated data sets 118
6.11 2D joint analyses results for forecasts 123
6.12 Improvement factor for forecasts 126

7.1 GP reconstructions for GRBs 133

7.2 Calibration results for the 3D Dainotti relation: gaussian priors . . . 137
7.3 Calibration results for the 3D Dainotti relation: impact of the priors 138
7.4 Calibration results for the 3D Dainotti relation: impact of CCH+GP correlations . . . 139
7.5 Calibration results for the 2D Dainotti relation . . . 140
7.6 MCMC results comparison between 3D and 2D Dainotti relations . . 141
7.7 Posteriors for the evolutionary coefficients of the 3D Dainotti relation 142
7.8 Whisker plot for the evolution of the 3D Dainotti relation . . . 143
7.9 The extended distance ladder for GRBs . . . 145

8.1 Calibration results for the Risaliti-Lusso relation . . . 153
8.2 The extended distance ladder for QSOs . . . 154

9.1 3D and 2D BAO data calibrated with r_d^{P18} . . . 165
9.2 $H(z)$ and $M(z)$ from Baseline_3D and Baseline_2D . . . 166
9.3 Posterior distributions of the transition redshift z_t . . . 166
9.4 $H(z)$, $M(z)$ and $q(z)$ from Baseline_3D in $0.09 < z_t < 0.15$ . . . 167
9.5 Curves of $\Delta(z)$ . . . 168
9.6 Minimum χ^2 values for fitting analyses with Baseline_2D . . . 169
9.7 WEC constraints . . . 170
9.8 Constraints on the ratio $\rho_{\rm de}(z)/\rho_{\rm de}^0$ . . . 172

10.1 Constraints on the 2D vs 3D BAO tension . . . 180
10.2 Constraints at 68% C.L. on the Etherington relation . . . 183

11.1 Constraints on the growth index and σ_{12} from RSD and peculiar velocity data . . . 193
11.2 Posterior distributions of H_0 and $R_8 = 8/h$ . . . 198
11.3 Constraints at 68% C.L. on σ_{12} and σ_8 . . . 200

B.1 Example of the application of the skewed-normal fit . . . 266

C.1 Triangle plot for Baseline_3D . . . 268
C.2 Triangle plot for Baseline_2D . . . 269
C.3 Triangle plot for ΛCDM . . . 270
C.4 Triangle plot for w_0w_aCDM . . . 271
C.5 Triangle plot for ΛCDM+$N_{\rm eff}$ . . . 272
C.6 Triangle plot for ΛCDM+$N_{\rm eff} + \Sigma m_\nu$ . . . 273
C.7 Triangle plot for EDE . . . 274

List of Tables

6.1 Results of the $\tilde{\chi}^2_\mu$ test for GP kernels in $H(z)$ reconstruction 100
6.2 Results on (M, Ω_k, r_d) with baseline data sets 110
6.3 Results on (M, Ω_k, r_d) including SNIa employed by SH0ES 111
6.4 Results on (M, Ω_k, r_d) with updated data sets 114
6.5 Errors at 68% C.L. on (M, Ω_k, r_d) from forecasts analyses: pessimistic scenario 122
6.6 Errors at 68% C.L. on (M, Ω_k, r_d) from forecasts analyses: optimistic scenario 122

7.1 Priors adopted for the calibration of 3D and 2D Dainotti relations. . 136
7.2 Constraints on 3D and 2D Dainotti relations parameters 138

8.1 Constraints on Risaliti-Lusso relation parameters 151

10.1 Constraints on the 2D vs 3D BAO tension 181

11.1 Priors for the baseline parameters of the models for σ_8 vs σ_{12} analysis 196
11.2 Fitting results for σ_8 vs σ_{12} analysis 199

A.1 List of CCH measurements 261
A.2 3D BAO data points from 6dFGS, BOSS, eBOSS, WiggleZ and DES Y3 262
A.3 3D BAO data points from BOSS/eBOSS and DESI-DR1 262
A.4 2D BAO data points 263
A.5 Platinum sub-sample for GRBs 264

C.1 Best-fit parameters from Baseline_3D and Baseline_2D analyses . . 267